University of Glasgow

The utility of multimodal imaging platforms to identify antiviral inhibitors to influenza A virus infection

Lauren Orr

Submitted in fulfilment of the requirements for the degree of
Doctor of Philosophy in Virology

MRC – University of Glasgow Centre for Virus Research
School of Infection and Immunity
College of Medical, Veterinary, and Life Sciences
University of Glasgow

October 2024

Abstract

Globally, there are approximately one billion cases of influenza annually, including 3-5 million severe respiratory infections and over 290,000 fatalities. Influenza A viruses (IAVs) have historically caused multiple pandemics, and the continued spillover of highly pathogenic avian IAV into the human population poses a significant public health threat. The rapid development and deployment of effective therapeutics against IAV are crucial for pandemic preparedness. However, the emergence of drug-resistant IAV strains from the use of current antiviral inhibitors necessitates the development of new classes of inhibitors. Conventional *in vitro* antiviral screening assays predominantly rely on 2D immortalised cell lines, though they poorly reflect the microenvironment of the human lung and often demonstrate drug efficacy that does not translate well to complex animal models or clinical trials. Here, we employed primary human bronchial epithelial (HAEC-b) cells in both 2D and 3D culture systems to assess the efficacy of inhibitors against IAV using advanced imaging platforms. 2D antiviral screening assays revealed significant variability in inhibitor efficacy between immortalised canine kidney (MDCK) cells, immortalised primary human bronchial epithelial (HBEC3-KT) cells, and HAEC-b cells. Established IAV antivirals, favipiravir and oseltamivir, exhibited reduced efficacy in HBEC3-KT and HAEC-b cells relative to MDCK cells. Given that host-directed antivirals are less likely to produce drug resistant mutants, we investigated the antiviral potential of epigenetic inhibitors. Two repurposed cancer drugs, CM272 and CM579, demonstrated inhibition of IAV replication across all cell types, achieving complete viral inhibition in HAEC-b cells at a concentration of 10 μM, whilst maintaining cell viability. Additionally, we established two 3D air-liquid interface (ALI) models by differentiating HAEC-b cells on novel bioprinted scaffolds and Transwell inserts. These models, combined with advanced imaging techniques, enabled us to visualise the spatial localisation of IAV replication within the native tissue architecture. Favipiravir was shown to inhibit IAV replication and alter the spatial distribution of viral populations, potentially in a donor-dependent manner. Collectively, these findings underscore the importance of screening antiviral inhibitors in biologically relevant *in vitro* models and highlight the potential of repurposed epigenetic inhibitors as host-directed therapies against IAV.

Table of Contents

List of figures

Chapter 5: Establishing influenza virus inhibitor screening in biologically relevant cells

Chapter 6: Screening epigenetic inhibitors to assess their potential as influenza virus antivirals

List of tables

Acknowledgements

First and foremost, I'd like to thank my supervisors, Dr. Chris Boutell and Prof. Nikolaj Gadegaard. Chris, you encouraged me to pursue my wild scientific ideas and handed me unlimited freedom to explore them. Your guidance and support – whether in matters of science or life – have been invaluable. Your belief in me never wavered, even when mine did. And Ed, for your kindness and support throughout my MSc and PhD, especially in times of difficulty.

A huge thank you to Jo – the best mentor I could have asked for, equipped with infinite patience, sass, and, most importantly, snacks. To wee Chris, your terrible puns were the comic relief we never knew we needed. #TeamRespiratory. To Steven for answering all my silly questions, and Zhousiyu for the dumplings and suspiciously high-percentage alcohol. Thank you to the past members of the Boutell group: Victor, Franzi, Mila, Betty, and Anne. And of course, a massive thanks to Ila for adopting the role as the team mum. You've all been there for me over the years, and I have no doubt that each one of you are destined to succeed – no matter the hurdles.

I would like to give a special shout out to Charlotte and Diego. I'm not sure how I would've survived without you both and the endless supply of Costa and McDonalds treats. Your love, kindness, and unwavering support kept me sane (mostly). I am eternally grateful.

Thank you to Rute, Mickey, and Stephen for keeping me company during my chaotic working hours and bringing some life (and sea shanties) to the mundane 3 a.m. tissue culture grind. Thanks to the Cellbricks team for hosting me in Berlin, especially Aramis, who managed to coax me out of my shell – no small feat! To my friends Lucy, Stephen, and Victoria: thank you for always being just a Spoons, Cathouse, or Ryanair flight away. And to my first scientific role model, Paul, who inspired me to pursue my passions.

Lastly, to my family: thank you for all your support over the years. In hindsight, you might have had a point about starting university at sixteen, but honestly, where's the fun in listening to sensible advice?

COVID-19 impact statement

The COVID-19 pandemic significantly disrupted the first year of my PhD project, which began in October 2020. During lockdown periods, access to laboratory facilities at the MRC – University of Glasgow Centre for Virus Research (CVR) was severely limited due to social distancing measures. Access to tissue culture facilities was especially restricted, directly impacting my ability to perform the necessary cell culture and virus infection assays required for my work on 3D cell culture models in collaboration with our industrial partners. These restrictions had a profound effect on my training and the progression of my project as they were heavily reliant on tissue culture methodologies.

Faced with limited laboratory access, I prioritised fulfilling postgraduate researcher training requirements. I attended online courses offered by the University of Glasgow Graduate School, aligned with the Researcher Development Framework, to complete the 20-credit requirement for PhD students. These courses improved my skills in presentations, coding, public engagement, and data management. Additionally, as part of the Precision Medicine Doctoral Training Programme, I completed 30 credits of MSc-level modules in transferable skills. This included modules from both the University of Glasgow and Edinburgh, focussing on bioinformatic analysis of RNA-sequencing data, image analysis, and statistics. This diverse training expanded my skillset beyond the scope of my PhD project.

In June 2020, a collaboration with Cellbricks was established to explore the potential of their novel bioprinted scaffolds in 3D cell culture systems for SARS-CoV-2 antiviral drug discovery. Initial experimentation on the Cellbricks scaffolds, led by Joanna Wojtus, became part of the CVR's response to the COVID-19 pandemic. Additionally, I underwent containment level 3 training to carry out SARS-CoV-2 assays. The collaboration offered a three-month placement on-site at Cellbricks in Berlin, with the aim of integrating this work with the development of the Membrick model, as detailed in Chapter 3. However, due to COVID-19-related travel restrictions, the placement was postponed until 2023, resulting in an alternative project unrelated to the work presented in this thesis.

I hope these circumstances are taken into consideration in the assessment of my thesis.

Author’s declaration

I, Lauren Orr, declare that, except where explicit reference is made to the contribution of others, this thesis is the result of my own work and has not been submitted for any other degree at the University of Glasgow or any other institution.

Lauren Orr
October 2024

List of abbreviations

2D	Two-dimensional
3D	Three-dimensional
A549	Human lung adenocarcinoma cells
ALI	Air-liquid interface
ARDS	Acute respiratory distress syndrome
Calu-3	Immortalised human bronchial epithelial cells
CC_{50}	50% cytotoxic concentration
CDK4	Cyclin-dependent kinase 4
COVID-19	Coronavirus disease 2019
cRNA	Complementary RNA
DAPI	4′,6-diamidino-2-phenylindole
DMEM	Dulbecco's minimum essential medium
DMSO	Dimethyl sulfoxide
DNA	Deoxyribonucleic acid
DNMT	DNA methyltransferase
ER	Endoplasmic reticulum
FCS	Fetal calf serum
GelMA	Methacrylated gelatin
H&E	Hematoxylin and eosin
HA	Haemagglutinin
HAEC-b	Primary human bronchial epithelial cells
HAMA	Methacrylated hyaluronic
HAT	Human airway trypsin-like protease
HBEC3-KT	Immortalised primary human bronchial epithelial cells
HDAC	Histone deacetylase
h.p.i.	Hours post-infection
hPSC	Human pluripotent stem cells

hTERT	Human telomerase reverse transcriptase
Huh7.5	Immortalised human hepatocyte cells
IAV	Influenza A virus
IBV	Influenza B virus
IC_{50}	50% inhibitory concentration
ICV	Influenza C virus
IDV	Influenza D virus
IFITM	Interferon-induced transmembrane
IFN	Interferon
ISG	Interferon-stimulated gene
JAK-STAT	Janus kinase–signal transducer and activator of transcription
LAIV	Live attenuated influenza vaccines
M1	Matrix protein 1
M2	Matrix protein 2
mAb	Monoclonal antibody
MaCal/09	Mouse-adapted A/California/07/2009
MDCK	Madine-Darby canine kidney epithelial cells
mL	Millilitre
MOI	Multiplicity of infection
mRNA	Messenger RNA
MTS	3-(4,5-dimethylthiazol-2-yl)-5-(3-carboxymethoxyphenyl)-2-(4-sulfophenyl)-2H-tetrazolium)
NA	Neuraminidase
NAI	Neuraminidase inhibitor
NEP/NS2	Nuclear export protein/non-structural protein 2
nm	Nanometre
NP	Nucleoprotein
NS1	Non-structural protein 1
P/S	Penicillin / streptomycin

PA	Polymerase acid
PB1	Polymerase basic 1
PB2	Polymerase basic 2
PBS	Phosphate-buffered saline
PFA	Paraformaldehyde
PFU	Plaque forming units
PML	Promyelocytic leukaemia protein
PR8	A/Puerto Rico/8/1934
RdRp	RNA-dependent RNA polymerase
RFU	Relative fluorescent units
RNA	Ribonucleic acid
SARS-CoV-2	Severe acute respiratory syndrome coronavirus 2
SFM	Serum-free medium
TEER	Transepithelial electrical resistance
TMPRSS2	Transmembrane protease serine S-1 member 2
ULA	Ultra-low adhesion
Vero	African green monkey kidney epithelial cells
vRNA	Viral RNA
vRNP	Viral ribonucleoprotein
WHO	World Health Organization
WSN	A/WSN/1933
µg	Microgram
µL	Microlitre
µm	Micrometre
µM	Micromolar

1. Introduction

1.1. Importance of influenza viruses

Influenza is an acute and contagious respiratory disease caused by influenza viruses (Krammer *et al.*, 2018). In humans, the incubation period, which is the time from infection to symptom onset, ranges from one to four days (Cox and Fukuda, 1998; Lessler *et al.*, 2009). Symptoms can vary widely, some infections are asymptomatic, while others may present with symptoms such as headaches, myalgia, dry cough, sore throat, nasal congestion, fever, and malaise. In children, symptoms can also include nausea, vomiting, and diarrhoea. Typically, symptoms resolve within three to seven days, but a small proportion of cases may develop severe complications such as direct viral pneumonia and indirect secondary bacterial infection, which can lead to respiratory failure, acute respiratory distress syndrome (ARDS), septic shock, and multiorgan failure (MacIntyre *et al.*, 2018). The severity of influenza is influenced by factors including age, health status, genetics, and immune function (Uyeki *et al.*, 2022). While influenza can cause serious illness in previously healthy individuals, certain at-risk groups – such as infants, the elderly, the immunocompromised, and pregnant individuals – are particularly vulnerable (Paules and Subbarao, 2017).

The Global Burden of Disease Study estimated that in 2017, influenza virus caused 54.5 million cases of lower respiratory tract infections, of which 8.2 million severe cases lead to 145,000 deaths (GBD 2017 Influenza Collaborators, 2019). However, other estimates suggest that the annual death toll from influenza may be much higher, ranging from 290,000 to 650,000 (Iuliano *et al.*, 2018). Influenza A viruses are also known to cause pandemics, such as the 1918 Spanish Flu outbreak, which resulted in an estimated 50 million deaths (Johnson and Mueller, 2002). Subsequent pandemics in 1957, 1968, and 2009 demonstrate the ongoing pandemic potential of influenza virus (Taubenberger and Morens, 2010).

Beyond its impact on global health, influenza represents a significant economic burden (Brown *et al.*, 2023). Absenteeism related to seasonal

influenza is estimated to result in a £644m loss to the UK's economy (Romanelli *et al.*, 2023). The cost of an influenza pandemic is predicted to reach $60 billion per year, whereas the proposed cost for effective pandemic preparedness is approximately $4.5 billion (Commission on a Global Health Risk Framework for the Future and National Academy of Medicine, Secretariat, 2016; Sands, Mundaca-Shah and Dzau, 2016). The World Health Organization (WHO) describes pandemic preparedness as “a continuous process of planning, exercising, revising, and translating into action pandemic preparedness and response plans” (World Health Organization, 2011). Ideally, such plans involve many steps including surveillance of circulating strains in humans and animals, sequencing, phenotyping, antiviral testing, and vaccine development (Harrington, Kackos and Webby, 2021).

The incidence of seasonal influenza significantly declined during the severe acute respiratory syndrome coronavirus 2 (SARS-CoV-2) pandemic due to the introduction of mask-wearing, social distancing, and reduced travel (Feng *et al.*, 2021; Groves *et al.*, 2021). However, the reduced circulation of influenza viruses may have led to decreased population-level immunity (Baker *et al.*, 2020). With the relaxation of coronavirus disease 2019 (COVID-19) prevention measures, concerns emerged about increased susceptibility to influenza and the potential for more severe disease (Ali *et al.*, 2022). Indeed, from 2021 onwards, seasonal influenza epidemics have surged, exhibiting unusually late and extended seasonal patterns, resulting in higher case numbers than those observed pre-pandemic (Lee, Viboud and Petersen, 2022). Concurrently, outbreaks of highly pathogenic avian influenza have caused millions of deaths in poultry and wild birds, with spillover cases detected many mammals including cattle, and humans who have been in direct contact with infected animals (Wille and Barr, 2022; Caserta *et al.*, 2024; Centers for Disease Control and Prevention, 2024).

Taken together, influenza continues to be a significant global health threat due to its capacity for rapid spread, its pandemic potential, its potential to cause severe disease, and its substantial economic impact.

1.2. Influenza A virus

1.2.1. Introduction to influenza viruses

Influenza viruses are enveloped, single-stranded, negative-sense RNA viruses belonging to the *Orthomyxoviridae* family. They are classified into four types – A, B, C, and D – based on antigenic differences in their viral proteins (Sugawara *et al.*, 1991; Hause *et al.*, 2014). Among these, influenza A viruses (IAVs) and influenza B viruses (IBVs) are the major cause of seasonal influenza epidemics in humans (World Health Organization, 2023). IAVs have the widest host range, highest mortality rates, and cause the most severe disease (Ghebrehewet, MacPherson and Ho, 2016). IAVs can be further subdivided based on the antigenic properties of two surface glycoproteins: hemagglutinin (HA) and neuraminidase (NA). 18 HA and 11 NA subtypes have been identified, predominately in birds, which can give rise to novel strains with pandemic potential (Shao *et al.*, 2017). IBVs are classified into two antigenically diverse lineages: B/Victoria and B/Yamagata, with the latter trending towards extinction as of 2020 (Rota *et al.*, 1990; Barr and Subbarao, 2024). Unlike IAVs, IBVs lack an established host reservoir and have not been associated with influenza pandemics (Chen and Holmes, 2008; Lee *et al.*, 2019). IBV infections typically causes less severe disease than IAVs, though both viruses frequently circulate together during seasonal influenza epidemics (Webster *et al.*, 1992; Krammer *et al.*, 2018; Tang *et al.*, 2021). Influenza C viruses (ICVs) generally cause less severe disease than IAVs and IBVs, and are less commonly found in humans, predominantly affecting children (Sederdahl and Williams, 2020). Influenza D virus (IDVs) have also been identified, but while antibodies against IDVs have been detected in humans, the virus itself has not been successfully isolated from human infections, suggesting that IDVs primarily infect animals (White *et al.*, 2016).

1.2.2. Influenza A virus virion structure and genome

Within the lipid envelope of IAV virions, there are three main proteins: HA and NA surface glycoproteins, and the matrix protein 2 (M2) ion channel.

Beneath the envelope, the matrix protein 1 (M1) lines the inside of the virion (Petrich *et al.*, 2021). At the core of the virion is its genetic material, comprising eight segments of viral RNA (vRNA), each encoding one or more proteins (Jagger *et al.*, 2012). Each segment forms a helical hairpin structure that is tightly bound by multiple nucleoprotein (NPs), and capped by the polymerase complex: polymerase basic 1 (PB1), polymerase basic 2 (PB2), and polymerase acid (PA) (Pflug *et al.*, 2017). The nuclear export protein (NEP), non-structural protein 1 (NS1), and host proteins, such as cytoskeletal proteins, are also found in the virion (Shaw *et al.*, 2008; Hutchinson *et al.*, 2014). Virion structure is illustrated in Figure 1.1 and the functions of gene products are summarised in Table 1.1.

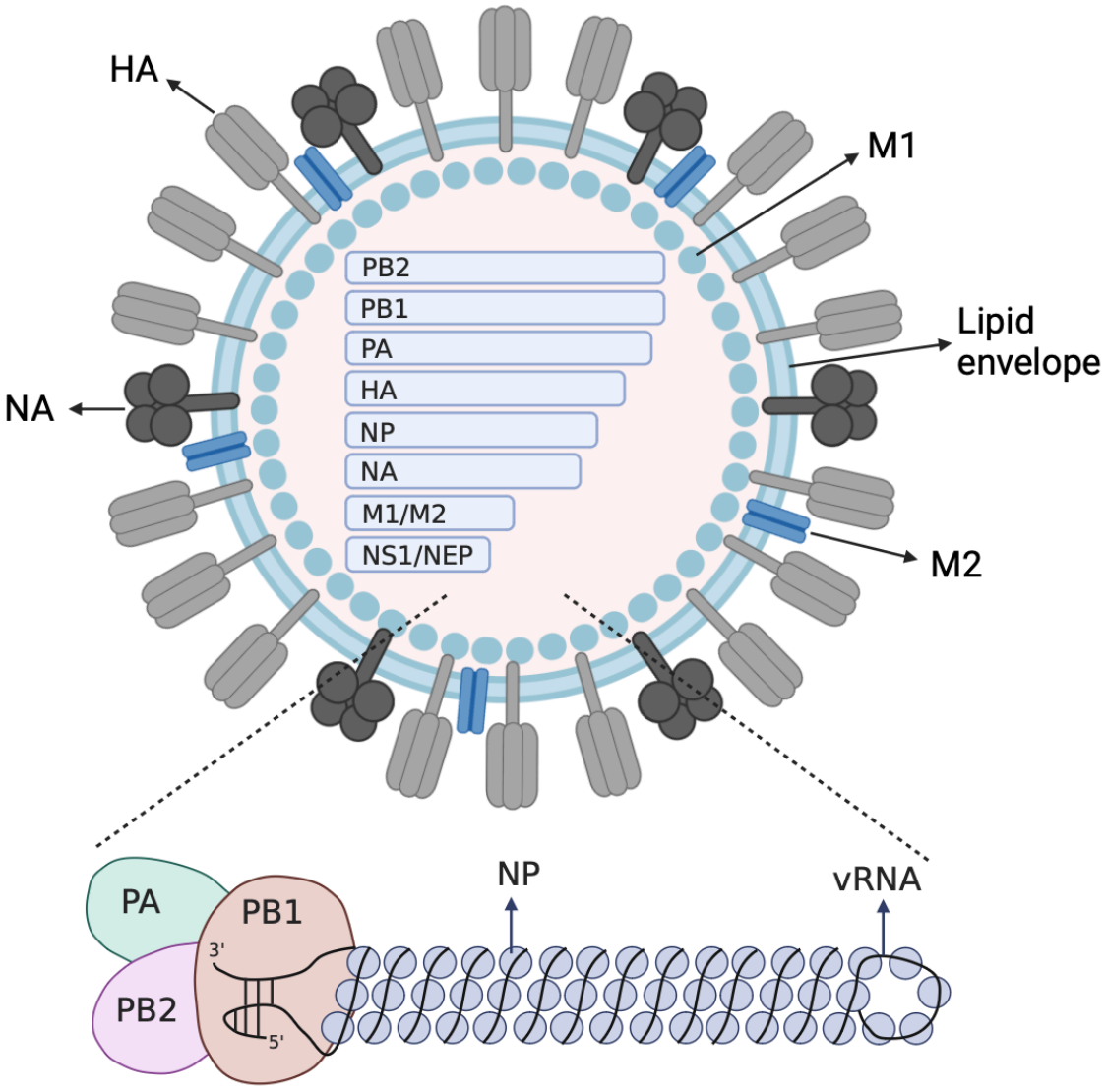

Figure 1.1: IAV virion structure. *Illustration of IAV virion particle containing the key proteins in order of genome segments. Polymerase complex is highlighted. Created on Biorender (https://app.biorender.com) and adapted from (Dou et al., 2018).*

Table 1.1: IAV proteins and functions.

Protein	Segment	Function
PB2	1	Polymerase subunit - recognises cap-binding domain to capture the 5′ cap of nascent host capped mRNA
PB1	2	Polymerase subunit – binds to vRNA, RNA elongation and polymerase activity
PB1-F2	2	Pro-apoptotic activity and interferon agonist, in a +1 alternate reading frame
PB1-N40	2	Unknown, truncated form of PB1
PA	3	Polymerase subunit – viral mRNA endonuclease responsible for cap snatching
PA-X	3	Endoribonuclease affecting host cell shut off, in a +1 ribosomal frameshift
HA	4	Surface glycoprotein – mediates receptor binding and entry
NP	5	Formation of vRNPs, vRNP nuclear import, required for transcription
NA	6	Surface glycoprotein – responsible for virion release
M1	7	Matrix protein – vRNP interaction, RNP nuclear export, viral assembly, and budding
M2	7	Transmembrane ion channel – virion acidification, uncoating, and budding
NS1	8	Interferon antagonist – regulation of host gene expression
NEP/NS2	8	Mediates nuclear export of vRNA

Adapted from Pinto et al. (2021) with additional information: (O'Neill, Talon and Palese, 1998; Varga and Palese, 2011; Wise et al., 2012; Levene, Shrestha and Gaglia, 2021).

1.2.3. Influenza A virus replication cycle

The IAV replication cycle begins with the HA protein on the viral envelope recognising and binding to sialic acid (SA) receptors on the host cell membrane (Weis *et al.*, 1988; Gao *et al.*, 2009). The HA protein is composed of two subunits: HA1 and HA2, linked by disulfide bonds (Laver, 1971; Chen *et al.*, 1998). The HA1 subunit binds to the SA receptor, while HA2 mediates fusion of the virus with the host cell membrane (Wiley and Skehel, 1987; Chen *et al.*, 1998). Human IAV HA proteins preferentially recognise α-2,6 SA receptors, while avian IAV HA proteins preferentially recognise α-2,3 SA receptors (Matrosovich *et al.*, 2000; Skehel and Wiley, 2000; Xiong *et al.*, 2013). The carbon-2 of SA binds to the carbon-6 or 3 of HA1 to form α-2,6 or 2,3 linkages, respectively (Bouvier and Palese, 2008). α-2,6 SA receptors are found in bronchial epithelial cells of the human upper respiratory tract, and α-2,3 SA receptors are located in intestinal epithelial cells and lower respiratory tract cells of birds (Shao *et al.*, 2017). Receptor specificity is thus a critical determinant of host range and can create a barrier to cross-species transmission, although mutations in the HA protein can enable a switch from avian to human receptor specificity (Matrosovich *et al.*, 2000; Imai *et al.*, 2012; Yang *et al.*, 2012; de Graaf and Fouchier, 2014).

IAV enters the host cell via endocytosis, predominantly through clatherin- and clavoline-dependent pathways (Rust *et al.*, 2004; Mazel-Sanchez *et al.*, 2023). The low pH environment of the endosome triggers a conformational change in the HA protein, exposing the HA2 fusion peptide, which inserts into the endosomal membrane, facilitating the fusion of viral and endosomal membranes (Skehel *et al.*, 1982; Bullough *et al.*, 1994; Böttcher *et al.*, 1999). The pH stability of the HA protein is a key determinant of IAV tropism, as endosomal pH differs among host species (DuBois *et al.*, 2011; Zaraket, Bridges and Russell, 2013). Following membrane fusion, the M2 ion channel on the viral envelope opens, allowing hydrogen ions to enter the virus particle, leading to its acidification (Martin and Helenius, 1991; Pinto and Lamb, 2006; Bouvier and Palese, 2008). This acidification disrupts the protein-protein interactions that stabilise viral ribonucleoproteins (vRNPs), resulting in viral uncoating and the

release of vRNPs into the cytoplasm (Martin and Helenius, 1991; Bui, Whittaker and Helenius, 1996; Bouvier and Palese, 2008).

vRNPs contain nuclear localisation signals (NLS) that bind to importin proteins, which transport the vRNPs to the nucleus (Gottlieb *et al.*, 1993; O'Neill *et al.*, 1995; Cros and Palese, 2003; Hutchinson and Fodor, 2012). The replication of the negative-sense genome involves two steps: the synthesis of positive-sense mRNA templates for viral protein translation, and the synthesis of complementary RNA (cRNA) to replicate the negative-sense genomic vRNA (Dou *et al.*, 2018). The viral polymerase complex engages in "cap snatching" to initiate transcription, where the PB2 subunit binds to the 5' caps of nascent host pre-mRNA transcripts, and the PA endonuclease subunit subsequently cleaves 10-13 nucleotides downstream of the cap (Plotch *et al.*, 1981; Li, Rao and Krug, 2001; Dias *et al.*, 2009). The PB2 cap-binding domain facilitates the movement of the capped primer to the PB1 subunit, which extends the viral mRNA transcript (Li, Rao and Krug, 2001; Reich *et al.*, 2014). The viral mRNA tail is encoded in negative-sense vRNA as multiple uracil residues, which is transcribed by the viral polymerase into a positive-sense poly(A) tail (Robertson, Schubert and Lazzarini, 1981; Bouvier and Palese, 2008).

After capping and polyadenylation, viral mRNA binds to M1 and NEP, which binds to exportins, such as chromosome region maintenance 1 protein (CRM1), for nuclear export (O'Neill, Talon and Palese, 1998; Neumann, Hughes and Kawaoka, 2000; Schreiber *et al.*, 2020). PB1, PB2, PA, NP, NS1, NEP/NS2, and M1 are translated on cytosolic ribosomes and are imported back into the nucleus to further assist in the replication cycle and assembly of vRNPs (Dou *et al.*, 2018). HA, NA, and M2 are translated on endoplasmic reticulum (ER) membrane-bound ribosomes, folded in the ER, and trafficked to the Golgi apparatus for post-translational modification (Copeland *et al.*, 1986). The HA protein is transported from the ER as a precursor (HA0) and is cleaved into HA1 and HA2 subunits to become functionally active (Klenk *et al.*, 1975; Lazarowitz and Choppin, 1975). In humans, HA0 is cleaved at the carboxyl terminus of the arginine residue by serine endoproteases secreted by cells in the respiratory tract (Klenk and Garten, 1994; Bertram *et al.*, 2010). Such proteases include transmembrane protease serine S-1 member 2 (TMPRSS2) and human airway

trypsin-like protease (HAT), located at the Golgi and plasma membrane, respectively (Böttcher *et al.*, 2006; Dou *et al.*, 2018). In contrast, avian IAV strains have an insertion mutation at the HA0 cleavage site, allowing ubiquitously expressed proteases to cleave HA0 in multiple organs in birds (Rott *et al.*, 1995; Taubenberger, 1998).

vRNPs are transported to the cell membrane either by diffusion or via Rab11-dependent vesicles that move along actin filaments (Digard *et al.*, 1999; Amorim *et al.*, 2011; Hutchinson and Fodor, 2012; de Castro Martin *et al.*, 2017). Membrane budding is potentially initiated by the accumulation of viral proteins at the lipid bilayer, particularly the M1 protein, which alters membrane curvature (Rossman and Lamb, 2011; Dahmani, Ludwig and Chiantia, 2019). All eight viral segments are packaged into budding virus particles (Hutchinson *et al.*, 2010). To complete the viral replication cycle, the NA protein cleaves SA from the host cell surface, breaking the bond between HA and SA, and releasing the newly formed progeny virus particles from the infected cell (Lai *et al.*, 2010; Long *et al.*, 2019).

1.2.4. Antigenic drift and shift

Both antigenic drift and shift contribute to IAVs ability to evade the immune system and cause recurrent seasonal epidemics and sporadic pandemics. Antigenic drift refers to the gradual accumulation of minor changes in key viral epitopes, principally HA and NA, through point mutations in the viral genome (Both *et al.*, 1983). IAV mutates at a high frequency due its low-fidelity RNA polymerase which lacks proof-reading abilities; therefore, nucleotide substitutions are not corrected, and genome diversity expands upon selection (Parvin *et al.*, 1986; Drake, 1993). When the mutation rate surpasses a critical threshold, slower but more robust replicating viruses tend to outperform their faster-mutating counterparts – a phenomenon termed "survival of the flattest" (Wilke *et al.*, 2001). RNA viruses typically replicate near the edge of an "error catastrophe" limit, which allows them space to explore available mutations whilst maintaining essential viral components (Domingo, 1997; Drake and Holland, 1999). The continually changing epitopes are selected by host immunity, leading to the immune escape from seasonal vaccinations or previous infections (Couceiro, Paulson and Baum, 1993).

In contrast to the gradual changes seen with antigenic drift, antigenic shift involves a sudden and substantial change in the HA and NA proteins, due to the exchange of entire gene segments (Webster *et al.*, 1982). This can lead to the introduction of unrecognised HA or NA surface antigens into the human population from alternate animal reservoirs. This process, known as reassortment, can occur when two different strains of IAV infect the same host cell and exchange genetic material, resulting in a virus with human pandemic potential and increased disease severity (Cox and Subbarao, 2000). Historically, several influenza pandemics have resulted from antigenic shift. The 1918 H1N1 pandemic, which led to an estimated 50-100 million deaths, is believed to have originated from an avian virus that crossed over to humans (Johnson and Mueller, 2002). Subsequent pandemics, 1957 H2N2 and 1968 H3N2, have been linked to avian origins (Kawaoka, Krauss and Webster, 1989; Claas *et al.*, 1998). Swine, which can be infected with both human and avian IAV strains, are proposed to serve as intermediary hosts that facilitate reassortment events (Ludwig *et al.*, 1995). The 2009 H1N1 pandemic originated from pigs, with a

triple-reassortant virus containing swine, avian, and human genes, underscoring the critical role swine play in the emergence of novel IAVs (Trifonov, Khiabanian and Rabadan, 2009; Zeng *et al.*, 2011; Nelson and Worobey, 2018).

1.3. Host immune barriers to influenza virus infection

1.3.1. Physical barriers to infection

To protect the respiratory tract from infection, the epithelium is coated with mucus secreted by goblet cells and submucosal glands (Rubin, 2002; Ganesan, Comstock and Sajjan, 2013). The lower layer of mucus is less viscous than the upper layer, allowing ciliated cells underneath to beat in coordination to expel mucus from the airway (Wanner, Salathé and O'Riordan, 1996; Knowles and Boucher, 2002). Mucus contains mucin glycoproteins which act as decoy receptors for IAV, as they express SA allowing the binding of HA proteins (Rose and Voynow, 2006; Ehre *et al.*, 2012; Zanin *et al.*, 2016; McAuley *et al.*, 2017). IAV becomes trapped within the mucus layer and is removed from the body via mucociliary clearance (Button *et al.*, 2012). To evade this defence, the IAV NA protein constantly removes SA from mucins, allowing the virus to penetrate the mucus layer (Matrosovich *et al.*, 2004b; Cohen *et al.*, 2013).

Epithelial cells also present a physical barrier to IAV infection as they form tight junctions with neighbouring cells to stabilise the epithelium. Tight junctions are composed of proteins including claudins, occludins, junction adhesion molecules, and ZO-1 (Otani and Furuse, 2020). However, IAV can impair this barrier by downregulating key components of tight junctions, such as Claudin-4 (Short *et al.*, 2016). Additionally, IAV NS1 protein has been shown to bind to tight junctions through a PDZ-binding motif, rearranging ZO-1 and occludin, to disrupt barrier integrity (Golebiewski *et al.*, 2011). Damage to the epithelial–endothelial barrier in alveolar cells can lead to fluid leaking into the alveolar space, and the subsequent development of ARDS, highlighting the critical role of the epithelial barrier (Short *et al.*, 2014).

1.3.2. Intrinsic immune response to infection

The intrinsic immune response provides an immediate defence against infection by directly restricting viral replication before the onset of innate immune defences (Bieniasz, 2004). Intrinsic restriction factors are constitutively

expressed, providing cells with a pre-existing level of immunity to infection (Yan and Chen, 2012). Interferon-induced transmembrane (IFITM) proteins play a significant role in inhibiting the cellular entry of a broad range of viruses (Meischel *et al.*, 2021; Majdoul and Compton, 2022). IFITM3, in particular, is constitutively expressed in endosomes and impedes the fusion of IAV and cellular membranes, thus blocking the internalisation of IAV vRNPs (Brass *et al.*, 2009; Desai *et al.*, 2014; Klein *et al.*, 2023). It modulates lipid composition of the endosomal membrane, increasing the energy barrier required for fusion pore formation, resulting in the virus being degraded by host proteases and lipases (Feeley *et al.*, 2011; Everitt *et al.*, 2012; Klein *et al.*, 2023). Other members of the IFITM family, such as IFITM1 and IFITM2, also contribute to the inhibition of IAV entry and can be upregulated to enhance the antiviral response (Meischel *et al.*, 2021).

Another key player in intrinsic immunity is zinc metallopeptidase STE24 (ZMPSTE24), which is constitutively expressed in nuclear membranes and organelles (Fu *et al.*, 2017). While its endoprotease activity is necessary for the biogenesis of lamin A and maintaing structural integrity of nuclear membranes, it also contributes to antiviral defence in conjunction with IFITM proteins (Pendás *et al.*, 2002; Wang *et al.*, 2017). ZMPSTE24 also shows independent inhibition of IAV, proposed to act similarly to IFITM proteins, though it is not further upregulated by IFN (Fu *et al.*, 2017).

The TRIpartite Motif (TRIM) proteins are another class of restriction factors that play a role in defence against both RNA and DNA viruses (Wei *et al.*, 2024). These proteins function as E3 ligases due to their RING domains, facilitating the ubiquitination and degradation of viral proteins (Meroni and Diez-Roux, 2005; Cai *et al.*, 2022). For instance, TRIM22 is constitutively expressed in bronchial epithelial cells and has been shown to target IAV NP for polyubiquitination and degradation (Di Pietro *et al.*, 2013; Charman *et al.*, 2021). Similarly, TRIM41 constitutively expressed in alveolar cells and has been shown degrade NP (Patil *et al.*, 2018). TRIM32 is also constitutively expressed in alveolar cells where it targets IAV PB1 and directly ubiquitinates it, consequently reducing viral polymerase activity (Fu *et al.*, 2015). Thus, intrinsic immune

barriers can inhibit the initiation of infection by blocking the virus from entering a productive infectious cycle.

1.3.3. Innate immune response to infection

The innate immune response begins shortly after infection and plays a crucial role in controlling viral replication and spread. Unlike intrinsic immunity, innate immunity inhibits viral infection following the activation of signalling cascades that directly upregulate the expression of antiviral proteins. Conserved components of IAV vRNA, not typically shared by host cellular RNAs, can act as pathogen-associated molecular patterns (PAMPs) (Chen *et al.*, 2018). These are recognised by host pattern recognition receptors (PRRs), such as retinoic acid-inducible gene-I protein (RIG-I) and Toll-like receptors (TLR) (Rehwinkel *et al.*, 2010). RIG-I-like receptors (RLRs) are constitutively expressed in the cytoplasm of bronchial epithelial cells (Le Goffic *et al.*, 2007). RLRs caspase activation and recruitment domains (CARD) domains are exposed upon recognition of intracellular foreign single-stranded RNA (ssRNA) (Pichlmair *et al.*, 2006; Yoneyama and Fujita, 2007). CARD is ubiquitinated by the E3 ligase TRIM25, which translocates RIG-I to the mitochondria, where it interacts with mitochondrial antiviral signalling protein (MAVS) (Gack *et al.*, 2007). MAVS triggers downstream signal transduction pathways, and recruits transcription factors, such as interferon regulatory factor 3 (IRF3) and nuclear factor kappa-light-chain-enhancer of activated B cells (NF-κB)), to induce expression of type I IFNs (IFN-α/ß) and other proinflammatory cytokines (Seth *et al.*, 2005; Hiscott *et al.*, 2006; Kolakofsky, Kowalinski and Cusack, 2012). IAV infection can further upregulate the expression of RLRs via a positive IFN feedback loop (Le Goffic *et al.*, 2007)

In addition to RLRs, TLR3 and TLR4 also play a key role in the innate immune response to IAV by increasing the expression of IFNs (Ioannidis *et al.*, 2013). TLR3 is constitutively expressed on the surface of bronchial epithelial cells and within endosomes, where it recognises unidentified RNA in phagocytosed cells and double-stranded RNA (dsRNA) in endosomes (Alexopoulou *et al.*, 2001; Guillot *et al.*, 2005; Schulz *et al.*, 2005; Kumar, Kawai and Akira,

2011; Ioannidis *et al.*, 2013). TLR7, on the other hand, recognises IAV ssRNA within the endosomes of plasmacytoid dendritic cells (Diebold *et al.*, 2004; Lund *et al.*, 2004). Both TLR3 and TLR7 induce transcription of type I IFNs via the myeloid differentiation factor 88 (MyD88) and Toll-interleukin-1 receptor-domain-containing adaptor-inducing IFN-β (TRIF) signalling pathways (Alexopoulou *et al.*, 2001; Guillot *et al.*, 2005; Le Goffic *et al.*, 2007; Pang and Iwasaki, 2011).

Following PRR-PAMP recognition, the expression of type I IFNs leads to autocrine and paracrine signalling (Park and Iwasaki, 2020). IFN binds to the IFN-α/β receptor (IFNAR), which is associated with Janus kinases (JAKs) (Randall and Goodbourn, 2008). This creates a conformational change in IFNAR, and the activation of JAK, which phosphorylates signal transducer and activator transcription (STAT) proteins (Stark *et al.*, 1998). Phosphorylated STAT1/2 then recruit IRF-9 to form the ISGF3 complex, which binds to IFN-stimulated response elements (ISREs) to activate the transcription of IFN-stimulated genes (ISGs) (García-Sastre, 2002). Hundreds of ISGs are upregulated in response to IAV infection, including protein kinase R (PKR), MxA/1, and OAS family members, which creates a broadly neutralising intracellular antiviral state. PKR is a serine/threonine protein kinase that binds to IAV dsRNA and phosphorylates eukaryotic translation initiation factor 2 (elF-2), inhibiting the translation of mRNAs (Balachandran et al., 2000). MxA/Mx1 is a GTPase that blocks the nuclear import of vRNPs and binds to IAV NP to inhibit viral transcription (Turan et al., 2004; Xiao et al., 2013). Members of the OAS family, such as OAS3, bind to IAV dsRNA, activating RNase L endoribonuclease activity which cleaves and degrades vRNA (Min and Krug, 2006; Li *et al.*, 2016). Despite these defence mechanisms, IAV has evolved strategies to evade these cellular IFN-mediated immune defences (Table 1.2). For example, the NS1 protein is particularly important in counteracting immune responses activated in response to IAV infection, predominantly through immune antagonism functions, and IAV lacking NS1 demonstrate reduced replication and pathogenicity in IFN-competent *in vitro* and *in vivo* models (García-Sastre *et al.*, 1998; Nogales *et al.*, 2018).

Table 1.2: IAV proteins counteracting innate immune responses.

Protein	Function	Examples
NS1	IFN antagonist	NS1 blocks NF-κB, IRF3, and IRF7 activation to prevent transcription of type I IFNs (Talon *et al.*, 2000; Wang *et al.*, 2000; Geiss *et al.*, 2002).
		NS1 directly binds to ubiquitin ligase TRIM25, inhibiting RIG-I ubiquitination and activation, blocking signal transduction and subsequent type I IFN production (Gack *et al.*, 2009; Rajsbaum *et al.*, 2012).
	ISG antagonist	NS1 binds to dsRNA, blocking activation of IFN-induced protein kinase (PKR), inhibiting phosphorylation of elF-2, thus lifting the PKR translational block (Lu *et al.*, 1995; Min *et al.*, 2007).
		NS1 competes with OAS proteins for dsRNA binding, inhibiting RNase L viral degradation (Min and Krug, 2006).
	Host cell mRNA inhibitor	NS1 interacts with the cleavage and polyadenylation specificity factor (CPSF), an essential component of host cell mRNA processing, inhibiting cleavage and polyadenylation of host cell pre-mRNA, thus preventing their nuclear export and protein synthesis (Fortes, Beloso and Ortín, 1994; Qiu and Krug, 1994; Nemeroff et al., 1998). Nuclear export of vRNAs remains unaffected as the viral polymerase complex is responsible for their polyadenylation (Robertson, Schubert and Lazzarini, 1981).
NP	ISG escape	NP can acquire mutations, particularly at residues 100I/V, 283P, and 313Y, to escape the action of MxA (Mänz *et al.*, 2013). Though escape still results in decreased nuclear import of vRNPs by MxA (Götz *et al.*, 2016).
PB1-F2	IFN antagonist	PB1-F2 interacts with MAVS to inhibit type I IFN production (Varga and Palese, 2011).
PA-X	IFN antagonist	PA-X reduces expression of MAVS-dependent type I IFNs (Rigby *et al.*, 2019).

1.3.4. Epigenetic modulation of immune responses

Regulation and induction of the host immune response to infection can be significantly influenced by reversible epigenetic modification, which can alter gene expression levels. Epigenetic mechanisms are key in determining the accessibility of chromatin for transcription, thereby influencing cellular responses to viral infections.

Within the nucleus, genomic DNA is packaged into chromatin through the binding of histones. The fundamental unit of chromatin is the nucleosome, composed of DNA wrapped around octamers of core histone proteins H2A, H2B, H3, and H4 (Luger, Dechassa and Tremethick, 2012). Histone protein H1 links the DNA and histone octamers to stabilise the complex, and facilitates chromatin folding into higher order structures (Kalashnikova, Rogge and Hansen, 2016; Pan and Fan, 2016). Chromatin folding can render areas of the DNA transcriptionally active or inactive (Grigoryev, 2012). Most chromatin exists as heterochromatin, which is densely folded and transcriptionally inactive (Grewal and Jia, 2007; Morrison and Thakur, 2021). More loosely folded regions of chromatin, termed euchromatin, are more accessible for transcription factors to bind DNA, rendering these areas of chromatin more transcriptionally active (Morrison and Thakur, 2021). External chromatin modifications, such as DNA methylation and histone modification, can regulate gene expression without altering the DNA sequence, and is referred to as “epigenetics” (Kanwal and Gupta, 2012). Prior to viral infection, baseline levels of intrinsic immunity are known to be regulated by the epigenetic state of the cell (Sun and Barreiro, 2020; Felipe Fumero *et al.*, 2024). Upon infection, the epigenome is also known to be modified, further contributing to the levels of innate immune induction observed within cells, including ISG expression (Lefkowitz *et al.*, 2024).

DNA methylation involves the addition of methyl groups to DNA promoters to prevent transcription factor binding and gene expression (Lefkowitz *et al.*, 2024). This process is catalysed by DNA methyltransferases (DNMTs), such as DNMT1, DNMT3a, and DNMT3b, which are referred to as “writers” of epigenetic marks (Moore, Le and Fan, 2013). DNMT1 binds to hemimethylated sites on DNA during replication to copy and maintain methylation patterns throughout

replication cycles, while DNMT3a and DNMT3b are involved in *de novo* methylation (Moore, Le and Fan, 2013; Lefkowitz *et al.*, 2024). Ubiquitin-like containing PHD and RING finger (UHRF) proteins and methylated DNA binding domain (MBD) proteins are “readers” which can recognise epigenetic marks (Cheng *et al.*, 2019). UHRFs recruit DNMT1 to the binding site to maintain methylation, while MBDs help to induce histone modifications to alter the accessibility of DNA for transcription (Bashtrykov *et al.*, 2014; Cusack *et al.*, 2020). DNA demethylation can restore genes to their unmodified state and is catalysed by ten-eleven translocation (TET) methylcytosine dioxygenase proteins, such as TET1, TET2, and TET3, known as “erasers” (He *et al.*, 2011; Wu and Zhang, 2017).

During IAV infection, the expression of DNMT1, DNMT3a, and DNMT3b is downregulated, leading to changes in the methylation status of genes encoding inflammatory proteins (J. Fang *et al.*, 2012; Mukherjee, Vipat and Chakrabarti, 2013; Zhao *et al.*, 2023). For instance, DNMT1 and DNMT3b methylate the promoter of IL-32, a proinflammatory cytokine, silencing its transcription in uninfected cells (Li *et al.*, 2010). However, during IAV infection, the binding of DNMT1 and DNMT3b to the IL-32 promoter is reduced, increasing IL-32 expression which inhibits viral replication (Li *et al.*, 2008, 2010). Similarly, demethylation of IL-17C and IL-13 gene promoters during IAV infection leads to the upregulation of these interleukins, which increasing the production of proinflammatory cytokines and chemokines (Mukherjee, Vipat and Chakrabarti, 2013). Furthermore, the UHRF1 protein represses the production IFN-ß and ISGs, such as IFI30, OAS1l, OAS3, and Mx1 in uninfected cells (Gao *et al.*, 2021). IAV infection reduces UHRF1 expression, leading to the demethylation of the IFN-ß promoter and increased IFN-ß transcription. Thus, changes in host DNA methylation induced by IAV infection can increase the production of IFNs, ISGs, and interleukins to reduce viral replication.

In addition to DNA methylation, modifications of histone proteins play a critical role in regulating gene expression. The amino-terminal domains of histones, termed histone tails, serve as scaffolds for the assembly of protein complexes and are subject to post-translational modifications to control gene expression (Bowman and Poirier, 2015). Modifications involve the binding of

acetyl or methyl groups to histone tails which can alter the configuration of chromatin, thereby influencing the accessibility of DNA for transcription (Miller and Grant, 2013). Histone methylation, acetylation, and deacetylation is mediated by histone methyltransferases, histone acetyltransferases, and histone deacetylases (HDAC). HDACs, particularly HDAC1, have been shown to upregulate the expression of type I IFNs and ISGs, such as ISG15, ISG54, IFITM1, IFITM2, IFITM3, and viperin, to increase the innate immune response to IAV infection (Nagesh and Husain, 2016). Additionally, HDAC6 acetylates microtubules, decreasing the trafficking of IAV HA to the plasma membrane, thus preventing viral budding (Husain and Cheung, 2014). Thus, host histone modification can reduce IAV replication by increasing the production of IFNs and ISGs and reducing microtubule trafficking.

Epigenetic modifications at the RNA level, such as methylation, can also alter gene expression. The post-transcriptional N6-methyladenosine (m^6A) modification methylates the N6 position of adenosine in RNA and is known to impact mRNA function (X. Liu *et al.*, 2024). Methyltransferase dimers, METTL3/METTL14, and the co-factor Wilms tumour 1-associated protein (WTAP) interact to form the methyltransferase complex, which recognise and methylate RNA (Flamand, Tegowski and Meyer, 2023). The binding of WTAP promotes the complex to localise to mRNA-rich sites in the nucleus (Ping *et al.*, 2014). Upon viral infection, TBK1, a key component of the type I IFN signalling pathway, phosphorylates METTL3 to enhance its catalytic activity (Chen *et al.*, 2022). METTL3 stabilises IRF3 transcripts through m^6A modification to promote their expression, subsequently inducing IFN-β production and the expression of ISGs. Thus, host cell regulation of RNA methylation can increase the immune response to viral infection and reduce viral replication.

While host cells use epigenetic modifications to enhance immune responses, viruses have evolved strategies to manipulate host epigenetic machinery to their advantage (Locatelli and Faure-Dupuy, 2023). IAV heavily relies on host cellular machinery for its lifecycle and there is a growing body of evidence that IAV alters host epigenetics to reduce IFN production and enhance viral replication (Table 1.3) (Keshavarz *et al.*, 2021). Although much is known about epigenetic manipulation by DNA viruses, the strategies employed by IAV

are less explored and represents an important area of ongoing research (Hu, Zhang and Liu, 2020). Investigating the epigenetic regulation of the antiviral immune response to IAV infection, and proviral antagonism by IAV, is critical to better understand host-virus interactions and to identify new classes of inhibitors targeting epigenetic modification (X. Liu *et al.*, 2024).

Table 1.3: IAV exploitation of host cell epigenetics.

Epigenetic mechanism	Examples
DNA methylation	IAV NS1 binds DNMT3B and transports it to the cytoplasm for ubiquitination and degradation, preventing the methylation of suppressors of JAK-STAT signalling. This results in the overexpression of suppressors of JAK-STAT signalling which reduce the host cell immune response and enhance viral replication (Liu *et al.*, 2019).
RNA methylation	IAV HA, NA, M1, M2, and NP mRNAs contain m^6A sites and METTL3-mediated m^6A modification increased viral gene expression and replication, potentially by stabilising transcripts (Courtney *et al.*, 2017).
	IAV infection upregulates the expression of YTHDC1 – an m^6A "reader". YTHDC1 binds an m^6A site on NS1 mRNA at a splice site to inhibit splicing of NS1, decreasing NEP expression, thus increasing viral replication (Zhu *et al.*, 2020, 2023).
Histone methylation	Type I IFN produced upon IAV infection upregulates Setdb2, an ISG and lysine methyltransferase that trimethylates H3K9, which silences Mx1 and Isg15 *in vivo* and IL-2 and IL-10 *in vitro* (Kroetz et al., 2015; Schliehe et al., 2015).
Histone demethylation	IAV decreases H3K79 methylation, which suppresses IFN-β and ISGs Mx1 and ISG56 (Marcos-Villar *et al.*, 2018).
Histone acetylation	IAV downregulates HDAC1 expression by promoting its degradation, inhibiting STAT1 and ISG expression of IFITM3, ISG15, and viperin (Nagesh and Husain, 2016; Husain, 2024).
	IAV NP interacts with HDAC1, enhancing the acetylation of IAV proteins, promoting their stability and function to enhance viral replication (Chen *et al.*, 2017).
	HDAC8 enhances endocytosis and acidification of IAV virions by maintaining microtubule organisation for virion transport (Yamauchi *et al.*, 2011).
Histone deacetylation	IAV capsids mimic misfolded proteins, using ubiquitin chains to recruit HDAC6 to fusion sites, allowing the uncoating of capsids and vRNP entry to the cytosol (Banerjee *et al.*, 2014).
Histone mimicry	The C-terminus of IAV NS1 protein shares a similar sequence to histone H3K4, acting as a histone mimic to downregulate the transcription of type I IFNs and ISGs IFIT1 and IFI6 (Marazzi *et al.*, 2012; Qin *et al.*, 2014).

1.4. Vaccines

Vaccination is the primary strategy for preventing influenza infection, reducing severe disease, and managing the spread of drug-resistant strains (Krammer and Palese, 2015). The WHO Global Influenza Surveillance and Response System (GISRS) continuously monitors circulating strains to recommend the seasonal reformulation of vaccine compositions to keep pace with antigenic drift (Salk and Suriano, 1949; Payne, 1953; Ziegler *et al.*, 2022). However, vaccine composition decisions are made 9-12 months before the intended influenza season, and the circulating strains may differ from the predicted strains, which reduces vaccine efficacy (Carrat and Flahault, 2007; Treanor, 2020). Currently, licenced influenza vaccines target the HA protein to produce neutralising antibodies that block viral attachment to the host cell SA receptor (Houser and Subbarao, 2015; Han *et al.*, 2019). Since HA is under positive selection to escape neutralisation by pre-existing antibodies, the virus can mutate to evade immune detection (Chai *et al.*, 2016). There are three classes of licenced vaccines: live attenuated, inactivated, and recombinant HA vaccines, all of which are multivalent, comprising both influenza A and B virus components.

Live attenuated influenza vaccines (LAIV), Fluenz and Flumist, are administered intranasally and contain live viruses with temperature sensitive/attenuating mutations (Gould, Easton and Dimmock, 2017). These quadrivalent vaccines include a mix of H1N1 and H3N2 IAV and two lineages of IBV on an Ann Arbor backbone (Carter and Curran, 2011). LAIV viruses replicate at the cooler temperatures of the nasal cavity but are restricted by the higher temperatures of the lower respiratory tract (Chan *et al.*, 2008; Fischer *et al.*, 2015). It is recommended for children aged 2-18 years and provides protection for up to a year, although it is not suitable for individuals with egg allergies (Mohn *et al.*, 2015; UK Health Security Agency, 2024). The effectiveness of LAIV ranges from 18-48%, with suboptimal efficacy attributed to the mismatches between vaccine antigens and circulating strains (Caspard *et al.*, 2017).

Recombinant vaccines, Flublok and Fluzone, are administered intramuscularly and contain HA proteins expressed in insect cells (Baxter *et al.*,

2011). These trivalent and quadrivalent vaccines contain H1N1 and H3N2 IAV and 1 to 2 lineages of IBV (Baxter *et al.*, 2011; Kackos *et al.*, 2023). The manufacturing process is shorter than LAIV and does not contain egg proteins (Cox, Patriarca and Treanor, 2008). They are recommended for individuals over 6 months old, and shows protection in immunocompromised individuals over 65 year old (Keitel *et al.*, 1994, 1996; Hsiao *et al.*, 2023). Lastly, inactivated influenza vaccines, such as Flulaval, are trivalent and quadrivalent vaccines containing a mix of H1N1 and H3N2 IAV and 1 to 2 lineages of IBV. They are also licenced for individuals over 6 months old, immunocompromised individuals, and individuals over 65 years (Kieninger *et al.*, 2013; Tinoco *et al.*, 2014; Bekkat-Berkani *et al.*, 2016). In 2024, the WHO recommended trivalent formulations of both inactivated and recombinant vaccines for countries located within the northern hemisphere (World Health Organization, 2024).

Standard influenza vaccines necessitate continuous monitoring and predictions of circulating strains to formulate the most effective vaccine for the upcoming season. Given their varying efficacy, the development of a universal vaccine is of high priority. A successful universal vaccine would provide broad and long-term immunity against all strains by targeting conserved antigens. Research is ongoing, with clinical trials exploring vaccines targeting the exterior of M2, the stem of HA, NP, and M1, to assess their ability to produce cross-protective antibody responses (Francis *et al.*, 2015; van Doorn *et al.*, 2017; Boyoglu-Barnum *et al.*, 2021; Mezhenskaya *et al.*, 2021; Nachbagauer *et al.*, 2021). Moreover, next generation influenza mRNA vaccines are currently being developed due to their success in the COVID-19 pandemic (Isakova-Sivak and Rudenko, 2024). These vaccines can be produced quicker than traditional vaccinations, allowing for a more rapid response potential IAV outbreaks (Kackos *et al.*, 2023). Quadrivalent mRNA vaccines containing a mix of H1N1 and H3N2 IAV and 2 lineages of IBV have shown promise in recent phase I and II clinical trials, and pentavalent vaccines containing an additional H3N2 strain elicited enhanced antibody responses (I. T. Lee *et al.*, 2023; Hsu *et al.*, 2024). Nonetheless, immunity from previous infections and currently licenced vaccinations wanes over time due to antigenic drift and shift in circulating strains. The COVID-19 pandemic highlighted issues with vaccine supply chains,

underscoring the need for a broader range of effective therapeutics as part of global pandemic preparedness (Alam *et al.*, 2021; Shet *et al.*, 2021).

1.5. Antivirals

Current antiviral strategies against IAV can target viral proteins directly, or indirectly, by targeting the host's cellular machinery required to support viral replication. Licenced antiviral drugs are designed to inhibit various stages of the IAV lifecycle, including entry, uncoating, replication, assembly, and budding.

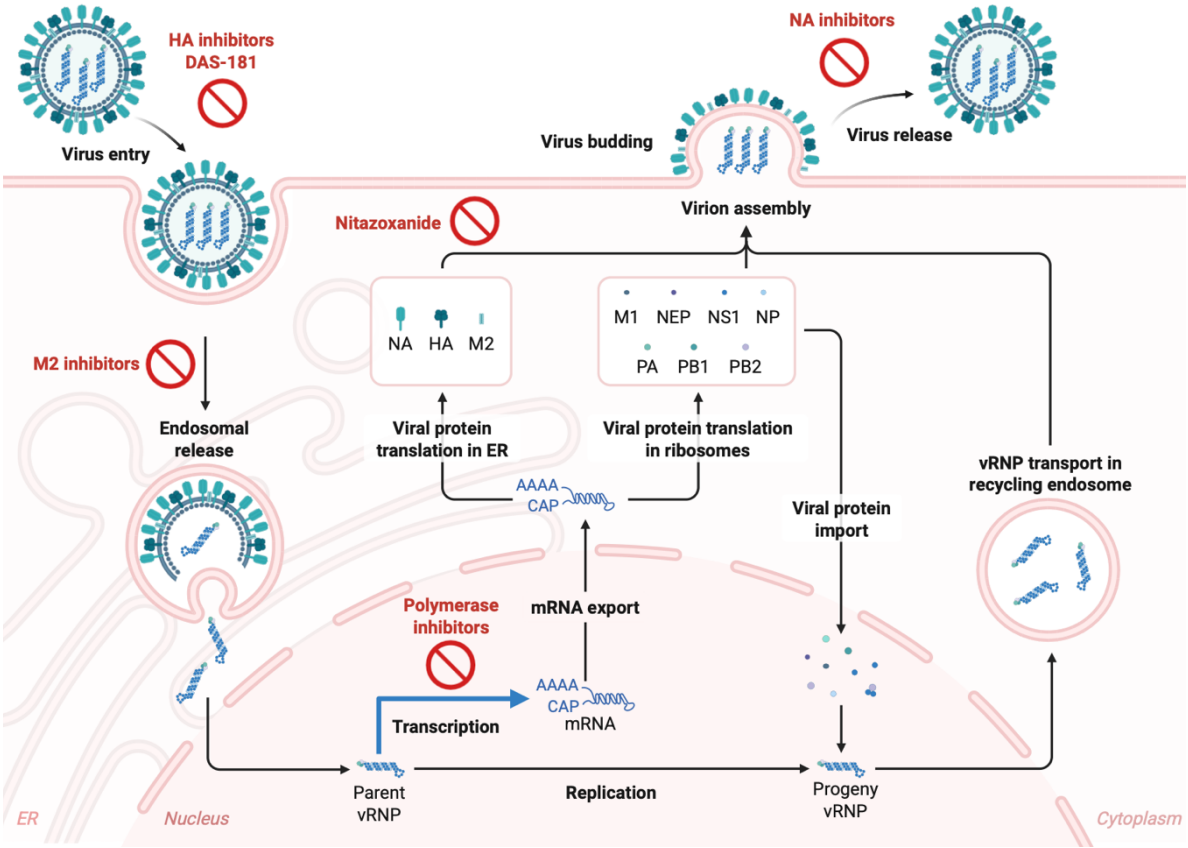

Figure 1.2: Mechanism of action of influenza virus antivirals. *Illustration of influenza virus lifecycle, highlighting the stages inhibited by HA, NA, M2, polymerase direct acting antivirals, and host directed antivirals DAS-181 and nitazoxanide. Adapted from template on Biorender (https://app.biorender.com).*

1.5.1. M2 protein inhibitors

Adamantanes, such as amantadine (Symmetrel®) and rimantadine (Flumadine®), were the first class of antiviral drugs approved for the treatment of influenza. These drugs block the M2 ion channel, preventing the influx of hydrogen ions into the viral interior, which is necessary for lowering the pH. This prevents viral uncoating and the subsequent release of viral RNA into the host cell. These inhibitors are effective only against IAV and must be administered within 48 hours of symptom onset to be effective. However, the emergence of drug-resistant variants has greatly reduced their clinical utility. By the 2005/2006 flu season, 90% of circulating strains were resistant to adamantanes (Bright *et al.*, 2006). These resistant isolates are genetically stable, transmissible, and equally as pathogenic as wild type IAV, and thus these inhibitors are no longer a recommended treatment.

1.5.2. Neuraminidase inhibitors

Neuraminidase inhibitors (NAIs) prevent the release of progeny viruses from infected cells by blocking the cleavage of SA, thus inhibiting further viral spread in the respiratory tract (Gubareva, Kaiser and Hayden, 2000). Two NAIs, zanamivir (Relenza, GG167) and oseltamivir phosphate (Tamiflu, GS4 104), are authorised for use in the European Economic Area for treatment and prophylaxis of influenza disease. These drugs, which are sialic acid analogues, fit into active site pocket of NA, acting as reversible competitive inhibitors of both IAV and IBV NAI treatment administered within the first 48 hours after symptom onset has been shown to shorten the duration of disease (Aoki *et al.*, 2003; Jefferson *et al.*, 2014; Dobson *et al.*, 2015). While NAIs are generally less likely to induce resistance compared to M2 inhibitors, mutations in NA altering the architecture of the active site, such as the His274Tyr mutation, weaken oseltamivir binding and have led to resistant strains emerging (Brown, 2000; Collins *et al.*, 2009; Bloom, Gong and Baltimore, 2010). NAI resistant mutants can be obtained when serial passaging in the presence of the drug, and more concerningly 100% of circulating strains in Japan were resistant to Tamiflu during the 2008/2009 flu season (Tai *et al.*, 1998; Baranovich *et al.*, 2010).

1.5.3. Polymerase inhibitors

Polymerase inhibitors target the subunits of the influenza virus RdRp, including PB1, PB2, and PA. Favipiravir (T-705) is recognised as a purine nucleoside analogue and gets incorporated into the nascent RNA strand (Sangawa *et al.*, 2013). This inhibitor competitively prevents adenosine and guanine triphosphates from being incorporated instead, thus inhibiting RNA elongation by PB1. Furthermore, favipiravir also induces lethal mutagenesis by increasing nucleotide mutation frequency, resulting in functionally impaired proteins (Baranovich *et al.*, 2013; Vanderlinden *et al.*, 2016). Favipiravir exhibits broad inhibition of RNA viruses, effective against IAV, IBV, ICV, IDV, and NAI and amantadine resistant strains (Furuta *et al.*, 2002a; Mishin *et al.*, 2019). There have been few reports of resistance to favipiravir, with only two *in vitro* studies observing resistant strains containing a mutation in the IAV H7N9 PB1 gene and compensatory mutation in PA gene, which do not show a viral fitness advantage *in vivo* (Goldhill *et al.*, 2018, 2021; Komeno *et al.*, 2022). Favipiravir is an approved anti-influenza treatment in Japan, and no resistant variants have been found in phase IIb and III clinical trials (Takashita *et al.*, 2016; Mu *et al.*, 2023)

Baloxavir marboxil (S-033188) inhibits the PA protein by binding to its endonuclease domain, blocking its cap-dependent endonuclease activity (Noshi *et al.*, 2018; Omoto *et al.*, 2018). Baloxavir is effective against IAV, IBV, ICV, and IDV, and is approved for use in Japan and the USA (Mullard, 2018; Mishin *et al.*, 2019). However, resistance due to PA amino acid substitutions has been observed *in vitro*, and up to 8% of IAV strains monitored in Japan contained a PA I38 substitution responsible for resistance, even in patients without prior inhibitor exposure, indicating human-to-human transmission of resistant strains (Noshi *et al.*, 2018; Omoto *et al.*, 2018; Gubareva *et al.*, 2019; Takashita *et al.*, 2019). Pimodivir (VX-787) is a PB2 inhibitor that binds to its cap-snatching domain, preventing RNA binding (Clark *et al.*, 2014). It inhibits IAV, including strains resistant to NAIs and amantadines (Byrn *et al.*, 2015). However, PB2 mutations conferring reduced susceptibility to pimodivir have been observed *in vitro* and in phase IIb clinical trials (Byrn *et al.*, 2015; Finberg *et al.*, 2019).

1.5.4. Hemagglutinin inhibitors

Monoclonal antibodies (mAbs) target the globular head or stalk regions of the HA protein. Importantly, antibodies targeting the HA stalk domain usually exhibit broad-spectrum activity against multiple subtypes (Throsby *et al.*, 2008; Kirkpatrick *et al.*, 2018). For example, mAbs like 9H10 and CR6261 recognise conserved pockets on the HA stalk, preventing pH-mediated conformational changes in HA, thus inhibit HA-dependent fusion of the viral and endosomal membranes, and disrupting viral egress (Ekiert *et al.*, 2009; Tan *et al.*, 2014). mABs have shown inhibition of IAV and IBV *in vitro* and *in vivo*, with some demonstrating reduced disease severity in phase II clinical trials (DiLillo *et al.*, 2014; Tan *et al.*, 2014; McBride *et al.*, 2017). Additionally, NA-targeting mAbs have demonstrated inhibition of IAV and IBV (Yasuhara *et al.*, 2022).

Umifenovir (Arbidol, DB13609) inhibits HA-induced virus-cell membrane fusion by binding to the HA stem and stabilising it before fusion, thus preventing the required conformational change for membrane fusion in the endosome (Kadam and Wilson, 2017). Umifenovir has demonstrated inhibition of IAV and IBV *in vitro* and *in vivo*, including amantadine-resistant strains, with no reported resistance (Leneva *et al.*, 2005, 2016; Shi *et al.*, 2007). Randomised control trials have shown umifenovir treatment shortens the time to relieve clinical symptoms, and is licenced for use in Russia and China (Wang *et al.*, 2004; Kolobukhina *et al.*, 2008; Blaising, Polyak and Pécheur, 2014; Pshenichnaya *et al.*, 2019).

1.5.5. Host-directed antivirals

The emergence of drug-resistant viruses necessitates the development of novel inhibitors targeting non-viral components, such as host cellular factors (Watanabe *et al.*, 2014). Host-directed antivirals have gained traction in recent years, particularly because they are less likely to produce drug-resistant mutants (van de Wakker, Fischer and Oosting, 2017; N. Kumar *et al.*, 2020). For example, Fludase (DAS-181) is an enzyme-based sialidase fusion protein which binds to respiratory epithelial cells and removes α2,6- and α2,3-linked SA receptors on

the surface to prevent HA attachment (Chan *et al.*, 2009). It inhibits IAV and IBV *in vitro* and *in vivo*, including NAI-resistant strains (Malakhov *et al.*, 2006; Belser *et al.*, 2007; Triana-Baltzer *et al.*, 2009). While phase II clinical trials showed a reduction viral load, the treatment did not significantly affect the severity of clinical symptoms, and prolonged use led to adverse effects (Moss *et al.*, 2012; Zenilman *et al.*, 2015).

Nitazoxanide inhibits HA glycosylation and transport from the ER to the Golgi apparatus, preventing the maturation of HA, and ultimately preventing virion assembly at the plasma membrane (Rossignol, 2014). It was originally used as antiparasitic drug but has been repurposed, showing inhibition of IAV and IBV, including NAI-resistant strains, with no resistance reported (Rossignol, 2014; Tilmanis *et al.*, 2017; Stachulski *et al.*, 2021). Phase IIb and III clinical trials have shown that it shortens the time to relieve clinical symptoms and reduces viral titres (Haffizulla *et al.*, 2014). Host-directed antivirals offer alternative therapeutic strategies by targeting essential host factors involved in the viral lifecycle. These approaches may overcome limitations associated with direct-acting antivirals; however, further research is required to explore potential host targets.

1.6. Cell culture models for influenza virus drug discovery

1.6.1. 2D vs. 3D cell culture models for antiviral drug discovery

In vitro cell culture is a crucial component in the drug development process. The majority of cell cultures used in drug discovery utilise two-dimensional (2D) monolayers of cells grown on flat plastic surfaces. For decades, 2D cell cultures have been instrumental in providing significant insights into disease mechanisms and drug discovery processes (Kapałczyńska *et al.*, 2018; Roman *et al.*, 2023). 2D models typically use laboratory-adapted, transformed, or immortalised cell lines, such as Madin-Darby canine kidney epithelial (MDCK) cells and human lung alveolar adenocarcinoma (A549) cells. Cell lines are highly valuable in virology research due to their susceptibility to infection by a wide range of viruses and their ability to produce high viral titres (Powell and Waters, 2017). 2D cultures offer several advantages: they are relatively inexpensive, highly replicable, and results are easy to interpretate (Kaur and Dufour, 2012). These features make them valuable for high-throughput drug screening, particularly in the initial stages of antiviral drug discovery. However, immortalised cell lines have dysregulated antiviral immune responses and are highly permissive to infection, thus not predictive of disease outcome in humans (Stojdl *et al.*, 2000). Primary cells isolated from biopsies can also be used, demonstrating more complex immune responses in comparison to transformed cell lines, resulting in increased viral restriction (Hsu *et al.*, 2012). Though, despite retaining many *in vivo* properties, they have limited life spans and are costly (Richter *et al.*, 2021). 2D cell cultures also lack cellular differentiation, so cannot mimic tissue structures and functions of the human lung (Ross *et al.*, 2007; Bhowmick *et al.*, 2018). Ultimately, 2D cultures are not physiologically representative of the human lung environment, and, as a result, often show drug efficacy that does not translate effectively to more complex, biologically relevant systems (Breslin and O'Driscoll, 2016; Cacciamali, Villa and Dotti, 2022; Sun *et al.*, 2022; Zarkoob *et al.*, 2022). A recent example being hydroxychloroquine, which demonstrated inhibition of SARS-CoV-2 in multiple 2D cell lines, though proved ineffective in human three-dimensional (3D) cell cultures, animal models, human clinical trials (Funnell *et al.*, 2020; Yuan *et al.*,

2022). While 2D cell cultures provide a useful starting point, promising drug candidates must be further tested in more biologically relevant systems.

Animal models are widely used to study IAV infection *in vivo* and are essential to obtain preclinical drug data (Oh and Hurt, 2016). Mice, ferret, guinea pig, hamster, chicken, swine, feline, and canine models have proven invaluable in studies of IAV pathogenesis, vaccine efficacy, antiviral drug efficacy, transmission, and surveillance (Nguyen, Rollon and Choi, 2021). Ferrets are considered to be the most suitable model for IAV antiviral studies as they can be infected with human IAV, demonstrate similar human lung pathology and SA receptor distribution, and exhibit similar clinical symptoms (Jia *et al.*, 2014; Belser *et al.*, 2016; Oh and Hurt, 2016). Additionally, ferret-to-ferret transmission of IAV can be monitored to investigate the efficacy of antivirals to limit virus transmission (L. Y. Y. Lee *et al.*, 2020). However, studies using ferret models are limited by small sample sizes, biological variability, high costs, and most importantly, ethical concerns (Oh and Hurt, 2016). Alternative animal models capable of overcoming some of these limitations are often less susceptible to human IAV, not suitable for transmission studies, or present less clinical symptoms (Nguyen, Rollon and Choi, 2021). Importantly, most drugs demonstrating efficacy in animal models fail in the clinical phases of drug development (Van Norman, 2019; Loewa, Feng and Hedtrich, 2023). Since no single animal model can accurately recapitulate influenza or predict drug efficacy in humans, the use of more accurate preclinical models is required to increase the success of clinical trials. Moreover, the use of complex *in vitro* models prior to animal testing adheres to the 3Rs (reduction, replacement, and refinement) framework by reducing the number of animal models required for drug research (Jaroch, Jaroch and Bojko, 2018).

To bridge the gap between 2D cultures and animal models, 3D lung models can be deployed. These models maintain the spatial architecture of the lung and preserve the natural cell shape, offering several advantages over 2D models (Bhowmick *et al.*, 2018). Primary cells can be differentiated into tissues containing multiple cell types maintained by tight junctions, creating a polarised structure which can mimic the microenvironment of the lung (Whitcutt, Adler and Wu, 1988; Ross *et al.*, 2007; BéruBé *et al.*, 2010). 3D cultures share similar

transcriptional profiles to human lung tissue, more closely resembling the *in vivo* state compared to 2D cultures (Dvorak *et al.*, 2011; Pezzulo *et al.*, 2011). Additionally, cellular differentiation increases the expression of α-2,6-linked SA receptors and HAT proteases to levels comparable to human tissues which allows better replication of human IAVs, and alters innate immune responses to IAV infection compared to undifferentiated cells (Matrosovich *et al.*, 2004a; R. W. Y. Chan *et al.*, 2010). The ciliary movements in 3D cultures mimic the mucociliary clearance observed in the human lung, showing decreased IAV replication by blocking viral attachment (Fu *et al.*, 2018). Importantly, 3D cultures often provide results that are more predictive of *in vivo* outcomes, as they tend to be more resistant to drug treatments compared to their 2D counterparts (Ponce de León and Barrera-Rodríguez, 2005; Balharry, Sexton and BéruBé, 2008; Wen *et al.*, 2013; de la Puente *et al.*, 2015; Breslin and O'Driscoll, 2016; Fang and Eglen, 2017). Additionally, the toxicity profiles and metabolism of drugs in 3D cell cultures is more predictive of human outcomes than in 2D models (Yamaya *et al.*, 1992; Pampaloni, Reynaud and Stelzer, 2007; Ramaiahgari *et al.*, 2019). Despite their advantages, 3D cell cultures also present challenges in drug discovery. In 2D cell monolayers, all cells are equally exposed to the drug, making it easier to interpret results. In 3D cultures, however, the drug may only impact the cells on the surface or treated section, complicating reproducibility and result interpretation (Breslin and O'Driscoll, 2016). 3D cultures are more expensive and labour intensive, making them less suitable for high-throughput screening – though efforts to increase their throughput capacity are ongoing (Wang and Jeon, 2022). Therefore, initial screening should be conducted with 2D cell cultures to identify lead compounds, with further validation using 3D models prior to animal testing. This combined approach utilising both 2D and 3D models allows for a comprehensive *in vitro* drug evaluation, balancing high-throughput drug screening capabilities with the need for physiologically relevant data.

1.6.2. 3D lung models for influenza virus drug discovery

Several 3D lung models – such as air-liquid interface (ALI) cultures, organoids, lung-on-a-chip systems, and bioprinting technology – are increasingly being used to simulate the complex microenvironment of the human lung (Table

1.4). These models use differentiated lung cells, which secrete serine proteases to allow IAV multicycle replication without the requirement for endogenous proteins, in contrast with 2D cultures (Zhou *et al.*, 2018). ALI cultures are created by harvesting primary epithelial cells from human lung biopsies and differentiating them on Transwell inserts (Fulcher and Randell, 2013). The cells are grown on the apical chamber and maintained in cell culture until reaching confluency, then medium is removed from the apical chamber, exposing the cells to air which triggers their differentiation process (Javaherian, Paz and McGuigan, 2014; Silva *et al.*, 2023). These cells differentiate into a tissue containing multiple epithelial cell types, including ciliated, goblet, and basal cells, mimicking the natural composition of the lung (Silva *et al.*, 2023). ALI cultures exhibit gene expression patterns similar to those observed in human lung epithelial tissue samples, making them a valuable model for studying IAV replication and drug responses (Ross *et al.*, 2007; Dvorak *et al.*, 2011; Pezzulo *et al.*, 2011).

Lung organoids are derived from human pluripotent stem cells (hPSCs), which are isolated from patient lung tissue and differentiated (Vaughan *et al.*, 2006; Rock *et al.*, 2009; Dye *et al.*, 2016). These cells are initially grown in a monolayer and manipulated to develop into cell types corresponding to the human airway, which then self-assemble into free-floating spheroids (Miller *et al.*, 2019). The spheroids are embedded in a 3D Matrigel droplet, forming an organoid that consists of an outer layer of basal cells, a luminal layer of ciliated cells, and goblet and secretory cells within (Kühl *et al.*, 2023). Lung organoids demonstrate gene expression profiles similar to *in vivo* lung tissues (W. Lee *et al.*, 2023). They have been successfully utilised in IAV research, with viral replication kinetics comparable to those observed in human *ex vivo* bronchus cultures (Hui *et al.*, 2018; Zhou *et al.*, 2018; Salgueiro *et al.*, 2022).

Lung-on-a-chip models are miniature lung systems on a microfluidic cell culture chip created using microfabrication techniques (Khademhosseini *et al.*, 2006). Primary human airway epithelial cells are differentiated into tissues on the chip, with a microfluidic device containing upper and lower channels surrounding the tissue that supply nutrients and remove waste products (Bennet *et al.*, 2021). The upper channel contains air circulation, while the lower

channel is perfused with cell culture medium, which allows cells to be exposed to air to trigger ALI conditions and continuous medium feeding (Sellgren *et al.*, 2014; Benam, Villenave, *et al.*, 2016). This model can also be used to simulate smoking environments, mimic breathing motions in the lung, and can be connected to other organ-on-a-chip models to study drug toxicity (Huh *et al.*, 2010; Sonntag *et al.*, 2010; Wagner *et al.*, 2013; Benam, Novak, *et al.*, 2016). Lung-on-a-chip technologies have been used to investigate the impact of lung breathing motions on IAV replication and to identify antiviral compounds effective against IAV (Si *et al.*, 2021; Bai *et al.*, 2022).

3D bioprinting is a relatively new tissue engineering technique that uses computer aided design (CAD) software and various printing technologies to construct 3D scaffolds. These scaffolds are made with polymer-based bioinks, which can be cross-linked and cured during printing processes, such as stereolithography (Gauvin *et al.*, 2012). The properties of bioinks can be customised with biocompatible components tailored to cell specific types. Cells can be seeded onto the scaffolds or printed directly within the bioink itself in a layer-by-layer design to facilitate co-culture methods (Gopinathan and Noh, 2018; Semba, Mieloch and Rybka, 2020). Spheroids and cells can be cultured on bioinks to generate lung organoids and ALI cultures, and can be integrated into lung-on-a-chip technologies (Huh *et al.*, 2010; Wilkinson *et al.*, 2017; Park *et al.*, 2018). 3D bioprinting has been employed in IAV studies, where viral replication was visualised within 2D cells bioprinted in a 3D configuration (Berg *et al.*, 2018). A detailed comparison of 3D cell culture models is given in Table 1.4. Collectively, 3D tissue models are becoming increasingly important and utilised alongside traditional 2D cell cultures to help bridge the gap between *in vitro* and *in vivo* drug discovery. Additionally, patient-derived cells can be utilised in all models to enable a personalised medicine approach to drug discovery to investigate antiviral efficacy on an individual basis.

Table 1.4: Summary of advantages and limitations of 3D cell culture models.

Model	Advantages	Limitations
Air-liquid Interface	- Primary cell differentiation - Comparable gene expression patterns to *in vivo* epithelium - Constrained internal dimensions - Standard protocol - Surfaces are exposed, easy to infect or apply inhibitors	- Labour intensive - Hard flat surface can influence cell physiology - No continuous airflow or blood flow
Organoids	- hPSC differentiation - Comparable gene expression patterns to *in vivo* epithelium - Resembles human lung shape - Mimic spatial organisation effectively by self-organisation - Co-culture with immune cells - Can be passaged long-term - Can be gene edited	- Variable in size and shape so lack reproducibility - Composition of extracellular matrix is largely undefined - Low/medium throughput capacity - Difficult to maintain - Hypoxic/necrotic core - Entrapped cells in lumen are difficult to sample - Must be dissociated to infect with virus - No standard protocols
Lung-on-a-chip	- Primary cell/hPSC differentiation - Controlled microenvironment including chemical gradients - Constrained internal dimensions - Use mechanical force similar to fluid sheer stress in lung - Mimic breathing motions - Can be linked to other organ-on-a-chip models - Potential for automation	- Requires external apparatus to operate - Lacking in scaffold/ extracellular matrix materials - Sensors are limited in sensitivity and throughput - Optimisation is needed for automation of the system - No standard protocols - Requires technical expertise
Bioprinted scaffolds	- Constrained internal dimensions - Customisable architecture - Controlled cell positioning - Customisable bioinks to support growth of various cell types - High-throughput manufacturing process	- Issues with cell viability and differentiation - Challenges with biocompatibility - Technology lacks resolution to print intricate structures - No standard protocols

References: (Bhatia and Ingber, 2014; Sellgren *et al.*, 2014; Berg *et al.*, 2018; Probst, Schneider and Loskill, 2018; Park, Georgescu and Huh, 2019; Rijsbergen *et al.*, 2021; Cacciamali, Villa and Dotti, 2022; Francis *et al.*, 2022).

1.7. Project aims

The main objectives of this project were as follows:

1. To establish the use of novel 3D cell culture models amenable to IAV infection studies.

2. To develop 2D cell culture assays to measure IAV replication and to utilise them for drug discovery.

3. To adapt assays for use in more biologically relevant cell types.

4. To utilise the assays to measure IAV replication in the presence of epigenetic inhibitors and assess their inhibitory effects in biologically relevant cell types.

2. Materials and methods

2.1. Cells

2.1.1. Cell culture and passaging

All cells were grown and maintained in T75 cell culture flasks (ThermoFisher, #156499). Flasks were incubated at 37°C and 5% CO_2 in a humidified incubator. After cells grew to 80-90% confluency, they were washed with Versene (E&O Laboratories, #BM0400) and trypsinised using 2.5% trypsin/Versene (ThermoFisher Scientific, #15090-046) or TrypLE (ThermoFisher, #12604013). Medium (detailed in Table 2.1) was added to the flask and cells were split into fresh flasks. HBEC3-KT and hAECb cells required media changes every 2-3 days.

Table 2.1: Cell types and culture medium.

Cell Line	Description	Culture Medium
HAEC-b	Primary human bronchial epithelial cells. Three donors: 56 year old Hispanic female, 71 year old Caucasian male, 62 year old Hispanic male	hAEC medium for expansion (Epithelix, #EP09AM), Pneumacult-ALI medium for differentiation (STEMCELL Technologies, #07980)
HBEC3-KT	Normal human bronchial epithelial cells from a 65 year old female, immortalised with human telomerase reverse transcriptase (hTERT) and cyclin-dependent kinase 4 (CDK4)	KSFM (ThermoFisher, #17005042) + 1% P/S (ThermoFisher Scientific, #15140122)
HEK-293T	Human fetal embryonic kidney epithelial cells transformed with SV40 T-antigen	DMEM (ThermoFisher Scientific, #A4966029), 10% FCS (ThermoFisher Scientific, #10270106), 1% P/S
MDCK	Madin-Darby canine kidney cells from adult female cocker spaniel kidney	DMEM, 10% FCS, 1% P/S

2.1.2. Cell seeding

Cell counts were calculated using a haemocytometer cell counting chamber under a light microscope. Cells were seeded into plastic plates, glass coverslips, and flasks (Table 2.2). Cells were incubated at 37°C with 5% CO_2 to form a confluent monolayer over 1-3 days.

Table 2.2: Cell seeding apparatus.

Seeding apparatus	Manufacturer	Catalogue No.
12 well plate	Corning	3512
24 well plate	Corning	3524
96 well plate	Corning	3598
Black 24 well plate	Griener	662892
Black 96 well plate	Griener	655892
13 mm2 round glass coverslip	VWR	631-0148
T25 flask	ThermoFisher Scientific	156367
T75 flask	ThermoFisher Scientific	156499

2.2. Air-liquid interface cultures on Transwells

2.2.1. Differentiation on Transwells

HAEC-b cells between passage 2 – 5 were seeded into 6.5 mm Transwell inserts (STEMCELL Technologies, #38024; Falcon, #353292; Greiner Bio-One, #665640) with a 0.4 μM pore size at a seeding density of $4x10^4$ per insert in 100 μL hAEC medium. 500 μL of medium was added to the basal chamber and Transwells were incubated 37°C with 5% CO_2. Cells became confluent in 3 – 5 days, then media was removed from the apical chamber – creating an air-liquid interface. 500 μL of Pneumacult-ALI medium (STEMCELL Technologies, #05022) supplemented with heparin (STEMCELL Technologies, #07980) and hydrocortisone (STEMCELL Technologies, #07925) was added to the basal chamber. Basal media was changed every 2 days until Transwells were fully differentiated at 5 weeks. Airway secretions were washed from the apical chamber with 1X PBS (ThermoFisher Scientific, #14190-094) alongside every media change.

2.2.2. Transepithelial electrical resistance measurements

TEER measurements were taken using the Millicell ERS-2 Voltohmmeter (Merck, #MERS00002) and electrodes (Merck, #MERSSTX03). Transwells were washed with 1X PBS, then both apical and basal sides were submerged in 1X PBS. The short electrode was placed into the apical chamber and long electrode into the basal chamber. TEER values were taken and multiplied by the surface area to give Ohm's per cm^2.

2.2.3. Histopathology for Transwells

Tissues were washed in 1X PBS and fixed in 10% Neutral Buffered Formaldehyde overnight at room temperature. After fixation they were washed in 1X PBS and given to the Veterinary Diagnostic Services, University of Glasgow,

UK for paraffin-embedding and H&E staining. H&E stained sections were scanned using the Aperio VERSA Digital Pathology Scanner (Leica Microsystems) to create images for analysis in Aperio ImageScope 12.4.6 (Leica Microsysems) software.

2.3. Cellbricks

2.3.1. Cell culture in Haemobricks and Membricks

The Haemobrick is a bioprinted hollow cone shaped construct that allows cell seeding via a dedicated port (Florentino *et al.*, 2022). The 3D crescent-shaped ridges on the inside provide the construct with an uneven, textured shape similar to the native human lung tissue (Figure 2.1A). This construct measures six millimetres in diameter and rests at the bottom of an ultra-low adhesion (ULA) cell culture plate. Haemobricks were equilibrated in cell culture media at 37°C and 5% CO_2 for 1 hour then placed in holders raising them from the base of a 24 well ultra-low adhesion plate and filled with cell culture media. They were seeded with 6 μL of a $6x10^4$ cell suspension per brick, left to settle, then topped up to 900 μL of media. Haemobricks were incubated at 37°C with 5% CO_2 for 2-3 days until confluent.

The Membrick features a flat bioprinted base attached perpendicularly to a plastic cylinder to replicate the design of a standard Transwell insert (Figure 2.1B). The lateral plastic supports allow the Membrick to hook onto the edge of a cell culture plate well, so the bioprinted scaffold is suspended a few millimetres above the bottom of the plate (Kreuder *et al.*, 2020). Membricks were placed into 24 well plates and equilibrated in cell culture medium for 1 hour at 37°C. They were seeded with 100 μL of a $4x10^4$ cell suspension per brick, left to settle, then topped up to 200 μL of media.

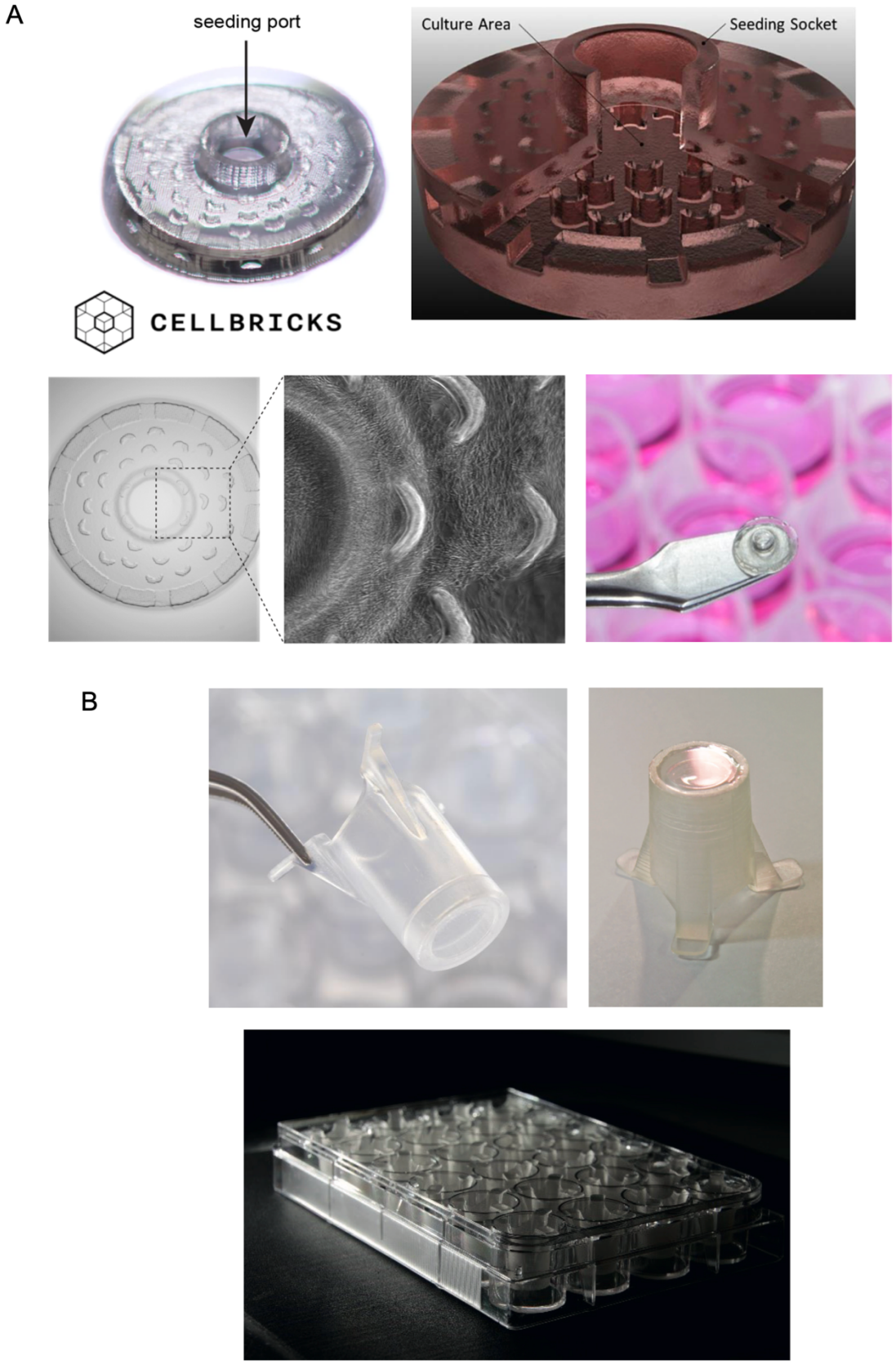

Figure 2.1: Cellbricks bioprinted scaffolds. *A – Haemobrick construct side and top views with human lung fibroblast monolayer inside. B – Membrick construct without plate (References: Cellbricks and Florentino et al., (2022)).*

2.3.2. Differentiation on Membricks

Membrick cultures were equilibrated in cell culture medium for 1 hour at 37°C, 5% CO_2 in an incubator. Cell seeding and TEER measurements followed the same protocols as Transwells.

2.3.3. Histopathology for Membricks

Tissues were washed with 1X PBS and frozen in OCT medium (CellPath, #KMA-0100-00A) using Cryofreeze spray (CellPath, #KNA-0173-00A). They were given to the Histopathology Services at the Beatson Institute for Cancer Research, UK for H&E staining. H&E-stained sections were imaged following the same protocol as Transwells.

2.4. Virus infections and assays

2.4.1. Virus propagation

IAV stocks were grown in MDCK cells when T75 flasks were 80% confluent containing a predicted $1x10^7$ cells. Cells were washed with 1X PBS and 2 mL of virus inoculum was added. Inoculum consisted of SFM and a low MOI of 0.01 PFU/mL or an unknown concentration for untitrated viruses. The flask was incubated at 37°C with 5% CO_2 for 1 hour with frequent shaking. Inoculum was removed and cells were washed with 1X PBS and overlayed with serum free media (SFM): DMEM and 1% P/S. Influenza A/Puerto Rico/8/1934 (PR8) (Public Health England), mouse-adapted influenza A/California/07/2009 (MaCal/09), and BrightFlu (generously provided by the Hutchinson group (MRC – University of Glasgow Centre for Virus Research)) viruses were supplemented with 1.0µg/mL TPCK-trypsin (Sigma-Aldrich, #4352157) and 5% bovine serum albumin (BSA). BrightFlu is a fluorescently tagged influenza A/Puerto Rico/8/1934 (PR8) virus, containing a ZsGreen fluorophore within in the NS1 genome segment. Influenza A/WSN/1933 (WSN) virus was supplemented with 2% FCS. Flasks were incubated at 37°C with 5% CO_2 for 48-72 hours until most cells had detached. Supernatant was harvested and centrifuged at 1500 RPM to pellet cellular debris, filtered through a 0.4 μM filter, frozen at -70°C, and titrated.

2.4.2. Virus titration by plaque assay

MDCK cells were seeded in 12 well plates at a density of $4x10^4$ cells per well. The next day cells were washed with SFM and infected with 250 μL of virus inoculum over a 10-fold dilution series and incubated at 37°C with 5% CO_2 for 1 hour, with shaking every 10 minutes. Inoculum was removed, cells were washed with SFM, and overlayed with Avicel prior to incubation at 37°C with 5% CO_2 for 48 hours. The avicel overlay consists of SFM, 1% DEAE Dextran (Sigma-Aldrich, #D9885), 7.5% $NaHCO_3$ (ThermoFisher Scientific, #25080060), 2.4% Avicel (DuPont, #RC-591); with an additional 1 mg/mL trypsin-TPCK and 5% BSA for BrightFlu and MaCal/09, and 2% FCS for WSN. After 48 hours, avicel overlay was removed and cells were washed with 1X PBS. Cells were fixed and permeabilised

using fixing solution for 30 minutes at room temperature, washed with 1X PBS, then blocked in PBS containing 5% milk powder for 30 minutes at room temperature. Blocking solution was removed and 250 μL of 1:2000 diluted mouse anti-NP primary antibody (Abcam, #ab20343) was added overnight at 4°C. Cells were washed three times with 1X PBS then 250 μL of 1:1000 donkey anti-mouse secondary antibody (ThermoFisher, #A-21202) was added for 1 hour at room temperature. Cells were washed with 1X PBS then number of plaques within the linear range of dilution were counted using the Celigo Imaging Cytometer (Nexcelom Bioscience). Virus stock was calculated using: $PFU/mL = (number\ of\ plaques / 0.25\ mL) * dilution\ factor$.

2.4.3. Real-time virus replication kinetic assays

For real-time virus replication kinetic assays, MDCK cells were seeded onto 96 well black glass bottom plates and incubated at 37°C with 5% CO_2 overnight. The following day, cells were washed with SFM and infected with BrightFlu and incubated for 1 hour, with frequent tilting of the plate. Cells were washed with SFM and overlayed. The overlay consisted of FluoroBrite DMEM (ThermoFisher Scientific, #A1896701) supplemented with 1% P/S, 5% L-Glutamine (ThermoFisher Scientific, #25030024), 1 mg/mL trypsin-TPCK, and 5% BSA. Virus replication was monitored by measuring fluorescence intensity (ZsGreen: excitation 470 nm, emission 515 nm) every 15 minutes using a CLARIOstar Plus microplate reader (BMG Labtech) for 24-48 hours. Data were analysed using MARS Data Analysis Software (BMG Labtech) and visualised using GraphPad Prism (GraphPad Software, San Diego, California USA).

2.4.4. Endpoint focus forming assay

MDCK, HBEC3-KT, and HAEC-b cells were seeded into 24 well plates and incubated until confluent at 37°C with 5% CO_2. Following this, cells were infected with WSN, BrightFlu, or MaCal/09 and incubated for 1 hour, with frequent tilting of the plate. Cells were washed with SFM and overlayed. Overlay

medium consisted of SFM and 2% FCS for WSN, and SFM, 1 mg/mL trypsin-TPCK, and 5% BSA for BrightFlu and MaCal/09. Cells were fixed and permeabilised at 24 or 48 hours post infection using 4% paraformaldehyde (PFA)/1% Triton-X-100 in PBS. After antibody staining, a Celigo Imaging Cytometer was used to image plates and to quantify numbers of infected cells and cell counts.

2.4.5. Virus infections in 3D

ALI cultures were washed with 1X PBS to remove secretions in the apical chamber. The apical chamber was infected with 1,000 PFU/mL per tissue in 100 uL of hAEC medium, then incubated at 37°C with 5% CO_2 for 2 hours, with frequent shaking. Inoculum was removed and both chambers were washed with 1X PBS. 500 uL of Pneumacult-ALI medium was placed in the basal chamber and cultures were incubated at 37°C with 5% CO_2 for up to 72 hours.

2.4.6. Reverse genetics of influenza viruses

A pDUAL 8 plasmid reverse genetics system as described in deWit/Fouchier 2004 was used. HEK 293T cells were split and seeded at a density of $1x10^6$ into 6-well plates and incubated overnight at 37°C and 5% CO_2. 250 ng of each plasmid segment were added to 100 µL Optimem (Invitrogen, #31985-047) to create a mastermix for both WSN and MaCal/09 viruses. This included segments 1-7 from each virus in individual plasmids, then the 8^{th} segment from BrightFlu. Plasmids were a kind gift from the Hutchinson group (CVR). 4 µL lipofectamine 2000 (Invitrogen, #11668019) was added into 100 µL Optimem and left for 15 minutes at room temperature. The plasmid DNA mastermix was added into this, mixed, and left for 20 minutes at room temperature. HEK 293T cells transfected and incubated overnight at 37°C and 5% CO_2. The next day media was changed (SFM, 0.14% BSA, and 1 µg/mL TPCK trypsin) and incubated for a further 48 hours. P0 supernatants were harvested, centrifuged at 1300 rpm for 1 minute to pellet cells, supernatant removed, and frozen at -70°C. MDCK cells were seeded into T25 flasks at a density of $4x10^6$ in DMEM, 10% FCS, 1% P/S and incubated overnight at 37°C and 5% CO_2. 100 µL of

P0 supernatant from HEK 293T cells and 100 µL SFM was added to each flask and incubated for 1 hour at 37°C and 5% CO_2. Flasks were washed then overlayed with SFM, 0.14% BSA, +/- 1 µg/mL TPCK trypsin and incubated for 48 hours. Supernatants were harvested, centrifuged at 1300 rpm for 5 minutes at 4°C, supernatant removed, and frozen at -70°C. P1 stock of virus was titrated using focus forming and plaque assays.

2.5. Immunofluorescence staining

2.5.1. Staining cells on glass coverslips

Cells on glass coverslips were washed with cytoskeletal (CSK) buffer (10 mM HEPES, 100 mM NaCl, 300 mM sucrose, 3 mM $MgCl_2$, 5 mM EGTA, distilled water). Cells were fixed and permeabilised using a 4% PFA/1% Triton-X-100 solution in CSK buffer for 30 minutes at room temperature. Cells were washed with CSK buffer and blocked with CSK buffer plus 2% FCS for 1 hour. 50 µL of primary antibody was applied overnight and left at 4°C. Cells were washed with CSK buffer, and secondary antibody and 4′,6-diamidino-2-phenylindole (DAPI) (Sigma-Aldrich, #D9542) were applied for 1 hour. Cells were washed with CSK buffer twice and with distilled water. Coverslips were mounted on a glass microscopy slide (ThermoFisher Scientific, #B7011/2) using CitiFluor AF 1 mounting medium (Science Services, #E17970-25) and sealed with a clear nail polish.

2.5.2. Staining Haemobricks

Haemobricks were removed from the cell culture plate and transferred into a glass-bottom 24 well plate. They were fixed with 4% PFA and permeabilised with 4% NP40 for 20 minutes, washed with then stained with 1:700 dilution of DAPI.

2.5.3. Staining Membricks and Transwells

Membricks/Transwells were washed with CSK buffer and then fixed and permeabilised using a 4% PFA/1% Triton-X-100 solution in CSK buffer overnight at 4°C. Then, Membricks/Transwells were washed with filtered 1X PBS/2% FCS solution and blocked for 1 hour at room temperature with 1X PBS/2% FCS solution added to both apical and basal chambers. All antibody dilutions used 1X PBS/2% FCS solution as a blocking buffer. Membrick biomaterial/Transwell

membrane was cut out of the plastic scaffold with a scalpel and placed in a 24 well cell culture plate. 100 µL of primary antibody solution was added to wells and left overnight at 4˚C. Primary antibody was removed, washed with 1X PBS/2% FCS, and 100 µL of secondary antibody and/or DAPI (Sigma-Aldrich, #D9542) (1:500) was added and left for 1hr at room temperature. The secondary antibody was removed, washed with 1X PBS/2% FCS, then washed with distilled water. The biomaterial/membrane was mounted on a glass microscopy slide (ThermoFisher Scientific, #B7011/2) using CitiFluor AF 1 mounting medium (Science Services, #E17970-25) and sealed with a clear nail polish.

Table 2.3: Primary antibodies.

Target	Species Raised	2D Dilution	3D Dilution	Cat No.
PML	Mouse	1:500	1:300	Abcam, #ab96051
ß IV Tubulin	Rabbit		1:100	Abcam, #ab179509
Mucin 5AC	Rabbit		1:100	Abcam, #ab78660
p63	Mouse		1:200	Abcam, #ab735
IAV NP	Mouse	1:1000	1:500	Paul Digard Lab (University of Edinburgh)

Table 2.4: Secondary antibodies.

Target Species	Fluorophore	Species Raised	2D Dilution	3D Dilution	Cat No.
Rabbit	Alexa 488	Donkey	1:1000	1:500	Invitrogen, #A-21206
Mouse	Alexa 488	Donkey	1:1000	1:500	Invitrogen, #A-21202
Rabbit	Alexa 555	Donkey	1:1000	1:500	Invitrogen, #A-31572
Mouse	Alexa 555	Donkey	1:1000	1:500	Invitrogen, #A-31570

Table 2.5: Secondary nanobodies.

Target Species	Fluorophore	Species Raised	2D Dilution	3D Dilution	Cat No.
Mouse	568	Alpaca	1:1000	1:500	ChromoTek, #sms1AF568-1-10
Mouse	647	Alpaca	1:1000	1:500	ChromoTek, #sms1AF647-1-10
Rabbit	568	Alpaca	1:1000	1:500	ChromoTek, #srbAF568-1-10
Rabbit	647	Alpaca	1:1000	1:500	ChromoTek, #srbAF647-1-10

2.6. Microscopy

2.6.1. Imaging 2D cells

Samples were imaged using a Zeiss Confocal Laser Scanning Microscope 880 (LSM880) using the 63x Plan-Apochromat oil immersion lens with 405, 488 nm, 555 nm laser lines. ZEN Black (Zeiss) software was used for capturing Z-stack images and exporting the maximum intensity projection images.

2.6.2. Imaging Haemobricks

A multi-modal approach was employed to image the Haemobricks. The Celigo Imaging Cytometer was used to cover a range of different Haemobrick depths by manually moving the X3 objective. The EVOS M5000 Imaging System (ThermoFisher Scientific) was used for 3D imaging of the Haemobrick. 100 Z-slices were taken spanning the depth of each brick at different focal points in order to image the whole brick using the X4 objective. Fiji (Schindelin *et al.*, 2012) and IMARIS v9.7.1 (BitPlane, South Windsor, CT, USA) software were used to stitch together individual TIFF files and ZEN Black (Zeiss) software was used to view the 3D model. “Optimal” spacing between Z-slices was used on ZEN Blue (Zeiss) software (Heintzmann and Sheppard, 2007). The Zeiss AxioObserver Z1 Microscope was used for automated imaging of the Haemobrick. A depth of 300 µm over 201 Z-slices spanning 252 tiles was captured with the LD Plan-Neofluar 20x/0.4 Corr Ph2 M27 air objective (NA 0.4) using a 405 nm laser line with an exposure time of 166 ms. The Zeiss Confocal LSM880 was used for automated imaging at greater resolution. A depth of 119 µm over 120 Z-slices spanning 100 tiles was captured with the Plan-Apochromat 10x/0.45 M27 air objective (NA 0.45) or Plan-Apochromat 20x/0.8 M27 air objective (NA 0.8) using a 405 nm laser line. Microscopes were focussed manually for both brick models with image processing using ZEN Black/Blue editions and IMARIS.

2.6.3. Imaging Membricks and Transwells

To image cells on the entire Membrick the Zeiss Confocal LSM880 was used. The depth of the Membrick was captured over 120 Z-slices spanning 100 tiles was captured with the Plan-Apochromat 10x/0.45 M27 air objective (NA 0.45) or Plan-Apochromat 20x/0.8 M27 air objective (NA 0.8) using a 405 nm laser line. The same confocal microscope was used to image tissues grown on Membricks and Transwells. Regions of interest were captured over 120 Z-slices over the entire tissue depth using a Plan-Apochromat 63x/ 1.4 oil DIC M27 objective with Airyscan (AU = 1) and deconvolution. 405 nm, 488 nm, and 561 nm laser wavelengths were used at varying intensities. IMARIS image analysis software was used to render each channel captured (https://imaris.oxinst.com). Images were opened in IMARIS, automatically reconstructing Z-stacks (.czi files) into 3D projections (.ims files). The surface tool was used to transform signal captured by microscopy into rendered objects by tracing the boundaries of signals. The statistics tool was used to measure BrightFlu volume (volume of green objects) and depth of BrightFlu infection (distance from red object to furthest point of green object). Data were compiled into a tabular format for further analyses.

2.7. Inhibitors

2.7.1. Drug preparations

All inhibitors were resuspended in (dimethyl sulfoxide) DMSO (Sigma, #D2650) to a working stock of 10 mM with the exception of IFN-β. The master stock of IFN-β was diluted to a working stock of $2.8x10^4$ IU/mL in SFM. Working stocks were stored at -70°C or -20°C depending on manufacturer's instructions.

Table 2.6: Drugs and inhibitors.

Name	Cat. No.
CM272	MedchemExpress, #HY-101925
CM579	MedchemExpress, #HY-117421A
SYC-522	Sigma-Aldrich, #5.31711
DZNep	Abcam, #ab145628 and Selleckchem, #S7120
El1	Selleckchem, #S7611
EPZ (Tazemetostat)	Selleckchem, #S7128
Favipiravir	Selleckchem, #S7975
IFN-β	R&D Systems, #8499-IF-010
JIB-04	Selleckchem, #S7281
JQ1	Selleckchem, #S7110
OM173- αA (Nanaomycin A)	Abcam, #ab144849
Oseltamivir	MedchemExpress, #HY-13318
Ruxolitinib	ThermoFisher Scientific, #AC469381000

2.7.2. Drug toxicity assays

An MTS (3-(4,5-dimethylthiazol-2-yl)-5-(3-carboxymethoxyphenyl)-2-(4-sulfophenyl)-2H-tetrazolium) assay was used to assess drug cytotoxicity. MDCK cells were seeded and incubated overnight at 37°C with 5% CO_2. The following day, cells were washed with FluoroBrite DMEM, overlayed with 100 μL of drug dilutions (0-500 μM) in FluoroBrite, and incubated for 48 hours at 37°C with 5% CO_2. Controls included: puromycin as a death control, and no drug treatment. After the incubation period, 20 uL of MTS reagent (Abcam, #ab197010) was added and cells were incubated for 1 hour. Absorbance at 490 nm was recorded using a PHERAstar plate reader (BMG Labtech) to quantify levels of formazan dye. Absorbance fold changes were calculated relative to no drug treatment. Identically treated plates were also processed for cell counting to assess drug toxicity. Cells were fixed and permeabilised at 48 hours with 4% PFA/1% Triton-X-100 in PBS. Cells were stained with DAPI, images were captured using the Celigo Imaging Cytometer at 405 nm, and the number of nuclei counted using a haemocytometer cell counting chamber under a light microscope. Cell counts were expressed as fold change relative to no drug treatment.

2.7.3. Drug treatment for infection assays

Real-time and end point assays were used to assess the efficacy of inhibitors on BrightFlu and WSN replication, respectively. For real-time assays assessing the efficacy of favipiravir and favipiravir analogues, inhibitors were added to the medium immediately post-infection. For real-time assays assessing epigenetic inhibitor efficacy, inhibitors were added to cell culture medium 24 hours prior to virus infection to pre-treat cells and re-applied immediately post-infection for the 36-hour incubation period. Treatment conditions for end point assays assessing the efficacy of epigenetic inhibitors also involved a 24-hour pre-treatment and 24-hour post-treatment with the inhibitors.

3. Validation of novel 3D bioprinted scaffolds to support bronchial airway differentiation

3.1. Introduction

Conventional cell culture models used to study respiratory virus infections often fail to accurately recapitulate the complex microenvironment of the lung (Petpiroon *et al.*, 2023). These two-dimensional (2D) models typically utilise various laboratory-adapted, transformed, or immortalised cell lines, such as Madin-Darby canine kidney (MDCK) epithelial cells and human lung alveolar adenocarcinoma (A549) cells. While these cell lines are valuable for high-throughput drug screening, they are not physiologically representative of the human lung. To complement 2D models, three-dimensional (3D) lung models, including air-liquid interface (ALI) cultures, organ-on-a-chip systems, and organoids, are increasingly used to better simulate the microenvironment of the human lung (Ross *et al.*, 2007; Huh *et al.*, 2010; Dvorak *et al.*, 2011; Dye *et al.*, 2016; Lacroix *et al.*, 2018; Huang *et al.*, 2021).

In Mid-2020 our group formed a collaboration with Cellbricks, a small to medium enterprise in Berlin, Germany (https://cellbricks.com). Cellbricks specialised in the chemical engineering of bioinks for use in multi-material stereolithographic bioprinting of miniature organ models. At the time of collaboration, Cellbricks was developing bioprinted scaffolds aiming to support the differentiation of airway cells, with the goal of facilitating SARS-CoV-2 research as part of the global COVID-19 pandemic response. This chapter details the development of bronchial ALI cultures on Cellbricks' bioprinted scaffolds. Within the scope of our collaboration, Cellbricks designed two models: the Haemobrick and the Membrick.

The exact composition of the biomaterials was proprietary and undisclosed to us, though they were primarily based on methacrylated gelatin (GelMA) and methacrylated hyaluronic acid (HAMA). GelMA, a photocrosslinkable hydrogel containing denatured collagen, retains arginyl-glycyl-aspartic acid sequences and matrix metalloproteinase sensitive sites, which promote cell adhesion (Nichol *et al.*, 2010). HAMA, a glycosaminoglycan found in the

extracellular matrix, is nonimmunogenic, biocompatible, and has rapid photosensitive responses (Schuurmans *et al.*, 2021). Together GelMA and HAMA provide ideal properties for bioprinting scaffolds suitable for cell culture applications (Wang *et al.*, 2022). A photoinitiator, lithium phenyl-2,4,6-trimethylbenzoylphosphinate, was incorporated into the bioink for photopolymerisation. The bioink was printed using stereolithography, layer by layer onto the print head, where it was cured with blue light illumination (Lam *et al.*, 2019). Bioinks can be customised with additional materials to enhance cellular health, and cells can be printed directly within the bioink itself (Grix *et al.*, 2018; Lam *et al.*, 2019; Kreuder *et al.*, 2020; Amler *et al.*, 2021).

The aim of this collaboration was to optimise the Haemobrick and Membrick scaffolds for bronchial epithelial cell adhesion, differentiation, infection studies, and bioimaging in 3D tissues.

3.2. Results

3.2.1. Haemobricks support epithelial cell attachment and proliferation

The potential of the Haemobrick to support the adhesion and proliferation of epithelial cells was evaluated. Normal human lung fibroblast (NHLF) cells have previously been shown to adhere and proliferate in the first-generation Haemobrick (work carried out by Joanna Wojtus at the MRC – University of Glasgow Centre for Virus Research). MDCK cells and NHLF cells (positive control) were seeded into first-generation Haemobricks and maintained in culture for 14 days. Additionally, MDCK cells were seeded onto an ultra-low adhesion (ULA) plate as a negative control to visualise cell adherence without a growth support. Images were captured every 2-3 days to monitor cell growth over the 14-day period. MDCK cells showed minimal adhesion to the Haemobrick and limited growth by day 14 (Figure 3.2A). In contrast, NHLF cells adhered and proliferated rapidly – forming an extended bridge over the seeding port by day 14 (Figure 3.2B). MDCK cells in ULA plates did not attach or proliferate by day 14 (Figure 3.2C). Under these seeding conditions, the MDCK cells clumped together and were removed during media changes. The biomaterial composition of the first-generation Haemobrick supported the adhesion and proliferation of NHLF cells but was not suitable for MDCK cells. Correspondingly, Cellbricks developed a second-generation Haemobrick, which supported MDCK cell adhesion and growth, achieving confluency by day 14 (Figure 3.2D). This indicates that the composition of the bioink plays an important role in the scaffold's ability to support cell adhesion and growth in a cell type-dependent manner.

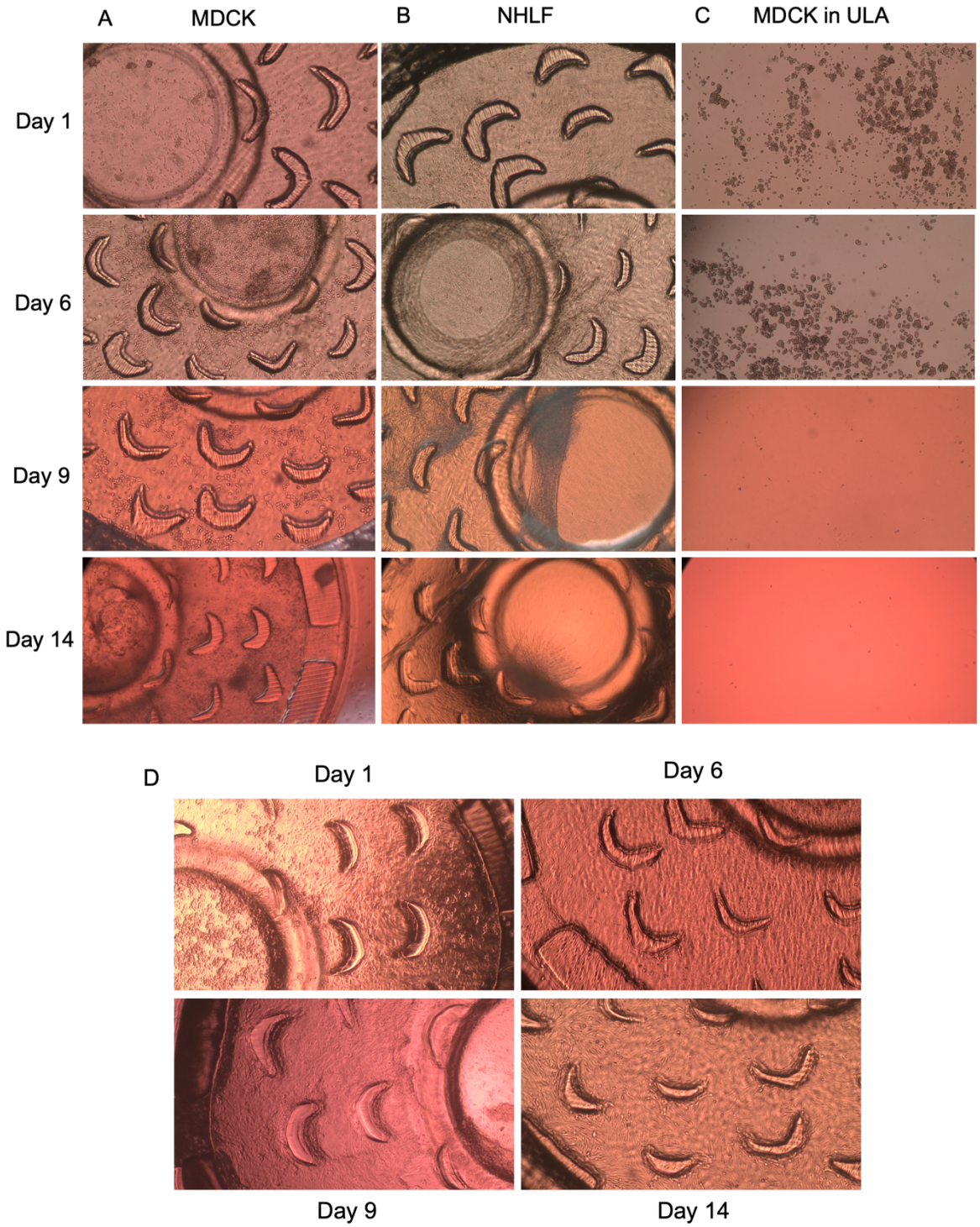

Figure 3.2: Improved bioink supports epithelial cell attachment and proliferation. *MDCK and NHLF cells were seeded into Haemobricks and ultra-low adhesion (ULA) plates and incubated for 14 days. Representative phase contrast images were captured of cells on first-generation Haemobricks and ULA plates over 14 days. A - MDCK cells; B - NHLF cells; C - MDCK cells on ULA plates. D - MDCK cells on second-generation Hemobricks over 14 days. N = 3 per condition.*

3.2.2. Membricks support human bronchial epithelial cell attachment and proliferation

Given that the second-generation Haemobrick could support the growth of transformed epithelial cells, the bioink was tested to determine if it could support the growth of primary bronchial epithelial cells. The 3D crescent structures within the Haemobrick enhance its ability to simulate the human lung; however, the enclosed design presents challenges under ALI conditions. The small seeding port of the Haemobrick prevents the complete removal of cell culture media, a necessary step to trigger the differentiation process into a ciliated respiratory epithelium (Gerovac *et al.*, 2014). Consequently, the Membrick model was used for further optimisation of bioinks, as its apical chamber is more accessible. Cellbricks developed multiple Membricks using a range of bioinks, with four materials showing promising results in their in-house testing using small airway epithelial cells. To evaluate whether these biomaterials support airway cell attachment, primary human bronchial epithelial (HAEC-b) cells were seeded onto the Membricks and cultured for five days. Material 1 and 3 did not support cell adhesion, material 4 supported cell adhesion until day 3, and material 2 supported cell adhesion until day 5 (Figure 3.3). Thus, only material 2 successfully supported the attachment and proliferation of HAEC-b cells for up to five days.

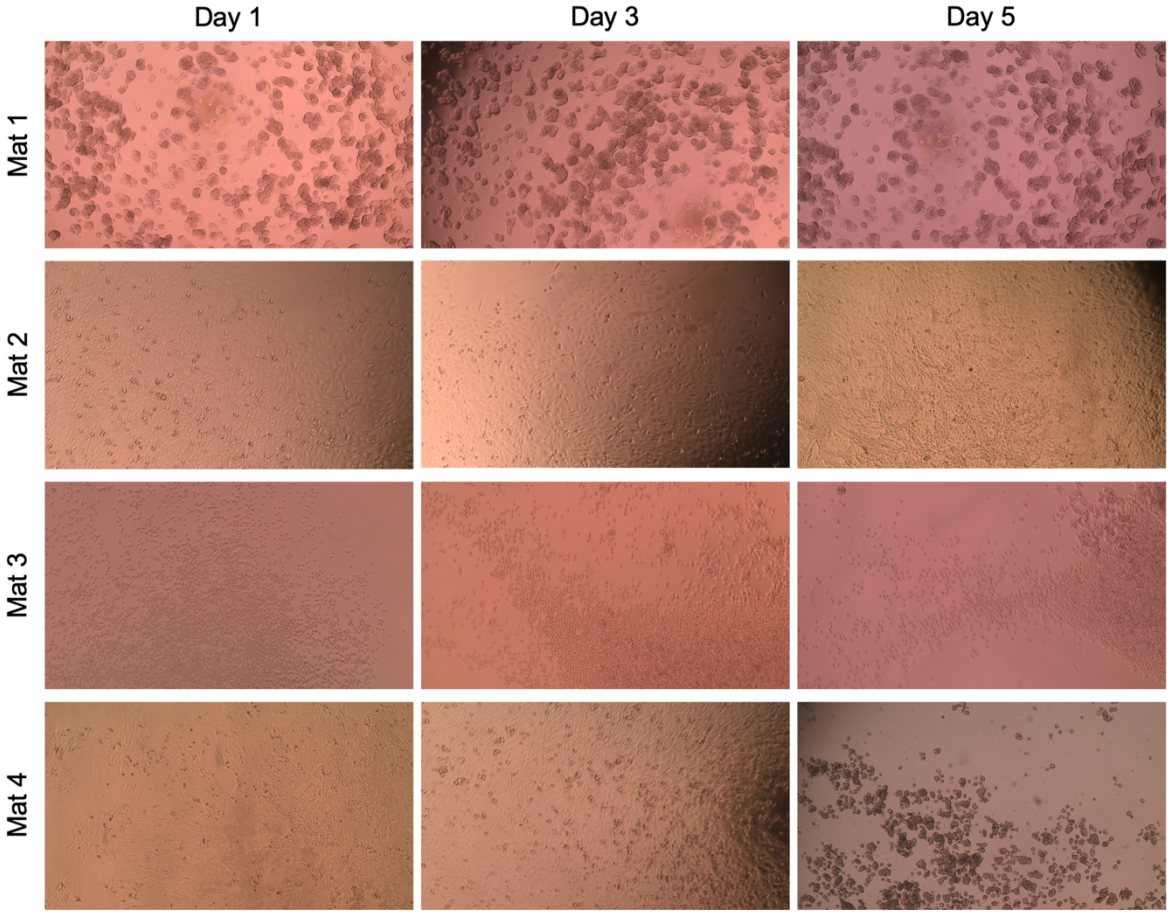

Figure 3.3: Membricks support adherence and proliferation of human bronchial epithelial cells. *HAEC-b cells were seeded onto four different biomaterials and cultured for five days. Phase contrast images were captured on days 1, 3 and 5, and representative images are shown. N = 3 Membricks for each biomaterial.*

3.2.3. Membricks support the differentiation of human bronchial epithelial cells

To evaluate whether HAEC-b cells grown on Membricks can successfully differentiate into a tissue, cells differentiated on Membricks and Transwells (positive control) were compared. ALI triggers a differentiation process via increase in oxidative cellular metabolism and basolateral medium feeding, resulting in the formation of a pseudostratified epithelium with apical-basal polarisation (Javaherian, Paz and McGuigan, 2014; Silva *et al.*, 2023). HAEC-b cells from three donors – male, 62, Hispanic; female, 56, Hispanic; male, 71, Caucasian were seeded onto Membricks and Transwells. Cells grew to confluency 3-4 days post-seeding, and cell culture medium was removed from the apical chamber to establish ALI conditions. After five weeks in culture, tissues were fixed and processed for H&E staining to visualise the morphology of the tissue. Sections were imaged by Joanna Wojtus (MRC – University of Glasgow Centre for Virus Research) using an Aperio VERSA Digital Pathology Scanner, and representative images were obtained using Aperio ImageScope software. No substantial differences were observed between HAEC-b cells differentiated into tissues on Membricks relative to those on Transwells (Figure 3.4).

Additionally, transepithelial electrical resistance (TEER) measurements were taken to assess the integrity of the epithelial barrier within the tissues. HAEC-b cells from the same three donors were differentiated on Transwells and Membricks over five weeks. After washing with PBS, TEER measurements were taken from three tissues for each condition. TEER values from empty (unseeded) Transwells and Membricks were subtracted from TEER values of tissues grown on both scaffolds. An unpaired t-test was performed to determine if there were statistically significant differences between Membrick and Transwell TEER measurements for each donor. Although Membrick TEER values were lower than Transwells, no significant differences in the epithelial barrier integrity were observed between tissues grown on both scaffolds across all three donors (Figure 3.5). Taken together, these data confirm that HAEC-b cells differentiated on Membricks can successfully differentiate into tissues which are comparable to tissues differentiated on Transwells.

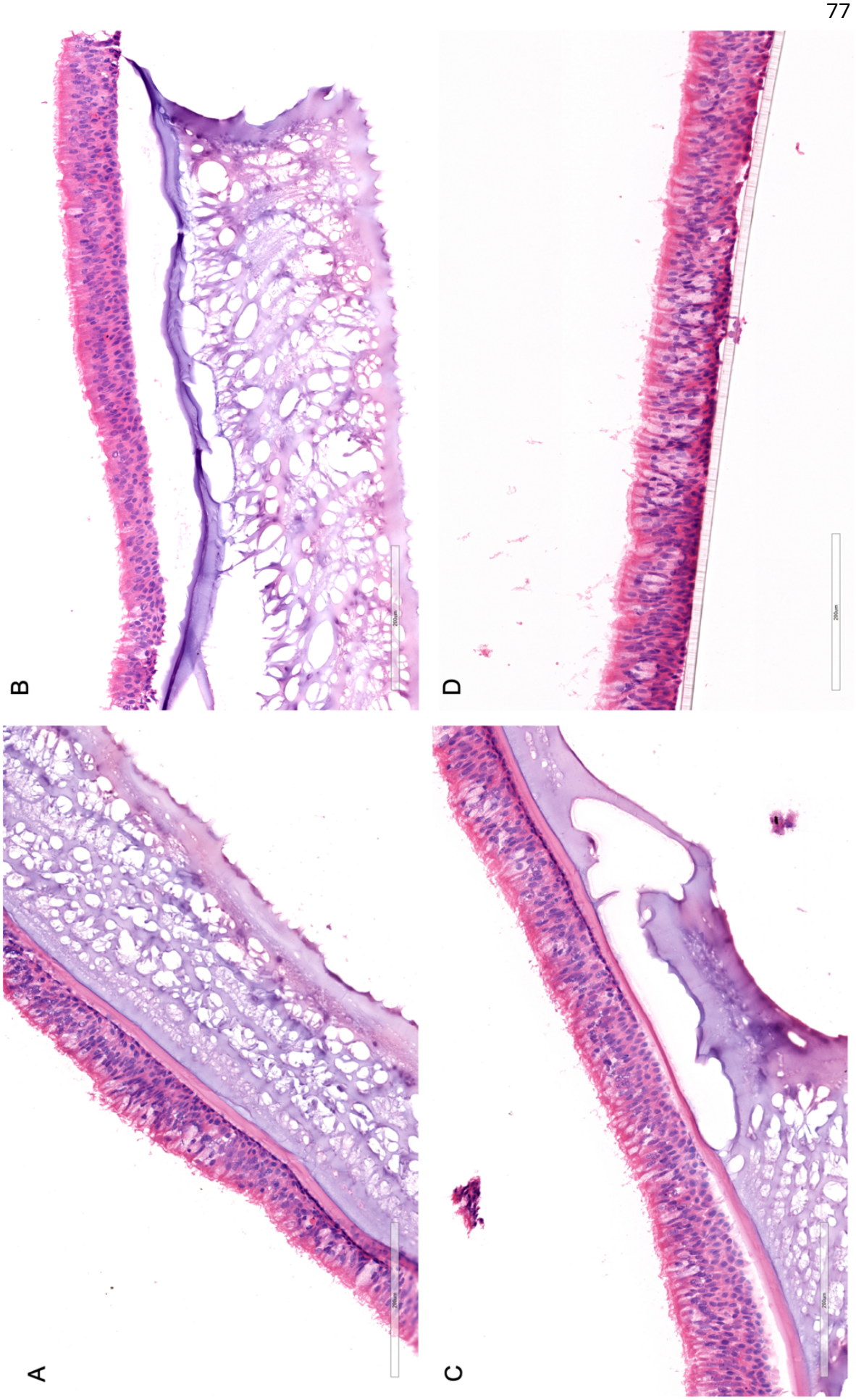
A
B
C
D

Figure 3.4: Tissues differentiated on Membricks and Transwells are similar in appearance. *HAEC-b cells were differentiated on Membricks and Transwells over five weeks. Tissues were washed, fixed in 10% NBF, and frozen for cryosectioning and H&E staining. Slides were imaged using an Aperio VERSA Digital Pathology Scanner and representative images were obtained using Aperio ImageScope software. A – female, 56, Hispanic on Membrick, B – male, 62, Hispanic on Membrick, C – 71, Caucasian on Membrick, D – female, 56, Hispanic on Transwell.*

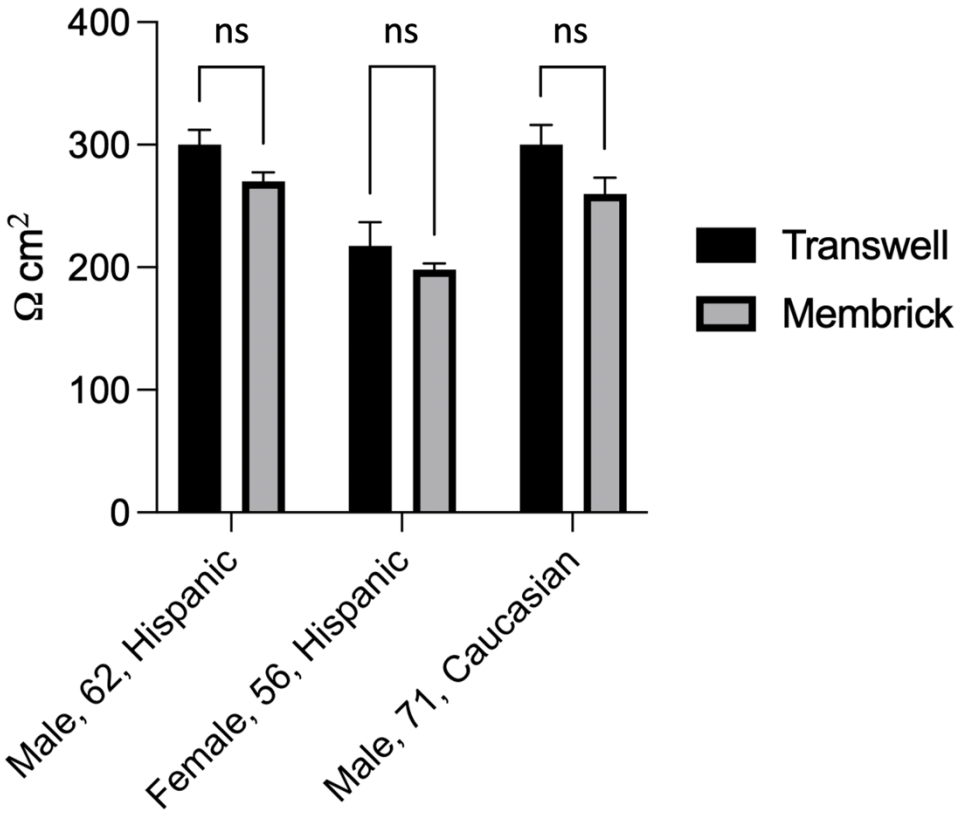

Figure 3.5: Epithelial barrier integrity is comparable between tissues on Transwells and Membricks. *Transepithelial electrical resistance (TEER) measurements were taken from tissues on Transwells and Membricks from three donors using a voltohmmeter. TEER values from empty (unseeded) Transwells and Membricks were subtracted from values and multiplied by surface area to give Ω per cm^2. The difference in TEER measurements between Transwell and Membricks was assessed using an unpaired t-test. N = 3 per condition. Error bars = mean ± 1 SD.*

3.2.4. Biomaterial composition impacts imaging quality

The porous polyethylene terephthalate and polycarbonate membranes commonly used in Transwells emit autofluorescence, resulting in images with high background fluorescence (Gillespie *et al.*, 2016). The base of the Membrick is transparent which should, in theory, provide enhanced imaging properties compared to standard Transwell inserts used for ALI. However, components added to the bioink can alter its refractive properties and optical transparency, potentially impact imaging quality. To reduce autofluorescence, Cellbricks developed four new bioinks based on material 2 to test their imaging potential. HBEC3-KT cells were seeded onto Membricks, and after two days in culture, images were captured using a phase contrast microscope. Materials 1, 2, and 0.5L supported cell attachment and proliferation, while material 3 only partially supported cell attachment (Figure 3.6A).

Membricks were fixed and stained with DAPI to visualise the nuclei of cells, and images were captured using confocal microscopy. Material 2 provided the most well-defined images with relatively low background signal, closely followed by material 1 (Figure 3.6B). Material 0.5L showed greater background signal, and material 3 very high background signal. To quantify the differences in background signal between materials, the frequency of pixel intensity values for each image was plotted. High intensity values indicate greater background fluorescence, with lower intensity values being more optimal for imaging. For material 1, most pixels had an intensity of 21, SD = 20; for material 2, an intensity of 22, SD = 16; for material 0.5L, an intensity of 27, SD = 18; and for material 3, and intensity of 40, SD = 17 (Figure 3.6C). To better visualise the comparison between materials, histograms from each material were overlapped and a heatmap of pixel intensity was created. Materials 1 and 2 displayed lower intensity values compared to materials 0.5L and 3 (Figure 3.6D and E). Therefore, materials 1 and 2 were identified as the best bioinks for confocal imaging of 2D cells on Membricks.

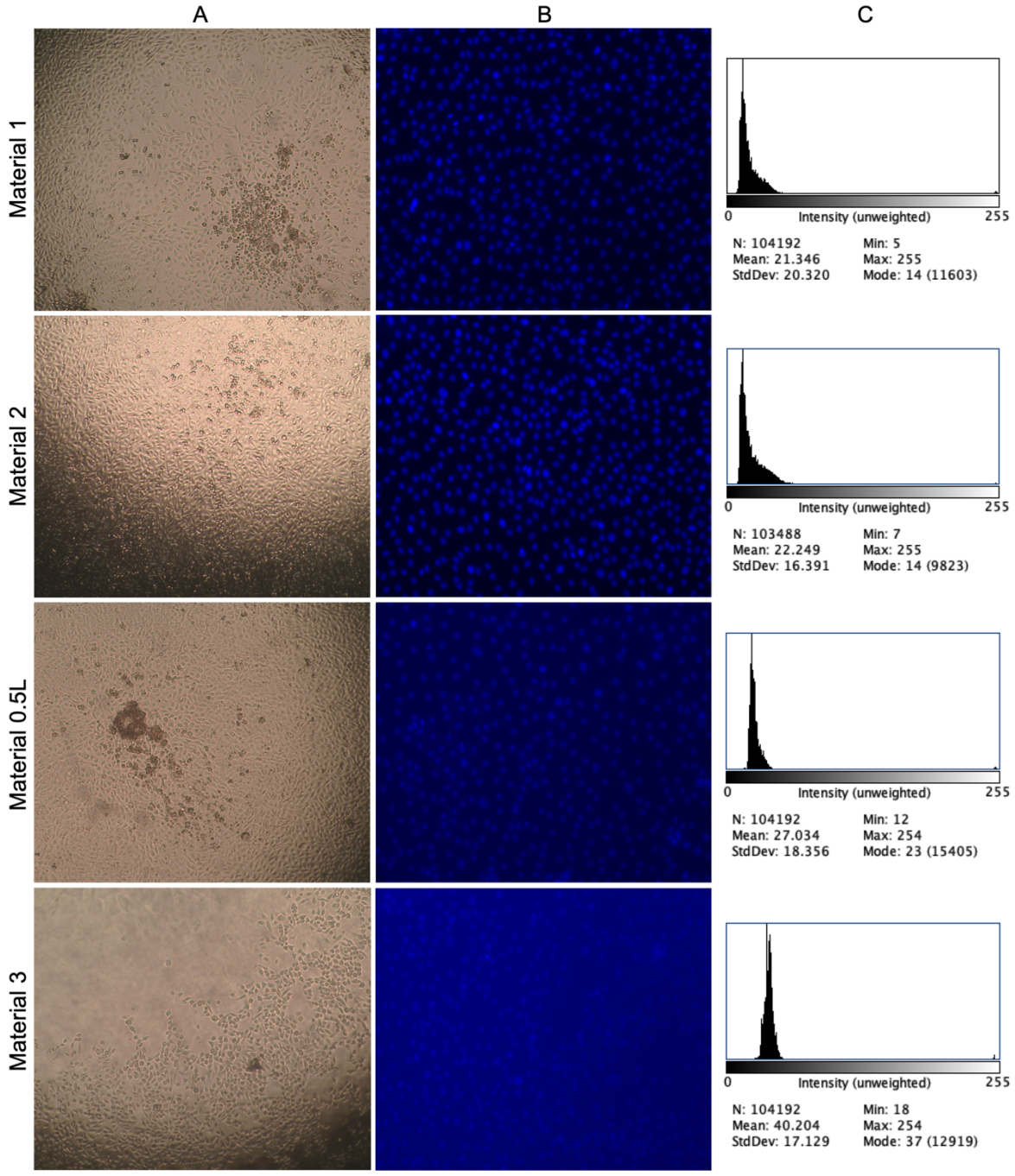
A
B
C
Material 1
Material 2
Material 0.5L
Material 3
0
Intensity (unweighted)
255
N: 104192
Mean: 21.346
StdDev: 20.320
Min: 5
Max: 255
Mode: 14 (11603)
N: 103488
Mean: 22.249
StdDev: 16.391
Min: 7
Max: 255
Mode: 14 (9823)
N: 104192
Mean: 27.034
StdDev: 18.356
Min: 12
Max: 254
Mode: 23 (15405)
N: 104192
Mean: 40.204
StdDev: 17.129
Min: 18
Max: 254
Mode: 37 (12919)

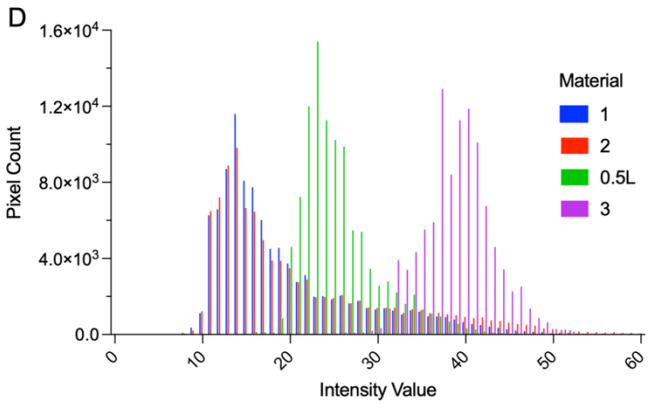
D
Pixel Count
1.6×10^4
1.2×10^4
8.0×10^3
4.0×10^3
0.0
0
10
20
30
40
50
60
Intensity Value
Material
1
2
0.5L
3

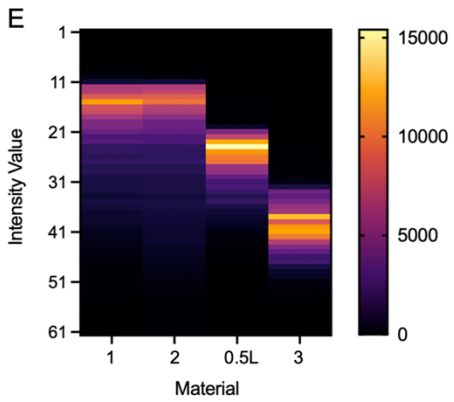
E
Intensity Value
1
11
21
31
41
51
61
1
2
0.5L
3
Material
15000
10000
5000
0

Figure 3.6: Biomaterial composition impacts image quality. *HBEC3-KT cells were seeded onto four Membrick bioinks and cultured for two days. A – Membricks imaged with phase contrast microscope. B – cells were fixed, stained with DAPI, and imaged with confocal microscopy using a 63X magnification objective lens. C – histograms of pixel intensity values. D – overlapping histograms from all materials. E – heatmap of intensity values from all materials.*

3.2.5. Developing imaging methods for 2D cells on Haemobricks and Membricks

To investigate the imaging properties of Haemobricks and Membricks, various imaging methods were explored. MDCK cells were seeded into Haemobricks and Membricks, incubated for 24 hours, then fixed, permeabilised, and stained with DAPI. Initially, the Celigo Imaging Cytometer (Nexcelom Bioscience) was used to image the Haemobrick by manually setting the Z-plane to capture different depths of the biomaterial. Cells were observed at the base of the Haemobrick at a depth of 2.5, growing up the side of the crescents at 2.9 and 3.0, and the seeding port at 3.4 (Figure 3.7A). The Celigo Imaging Cytometer was restricted to a single field of view (FOV) with a 3X objective lens, so the Invitrogen EVOS M5000 Imaging System with a 4X objective lens was trialled next. This allowed for the acquisition of 100 Z-stacks from a single FOV to capture Haemobrick's depth. Six FOVs were taken to cover the entire width of the Haemobrick, then images were manually stitched together with IMARIS Stitcher and projected together in ZEN Blue (Figure 3.7B).

To improve upon the manual stitching process and automate sample movement between imaging FOVs, the Zeiss Axio Observer with a 10X objective lens was used. The integrated ZEN Black software facilitates automatic sample movement and image stitching (Figure 3.7C). For higher resolution images, the Zeiss confocal laser scanning microscope (LSM) 880 was used, as its pinhole feature eliminates out-of-focus light. Similarly, the sample was moved automatically with greater accuracy and resolution using a 40X oil objective lens. Among all the microscopes tested, the Zeiss confocal LSM 880 provided the highest resolution images, though it had the smallest FOV (Figure 3.7D).

Widefield microscopy allowed imaging of the entire Haemobrick, while confocal microscopy enabled imaging at high resolution. Confocal microscopy was also used to image MDCK cells on the Membrick, providing high-resolution images of the entire scaffold when stitched together (Figure 3.8). Therefore, 2D cells on both Haemobricks and Membricks can be imaged using various microscopes and imaging software, demonstrating these bioprinted scaffolds provide an optically transparent platform for imaging-based studies.

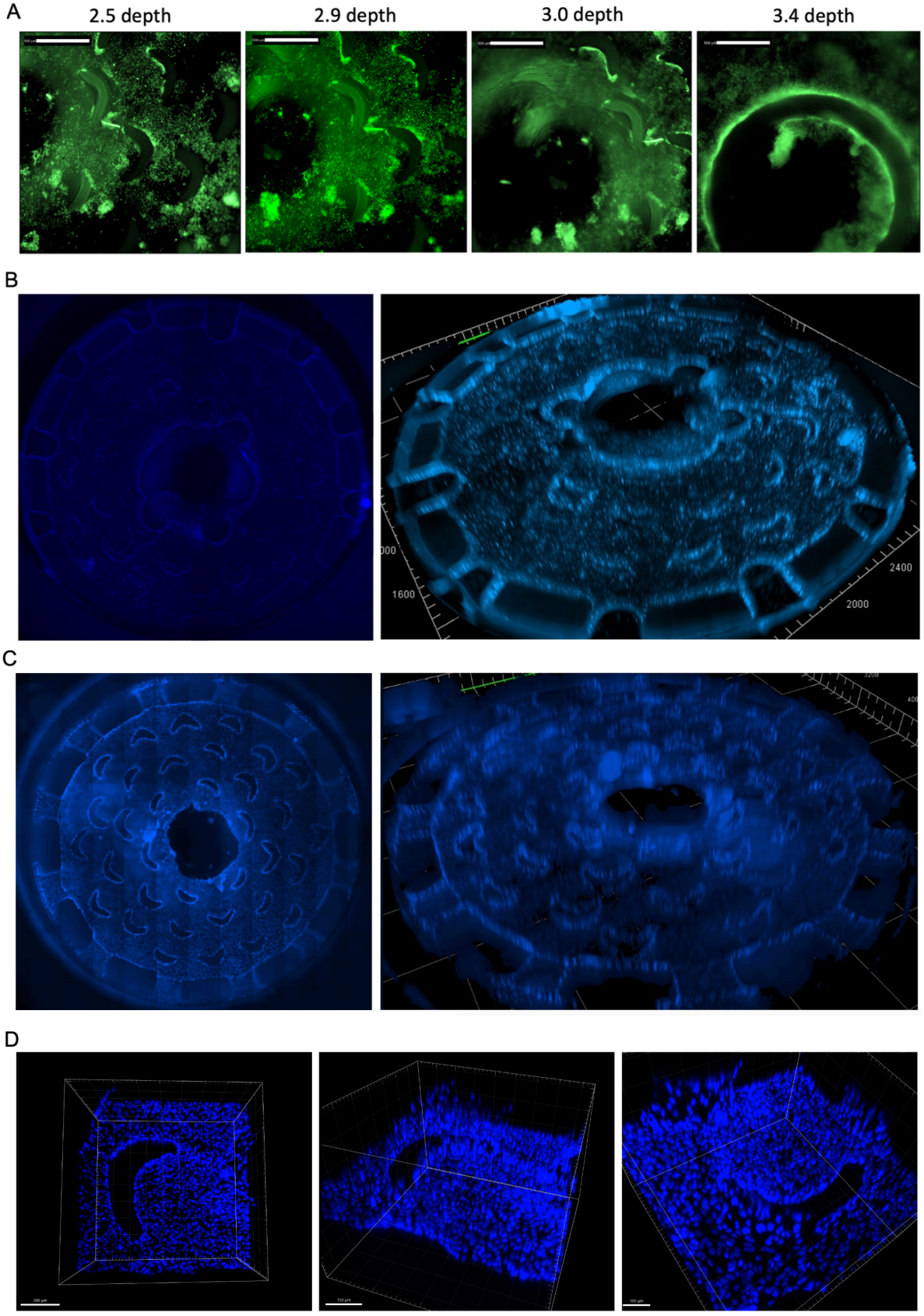

Figure 3.7: Imaging of Haemobricks using various microscopes. *MDCK cells were seeded into Haemobricks and cultured for 24 hours. Cells were fixed, permeabilised, and stained with DAPI. A – Celigo imaging of a single FOV at multiple depths using a 3X objective lens. B – EVOS imaging of six FOVs spanning the Haemobrick with a 4X objective lens. For each FOV, 100 images per stack were acquired and stitched*

manually using IMARIS, Zen, and Fiji software. C – Zeiss Axio Observer imaging using automated stitching with a 10X objective lens. D – Zeiss confocal laser scanning microscope 880 imaging using a 40X oil objective lens.

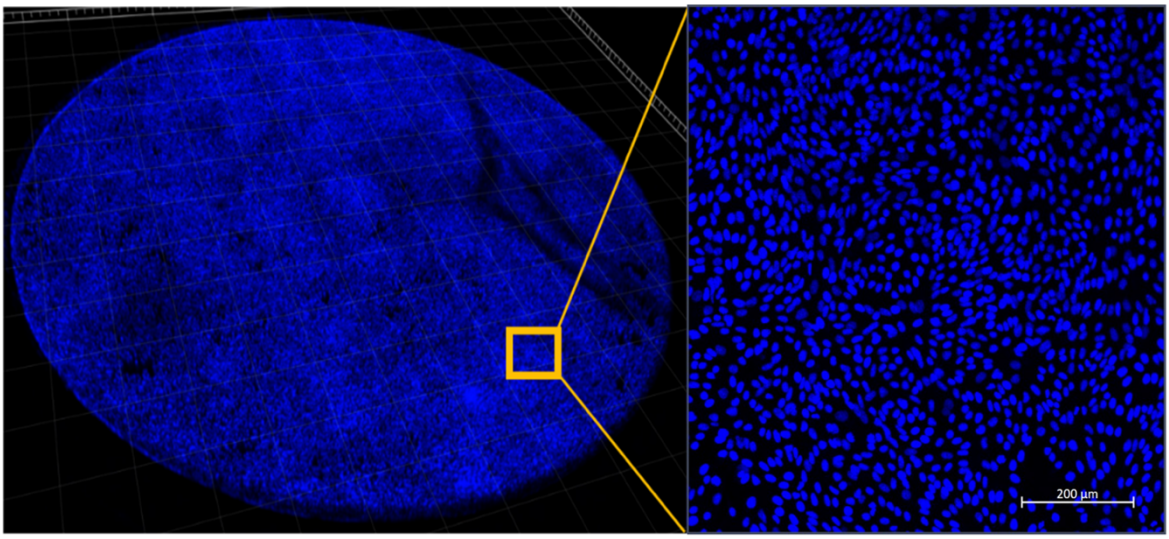

Figure 3.8: Imaging of Membricks using confocal microscopy. *MDCK cells were seeded onto Membricks and cultured for 24 hours. Cells were fixed, permeabilised, stained with DAPI, and mounted onto a glass coverslip. Zeiss confocal laser scanning microscope 880 was used for imaging with 40X oil objective lens and automated stitching to capture the width of the Membrick.*

3.2.6. Developing imaging methods for 3D tissues on Membricks

Antibody size can be a limiting factor in the immunofluorescent staining of 3D differentiated tissues. Conventional secondary antibodies, typically conjugated to an Alexa Fluor™, have a molecular weight of approximately 150 kDa and struggle to penetrate 3D tissues due to densely packed cells with tight junctions (Smyrek and Stelzer, 2017). This results in heterogenous staining, with strong fluorescence at the tissue surface, decreasing in quality deeper within the tissue. To combat this, paraffin embedding and tissue sectioning is commonly used to create thin slices, allowing antibodies to bind directly to the surface of the tissue following antigen retrieval. However, it is difficult to reassemble sections into a coherent 3D picture, resulting in potential loss of information inherent to the tissues native structure. The aim of using the Membrick is to bypass tissue sectioning to preserve the native 3D architecture to accurately reflect the parameters of virus replication within each tissue.

To determine whether antibody penetration was an issue, 3D tissues were fixed and permeabilised overnight, stained for promyelocytic leukaemia protein (PML) using conventional fluorescent secondary antibodies, and counterstained with DAPI. Tissues were imaged using confocal microscopy to capture Z-stacks throughout the tissue. PML, a major scaffolding protein of PML nuclear bodies, should be expressed in all cell types. (Human Protein Atlas, https://www.proteinatlas.org/ENSG00000140464-PML/single+cell+type/lung; GTex, https://gtexportal.org/home/gene/PML). PML staining was successfully achieved up to a depth of approximately 30 µm within the tissue, beyond which PML staining abruptly stopped (Figure 3.9). In contrast, nuclear DAPI staining was observed throughout the entire tissue. Thus, conventional immunofluorescent staining using primary and secondary antibodies is inadequate for visualising proteins deeper into the tissue.

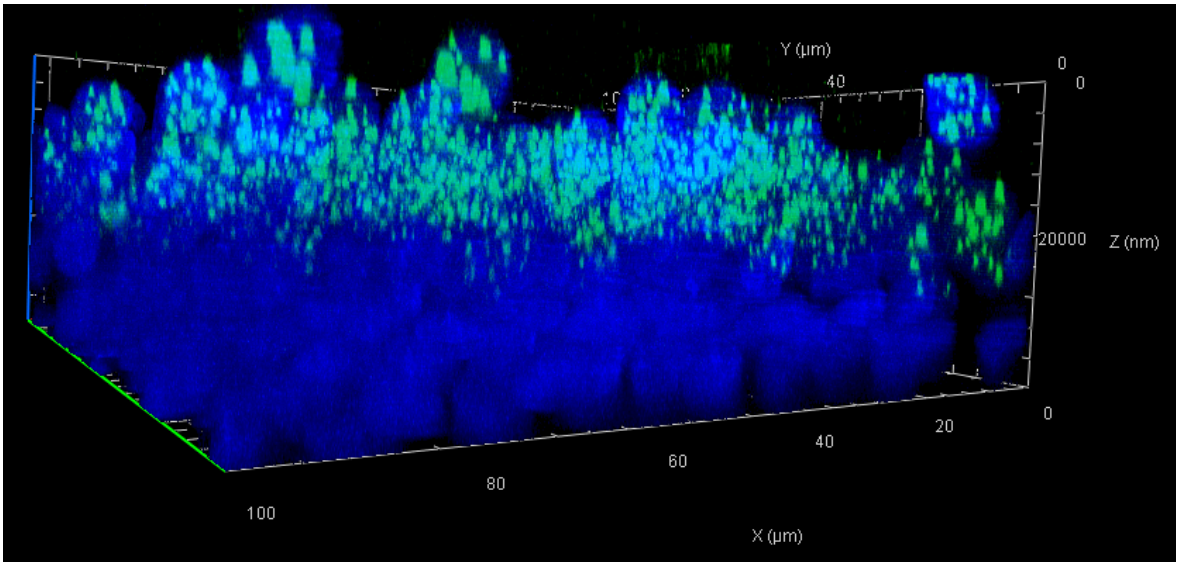

Figure 3.9: Immunofluorescent staining using conventional primary and secondary antibodies limits depth of staining. *HAEC-b cells were differentiated on Membricks over five weeks, then fixed and permeabilised overnight. Tissues were stained with PML primary antibody and conventional secondary antibodies conjugated to Alexa Fluor 488. Zeiss confocal laser scanning microscope 880 with 40X oil objective lens was used to capture Z-stacks throughout tissue depth. Green – PML, blue – DAPI.*

To address the limited penetration of conventional immunofluorescent staining, the application of nanobodies was tested. These heavy chain only antibodies are approximately 15 kDa in size – 1/10th the size of conventional secondary antibodies. Nanobodies lack the light chain and first constant domain, with the antigen-binding fragment consisting of a single variable domain (Beghein and Gettemans, 2017). Unlike traditional staining methods, which involve separate incubation steps for primary and secondary antibodies, nanobodies combine both steps into one. To evaluate whether the nanobody protocol performed equal to or better than conventional indirect immunofluorescence double staining, HBEC3-KT cells were seeded onto glass coverslips and stained for PML using either conventional antibodies or nanobodies. Two antibody incubation protocols were used: a 1-hour separate antibody incubation (primary, wash, secondary) and a 1-hour pre-conjugated antibody incubation (primary and secondary combined). Confocal microscopy revealed minimal differences in PML immunostaining between nanobodies and conventional secondary antibodies (Figure 3.10). Laser intensity was increased to obtain clearer images of the nanobody stained samples, which resulted in increased cellular autofluorescence, and cell outlines can be observed in the red channel. No signal was observed in the secondary antibody only control. Nevertheless, nanobodies performed similar to conventional secondary antibodies in the immunofluorescent staining of 2D cells, regardless of staining protocol.

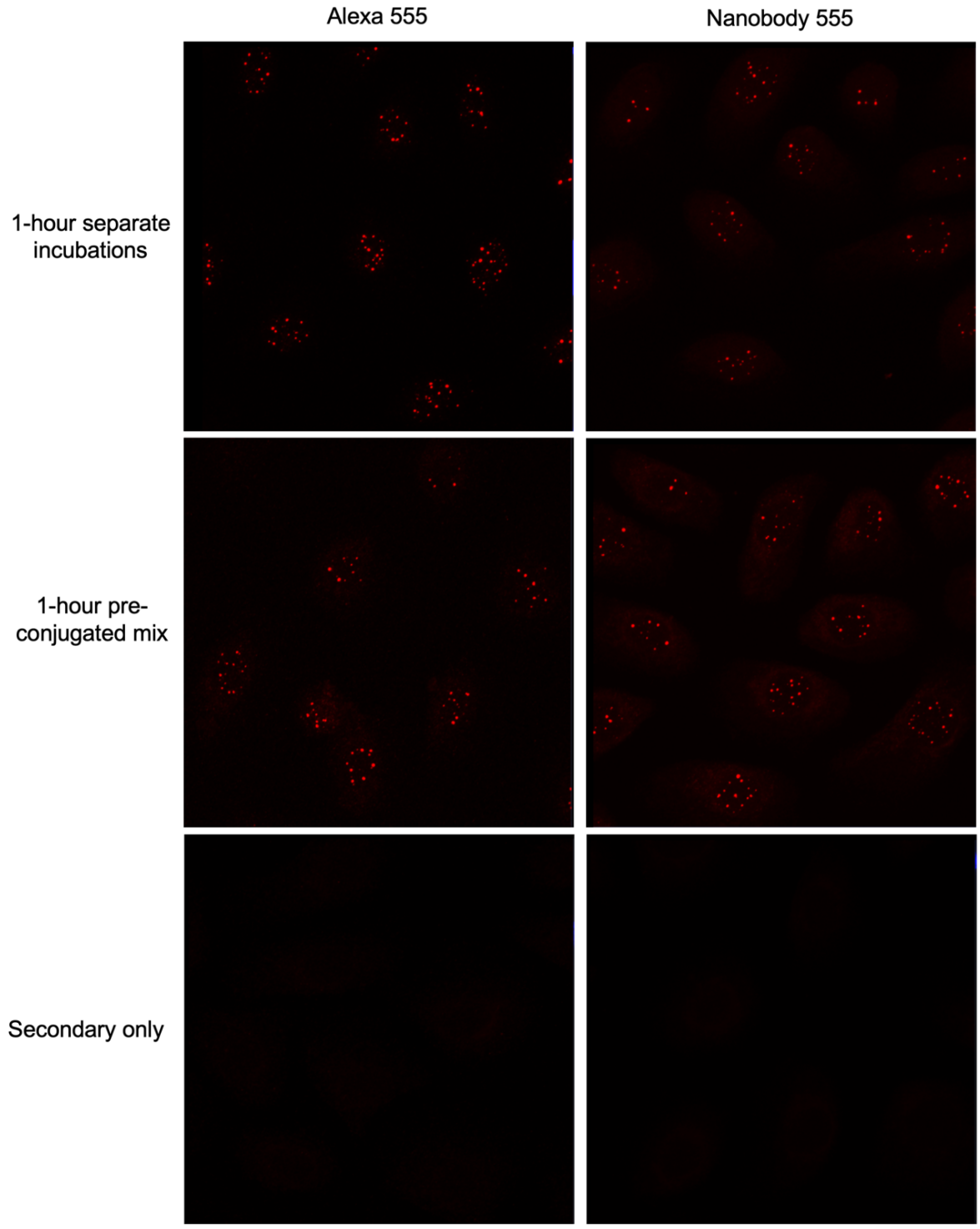

Figure 3.10: Nanobodies provide similar immunofluorescent staining to conventional secondary antibodies in 2D cells. *HBEC3-KT cells were seeded onto coverslips, cultured for 24 hours, fixed, permeabilised, and stained for PML. Left – staining with Alexa 555 conjugated secondary antibody. Right – staining with secondary nanobody. Two staining protocols were used: 1-hour separate incubations and 1-hour pre-conjugated incubation. Zeiss confocal laser scanning microscope 880 with 63X oil objective lens and airyscan were used to image cells.*

To determine if nanobodies can penetrate deeper into the tissue, they were used in the immunofluorescent staining of tissues grown on Membricks. Fixed and permeabilised tissues were stained with primary PML antibodies and secondary nanobodies. Confocal microscopy was used to capture Z-stacks throughout the tissue. PML staining was observed throughout the tissue depth, with the final slice of the Z-stack still showing PML staining (Figure 3.11). Increased green background fluorescence was observed compared to previous conventional antibody staining of 3D tissues, likely due to increased levels of laser excitation required to detect a visible signal. Thus, nanobodies can be used for deeper immunofluorescent staining of tissues grown on Membricks.

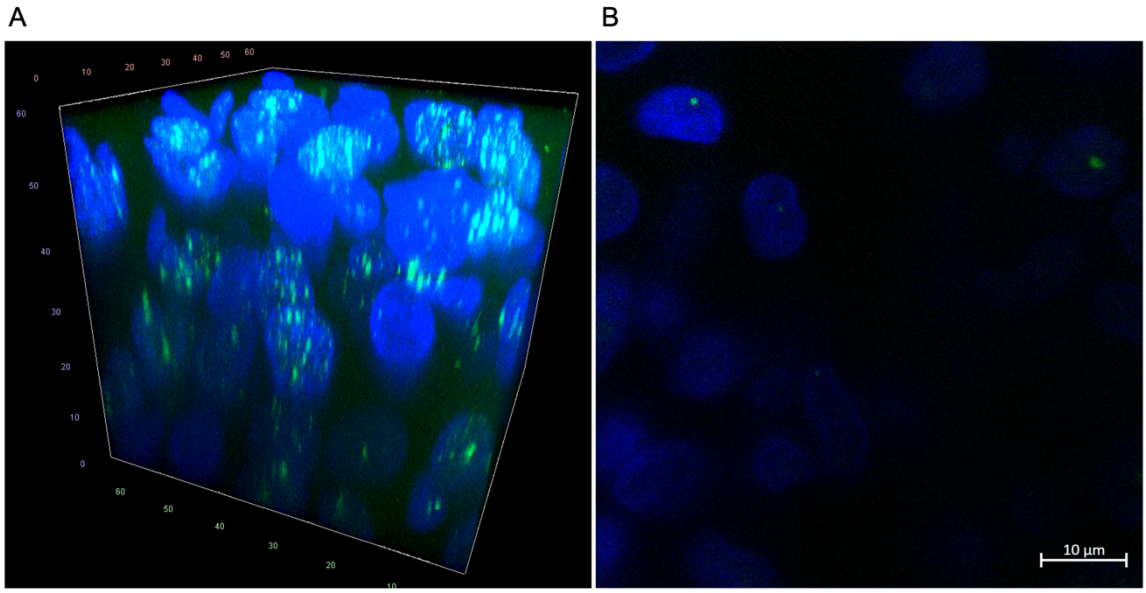

Figure 3.11: Nanobodies overcome antibody penetration limitations in tissue staining. *HAEC-b cells were differentiated on Membricks, fixed, permeabilised, stained for PML using a primary antibody and secondary nanobody, and counterstained with DAPI. A Zeiss confocal laser scanning microscope 880 with 63X oil objective lens was used to capture Z-stacks throughout tissue. A – Z-stack projection of the tissue on a Membrick. B – image of the bottom slice from the Z-stack. Green – PML, Blue – DAPI.*

Using these imaging techniques, 3D tissues were nanobody-stained to identify epithelial cell markers. The onset of ALI conditions initiates the differentiation process, leading to the development of multiple epithelial cell types, including ciliated, goblet, and basal cells (Silva *et al.*, 2023). After five weeks in culture, fully differentiated tissues were fixed, permeabilised, and stained for ß-tubulin (ciliated cells), Muc5AC (goblet cells), and p63 (basal cells) (Pharo *et al.*, 2020). Confocal microscopy was used to obtain Z-stack images throughout the tissue depth. All three cell types were observed within the differentiated cell population on Membricks. Ciliated cells were detected protruding from the apical surface, goblet cells were located beneath, and basal cells were found at the bottom of the tissue (Figure 3.12).

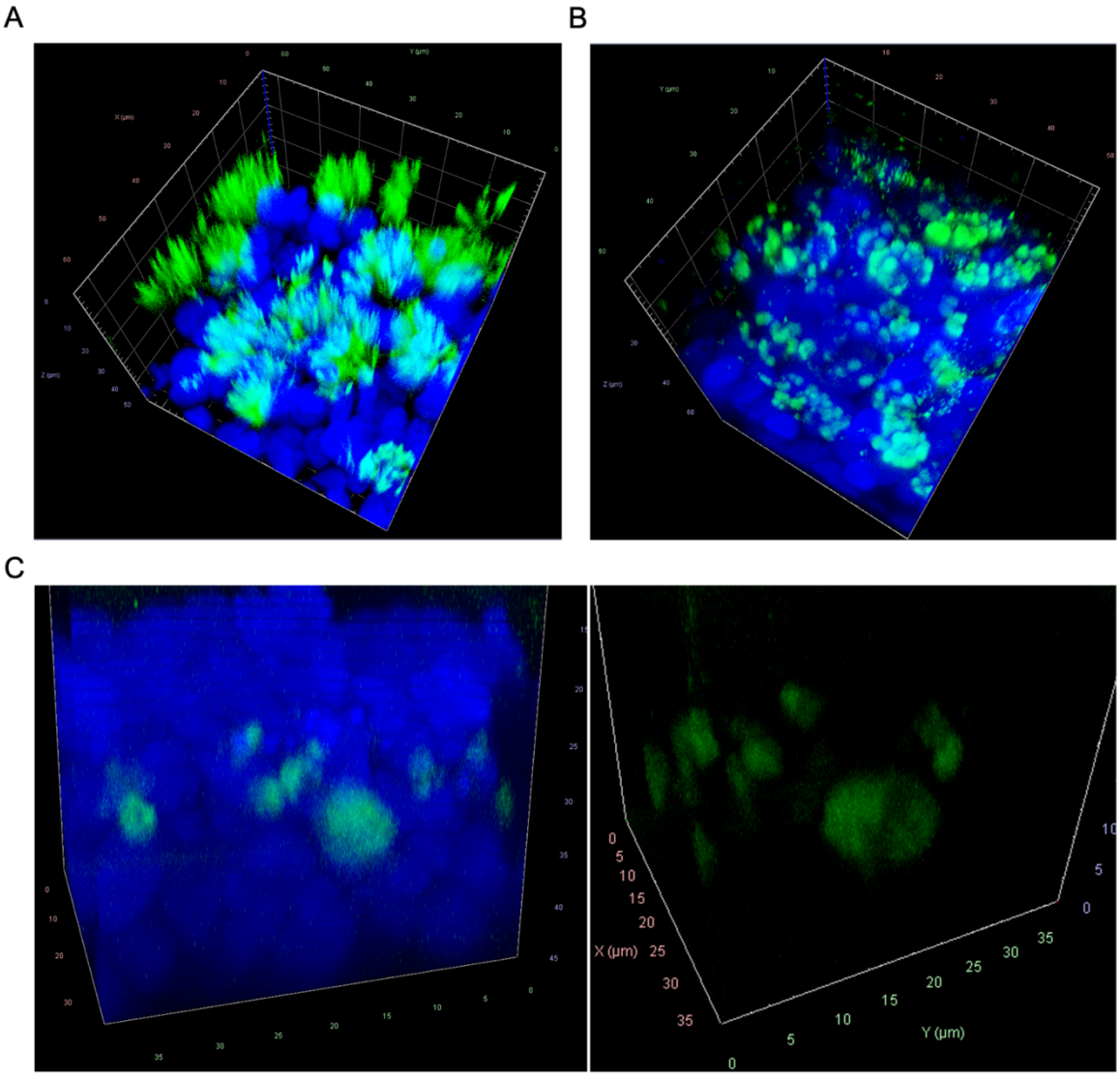

Figure 3.12: Cell marker staining of tissues differentiated on Membricks. *Tissues were fixed overnight, immunofluorescence stained for cell markers, then imaged with a Zeiss confocal laser scanning microscope 880 with 40X oil objective lens. A - ciliated cells, B - goblet cells, and C - basal cells. Green - cell marker. Blue - DAPI.*

3.2.7. Membricks have similar imaging properties in comparison to Transwells

To investigate the potential of Membricks for imaging studies, their imaging properties were compared to those of commercially available Transwell inserts. PML forms 10-30 nuclear bodies per nucleus, each approximately 0.2-1 µm in diameter (Zhong, Salomoni and Pandolfi, 2000). Due to their small size, lower resolution imaging methods cannot distinguish PML bodies due to their dense packing in the nucleus resulting in converging bodies, and therefore, higher resolution imaging is required (Osterwald *et al.*, 2012). Imaging cells on Membricks and Transwells alters imaging quality compared to conventional glass coverslips due to altered refractive indices and dispersion (Elliott, 2020; You *et al.*, 2023). Thus, confocal microscopy imaging of PML was used to compare imaging properties between products.

HBEC3-KT cells were seeded onto Membricks, glass coverslips, and three brands of Transwell inserts: Corning, Greiner, and Falcon. Cells were cultured for 48 hours, fixed and permeabilised overnight, immunostained for PML, and counterstained with DAPI. Transwells and Membricks were mounted onto coverslips and imaged using confocal microscopy with Airyscan. Compared to cells on glass coverslips, Membricks produced darker images with less well-defined structures when using the same laser intensity (Figure 3.13A). To quantify background fluorescence in Membricks and Transwells, intensity profiles were analysed from images acquired from each product. Profiles were created by drawing a straight line across images which encompassed three cells. Ideally, fluorescence should be confined to areas containing cells, with no signal in empty regions. Imaging of Corning Transwells showed blue speckles in the background, blurry nuclei, and barely visible PML staining (Figure 3.13B). Intensity profile analysis demonstrated small peaks of fluorescence in areas without cells, indicating background noise (Figure 3.13C). Falcon Transwells had slightly improved imaging with faint blue and green speckles, sharper nuclei, and more discernible PML staining. The intensity profile showed lower fluorescence in areas without cells, though it never reached zero. Greiner Transwells and Membricks displayed similar imaging quality with no speckles, and clear visualisation of nuclei and PML. The intensity profile reached zero in areas without cells, indicating little to no background signal. These results suggest

Membricks may offer enhanced imaging quality compared to Corning and Falcon Transwells for 2D cell imaging, and are comparable to Greiner Transwells. To further investigate if Membricks provide enhanced imaging quality, a higher number of replicates and statistical analysis should be carried out on fluorescence intensity between both Membricks and Transwells.

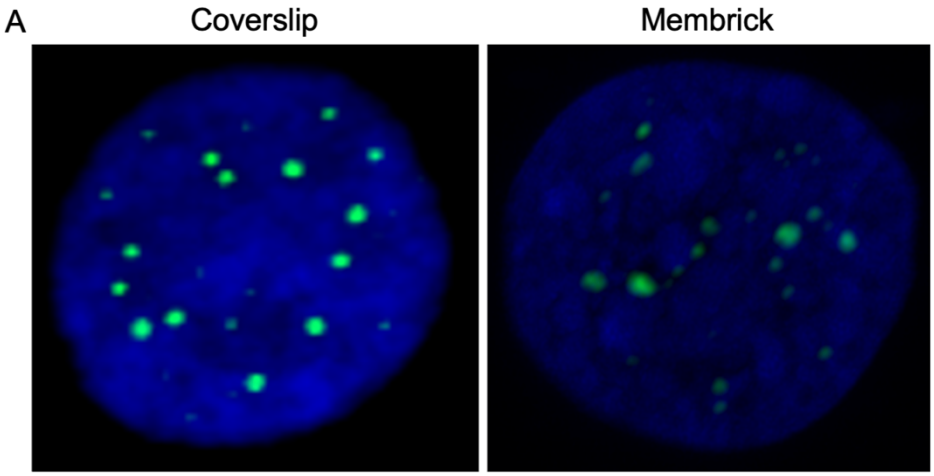
A
Coverslip
Membrick

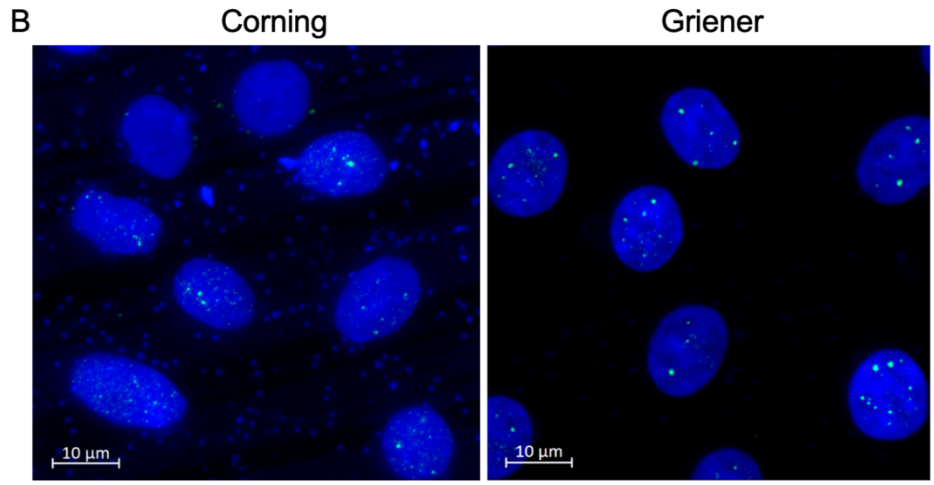
B
Corning
Griener
10 µm
10 µm

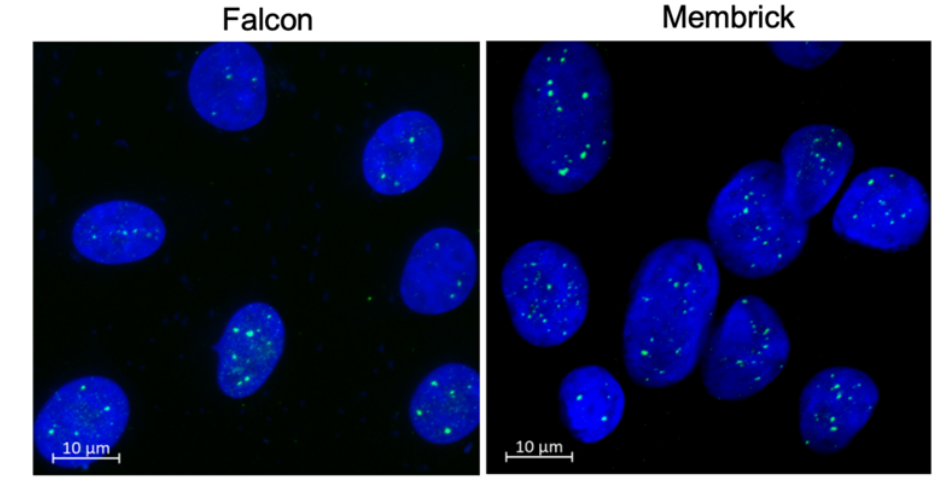
Falcon
Membrick
10 µm
10 µm

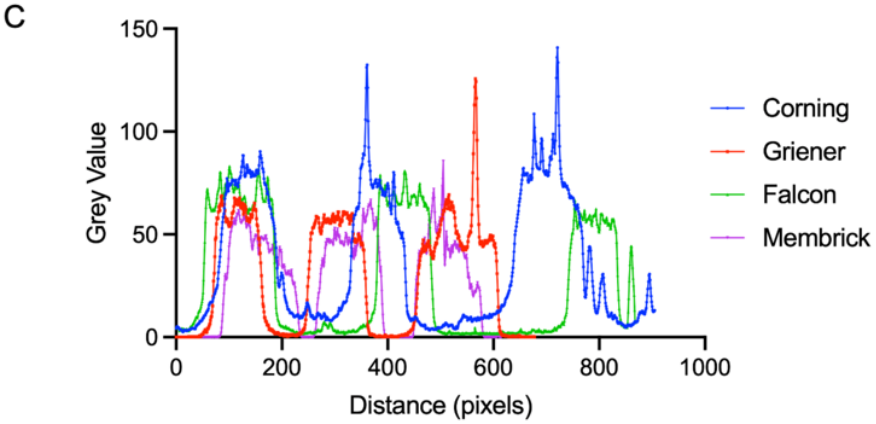
C
150
100
50
0
Grey Value
0
200
400
600
800
1000
Distance (pixels)
Corning
Griener
Falcon
Membrick

Figure 3.13: Imaging of 2D cells on coverslips, Membricks, and Transwells. *HBEC3-KT cells were seeded onto glass coverslips, Membricks, and Transwells, and cultured for 48 hours. Cells were fixed, permeabilised, and stained for DAPI (blue) and PML (green). Maximum intensity projections were captured using a Zeiss confocal laser scanning microscope 880 with 63X oil objective lens and Airyscan. A – cells on coverslip and Membrick. B – cells on Corning Transwell, Greiner Transwell, Falcon Transwell, and Membrick. C – intensity profiles of a line spanning three cells from images of Transwells and Membricks. X-axis represents the line distance and Y-axis represents the Grey Value (pixel intensity).*

Membricks and Greiner Transwells demonstrated the highest imaging quality, prompting an investigation of their imaging capabilities for 3D tissues. HAEC-b cells were seeded onto both scaffolds, differentiated over five weeks, fixed, permeabilised, and stained with DAPI. Confocal microscopy was used to capture Z-stack images of tissues on both Membricks and Transwells. Greiner Transwells showed elongation of the nuclei in the Z-plane which resulted in blurred images, and a noticeable decrease in signal intensity towards the basal side (Figure 3.14A). In contrast, Membricks showed less elongation of the nuclei resulting in a more defined shape and maintained consistent signal intensity throughout the tissue depth (Figure 3.14B). These findings indicate Membricks offer similar imaging properties with more well-defined nuclei compared to Greiner Transwells for tissue imaging.

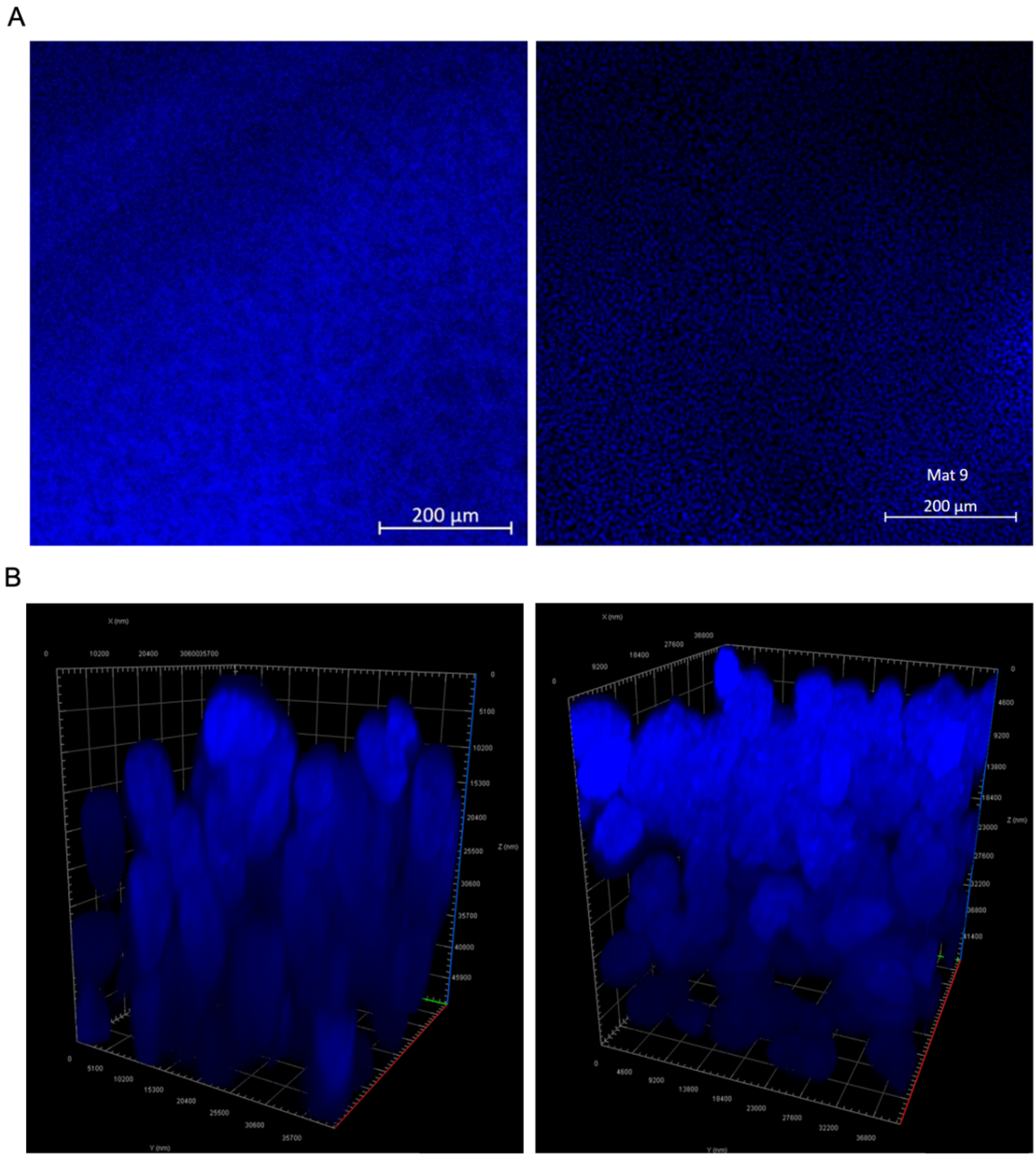

Figure 3.14: Membricks provide more well-defined images to Greiner Transwells for 3D tissue imaging. *HAEC-b cells were differentiated for 5 weeks on Membricks and Greiner Transwells. Tissues were fixed and permeabilised then stained for DAPI (blue). A Zeiss confocal laser scanning microscope 880 with 40X and 63X oil objective lens and Airyscan was used to capture Z-stacks throughout the tissues. A - top view of tissues and B - Z-stack projection. Left - Greiner Transwell and Right - Membrick.*

3.2.8. Imaging influenza virus infection in 3D cultures differentiated on Membricks

ALI cultures are known to be susceptible to IAV infection (M. C. W. Chan *et al.*, 2010; Davis *et al.*, 2015; Pharo *et al.*, 2020). IAV infection was imaged in ALI cultures on bioprinted scaffolds using the 3D confocal imaging techniques developed previously. The Membrick scaffolds were chosen for these experiments as they demonstrated successful cellular differentiation and have a fully exposed apical surfaces allowing for easier infection and washing compared to the partially enclosed Haemobrick scaffold. HAEC-b cells were differentiated on Membricks for five weeks, washed with PBS to remove secretions, and infected with mouse-adapted influenza A/California/07/2009 (MaCal/09) for two hours. Following infection, tissues were washed, and basal media was changed. After incubation at 37ºC and 5% CO_2 for 48 hours they were fixed and permeabilised overnight, washed, and antibody stained for IAV NP overnight. Tissues were stained with secondary nanobodies and DAPI for one hour, then the biomaterial was removed from the cylindrical plastic supports and mounted onto a glass coverslip. Confocal microscopy was used to capture Z-stacks throughout the depth of the tissue. IAV infection was observed only in cells at the apical surface (Figure 3.15). NP staining could not be seen beyond a tissue depth of 15 µm, although DAPI staining was visible throughout the entire tissue. This suggests that either IAV replication is limited to the surface layer of the tissue at 48 h.p.i., the fluorophores are photobleaching, or the nanobodies failed to penetrate deeper into tissues – contrasting with the deep tissue nanobody staining seen with PML (Figure 3.11).

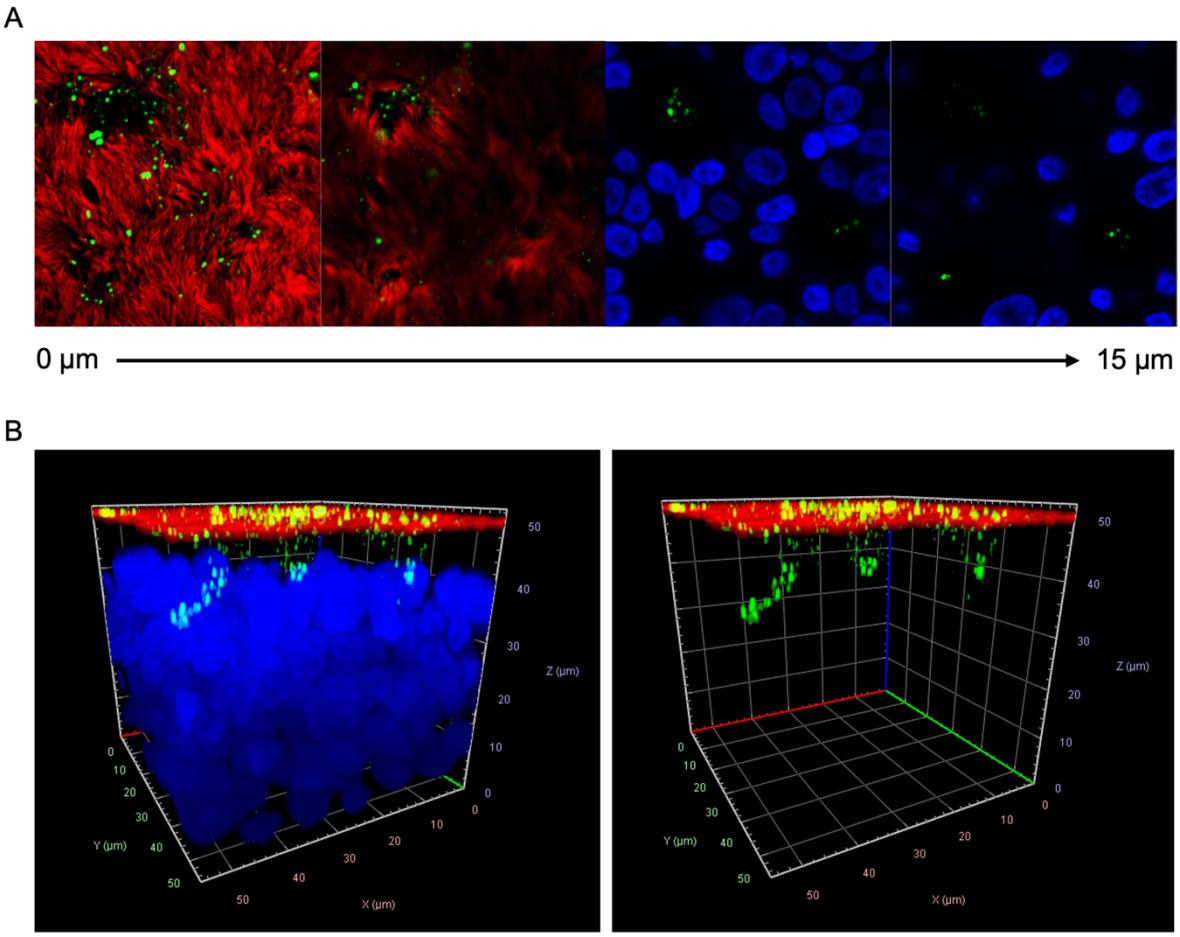

Figure 3.15: MaCal/09 infection of tissues differentiated on Membricks. *Tissues cultured on Membricks were infected with MaCal/09 and incubated for 48 hours at 37ºC. Tissues were fixed, permeabilised, antibody stained for IAV NP, and counterstained with DAPI. Z-stacks were captured using Zeiss confocal laser scanning microscope 880 with 40X oil objective lens. A - individual slices from Z-stack from apical layer (0 µm) to bottom of virus replication (15 µm). B - Z-stack with and without DAPI. Green - IAV, blue - DAPI, red - cilia.*

Instead of relying on immunofluorescent staining of IAV proteins, a fluorescently tagged influenza A/Puerto Rico/8/1934 (PR8) virus, termed “BrightFlu”, was utilised for infection assays (generously provided by the Hutchinson group (MRC – University of Glasgow Centre for Virus Research)). This virus contains a ZsGreen fluorophore within in the NS1 genome segment. 2A autoproteolytic sequences flank the ZsGreen gene, ensuring the fluorophore is cleaved from the NS1 protein upon replication, resulting in a fluorescent trail representing IAV replication from cell to cell, and bypassing the constraints of antibody-based staining. Tissues grown on Membricks were infected with 1,000 plaque forming units (PFU)/mL of BrightFlu per tissue for two hours, then fixed at 24- and 48-hours post-infection (h.p.i.) and stained for ciliated cells and DAPI. Confocal microscopy was used to capture areas of infection. Figure 3.16A illustrates the spatial localisation of BrightFlu, moving from the apical surface deeper into the middle of the tissue. Virus replication was observed up to 50 µm deep at 24 hours, whereas by 48 hours, it reached the bottom of the tissue at 90 µm (Figure 3.16B and C). Additionally, a gradual reduction in TEER was observed over the infection period, suggesting IAV replication progressively damaged the epithelial barrier of the tissues (Figure 3.16D).

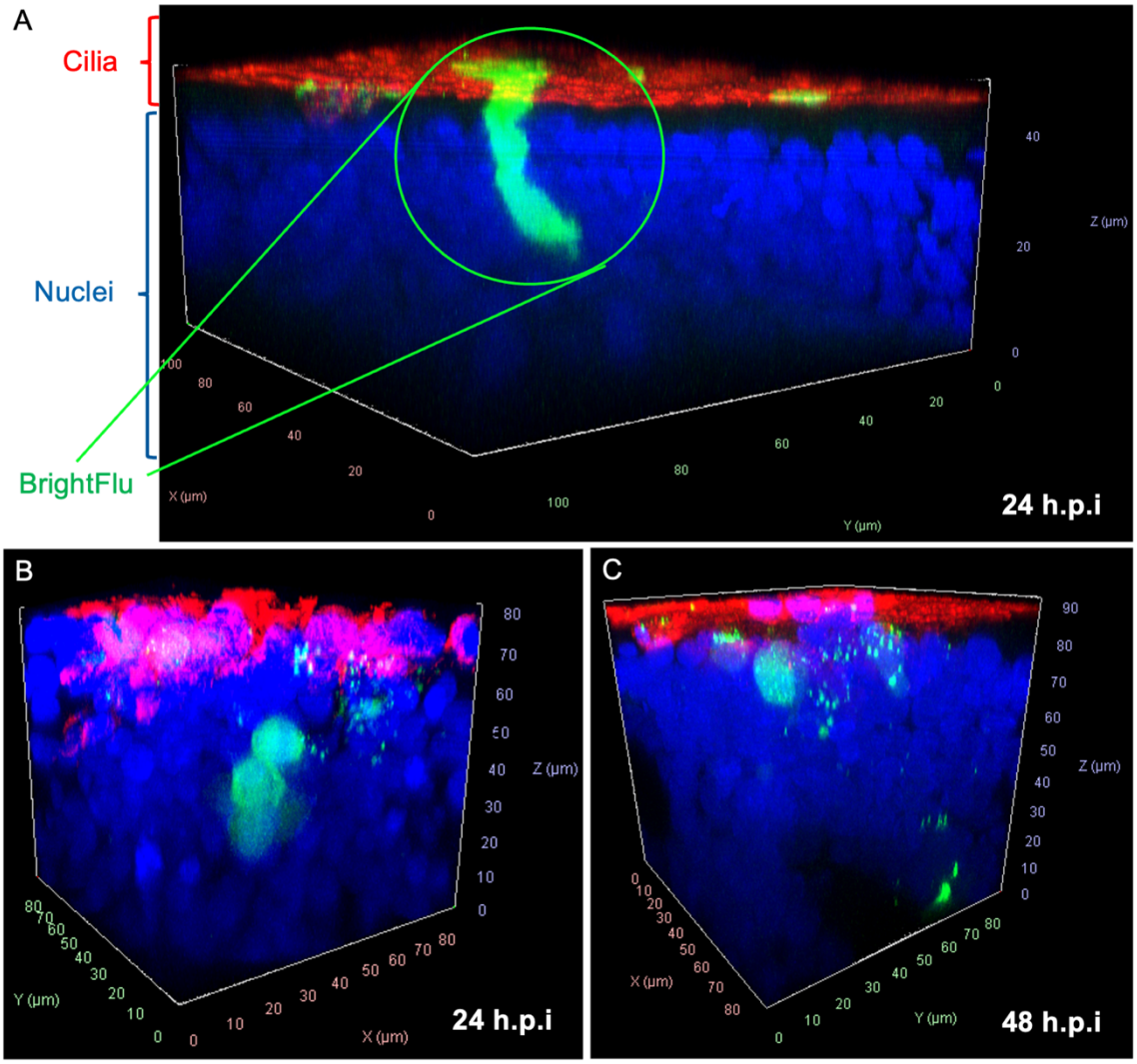

Figure 3.16: BrightFlu infection of tissue on Membricks. *Tissues were infected with BrightFlu and incubated up to 80 hours. Tissues were fixed and permeabilised at 24 (A and B) and 48 (C) hours post-infection (h.p.i.), stained for cilia (red) and DAPI (blue). Z-stacks were captured using a Zeiss confocal laser scanning microscope 880 with 40X oil objective lens and Airyscan. D – TEER measurements were recorded from 0-80 h.p.i.*

3.2.9. Membrick "delamination" is a critical product flaw

Cellbricks increased their supply of Membricks as differentiation, imaging, and infections were successful. However, due to changes in their manufacturing supply chain, they were no longer able to use the original materials. Shortly after they switched materials, a problem was identified when HAEC-b cells were cultured under ALI conditions. The bioink membrane began to spontaneously detach from the plastic cylinder, allowing cell culture medium to leak into the apical chamber, inhibiting epithelial differentiation under ALI conditions (Gerovac *et al.*, 2014). This defect was termed "delamination" and can be visualised in Figure 3.17C when compared to healthy Membricks in Figure 3.17A and B.

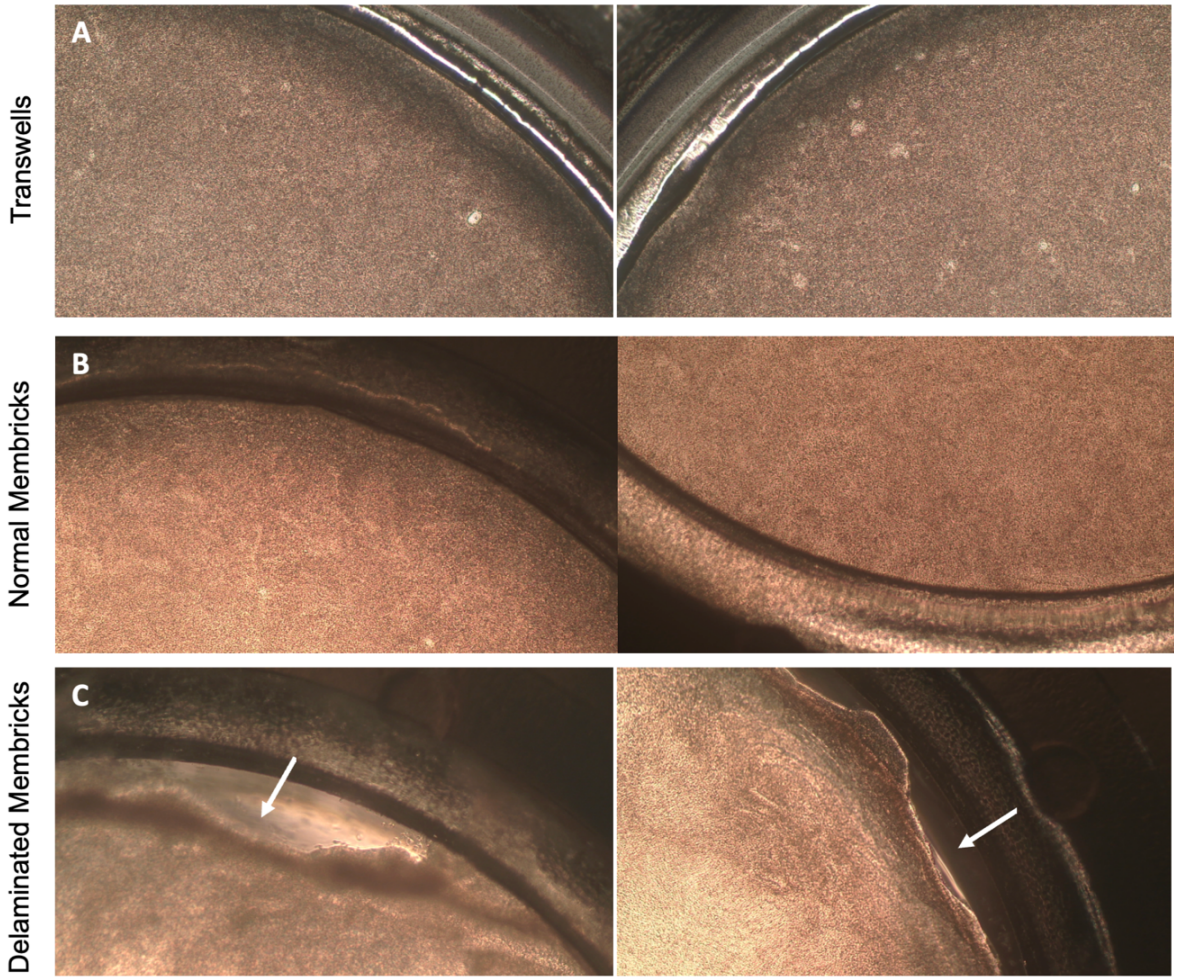

Figure 3.17: Spontaneous "delamination" of Membricks. *HAEC-b cells differentiated on Membricks and Transwells over 5 weeks and imaged with phase contrast microscope. A - Transwells, B - normal Membricks, C - "delaminated" Membricks.*

In response to the “delamination” issue, Cellbricks developed various materials over multiple batches in an effort to rectify the problem. As we communicated our observations, they created improved batches of Membricks, which we tested in rolling cycles to assess “delamination”. Due to our limited access to the specific compositions of these biomaterials, we lack information regarding the alterations made in each new batch of Membricks. Figure 3.18 illustrates the progression of material evolution based on the limited knowledge available to us.

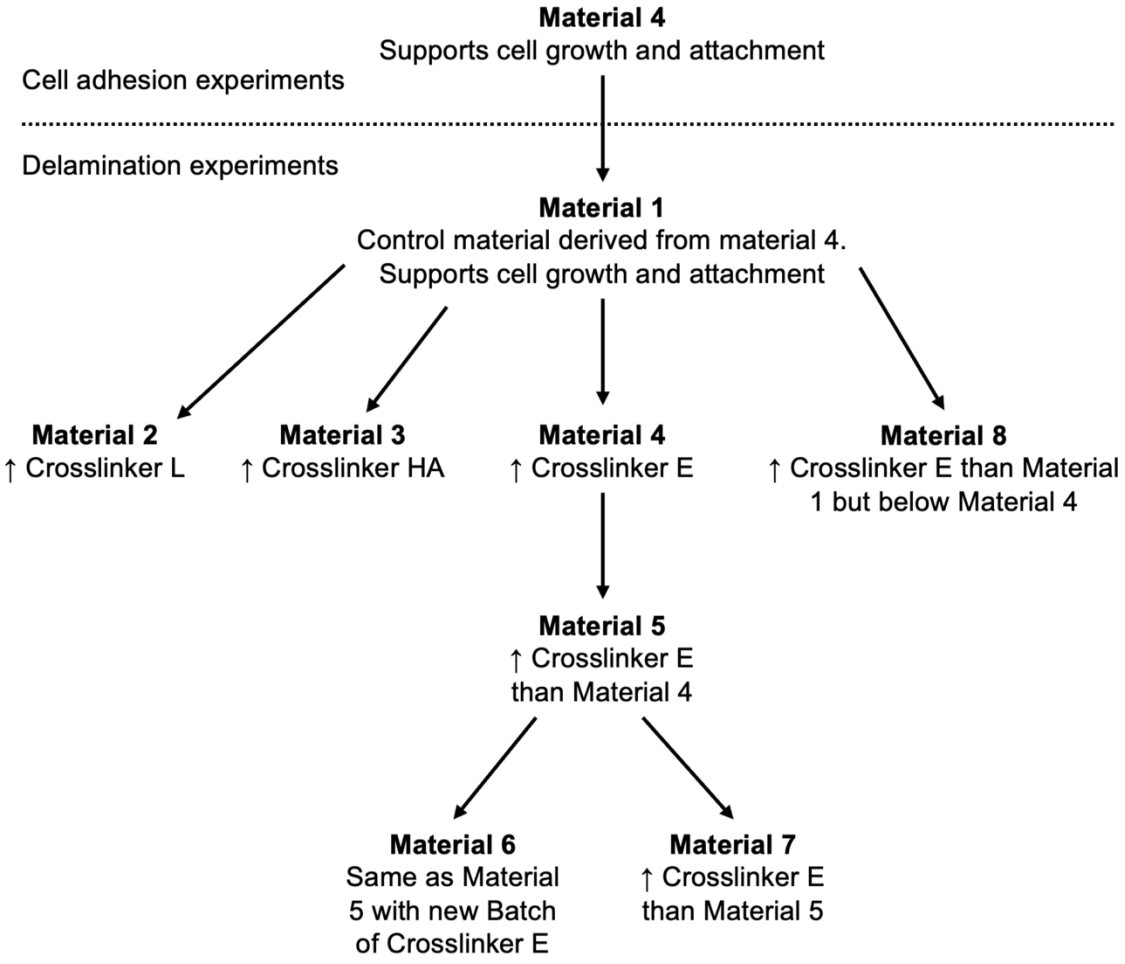

Figure 3.18: Schematic representation of Membrick material development. *Cellbricks supplied multiple batches of Membrick materials to address the “delamination” issue. Each successive material was modified based on feedback provided from our testing.*

Multiple batches of new Membricks were seeded with HAEC-b cells and put under ALI, alongside Transwells as a control. Over five weeks, Membricks were monitored every 2-3 days to record the rate of "delamination". The survival rate was calculated by dividing the number of intact and healthy Membricks by the total number of Membricks for each material after the five-week period. The number of Membricks varied for each material, ranging from 4-15, with three batches tested for materials 1-4, and one batch for materials 5-8. None of the tested materials demonstrated a consistent survival rate above 90%, a rate which had been observed in previous materials, and statistical analysis could not be carried out due to lack of power, and non-normal distribution and variance of datapoints (Figure 3.19). Due to the inconsistency in materials between batches and low survival rates, the Membrick became commercially unviable, leading to the discontinuation of its production.

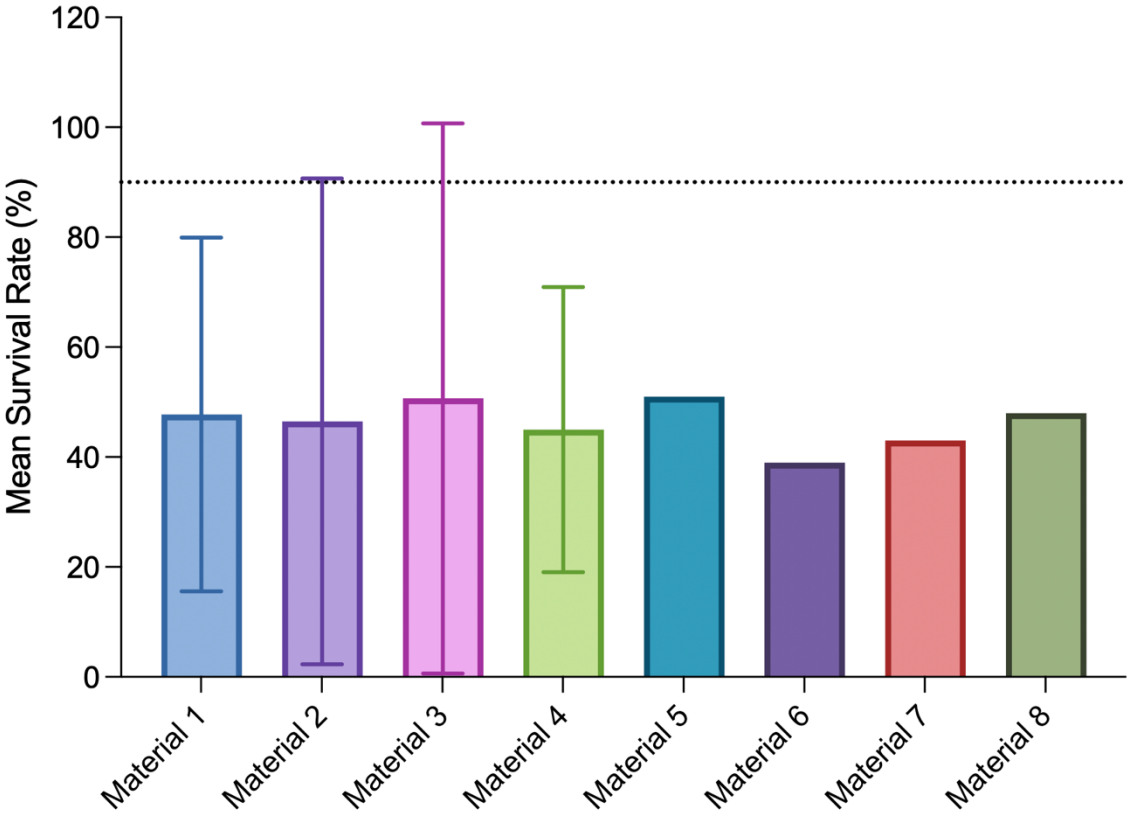

Figure 3.19: Delamination rates of different Membrick materials. *Membrick materials (1-8) were seeded with HAEC-b cells and differentiated over five weeks. They were monitored for regularly and numbers of "delaminated" Membricks were recorded. Materials 1-5 N = 4-15 over three independent batches. Error bars = mean survival rate (%) ± 1 SD across three batches. Materials 5-8 N = 4-15 over only one batch, mean was not calculated due to lack of reproducibility. Threshold was set to 90% survival rate as previous batches of Membricks provided 90% survival rates.*

3.3. Discussion

The field of bioprinting and its application in 3D tissue culture is rapidly advancing, with vast potential for innovation. While bioinks possess optimal properties for bioprinting scaffold structures, adapting these bioinks for the differentiation of primary cells requiring extended incubation periods poses significant challenges (Pepelanova *et al.*, 2018). Through frequent discussions with Cellbricks, the biomaterial composition was adjusted after each round of testing to enhance their compatibility with bronchial epithelial cells. This process led to the identification of biomaterials which successfully supported the adhesion and proliferation of 2D epithelial cells in both Haemobrick and Membrick formats. Furthermore, the Membrick supported the differentiation HAEC-b cells under ALI conditions, and the morphology of these tissues closely resembled those differentiated on conventional Transwell inserts. Together, these findings confirm that Membricks can be utilised for 3D ALI cultures of the lung epithelium.

The development of 2D and 3D microscopy methods allowed for the imaging of cells on Haemobrick and Membrick scaffolds, as well as tissues differentiated Membricks. Widefield microscopy proved the most efficient method to image entire scaffolds due to its ease and speed. For higher resolution imaging of tissues, confocal microscopy proved superior, albeit limited to capturing small sections of the scaffold. Additionally, the use of nanobodies in place of conventional secondary antibodies allowed immunofluorescence staining deeper into the tissues. The composition of the bioink greatly influenced the imaging quality, and through screening processes a biomaterial was identified with optimal imaging properties. Although ALI cultures on Transwells can be imaged, the quality and tissue depth of imaging are compromised by the PET membrane, and imaging can vary between Transwell materials (Gillespie *et al.*, 2016; Zaderer *et al.*, 2019; Möckel *et al.*, 2022; Awatade *et al.*, 2023). Confocal imaging of cells and tissues on Membricks and Transwells revealed that the Membricks had similar imaging properties. Together, these imaging advancements enabled the imaging of cells within the Haemobrick and Membrick scaffolds in both 2D cells and 3D tissues.

Using these bioimaging techniques and a fluorescently tagged PR8 virus, IAV infection was visualised within tissues cultured on Membricks. Virus replication was observed from the apical layer through the multiple cell layers at 24 hours, reaching the bottom cells at 48 hours. Notably, the virus was observed replicating vertically instead of horizontally. Traditional fluorescence imaging of ALI cultures typically involves fixing the tissue, embedding in paraffin, followed by sectioning, antigen retrieval, and immunofluorescent staining (Shinya *et al.*, 2006; Thompson *et al.*, 2006; Bhowmick *et al.*, 2018; Rayner *et al.*, 2019; Xia *et al.*, 2020). This approach often leads to challenges in reconstructing sections into a larger 3D tissue assembly, resulting in a loss of spatial information. In contrast, imaging intact, unsectioned tissues grown on Membricks retained the native tissue architecture, allowing for more data to be gathered on the spatial dynamics of virus replication.

Unfortunately, the Membrick model ultimately suffered from a critical design flaw that could not be resolved within the timeframe of our collaboration. The “delamination” problem caused basal media to leak into the apical chamber – disrupting ALI conditions essential for cellular differentiation (Gerovac *et al.*, 2014). Despite multiple material alterations, consistent survival rates of Membricks could not be achieved, rendering them unsuitable for commercialisation and the cessation of the project. Nonetheless, the potential applications of bioprinted scaffolds for 3D tissue culture models were clearly demonstrated prior to the “delamination” issue. The Membrick supported the cellular differentiation of HAEC-b cells into a tissue and provided higher quality images compared to Transwells. Moreover, it enabled the visualisation of IAV replication throughout the tissue without the need for sectioning. These findings highlight both the promise and challenges of utilising bioprinted scaffolds to advance tissue culture models.

4. Monitoring influenza virus replication kinetics for inhibitor screening

4.1. Introduction

The ALI model cultured on Membricks enabled the development of advanced 3D imaging techniques for studying IAV replication. However, the "delamination" issue necessitated the transition to a Transwell ALI model. As confocal microscopy of individual Transwells is extremely time consuming and labour intensive, we decided to adopt a more traditional 2D cell culture approach for inhibitor screening. The efficacy of IAV inhibitors are typically measured using endpoint assays in MDCK cells (Furuta *et al.*, 2002b; Takahashi *et al.*, 2003). To complement endpoint assays, real-time assays can be used to detect delays in virus growth and effects of inhibitors that may be missed using only a single timepoint. This chapter describes the development of a 2D real-time assay designed to monitor IAV replication kinetics throughout the entire time course of infection. This assay was then applied to investigate a range of potential antiviral inhibitors and translated to tissues using imaging methods.

Favipiravir (T-705), initially developed as an anti-influenza treatment, has broad-spectrum antiviral activity against RNA viruses by inhibiting RdRp (Furuta *et al.*, 2002b, 2013). As a prodrug, favipiravir is converted by cellular enzymes inside the body into its active form favipiravir-RTP. This active form is a purine analogue which is incorporated into the synthesis of complementary viral RNA in place of guanosine or adenosine, thereby terminating elongation and halting viral replication (Furuta *et al.*, 2005). Favipiravir has demonstrated broad *in vitro* and *in vivo* activity against influenza virus strains, including those otherwise resistant to antiviral drugs (Takahashi *et al.*, 2003; Sleeman *et al.*, 2010). In particular, favipiravir has shown greater antiviral efficacy against PR8 in MDCK cells and mouse models compared to oseltamivir (Takahashi *et al.*, 2003). Due to its antiviral properties, favipiravir was selected as a model inhibitor to validate assay design and establish a positive control benchmark for screening other putative inhibitors.

In 2023 a collaboration was initiated with Janet Scott (MRC – University of Glasgow Centre for Virus Research), and Glenn Burley's research group (University of Strathclyde (https://www.burleylabs.co.uk)). The Burley group specialises in synthetic organic chemistry and our primary collaborator, Otto Linden, focusses on difluoromethylation of nucleosides and nucleic acids. Using their established methodologies, the group have the capability to screen chemical databases, model chemical compounds, identify top drug candidates, and synthesise these compounds. As part of this collaboration, four novel favipiravir analogues were synthesised in an attempt to improve the antiviral potential of favipiravir. The primary objective was to investigate these analogues for their potential antiviral activity relative to favipiravir.

The aim of this chapter is to develop an assay to monitor the real-time replication kinetics of IAV and to utilise this assay for drug discovery using favipiravir and its analogue derivatives.

4.2. Results

4.2.1. Influenza virus replication kinetics can be monitored in real-time

A real-time assay was established to monitor IAV replication kinetics over a time course of infection. MDCK cells were infected with BrightFlu ranging from MOI 0.01 – 0.00001 and incubated in a plate reader up to 36 hours. Relative fluorescence units (RFU) from BrightFlu's ZsGreen expression were recorded at 488 nm every 15 minutes over the incubation period. To account for background fluorescence, RFU values were adjusted by subtracting the mock-infected negative control. A parallel plate was set up under the same conditions and was kept in a separate incubator. At 0, 12, 24, and 36 hours post-infection, cells were imaged using widefield microscopy at 488 nm to capture ZsGreen expression. The highest MOI (0.01) showed the quickest replication increase, starting at 6 hours, and reached a plateau by 24 hours (Figure 4.1A). The lowest MOI (0.00001) showed delayed replication that onset at 18 hours and plateaued by 36 hours. The MOI of 0.0001 showed a well-fitted sigmoidal curve of replication that stabilised by 36 hours, making it the optimal MOI for further experiments. Widefield images confirmed a gradual increase in green fluorescence from 0 to 36 hours (Figure 4.1B). This fluorescence-based assay successfully monitored ZsGreen expression from BrightFlu in real-time.

To validate that the increasing RFU recorded by the plate reader corresponded to virus replication, confirmatory plaque assays were carried out. MDCK were infected with BrightFlu at an MOI of 0.0001, At 0, 12, 24, and 36 hours post-infection, cells were fixed, permeabilised, and stained for IAV NP. Representative images were captured using the Celigo Imaging Cytometer (Figure 4.1C), and the number of plaques were counted to calculate plaque forming units (pfu) per mL. pfu/ml increased to $3.4x10^4$ at 12 h.p.i. and grew to $2.1x10^8$ at 24 and 36 h.p.i. (Figure 4.1D). The increasing trend in pfu/mL correlated with the increase in RFU, though pfu/mL had increased earlier at 12 h.p.i. relative to RFU, by 36 h.p.i, both pfu/ml and RFU start to plateau. These observations confirm that the fluorescence recorded by the plate reader was

associated with an increase in viral titre. Together, these results demonstrate that the plate reader assay can successfully monitor IAV replication kinetics in real-time.

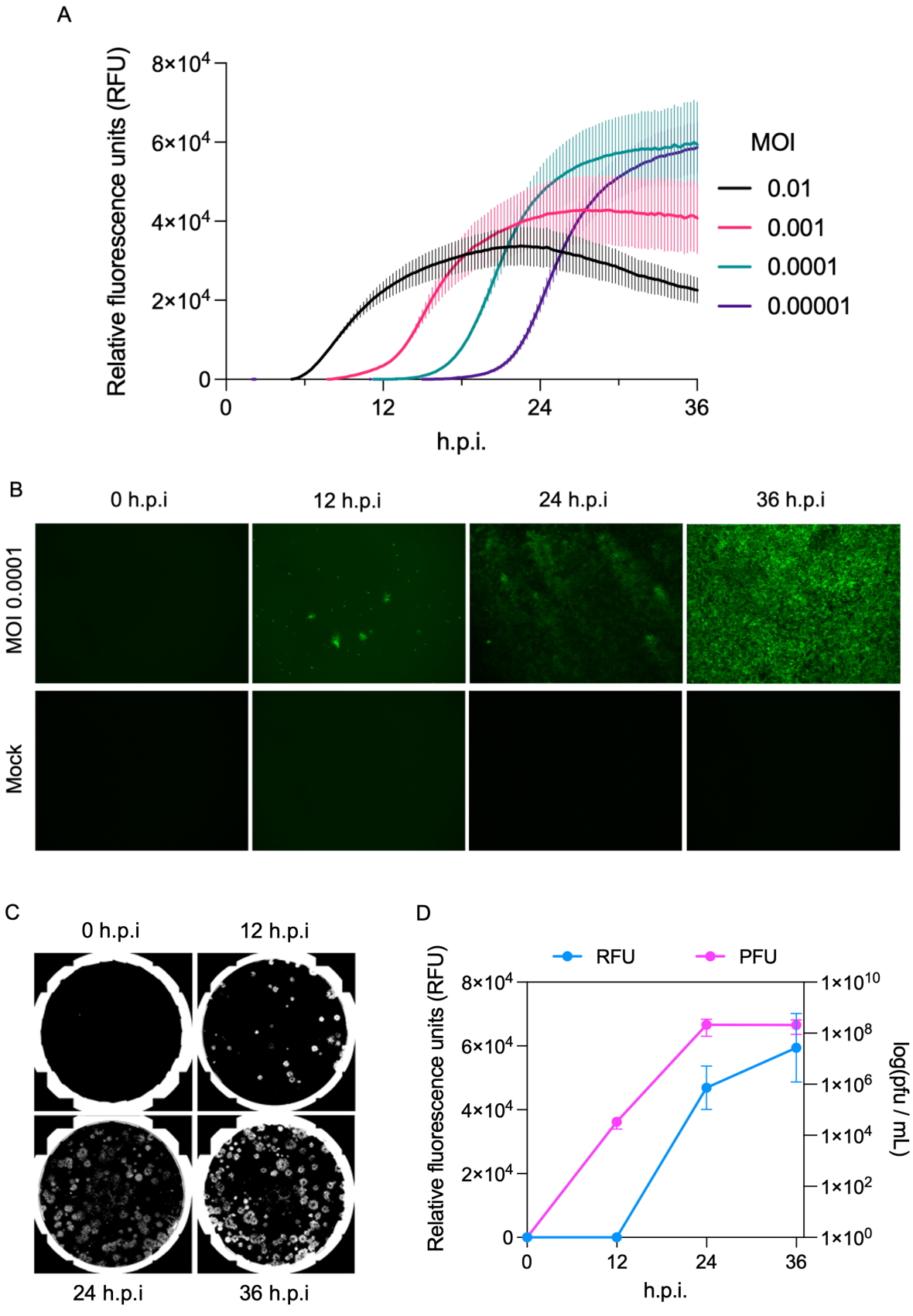

Figure 4.1: Influenza virus growth kinetics can be monitored in real-time in 2D cells*. MDCK cells were infected with BrightFlu (MOI 0.01- 0.00001) and incubated for 36 hours. A – replication kinetics of BrightFlu over 36 hours post-infection (h.p.i). ZsGreen expression was measured in relative fluorescent units (RFU) in 15-minute intervals and adjusted to subtract mock infected wells. B – representative widefield images from focus forming assay on MDCK cells infected with BrightFlu (MOI of 0.0001) at 0, 12, 24, and 36 h.p.i. C – representative images from plaque assay on MDCK cells infected with BrightFlu (MOI of 0.0001), fixed, and imaged at 0, 12, 24, and 36 h.p.i. D – plaque forming units (pfu) per mL at 0, 12, 24, and 36 h.p.i., with RFU datapoints from panel A (MOI of 0.0001). N = 3 biological replicates, with 3 technical repeats each. Error bars = mean ± 1 SD.*

4.2.2. Favipiravir inhibits influenza virus replication

Favipiravir has been shown to inhibit PR8 in MDCK cells (Furuta *et al.*, 2005). For this reason, favipiravir was used as a model drug to evaluate whether the real-time assay could identify compounds that impact IAV replication. MDCK cells were mock treated (negative control) or infected with BrightFlu (MOI of 0.01-0.0001). Favipiravir was added into the overlay medium at increasing concentrations with a negative control lacking favipiravir treatment. Cells were incubated in a plate reader and green RFU were recorded every 15 minutes up to 24 hours for an MOI of 0.01, 28 hours for MOI 0.001, and 30 hours for MOI 0.0001. Favipiravir demonstrated a clear dose-dependent inhibition in BrightFlu replication at MOI 0.01 and 0.001 (Figure 4.2A and B). At the lowest MOI of 0.0001, BrightFlu replication was significantly delayed and showed increasing deviation between biological replicates at 30 h.p.i, with dose-dependent inhibition being difficult to observe between different concentrations of favipiravir (Figure 4.2C).

Several measurements can be used to determine drug efficacy, one of which is the IC_{50} value. This indicates the drug concentration at which 50% of the virus is inhibited. Favipiravir IC_{50} values were obtained using real-time data from BrightFlu replication kinetic curves. Favipiravir concentrations were transformed into a logarithm and the maximum RFU value was extracted from each concentration. RFU values were normalised so that the maximum RFU value equals 100% and the minimum equals 0%. A nonlinear regression was then fitted to the normalised RFU values to obtain the log(IC_{50}), IC_{50}, and HillSlope values. Log(IC_{50}) represents the concentration where the dose-response curve reaches 50% of the maximum RFU. To obtain the inhibitory value in the original concentration, log(IC_{50}) was transformed back to IC_{50}. The R^2 value is an inadequate measure for goodness of fit in nonlinear regression models (Spiess and Neumeyer, 2010). Instead, the HillSlope, which describes the steepness of the curve, is more informative. A HillSlope value close to –1 represents a typical sigmoidal curve, which shows the gradual decrease in virus replication with increasing drug concentrations (Gadagkar and Call, 2015).

The results of the favipiravir dose-response curves were as follows:

- MOI 0.01: IC_{50} of 104 µM and HillSlope of -4.24.
- MOI 0.001: IC_{50} of 35 µM and HillSlope of -1.461.
- MOI 0.0001: IC_{50} of 9.99 µM and HillSlope of -1.297.

MOIs 0.001 and 0.0001 showed HillSlopes closest to -1, indicating a more optimal curve shape. However, MOI 0.0001 showed more deviation between replicates, likely due to the longer incubation time. It should be noted that gaps in the X-axis data points may impact the accuracy of regression calculations, as these datapoints are not spaced in continuous increments. Overall, this shows that the real-time assay can quantify the inhibition of IAV replication kinetics. However, further optimisation of both the virus MOI and favipiravir concentrations is necessary to improve the accuracy of nonlinear regression analyses.

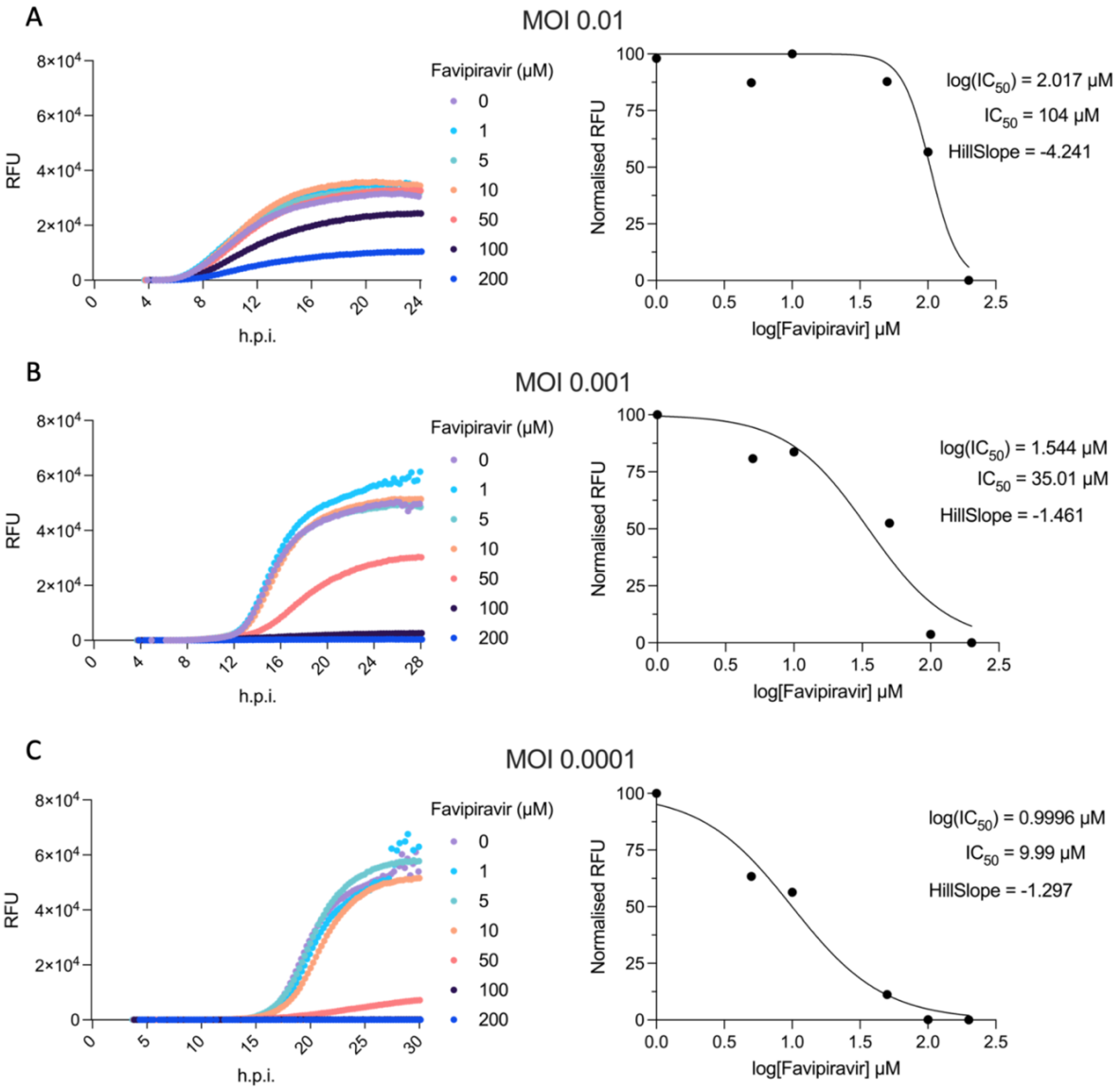

Figure 4.2: Favipiravir decreases BrightFlu replication kinetics. *Left - MDCK cells were infected with BrightFlu and overlayed with cell culture medium containing a range of favipiravir concentrations. Green relative fluorescent units (RFU) were recorded every 15 minutes from 0 to 24, 28, or 30 hours post-infection (h.p.i.), with mock infection values subtracted. Right - corresponding favipiravir dose-response curves generated using nonlinear regressions on the maximum RFU at each favipiravir dose. Calculated log(IC_{50}), IC_{50}, and HillSlope values shown on the right. A - MOI 0.01, B - MOI 0.001, C - 0.0001. N = 3 biological replicates with 3 technical replicates each. Datapoints on replication kinetic curves represent mean values.*

To optimise the nonlinear regression model used for calculating IC_{50} values, favipiravir dilutions were prepared in logarithmic increments. This prevents overcrowding specific areas of the dose-response curve and ensures datapoints are evenly distributed across the X-axis. Both a real-time assay and an endpoint assay were used to corroborate findings between them. An MOI of 0.001 was selected for its sigmoidal curve shape and can be monitored in a shorter time frame than an MOI of 0.0001, with less deviation between replicates. A 24-hour incubation period was selected as a middle ground timepoint for both assays as IAV replication kinetics plateau at 24-28 h.p.i. Two plates of MDCK cells were infected with BrightFlu at an MOI of 0.001, and mock infected as a negative control. Logarithmic increments of favipiravir concentrations were added to the overlay medium, with a negative control lacking favipiravir (Table 4.1). Replication kinetics were monitored in one plate using a plate reader to record RFU in the 488 nm range over 24 hours. The second plate was used for a focus forming assay, where cells were incubated for 24 hours, then fixed, permeabilised, and stained for NP. Representative images were captured using the Celigo Imaging Cytometer at 488 nm, and the number of foci were recorded. For nonlinear regression calculations, the maximum RFU and maximum number of virus positive cells from each well were used. Both assays demonstrated that favipiravir inhibited BrightFlu replication in MDCK cells with similar IC_{50} values of 24 and 28 μM (Figure 4.3). These results indicate that both the real-time assay and endpoint assay can be used to measure the impact of favipiravir on IAV replication.

Table 4.1: Favipiravir concentrations used in influenza replication kinetics assay.

Standard concentration (μM)	Log concentration (μM)
1	0
3.16	0.5
10	1
31.62	1.5
100	2
316.23	2.5

Favipiravir concentration increasing in 0.5 log increments. The standard concentrations are provided alongside corresponding log values.

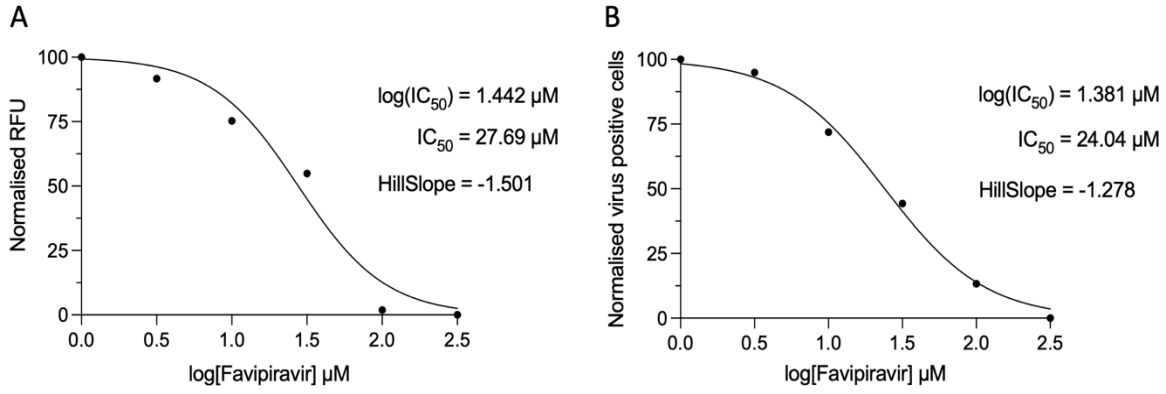

Figure 4.3: Favipiravir inhibits BrightFlu replication. *MDCK cells were infected with BrightFlu and incubated for 24 hours with favipiravir in the overlay medium added in logarithmic increments. A – dose-response curve of favipiravir inhibition using the real-time plate reader assay to record RFU. B – dose-response curve of favipiravir inhibition using the focus forming Celigo assay to record virus positive cells. The calculated log(IC_{50}), IC_{50}, and Hillslope values are shown from the nonlinear regression output. N = 3 biological replicates, containing 3 technical replicates each.*

4.2.3. Favipiravir analogues do not inhibit influenza virus replication

Favipiravir inhibits the replication of IAV in MDCK cells with an IC_{50} value of 24 – 28 μM. However, in the field of drug discovery, this inhibitory value can be considered relatively high. For example, oseltamivir, a licenced influenza virus antiviral, has an IC_{50} value of 0.559 ± 0.150 nM against PR8 in MDCK cells (McSharry *et al.*, 2004). Potent drugs typically have lower IC_{50} values, meaning the drug is more effective at lower concentrations, which reduces the dosage required to observe inhibitory effects in clinical trials. One approach to drug discovery involves designing new drug analogues by altering the composition of existing inhibitors to enhance their antiviral properties. In collaboration with Janet Scott (MRC – University of Glasgow Centre for Virus Research), Glenn Burley, and Otto Linden (University of Strathclyde), four favipiravir analogue derivatives were synthesised to determine whether the structural modification of favipiravir could improve its antiviral properties. The chemical names and molecular weights of these analogues are given in Table 4.2, and Figure 4.4 shows their chemical structures. All four analogues had a higher molecular weight than favipiravir and were each resuspended in DMSO to prepare a 10 mM stock solution.

Table 4.2: Properties of favipiravir and analogues.

Compound	Chemical name	Molecular weight (g/mol)
Favipiravir	6-Fluoro-3-hydroxy-2-pyrazine carboxamide	157.10
Analogue 1	O^4-Difluoromethyl-uridine	294.21
Analogue 2	O^2-Difluoromethyl-cytidine	293.23
Analogue 3	O^2-Difluoromethyl-deoxycytidine	277.23
Analogue 4	5-Fluoro-O^2-difluoromethyl-deoxycytidine	295.22

Chemical names and molecular weights of favipiravir and its synthesised analogues are given.

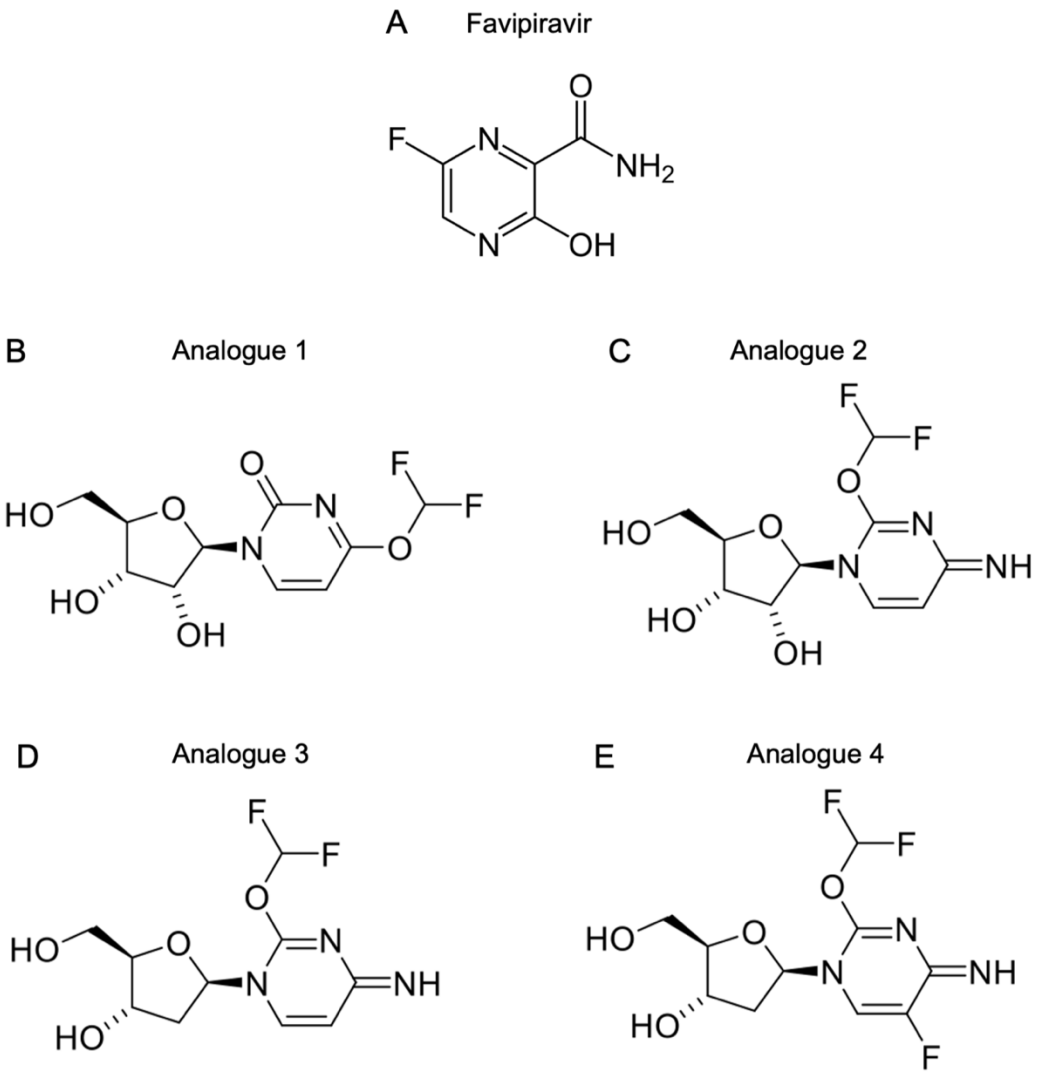

Figure 4.4: Chemical structures of favipiravir and analogues. *Chemical structures of A – Favipiravir, B – Analogue 1, C – Analogue 2, D – Analogue 3, E – Analogue 4.*

Favipiravir analogues were first evaluated for their impact on the health of MDCK cells. An MTS assay is commonly used to assess cell proliferation, viability, and cytotoxicity (Riss *et al.*, 2004). This assay relies on the reduction of an MTS tetrazolium compound by NAD(P)H-dependent dehydrogenase enzymes in metabolically active cells, resulting in a coloured formazan dye (Wong, Ong and Traini, 2022). MDCK cells were overlayed with a range of drug dilutions (0-500 µM) and incubated for 48 hours. Drugs included all four favipiravir analogues, favipiravir, puromycin (death control), and no drug treatment (positive control). After incubation, MTS reagent was added for 1 hour, and absorbance at 490 nm was recorded using a plate reader to quantify levels of formazan dye. Absorbance fold changes were calculated relative to no drug treatment. Figure 4.5A shows that absorbance decreased with increasing concentrations of analogue 2 from 200 µM onwards – dropping below the puromycin death control by 300 µM. The absorbance values from analogues 1, 3, 4, and favipiravir varied marginally relative to untreated cells and failed to reach the low absorbance values observed for puromycin (death control). These results suggest that of all the compounds tested, only analogue 2 caused MDCK toxicity at concentrations over 200 µM.

To further evaluate the impact of favipiravir analogues on cell health, the number of cells were counted after drug treatment (as described above). After 48 hours, cells were fixed and stained with DAPI, and images were captured using the Celigo Imaging Cytometer at 405 nm. The number of DAPI stained cell nuclei were counted and fold changes were calculated relative to no drug treatment. Figure 4.5B shows a decrease in cell numbers from 200 µM, 100 µM, 500 µM, and 10 µM onwards for analogues 1, 2, 3, and 4, respectively. By 300 µM, the cell counts for analogue 1 dropped to a value comparable to puromycin treated cells. Analogue 2 cell counts gradually decreased, reaching zero at 300 µM, consistent with puromycin (death control). Analogues 3 and 4 exhibited a 50% reduction in cell count at 500 µM and 100 µM, respectively. Favipiravir cell counts decreased from 300 µM onwards, and reached zero by 500 µM. Analogues 1, 2, and 4 resulted in increased MDCK cell detachment compared to favipiravir. With the exception of analogue 4, favipiravir and its derivative analogues had little impact on cell count at concentrations below 100 µM.

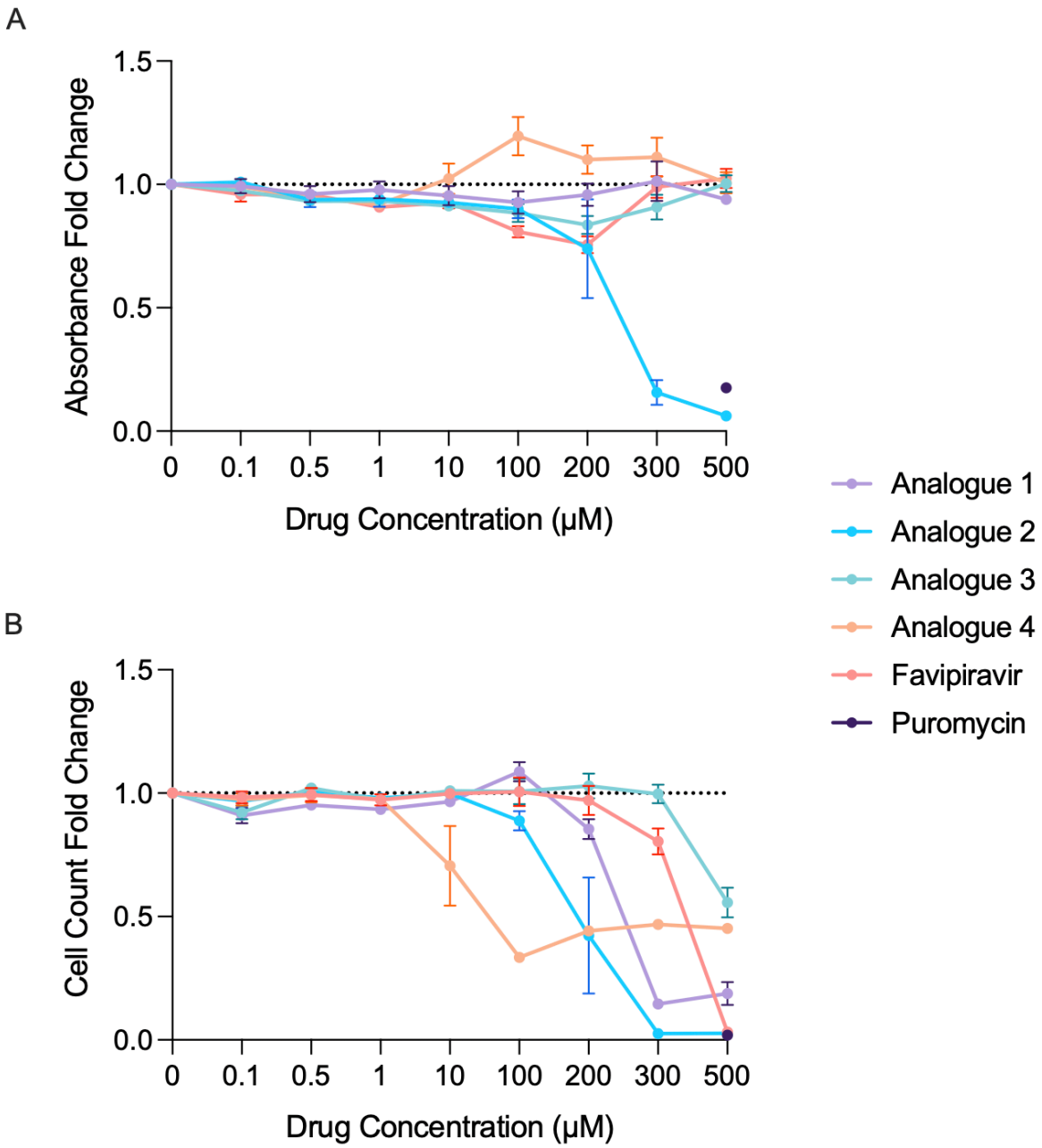

Figure 4.5: Impact of favipiravir analogues on MDCK cell health. *A - absorbance fold change relative to untreated cells. MTS assay absorbance readings taken at 490 nm after 48 hours of drug treatment. B - cell count fold change relative to untreated cells. DAPI stained cell count after 48 hours of drug treatment. Purple - analogue 1; Blue - analogue 2; Green - analogue 3; Orange - analogue 4; Pink - favipiravir; Black - puromycin death control. N = 3 biological replicates, with 2 technical replicates each. Error bars = mean ± 1 SD.*

The inhibitory effects of favipiravir analogues on IAV replication were investigated. MDCK cells were infected with BrightFlu at an MOI of 0.001 and analogues were added into the overlay at increasing concentrations, with a negative control of no drug treatment and positive control of favipiravir. After 24 hours incubation, cells were fixed, and images were captured using the Celigo Imaging Cytometer at 488 nm. The number of BrightFlu infected cells were counted, and fold change was calculated relative to no drug treatment. A dose-dependent relationship was observed between increasing favipiravir concentrations and decreasing number of BrightFlu positive cells (Figure 4.6). Analogues 1 and 3 increased in BrightFlu positive cells at 100 and 316 µM. For analogue 2, BrightFlu positive cell counts remained constant except for a small increase at 100 µM. Analogue 4 slightly increased BrightFlu positive cells at 1 and 3 µM before returning to levels comparable to no drug treatment at higher concentrations. From this selection of compounds, only favipiravir demonstrated dose-dependent inhibition of BrightFlu replication at 24 h.p.i. in MDCK cells.

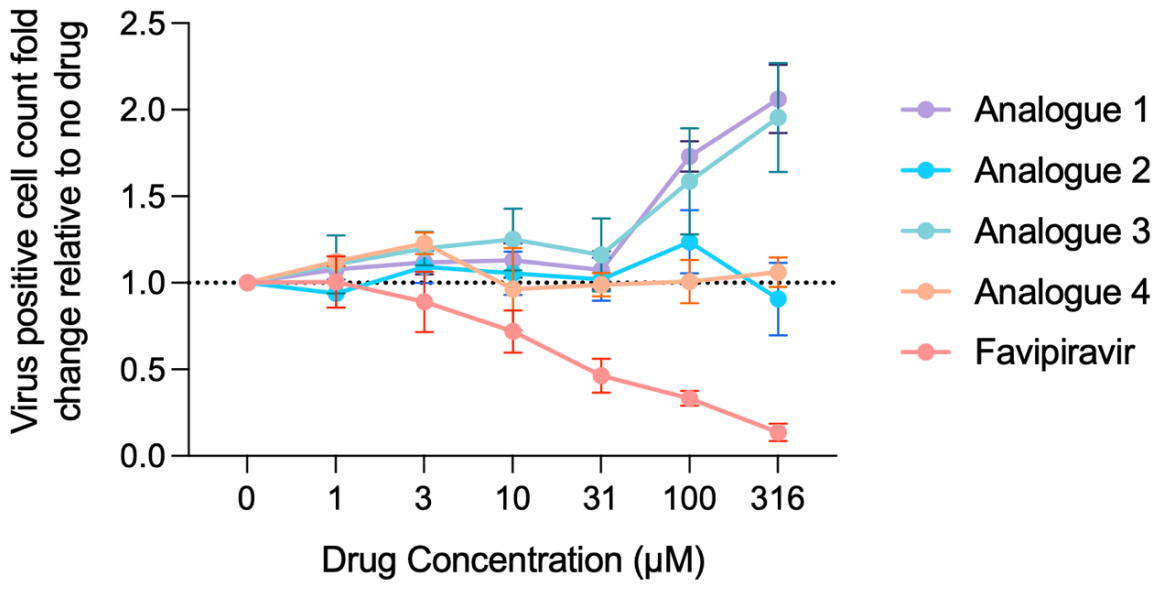

Figure 4.6: BrightFlu replication in the presence of favipiravir analogues. *MDCK cells were infected with BrightFlu MOI 0.001 and overlayed with analogues and favipiravir for 24 hours. Images were captured, and the number of virus positive cells were counted. Fold change was calculated relative to the no drug treatment control. N = 3 biological replicates, error bars = mean ± 1 SD.*

To determine whether favipiravir analogues influenced the replication kinetics of IAV beyond a 24-hour timepoint, the real-time plate reader assay was used. MDCK cells were infected with BrightFlu at an MOI of 0.001 and analogues were added into the overlay medium at increasing concentrations, with a negative control of no drug treatment and positive control of favipiravir. The cell culture plate was incubated in a plate reader to record green RFU expressed over 36 hours. To determine if a dose-dependent relationship existed between IAV replication and drug concentration, a two-tailed Mann-Whitney U-test was performed to assess whether there was a statistically significant difference in virus replication from 1 μM of each inhibitor to the maximum concentration that maintained cell viability.

Favipiravir demonstrated significant inhibition of IAV replication in a dose-dependent manner (Figure 4.7A). Analogues 1 and 2 significantly increased IAV replication in a dose-dependent manner, up to 100 μM, after which the concentration was detrimental to cell count, and thereby reduced the number of cells available for virus replication (Figure 4.7B and C). Similarly, analogue 3 significantly increased IAV replication up to 316 μM (Figure 4.7D). Analogue 4 significantly increased IAV replication until 100 μM, where it also became detrimental to cell viability (Figure 4.7E). The real-time assay showed that while favipiravir inhibited IAV replication in a dose-dependent manner, all analogues enhanced viral replication to varying degrees by 36 h.p.i. In conclusion, none of the four favipiravir analogues demonstrated inhibitory effects on IAV replication under dosing conditions that maintained cell viability.

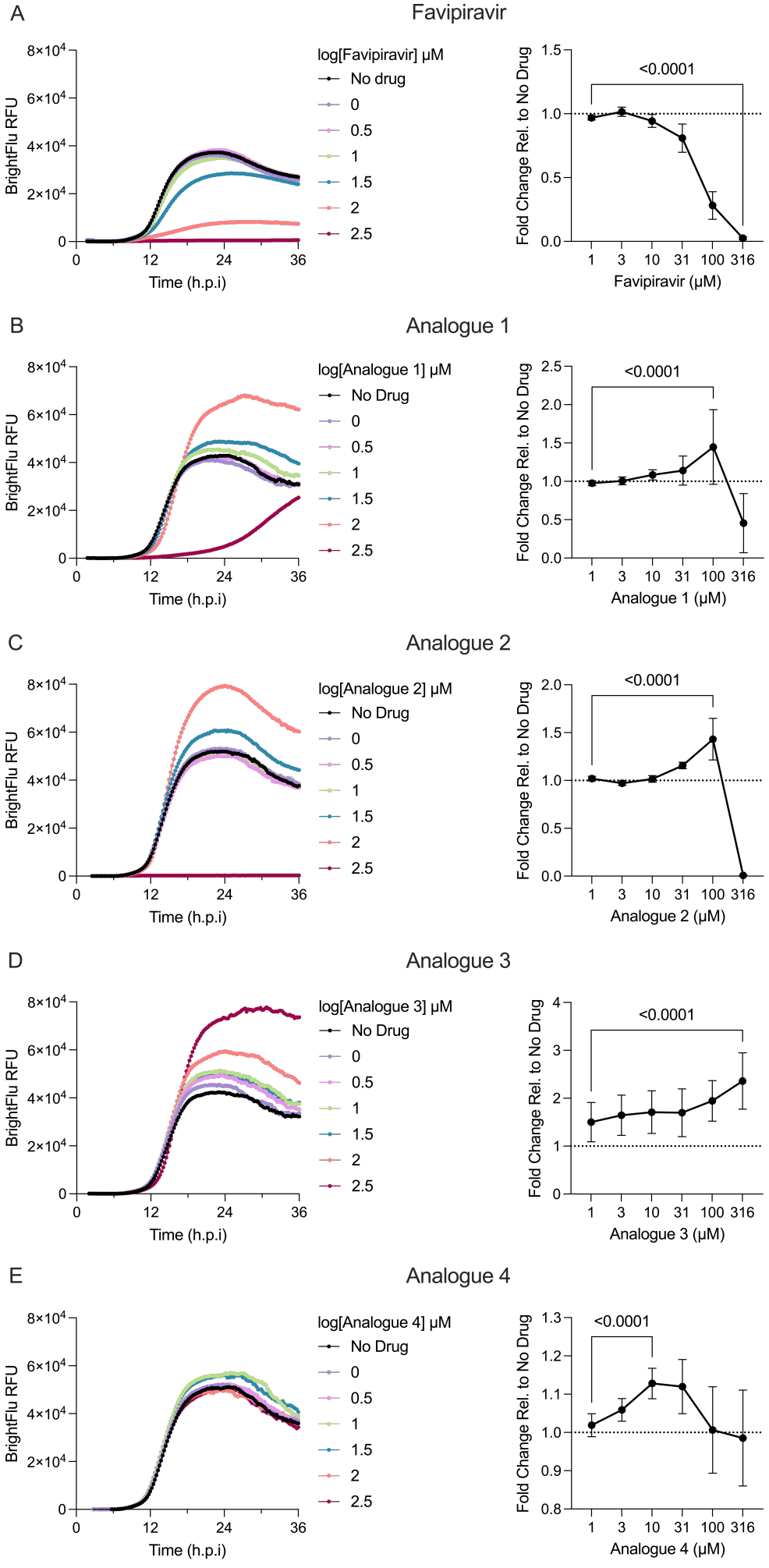
A
Favipiravir
BrightFlu RFU
Time (h.p.i)
log[Favipiravir] µM
No drug
0
0.5
1
1.5
2
2.5
Fold Change Rel. to No Drug
<0.0001
Favipiravir (µM)
B
Analogue 1
log[Analogue 1] µM
No Drug
Analogue 1 (µM)
C
Analogue 2
log[Analogue 2] µM
Analogue 2 (µM)
D
Analogue 3
log[Analogue 3] µM
Analogue 3 (µM)
E
Analogue 4
log[Analogue 4] µM
Analogue 4 (µM)

Figure 4.7: BrightFlu replication kinetic curves and fold changes with favipiravir and analogues. *MDCK cells were infected with BrightFlu MOI 0.001 and overlayed with cell culture medium containing a range of favipiravir and analogue concentrations. Left – Green relative fluorescent units (RFU) were recorded every 15 minutes from 0 to 36 hours post-infection (h.p.i.), with mock infected values subtracted. Right – Maximum RFU recorded for each drug concentration was extracted, and fold changes were calculated relative to no drug treatment. A two-tailed Mann-Whitney U-test was performed to determine statistical significance from 1 μM to the highest concentration before cell health declined. A – favipiravir, B – analogue 1, C – analogue 2, D – analogue 3, E – analogue 4. N = 2 biological replicates.*

4.2.4. Influenza virus replication kinetics cannot be monitored in ALI cultures

Since favipiravir was the only drug that successfully inhibited BrightFlu replication in MDCK cells, its effects were further investigated in 3D ALI models (described in Chapter 3). To determine whether the real-time assay could be applicable to 3D tissues, cells were trialled on Transwells to monitor viral replication. MDCK cells were seeded onto the apical chamber of Transwells and incubated overnight. The following day, cells were mock treated or infected with BrightFlu (MOI of 0.01 - 0.00001), and green RFU were recorded up to 36 hours. Figure 4.8A illustrates the plate reader settings used to monitor BrightFlu replication on Transwells. The focal plane on the Z-axis was adjusted to read RFU specifically from the Transwell apical chamber, on which the cells reside, instead of the bottom of the well. RFU were recorded across the entire diameter of the well, and values were extracted from the apical chamber by manually selecting regions of interest from the generated heatmap. This provided RFU values exclusively from the cells within the Transwell boundary. Values from the negative control (mock infected MDCK cells on Transwells) were subtracted to account for background fluorescence. The kinetics of virus replication could be observed to occur in an MOI-dependent manner – analogous to previous results observed in standard tissue culture plates (Figure 4.8B). This confirmed the real-time assay could be used to monitor IAV replication kinetics in cells grown on Transwells.

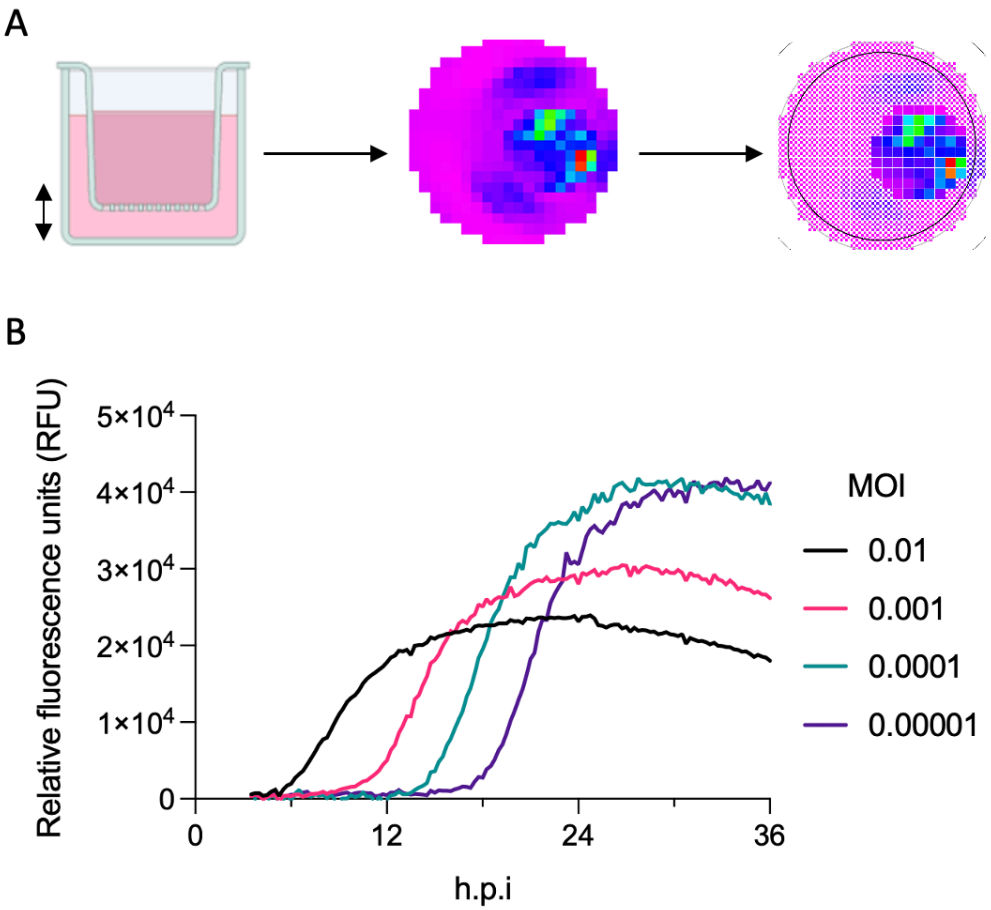

Figure 4.8: Influenza virus replication kinetics in MDCK cells on Transwells. *MDCK cells were seeded onto Transwells, infected with BrightFlu (MOI 0.01- 0.00001), and incubated over 36 hours in a plate reader. A - plate reader settings used to monitor relative fluorescence units (RFU) from the apical chamber of Transwells. B - replication kinetics of BrightFlu over 36 hours post-infection (h.p.i). BrightFlu ZsGreen expression was measured in RFU at 15-minute intervals, with values from mock infected wells subtracted.*

To determine if the real-time assay was suitable for 3D ALI cultures, HAEC-b cells from a 71 year old Caucasian male donor were seeded onto Transwells. Cells reached confluency 3-4 days post-seeding, after which cell culture media was removed from the apical chamber to establish ALI conditions. After 5 weeks in culture, tissues were infected with 1,000 PFU of BrightFlu per tissue for 2 hours, washed, and incubated up to 80 hours. At 24, 48, and 80 h.p.i, tissues were removed from the incubator, then TEER and green RFU were measured at each timepoint. Figure 4.9A shows TEER measurements after tissues were washed with PBS, subtracting TEER values from empty (unseeded) Transwells. TEER decreased from 300 Ohm's per cm^2 at 0 h.p.i to 100 by 80 h.p.i, reflecting a decline in epithelial barrier integrity due to virus replication over time. Figure 4.9B shows the green RFU of infected tissues without washing with PBS. 80,000 RFU were recorded at 24 h.p.i, which decreased to 50,000 at 48 h.p.i, then increased again to 90,000 at 80 h.p.i. The unexpected decrease in viral replication at 48 h.p.i. has not been previously observed, prompting further investigation. Representative images of tissues were captured using widefield microscopy. At 24 h.p.i .individual infected cells can be observed clearly (Figure 4.9C). Images captured at 48 h.p.i. appeared blurry with a dull green signal, making it difficult to identify individual infected cells. By 80 h.p.i the entire tissue appeared cloudy despite an increase in green signal observed visually. The cloudiness was attributed to mucus secretion from differentiated HAEC-b cells. ALI cultures are routinely washed every 1-2 days to remove mucus from the apical chamber. The thick layers of mucus formed from infection and extended timepoints likely obstructed fluorescence detection (Li and Tang, 2021). Thus, the fluorescence from BrightFlu replication using the plate reader cannot be accurately measured in real-time without manually removing mucus from the tissue.

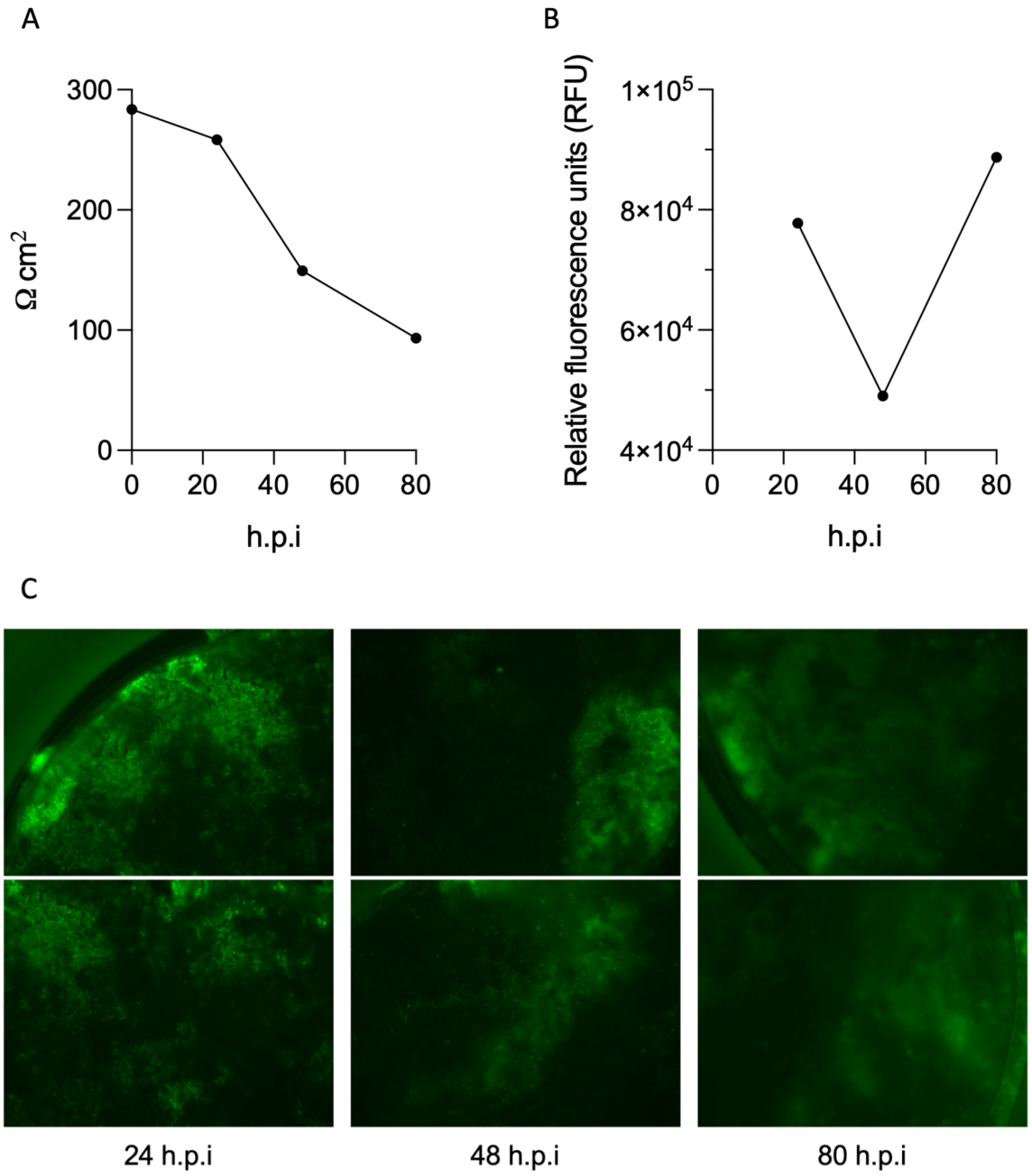

Figure 4.9: Influenza virus replication kinetics cannot be monitored in real-time in ALI cultures. *HAEC-b cells from a 71 year old Caucasian male donor were seeded onto Transwells and differentiated over 5 weeks, then infected with 1,000 PFU of BrightFlu per tissue or mock infected. Transwells were incubated and removed at 0, 24, 48, and 80 h.p.i. A - Transepithelial electrical resistance (TEER) measurements were taken at each timepoint using a voltohmmeter, after washing Transwells with PBS. Mock (empty) Transwell values were subtracted, and results were multiplied by the surface area to give Ω per cm^2. B – relative fluorescence units (RFU) were recorded at each timepoint using a plate reader, without washing with PBS. C – widefield images of Transwells were captured at each timepoint following RFU measurements. N = 2 Transwells per timepoint.*

4.2.5. Favipiravir's impact on influenza virus replication in ALI cultures

The real-time assay offered continuous monitoring of virus replication kinetics over the infection period; however, this method was not applicable to 3D ALI cultures. We therefore examined the utility of confocal microscopy to monitor IAV replication in 3D. HAEC-b cells were differentiated on Transwells and infected with 1,000 PFU of BrightFlu per tissue. Cultures were fixed at 24 h.p.i. and stained for ciliated cells and DAPI. Confocal imaging was used to capture areas of infection, and IMARIS image analysis software was used to render each channel captured (https://imaris.oxinst.com). Images were opened in IMARIS, which automatically reconstructed Z-stacks into 3D projections. The surface tool allowed objects to be rendered by tracing the boundaries of signals captured by confocal imaging. This rendering tool created measurable objects in the software within a 3D space. Figure 4.10 shows an example of an IAV infected 3D ALI culture on a Transwell, with cilia rendered in red, BrightFlu in green, nuclei in blue, and merged composite image.

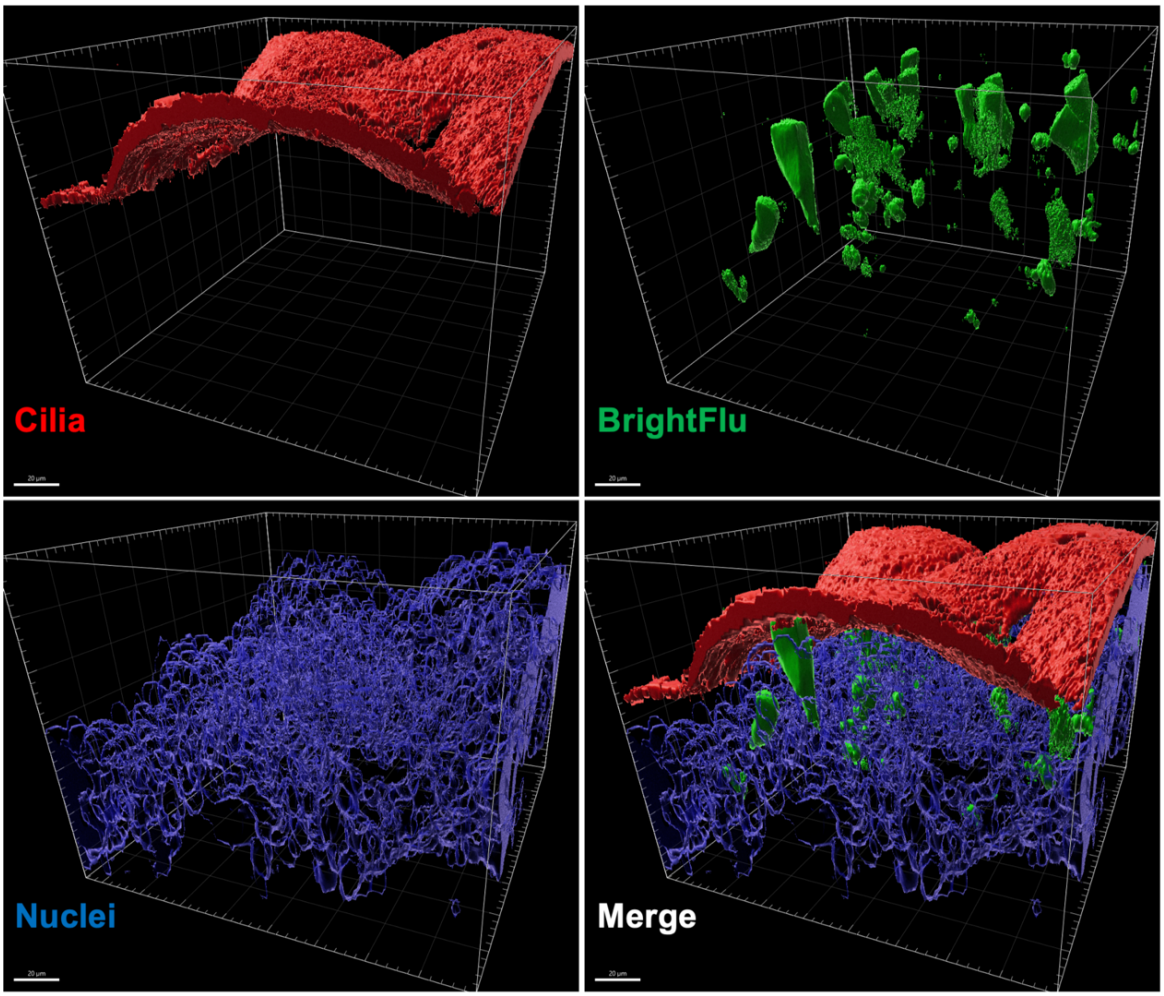

Figure 4.10: 3D rendered ALI cultures infected with BrightFlu. *HAEC-b cells from a 71 year old Caucasian male donor were seeded onto Transwells and differentiated over 5 weeks, then infected with 1,000 PFU of BrightFlu. The tissue was fixed and permeabilised at 24 hours post-infection (h.p.i) and stained for cilia and nuclei. A Zeiss confocal laser scanning microscope 880 with 40X oil objective lens and Airyscan was used to capture Z-stacks throughout the entire tissue. IMARIS image analysis software was used to reconstruct the 3D image and create objects using the surface tool. Red - cilia, green - BrightFlu, blue - nuceli, merge - composite image.*

Confocal imaging and IMARIS image analysis was used to investigate the effects of favipiravir on BrightFlu replication within tissues. HAEC-b cells from two different donors were used: male, 71, Caucasian (donor 1), and female, 56, Hispanic (donor 2). Cells were differentiated on Transwells and infected with 1,000 PFU of BrightFlu per tissue. Tissues were washed and overlayed with cell culture medium containing either 200 μM of favipiravir or DMSO as a control. After 48 h.p.i, cultures were fixed, permeabilised, and stained for ciliated cells and nuclei. Confocal imaging and IMARIS image rendering were carried out as described above. For each condition, three FOVs were selected for imaging – focussing on regions of the Transwells where BrightFlu replication was most pronounced. Representative 3D images from confocal imaging are shown in Figure 4.11. Notably, a loss of cilia was observed in DMSO treated donor 2 tissues (Figure 4.11D). The volume of BrightFlu was quantified by measuring the volume of each rendered object in the green channel. Volumes smaller than 20 μm^3 were excluded from the dataset, as uninfected ALI cultures often result in green channel autofluorescence artifacts of 1-20 μm^3. The depth of BrightFlu infection throughout the tissue was measured by recording the distance from the cilia to the furthest point of each BrightFlu object. These measurements were calculated using the statistics tool in IMARIS and compiled into a tabular format.

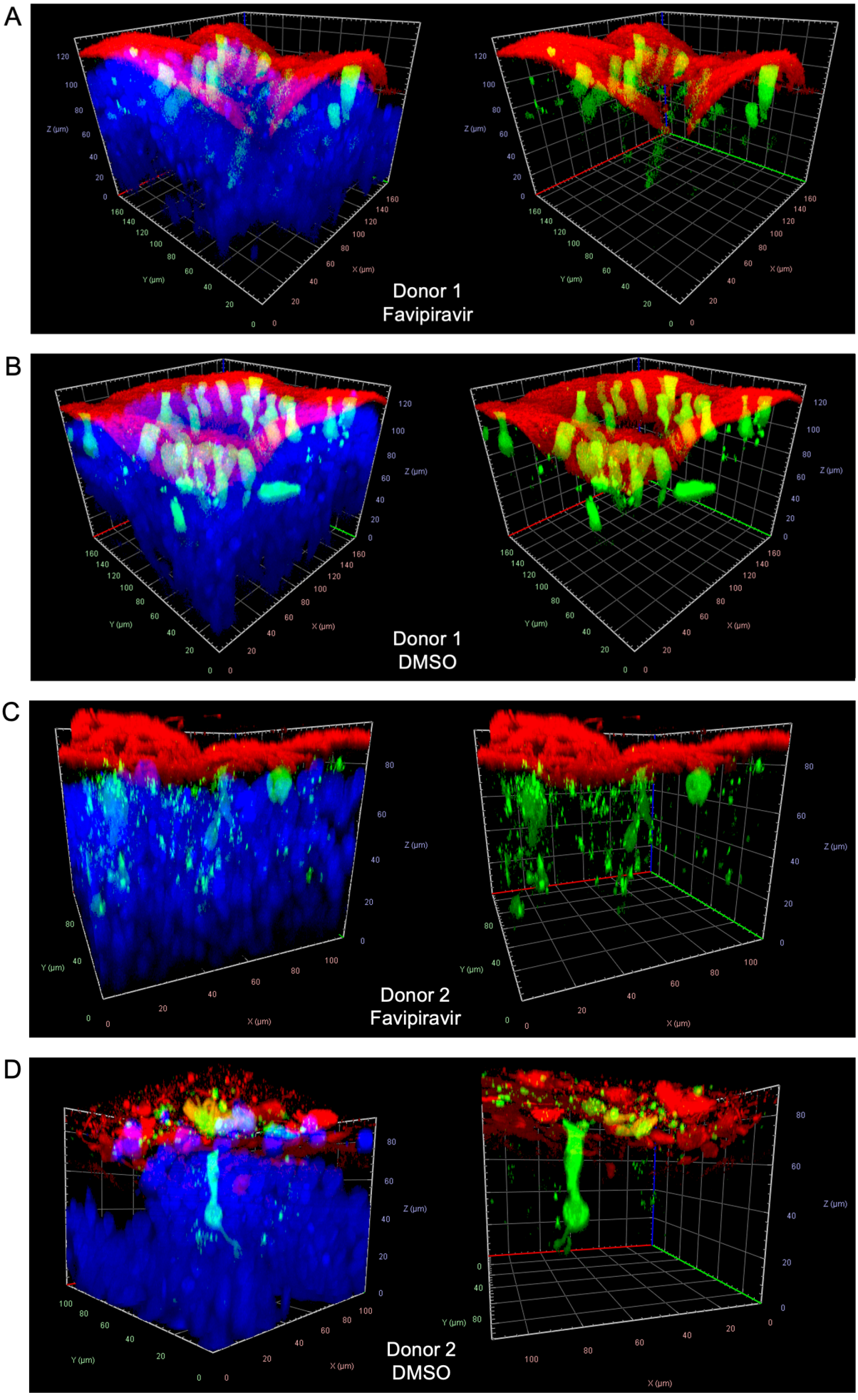
A
Donor 1
Favipiravir
B
Donor 1
DMSO
C
Donor 2
Favipiravir
D
Donor 2
DMSO
X (µm)
Y (µm)
Z (µm)

Figure 4.11: Confocal imaging of BrightFlu replication in ALI cultures treated with favipiravir. *Tissues were infected with BrightFlu and overlayed with 200 µM of favipiravir or DMSO. Tissues were fixed and permeabilised at 48 h.p.i., and stained for cilia (red) and DAPI (blue). Z-stacks were captured using a Zeiss confocal laser scanning microscope 880 with 40X oil objective lens and Airyscan. Representative images of donor 1 (male, 71, Caucasian) tissues treated with favipiravir (A) and DMSO (B); and donor 2 (female, 56, Hispanic) tissues treated with favipiravir (C) and DMSO (D). Z-stacks are shown with and without DAPI. Green – IAV, blue – DAPI, red – cilia. N = 2 biological repeats per treatment condition, with three FOVs captured per repeat.*

The analysis of BrightFlu volume in donor 1 tissue showed that the presence of favipiravir reduced the volume of virus within the tissues (Figure 4.12A). The highest volume observed in DMSO treated tissues reached almost 6,000 μm^3, whereas the highest volume in favipiravir treated tissues was approximately three times smaller at 2,000 μm^3. To take a closer look, a violin plot was created, focussing on the top five largest BrightFlu volumes from both DMSO and favipiravir treated tissues. The distribution of volume sizes showed that most BrightFlu objects had a smaller volume in favipiravir treated tissues compared to the DMSO control. The depth of infection appeared similar in both favipiravir and DMSO treated tissues (Figure 4.12B). In contrast, the analysis of BrightFlu volume in donor 2 tissues showed that the presence of favipiravir reduced the volume of virus by just one third (Figure 4.12C). Interestingly, BrightFlu infection was deeper after favipiravir treatment (Figure 4.12D). While most BrightFlu objects in DMSO treated tissues were located near the cilia, after favipiravir treatment the distribution was more binomial, with a significant proportion located deeper within the tissues. This suggests that favipiravir may alter the spatial distribution of viral replication within the tissue from donor 2.

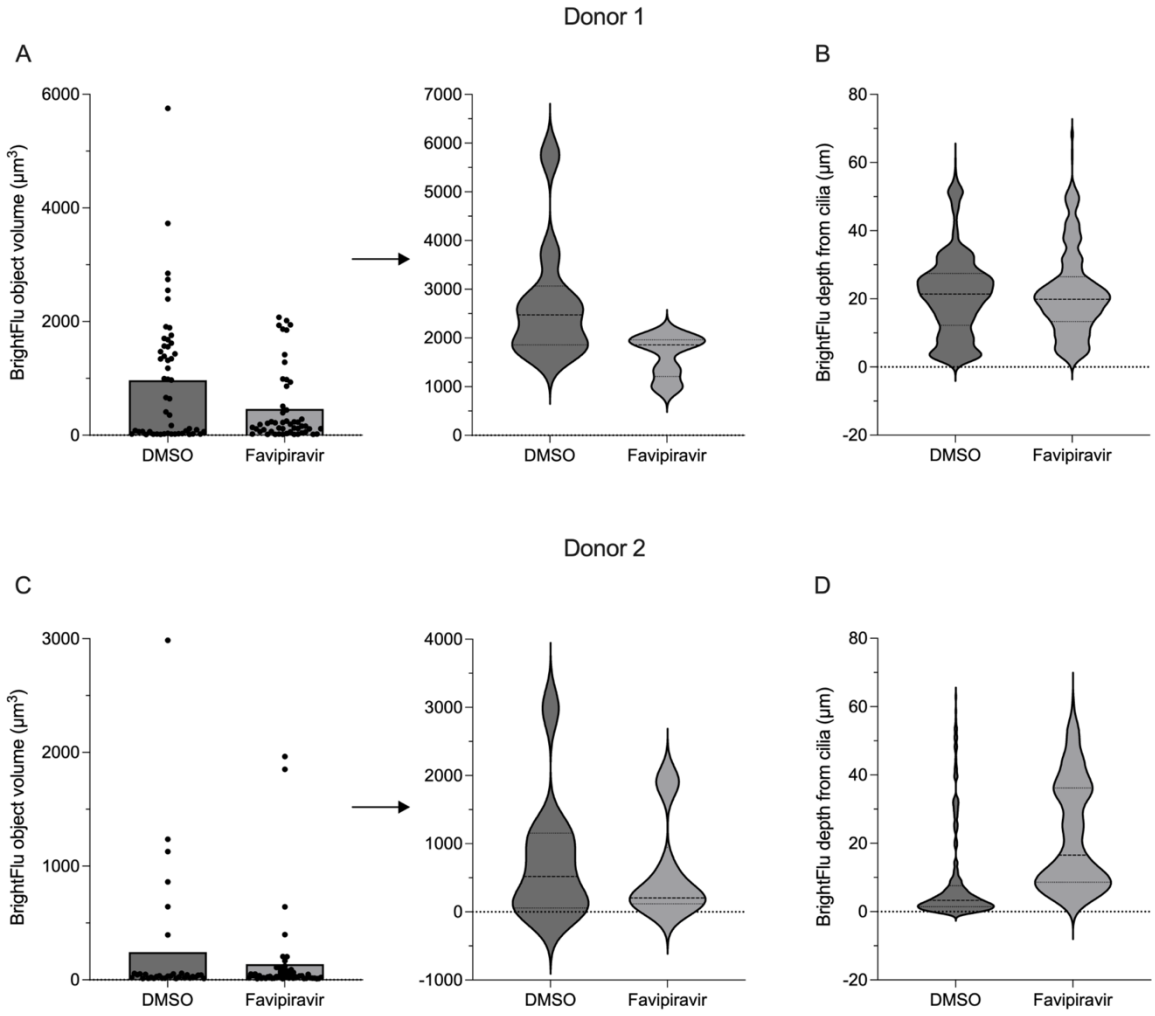

Figure 4.12: Volume and depth of BrightFlu infected ALI cultures treated with favipiravir. *Donor 1 (male, 71, Caucasian) and donor 2 (female, 56, Hispanic) cells were seeded onto Transwells and differentiated over 5 weeks, then infected with 1,000 PFU of BrightFlu. Tissues were overlayed with 200 µM of favipiravir or DMSO (carrier control). Tissues were fixed and permeabilised at 48 hours post-infection (h.p.i) and stained for cilia and nuclei. A Zeiss confocal laser scanning microscope 880 with 40X oil objective lens and Airyscan was used to capture Z-stacks throughout the tissues. IMARIS image analysis software was used to reconstruct the 3D image and create objects using the surface tool. Two measurements were taken from each of the rendered objects: the volume of BrightFlu (A and C), and the depth of BrightFlu (B and D). N = 2 biological repeats per treatment condition, with three FOVs captured per repeat.*

Since the number of objects measured in favipiravir treated tissues was higher than DMSO controls, the total volume of BrightFlu was calculated by finding the sum of all volumes within each sample. In donor 1 tissues, favipiravir treatment resulted in a reduction of total BrightFlu volume by approximately half compared to the DMSO control (Figure 4.13). In contrast, donor 2 tissues showed a minimal decrease in total BrightFlu volume with favipiravir treatment. Interestingly, the total volume of BrightFlu in donor 1 tissues under DMSO control conditions was six times higher than donor 2. This stark difference highlights variability in IAV replication between different donor cells and tissues. It is important to note, that although cells were isolated from healthy male and female donors, these observations do not pertain to sex, and simply refer to variability in donor cells. There are many additional factors, such as age, smoking status, ethnicity, and pathology, involved in donor variability in primary cell culture (Mori *et al.*, 2022).

Overall, favipiravir decreased BrightFlu replication in both donor tissues, although the degree of inhibition varied between them. Additionally, a difference in the spatial distribution of BrightFlu was observed after favipiravir treatment in donor 2 tissues. However, due to the limited number of biological repeats, the experiment lacked sufficient statistical power to determine whether the difference in BrightFlu volume and depth between favipiravir treated and control treated tissues were statistically significant. Despite this limitation, the imaging methodology can be applied to identify differences in IAV replication within 3D cell culture models. This approach can be utilised in future studies with a larger sample size to better assess the impact of drug treatments on viral replication and spatial distribution within tissues.

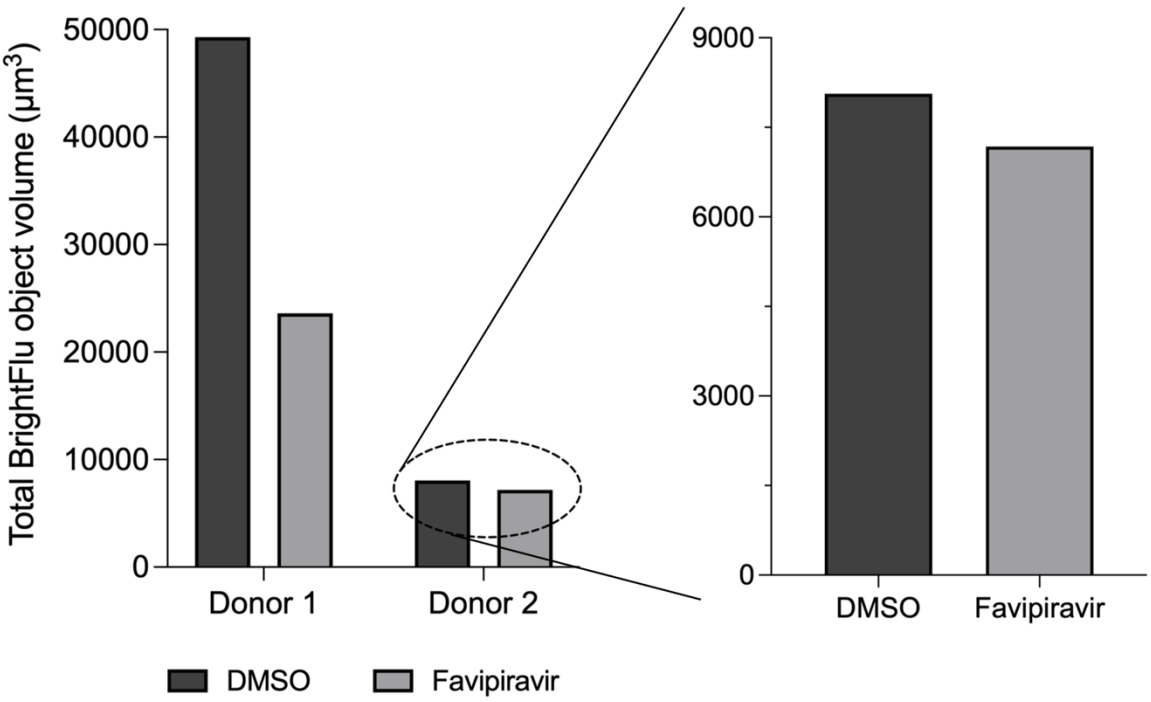

Figure 4.13: Total volume of BrightFlu in ALI cultures treated with favipiravir. *Total volume of BrightFlu was calculated for each treatment condition by summing the volumes of all BrightFlu objects in the rendered images. Left – total volumes for both donors under favipiravir and DMSO control conditions. Right – expanded donor 2 total volumes. N = 2 biological repeats per treatment condition, with three FOVs captured per repeat.*

4.3. Discussion

This chapter describes the development and application of a 2D cell culture assay to monitor influenza virus replication kinetics in real-time. As detailed in Chapter 3, the 3D Membrick ALI model was not suitable for initial antiviral inhibitor screening experiments, which led to the development of a real-time 2D cell culture assay. The use of a fluorescently tagged IAV enabled the continuous monitoring of virus replication kinetics over 36 hours across a range of MOI. The assay's ability to measure RFU as a proxy for virus replication proved successful, as RFU correlated well to pfu/mL measured by a traditional plaque assay. This confirmed that the plate reader assay can be used to monitor IAV replication kinetics in real-time in 2D cell culture models amenable to the growth of a range of cell types.

Favipiravir was selected as a model antiviral drug to determine whether the real-time assay could be applicable for drug discovery. Furuta *et al.* (2002) reported favipiravir exhibited an IC_{50} value of 1.0 ± 0.9 μM against influenza PR8 virus (70 PFU/well) using a plaque reduction assay over six days at 33°C in MDCK cells. However, replicating this precise experimental design is challenging due to variability in virus stock and preparation, cell lineage, and drug preparation. In this study, favipiravir inhibited BrightFlu replication in a dose-dependent manner, with IC_{50} range of 24 – 28 μM after 24 hours by endpoint and real-time assays, respectively. The MOI of 0.001 PFU/mL was selected based on the sigmoidal shape of the dose-response curve and time to saturation (plateau in virus replication). Though, the input MOI impacted the IC_{50} values of favipiravir – ranging from 10 to 104 μM. While IC_{50} values are valuable when comparing drug efficacy within experiments, discrepancies between reported values highlights the difficulties in standardising experimental conditions between research groups. Nonetheless, both the real-time and endpoint assays successfully measured the antiviral activity of favipiravir and allowed for the identification of antivirals within a three-day timeframe.

Both the real-time and endpoint assays were used to assess the antiviral activity of four favipiravir analogues synthesised in collaboration with the Burley group. While favipiravir demonstrated inhibition of IAV replication in a dose-

dependent manner, none of the analogues showed similar antiviral activity. Analogue 1 and 3 increased viral replication at 24 hours using the endpoint assay, and all four analogues increased replication over an extended 36-hour period using the real-time assay. These results indicate that the analogues lack the desired antiviral properties and are not suitable for further development as influenza virus inhibitors. Previous studies have explored various favipiravir analogues with mixed results. T-1105, a non-fluorinated analogue of favipiravir, inhibited IAV replication more effectively than favipiravir itself in MDCK cells (Huchting *et al.*, 2018). T-1105 is converted into its active metabolite, T-1105-RTP, which inhibits influenza virus RdRp. Notably, there were bottlenecks in the activation pathway from T-1105-RMP to T-1105-RDP, but no bottlenecks from T-1105-RDP to T-1105-RTP. These bottlenecks were more pronounced when further studied in A549 and Vero cells, concluding T-1105 was less effective than favipiravir in these two cell lines (Huchting *et al.*, 2019). These observations highlight the importance of prodrug activation and cell type specificity, which may be relevant factors for the analogues tested in this study. Expanding the testing of alternative analogues to established antivirals, such as oseltamivir, should be carried out, as it has been shown enhance antiviral activity (S. Kumar *et al.*, 2020). Future research also should focus on evaluating a more diverse panel of favipiravir analogues to identify more effective inhibitors potentially applicable to a variety of RNA viruses.

The cytotoxicity observed in some analogues raised concerns about the potential adverse effects of inhibitors in cell culture. Previous studies found favipiravir has a 50% cytotoxic concentration (CC_{50}) of over 6,370 μM in MDCK cells using an XTT assay, meaning that favipiravir would need to be present at concentrations greater than this to reduce cell viability by 50% (Furuta *et al.*, 2002b). This is consistent with CC_{50} values exceeding 1,000 uM reported in other studies cells using MTT and CellTiter-Glo assays (Baranovich *et al.*, 2013). The XTT and MTT are colorimetric assays using tetrazolium salts to measure cellular metabolic activity as an indicator of cell viability, proliferation, and cytotoxicity – comparable to the MTS assay. CellTiter-Glo is a luminescent assay measuring intracellular ATP using a luciferase reaction to assess cell viability. The MTS assay used in this study supports these findings, showing MDCK cell metabolism remained relatively stable up to the maximum concentration of 500 μM.

Conversely, cell counts decreased to almost zero by 500 μM, possibly due to washing cells before staining, which may have physically removed cells from the well. Therefore, multiple assays should be utilised to assess the toxicity of compounds in cell culture systems.

Application of the real-time assay measure virus replication kinetics on Transwells was successful; however, translating this assay to 3D ALI cultures proved difficult. The mucus produced from HAEC-b cells obstructed fluorescence readings, leading to inaccurate RFU measurements. Instead, confocal microscopy was used to visualise IAV replication in ALI cultures, following the imaging methods established in Chapter 3. This approach allowed for the visualisation of virus replication throughout the tissue depth. Favipiravir treatment of infected tissues reduced IAV replication in both donors relative to DMSO controls. Notably, the inhibitory effects of favipiravir were more pronounced in donor 1 derived tissues than those derived from donor 2. Additionally, in donor 2 derived tissues, favipiravir treatment resulted in two distinct populations of virus: one nearest the apical side, and one located deeper within the tissue. This suggests that favipiravir may alter the spatial distribution of viral replication within tissues in a donor-dependent manner. Notably, donor 1 showed a six-fold increase in total volume of infection compared to donor 2, highlighting the expected variability in donor cell sources (Ilyushina, Dickensheets and Donnelly, 2019; Bovard *et al.*, 2020). Although limited by sample size, these findings demonstrate the utility of 3D imaging methods in assessing the impact of antivirals on virus distribution and replication within 3D cell culture models. Taken together, these data demonstrate the plate reader and Celigo assays can be used to monitor virus replication in real-time and at a designated endpoint and confirmed inhibitory effects of favipiravir can be measured using both assays in 2D cell cultures, and by confocal imaging for 3D cell cultures.

5. Establishing influenza virus inhibitor screening in biologically relevant cells

5.1. Introduction

The study of antiviral inhibitors often involves the use of continuous cell lines, yet the efficacy of these antiviral inhibitors can differ significantly when tested across various primary and non-primary cell types from different species. Dittmar *et al.* (2021) highlights that while many direct-acting antivirals effectively reduce SARS-CoV-2 replication across multiple cell types, the efficacy of host-directed antivirals is often cell type specific. Their findings reveal that top drug candidates identified in Huh7.5 cells do not always translate effectively to Vero and Calu-3 cells, showing variations in antiviral efficacy and cellular toxicity. Additionally, mouse models are less permissive to certain human IAV strains due to differences in SA receptor binding preferences (Ibricevic *et al.*, 2006). Even within airway cells, the efficacy of IAV antivirals can vary; for instance, combined IFN λ1 and heptakis-(6-deoxy-6-thioundec)-beta-cyclodextrin grafted with 6'SLN(Neu5Ac-a-(2-6)-Gal-b-(1-4)-GlcNAc;6'-N-Acetylneuraminyl-N-acetyllactosamine (6'SLN-CD) treatment is more effective in secretory cells than in ciliated cells (Medaglia *et al.*, 2022). Therefore, to account for these species-specific and cell-type-specific differences in antiviral efficacy, it is essential to screen inhibitors across multiple cell types.

Primary cells offer significant advantages in drug screening over immortalised or cancer-derived cell lines. For example, A549 cells, which are frequently used in IAV studies, exhibit a limited immune response compared to primary cells. Recent transcriptomic analyses have shown ISGs (IFNα2 and IFNα8) and RIG-I like receptor signalling genes (IFITM1 and IFITM2) are significantly downregulated in A549 cells compared to primary type II alveolar epithelial cells during IAV infection (Bertrams *et al.*, 2022). Similarly, proteomic studies have found that ISGs (STAT1, RIG-I, SAMD9, SAMHD1, IFIT1, IFIT2, IFIT3) are upregulated in primary bronchial epithelial cells compared to A549 cells during IAV infection (Kroeker *et al.*, 2012). These findings suggest that both cell type (bronchial vs. alveolar) and cell properties (primary vs. transformed) influence

the immune response to IAV infection and, consequently, the permissivity to infection and efficacy of antiviral inhibitors.

HAEC-b cells can be differentiated to form 3D tissues in ALI cultures, which are among the closest *in vitro* models to mimic the human lung environment (as described in Chapter 3). The immune response observed in ALI cultures upon SARS-CoV-2 infection closely aligns with responses seen in infected patient samples and animal models (Assou *et al.*, 2023). While high-throughput antiviral screening is impractical in 3D cultures, HAEC-b cells represent the most biologically relevant cell type currently available for 2D inhibitor screening (Orr and Hynds, 2021). Moreover, the use of patient-derived cells allows for the study of drug efficacy on an individual basis, thereby supporting the development of personalised medicine therapies (Dugger, Platt and Goldstein, 2018; Goetz and Schork, 2018; Lattanzi *et al.*, 2021).

The previous chapter described the development of 2D cell culture assays to monitor IAV replication and their application for inhibitor screening in MDCK cells. The aim of this chapter is to adapt these assays for use in more biologically relevant cell types, which will be employed in Chapter 6 to screen for novel inhibitors of IAV replication.

5.2. Results

5.2.1. TPCK trypsin required for BrightFlu replication prevents inhibitor screening in biologically relevant cells

To ensure that the observed effect of any inhibitor is not cell type specific, it is crucial to evaluate their impact across multiple cell types. This study aimed to develop a screening assay using bronchial epithelial cells pertinent to IAV infection. HBEC3-KT cells, Cdk4/hTERT-immortalised primary human bronchial epithelial cells, were chosen for initial testing and inhibitor screening prior to studies using primary human bronchial cells (Ramirez *et al.*, 2004). For multicycle replication, the IAV HA precursor (HA0) must be cleaved by host proteases into its active subunits, HA1 and HA2 (Lazarowitz, Compans and Choppin, 1973). Cell types lacking endogenous proteases must be supplemented with TPCK to facilitate HA0 cleavage to promote IAV multicycle infection in cell culture experiments. However, challenges arose when all BrightFlu infected wells supplemented with TPCK exhibited detachment of HBEC3-KT cells (data not shown). TPCK trypsin is a serine endoprotease that cleaves peptide bonds on the carboxyl side of arginine and lysine residues, which unfortunately leads to the detachment of cells, complicating experiments involving more sensitive cell types.

To determine whether TPCK trypsin is essential for BrightFlu replication, MDCK cells were mock treated or infected with BrightFlu (MOI 0.01-0.00001), and overlayed with cell culture medium either without TPCK or with 1 µg/mL TPCK as a positive control. Cells were incubated in a plate reader to monitor green RFU expressed over 44 hours. The results demonstrate that BrightFlu replication kinetics without TPCK trypsin were comparable to mock infected wells, and were considerably lower than conditions with TPCK (Figure 5.1A-D). These findings confirm that TPCK trypsin is essential for the multicycle replication of BrightFlu in MDCK cells.

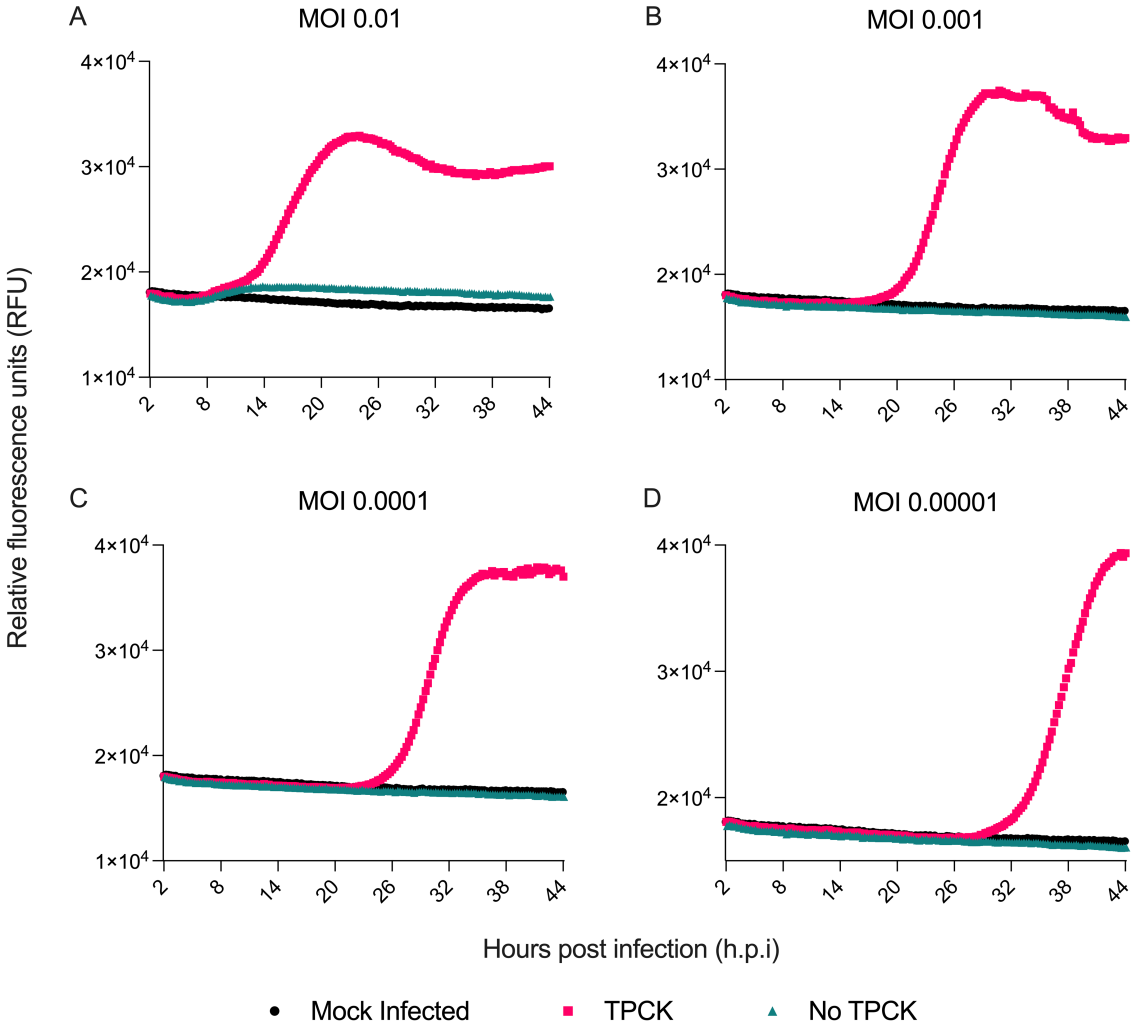

Figure 5.1: TPCK is required for BrightFlu replication. *MDCK cells were mock treated or infected with BrightFlu at range of MOIs (0.01-0.00001). Overlay medium was supplemented with 1 µg/mL TPCK trypsin or left untreated. Replication kinetics of BrightFlu replication were monitored over 44 h.p.i.. BrightFlu ZsGreen expression was measured in RFU at 15-minute intervals.*

To determine if TPCK trypsin could be titrated down to avoid cell detachment, HBEC3-KT cells were overlayed with medium containing a range of TPCK concentrations. After 24 hours, cell nuclei were stained with NucBlue, and images were captured using the Celigo Imaging Cytometer. The number of cells were counted, and fold changes were calculated relative to untreated controls. TPCK concentrations between 0.00001 and 0.01 µg/mL did not affect cell count (Figure 5.2). However, concentrations between 1 and 10 µg/mL led to a substantial decrease in cell number, indicating cell detachment at these higher concentrations. The maximum concentration of TPCK trypsin that HBEC3-KT cells could tolerate without significant detachment was 0.1 µg/mL.

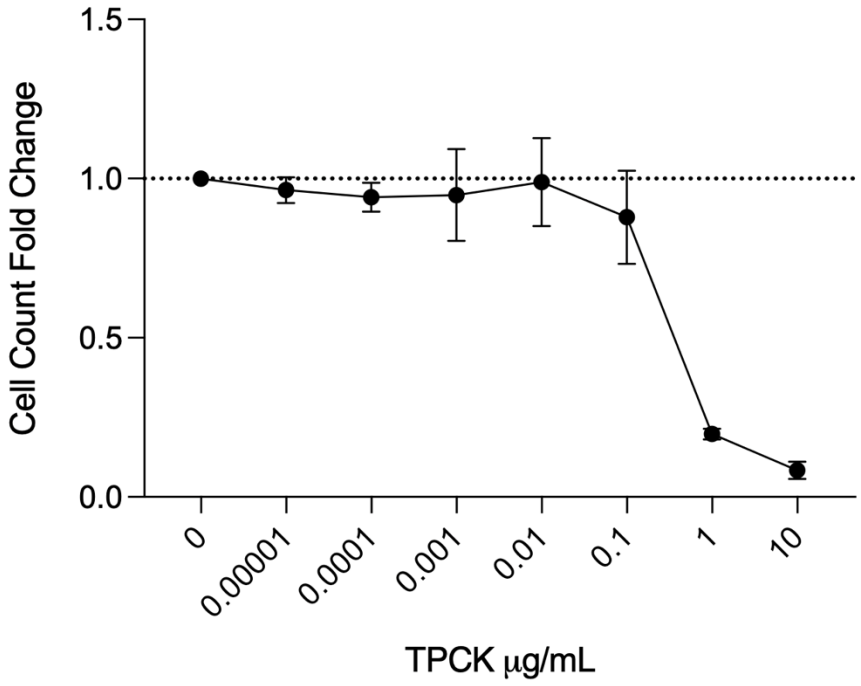

Figure 5.2: Effect of TPCK trypsin on HBEC3-KT cell counts. *HBEC3-KT cells were treated with TPCK trypsin at concentrations ranging from 0-10 µg/mL for 24 hours. After treatment, cells were stained with NucBlue to visualise the nuclei, and cell counts were quantified. The cell count fold change was calculated relative to untreated control cells. N = 3 technical replicates. Error bars = mean ± 1 SD.*

To assess whether the concentration of TPCK trypsin that HBEC3-KT cells can tolerate (0.1 µg/mL) is sufficient to support BrightFlu replication, MDCK cells were infected with BrightFlu (MOI 0.0001 or 0.00001) and overlayed with a dilution range of TPCK (0-1 µg/mL). Cells were imaged using the Celigo Imaging Cytometer at 488 nm at 24 h.p.i. The number of virus positive cells were counted and fold change was calculated relative to no TPCK treatment. Wells treated with 0.1 µg/mL TPCK showed viral replication levels similar to those without TPCK, indicating that this concentration was insufficient for BrightFlu replication (Figure 5.3). Thus, BrightFlu replication kinetics cannot be monitored in HBEC3-KT cells supplemented with TPCK.

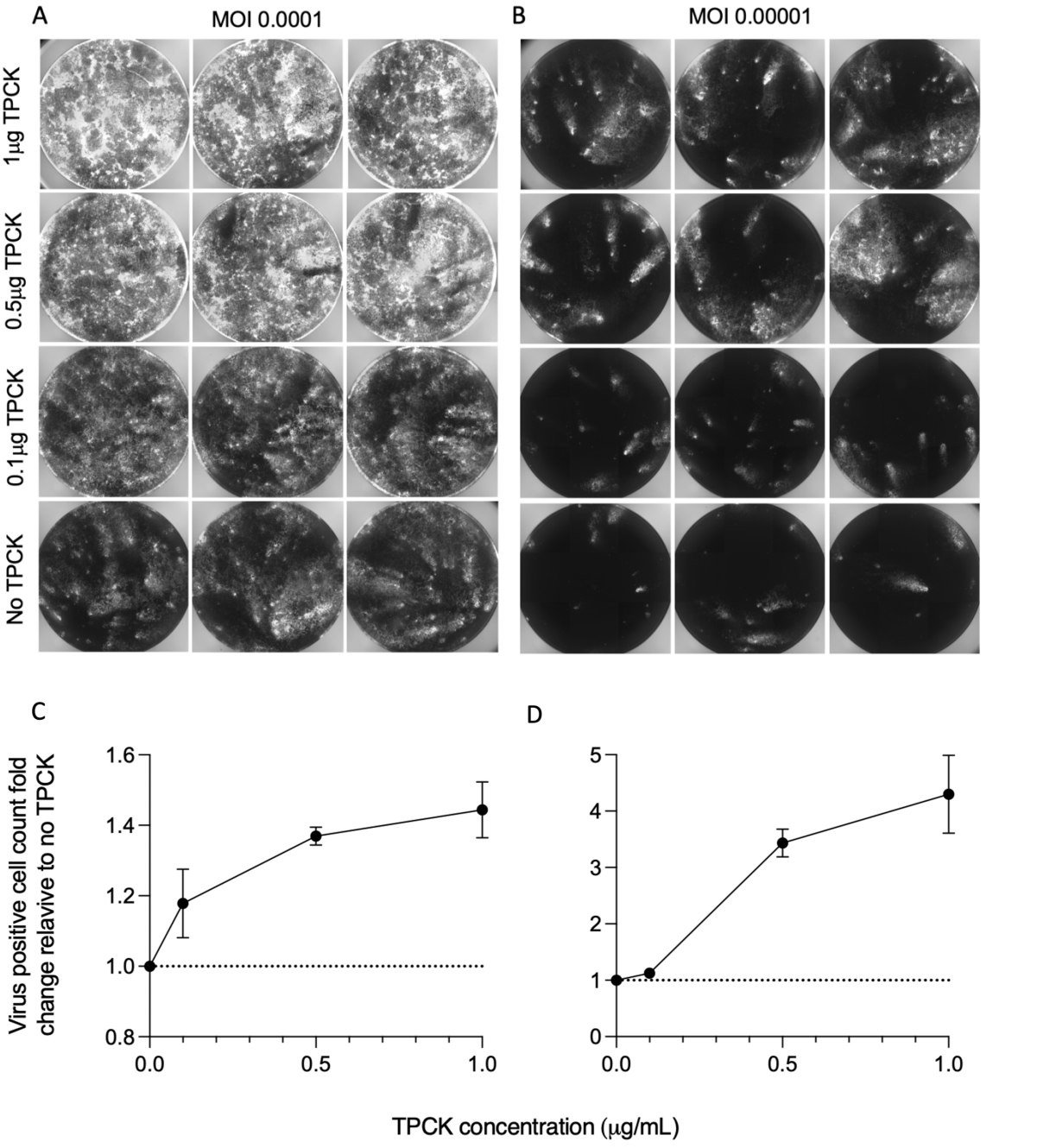

Figure 5.3: 0.1 µg/mL TPCK does not support optimal BrightFlu replication. *MDCK cells were infected with BrightFlu at an MOI of 0.0001 and 0.00001. TPCK concentrations of 0- 1 µg/mL were added to the overlay medium. After 24 hours incubation, images were captured at 488nm for MOI 0.0001 (A) and 0.00001 (B). The number of virus positive cells were counted, and fold change was calculated relative to no TPCK trypsin treatment for MOI 0.0001 (C) and 0.00001 (D). N = 3 biological replicates, error bars = mean ± 1 SD.*

5.2.2. Adaptation of BrightFlu by serial passage

Given the difficulty to monitor BrightFlu replication kinetics in bronchial epithelial cells using the established real-time assay in the presence of TPCK, alternative approaches were explored to enable multicycle infection in these cell types. Previous studies have shown that serial passaging of IAV in MDCK cells can lead to the selection of viral variants with H0 proteins that are susceptible to proteolytic activation in the absence of TPCK (Rott *et al.*, 1984). To test if a similar adaptation could be achieved, BrightFlu was serially passaged through MDCK cells with the goal of adapting the virus to replicate without exogenous trypsin. MDCK cells were infected with BrightFlu (MOI of 0.0001) and overlayed with cell culture medium either containing or lacking TPCK trypsin. After 24 hours, the supernatant was harvested and used to infect fresh MDCK cells. This procedure was repeated for a total of five times. Following this, MDCK cells were infected with each of the supernatants and incubated in TPCK-free medium for 24 hours. Representative widefield images were captured at 488 nm using an EVOS M5000. The results revealed a gradual decrease in fluorescence intensity from P1 to P5 in the virus passaged with TPCK (Figure 5.4). In contrast, the virus passaged without TPCK exhibited an increase in fluorescence intensity by P5, suggesting that BrightFlu had undergone adaptation, enabling replication independently of trypsin.

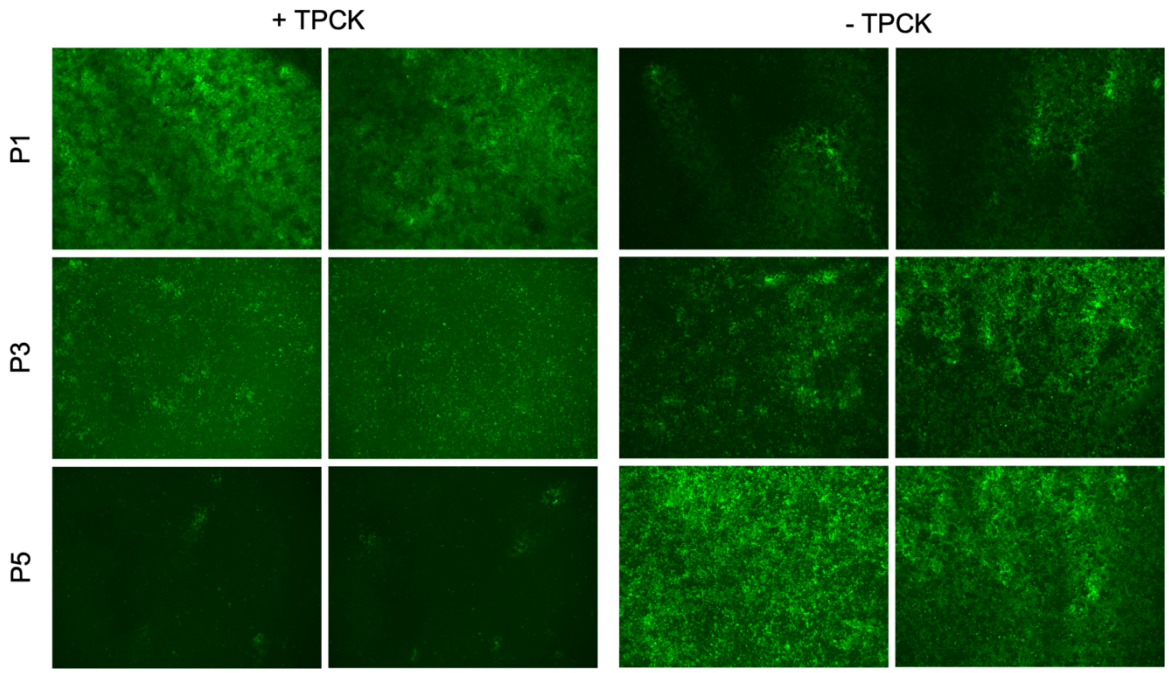

Figure 5.4: Serial passaging of BrightFlu in MDCK cells. *Widefield fluorescent images of BrightFlu replication were captured at passage 1, 3, and 5 (P1, 3, 5) in MDCK cells. Left – virus passaged with TPCK. Right – virus passaged without TPCK.*

Multicycle replication is required to monitor virus replication kinetics using the real-time assay. A plaque assay was conducted to verify that the increase in green fluorescence observed with serial passaging without trypsin correlated to infectious virus capable of multicycle replication. MDCK cells were infected with BrightFlu stocks from P1 and P5 stocks for 1 hour, and overlayed with medium either containing or lacking TPCK trypsin. After 48 hours, images were captured using the Celigo Imaging Cytometer at 488 nm. In the presence of TPCK, visible plaques were detected at dilutions of 10^{-4} and 10^{-5} for P1, with higher dilutions (10^{-2} and 10^{-3}) leading to the destruction of the cell monolayer (Figure 5.5). In the absence of TPCK, countable plaques were observed at a dilution of 10^{-4}, but these were smaller and fewer compared to those with TPCK. By P5, plaques in the presence of TPCK were larger in both number and size, observed at dilutions of 10^{-4}, 10^{-5}, and 10^{-6}. Conversely, in the absence of TPCK, plaques at P5 were observed only at dilutions of 10^{-3} and 10^{-4}, with no increase in size. These findings indicate that while some plaque formation occurred without TPCK trypsin, optimal multicycle replication of BrightFlu was still dependent on the addition of TPCK. Thus, serial passaging of BrightFlu in MDCK cells did not result in the amplification of a virus capable of replicating efficiently without TPCK trypsin.

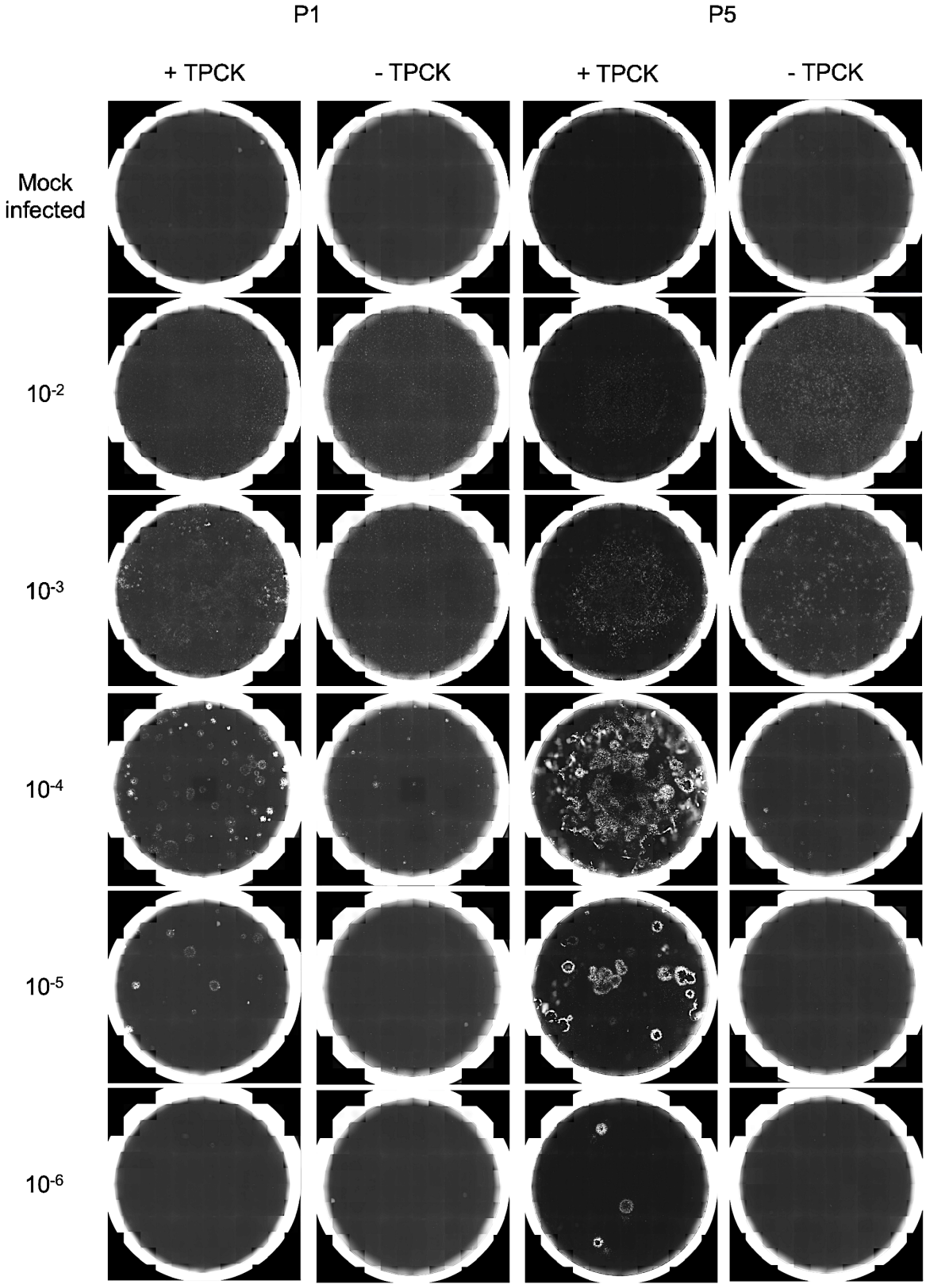

Figure 5.5: TPCK is essential for serially passaged BrightFlu multicycle infection. *Plaque assay of serially passaged BrightFlu in MDCK cells showing 10^{-2} to 10^{-6} virus dilutions. Left – plaques from BrightFlu at passage 1 with and without TPCK. Right – plaques from BrightFlu at passage 5 with and without TPCK.*

5.2.3. TrypLE does not support BrightFlu replication in MDCK cells

Given that 0.1 µg/mL of TPCK is insufficient for supporting BrightFlu replication and that serial passaging did not yield a virus capable of efficiently replicating without TPCK, an alternative protease was assessed for its ability to facilitate BrightFlu replication. TrypLE is a recombinant trypsin-like substitute used in primary cell cultures to enhance cell viability during passaging (Aghayan, Goodarzi and Arjmand, 2015; Z. Liu *et al.*, 2024). HBEC3-KT cells were treated with TrypLE dilutions ranging from a 1 in 10 (1:10) dilution to 1:200, with no TrypLE treatment as a positive control. After 48 hours, representative images were captured using a phase contrast microscope. Cells maintained confluency at dilutions of 1:50 to 1:200, whereas higher dilutions of 1:10 and 1:20 resulted in significant cell detachment (Figure 5.6A). The data indicate that HBEC3-KT cells can tolerated up to a 1:50 dilution of TrypLE before dissociation occurs at higher concentrations.

To determine whether a 1:50 dilution of TrypLE supports BrightFlu replication, HBEC3-KT cells were infected with BrightFlu (MOI 0.01- 0.00001) and overlayed with TrypLE at dilutions of 1:25-1:200. After 24 hours, cells were washed, stained with DAPI, and imaged using the Celigo Imaging Cytometer at 405 and 488 nm. The number of total cells and virus positive cells were counted, and fold changes were calculated relative to no TrypLE treatment controls. At an MOI of 0.001, BrightFlu replication increased with a 1:100 dilution of TrypLE, reaching a peak with a 1:50 dilution, although cell counts at this dilution were reduced by approximately 50% (Figure 5.6B). Similarly, at an MOI of 0.0001, BrightFlu replication increased with a 1:100 dilution, showing a substantial peak at a 1:50 dilution (Figure 5.6C). However, cell counts at this dilution decreased by approximately 30%, with variability between replicates, including a 50% reduction in one well. These results suggest that while TrypLE at a 1:50 dilution can support BrightFlu replication, it simultaneously promotes cell detachment at this dilution within infected cell monolayers, and is therefore is unsuitable for infection assays in HBEC3-KT cells.

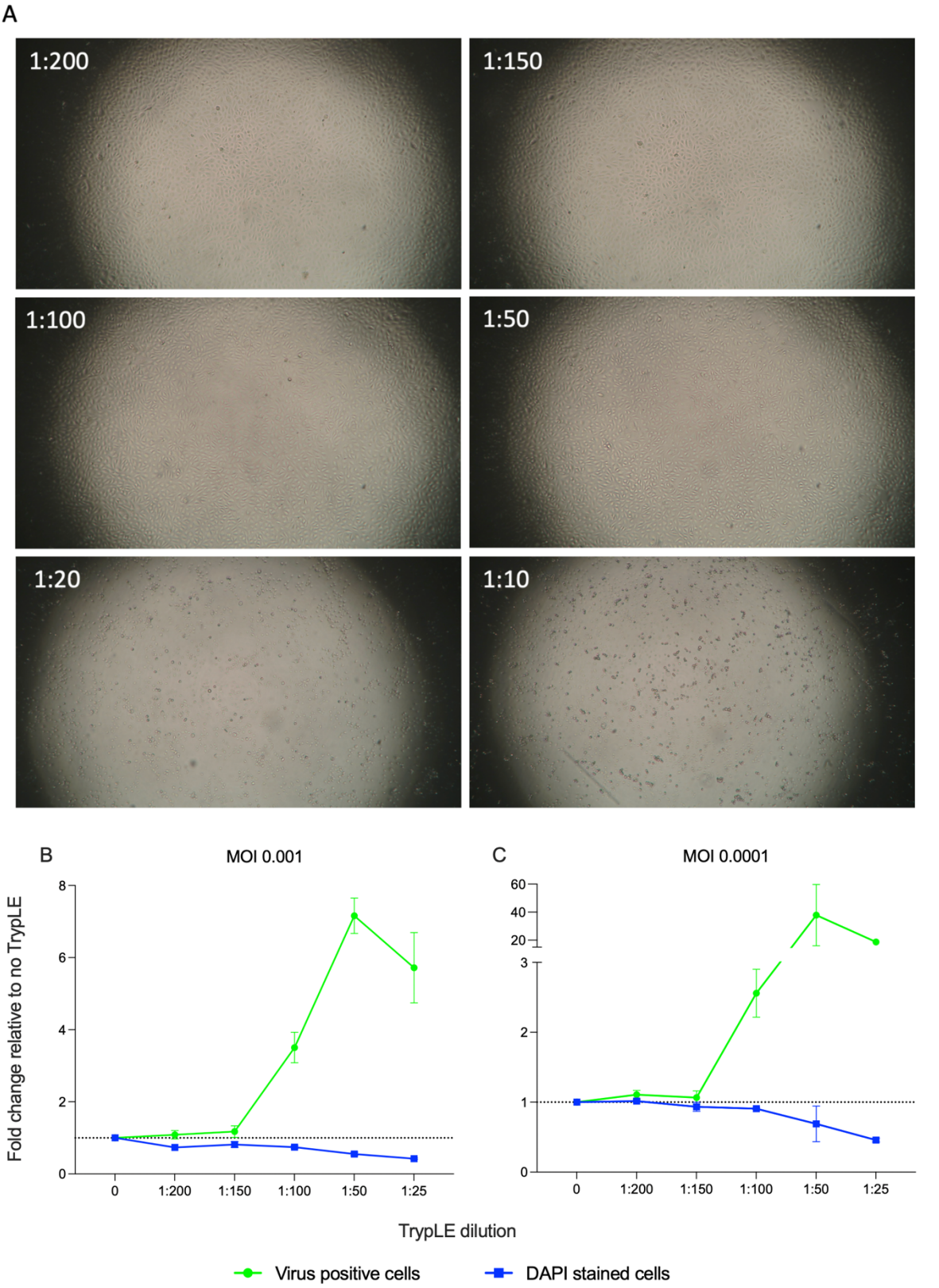

Figure 5.6: TrypLE allows BrightFlu replication but causes cell detachment. *HBEC3-KT cells were treated with TrypLE dilutions ranging from a 1:10 dilution of the stock trypsin to a 1:200 dilution. A - representative phase contrast images after 48 hours of TrypLE treatment. HBEC3-KT cells were infected with BrightFlu (MOI 0.001-0.0001) and overlayed with cell culture medium containing TrypLE dilutions. After 24 hours cells were washed and stained with DAPI. Images were captured, and total cell count and*

virus positive cells were counted. Fold change was calculated relative to no TrypLE treatment. N = 6 technical replicates for panel A. N = 2 technical replicates for panel B and C. Error bars = mean ± 1 SD. Green – virus positive cells, blue – cell count.

5.2.4. ALI culture secretions do not support BrightFlu replication in MDCK cells

Respiratory tract mucus is a crucial barrier against infection and can impede the passage of IAVs (Zanin *et al.*, 2016). Prior studies have shown that primary bronchial epithelial cells, and patient airway tissues and sputum samples contained proteases, including human airway trypsin-like protease (HAT) (Yasuoka *et al.*, 1997; Takahashi *et al.*, 2001; Miki *et al.*, 2003). HAT is capable of cleaving the HA0 precursor protein of IAVs, thereby enabling multicycle infection (Böttcher *et al.*, 2006; Böttcher-Friebertshäuser *et al.*, 2010). Additionally, HAT protease activity is required to induce MUC5AC expression, which was previously observed in ALI cultures in Chapter 3 (Chokki *et al.*, 2004). ALI cultures were washed with PBS every two days to remove airway secretions produced on the apical chamber. These washes were collected and frozen to later determine if the proteases found within secretions could support BrightFlu replication. MDCK cells were mock treated or infected with BrightFlu (MOI 0.01-0.00001). Dilutions of airway secretions (1:10 to 1:1000) were added into the overlay, alongside TPCK treatment as a positive control and no TPCK as a negative control. One plate was incubated for 24 hours, fixed, and imaged using the Celigo Imaging Cytometer at 488 nm. Another plate was incubated in a plate reader to monitor green RFU expression over 44 hours.

Figure 5.7A illustrates that at 24 h.p.i., BrightFlu replication with TPCK resulted in the formation of comets at lower MOIs (0.0001 and 0.00001), reaching saturation at higher MOIs (0.01 and 0.001). In contrast, in the absence of TPCK and in the presence of airway secretions, only individual infected cells were observed at MOI 0.01, with no comet formation, indicating the absence of cell-cell spread of BrightFlu. Figure 5.7B shows that the replication kinetics of BrightFlu in the presence of airway secretions were comparable to those observed in no-TPCK and mock infected conditions, significantly lower than replication levels observed with TPCK. These results suggest that secretions isolated from ALI cultures do not support BrightFlu multicycle replication in 2D cell culture assays.

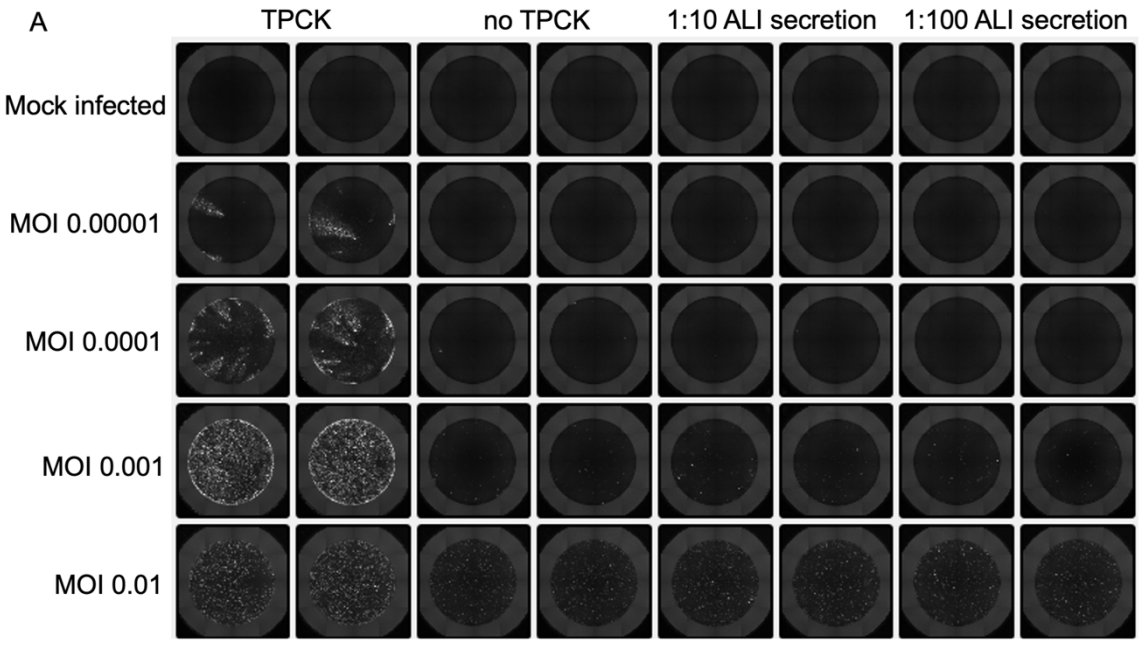
A
TPCK
no TPCK
1:10 ALI secretion
1:100 ALI secretion
Mock infected
MOI 0.00001
MOI 0.0001
MOI 0.001
MOI 0.01

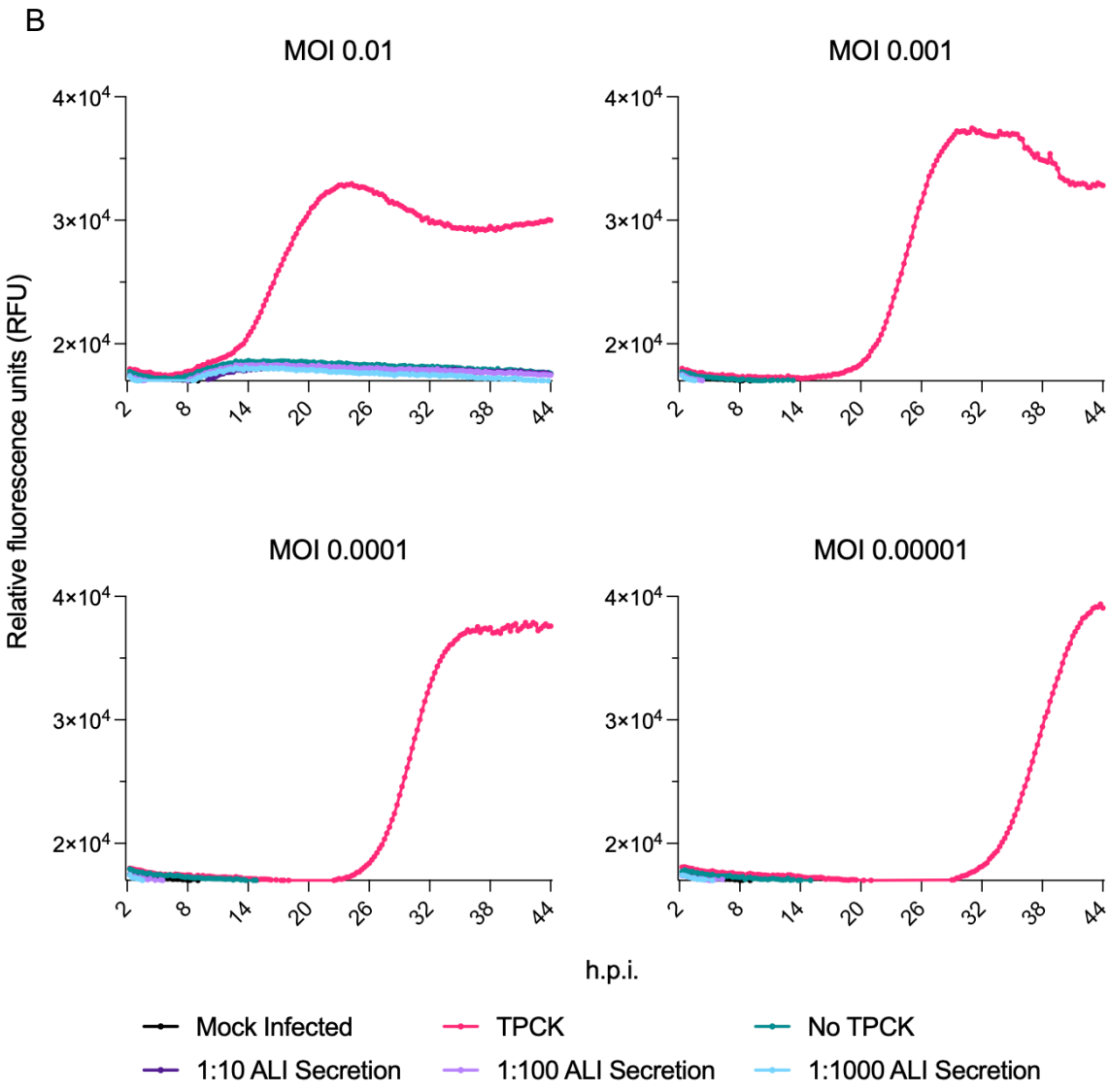
B
MOI 0.01
MOI 0.001
MOI 0.0001
MOI 0.00001
Relative fluorescence units (RFU)
4×10^4
3×10^4
2×10^4
2
8
14
20
26
32
38
44
h.p.i.
Mock Infected
TPCK
No TPCK
1:10 ALI Secretion
1:100 ALI Secretion
1:1000 ALI Secretion

Figure 5.7: ALI culture secretions do not support BrightFlu replication. *MDCK cells were mock treated or infected with BrightFlu, then overlayed with TPCK, no-TPCK, or ALI secretions (1:10-1:1000 dilution). A – cells were fixed at 24 h.p.i and representative images were captured using widefield microscopy. B – Green relative fluorescent units (RFU) were recorded every 15 minutes from 0 to 44 hours post-infection (h.p.i.), with mock infected values subtracted.*

5.2.5. Plasminogen supports BrightFlu replication in MDCK cells

The influenza A/WSN/1933 (WSN) strain can replicate in cell cultures without trypsin by utilising a unique mechanism to replicate outside of its normal host cells (Francis and Moore, 1940; Taubenberger, 1998). WSN NA directly binds to and sequesters plasminogen on the cell surface (Goto and Kawaoka, 1998). Plasminogen is subsequently converted to the active enzyme plasmin, by activators within the host cell, which cleaves WSN HA0 into active HA1 and HA2, thus enabling multicycle replication (Lazarowitz, Goldberg and Choppin, 1973). Plasminogen has also been shown to support replication of several IAV strains, including PR8, albeit less effectively than WSN (LeBouder *et al.*, 2008).

To evaluate if plasminogen could support BrightFlu replication, MDCK cells were mock treated and infected with BrightFlu at an MOI of 0.0001. Cells were overlayed with plasminogen (0-5 µg/mL) and TPCK trypsin (0-5 µg/mL) as a positive control. After 24 hours, cells were fixed, and images were captured using the Celigo Imaging Cytometer at 488nm. In contrast to the dose-dependent replication observed with TPCK, these results indicated that plasminogen at the tested concentrations did not significantly enhance BrightFlu replication (Figure 5.8A).

To further explore the effects of higher plasminogen concentrations, MDCK cells were infected with BrightFlu at an MOI of 0.0001 and treated with plasminogen up to 300 µg/mL. TPCK was included as a positive control and no proteases as a negative control. Cells were incubated in a plate reader to monitor green RFU expressed over 42 hours. A dose-dependent increase in BrightFlu replication was observed up to 250 µg/mL of plasminogen, where replication was twofold higher than the no-protease control and nearly comparable to 1 µg/mL TPCK (Figure 5.8B). Additionally, plasminogen induced a delay in the onset of replication compared to TPCK. These findings suggest that very high concentrations (250 µg/mL) of plasminogen can support BrightFlu replication. Notably, this concentration is ten-fold higher than that previously reported for IAV replication in MDCK and MDBK cells, ranging from 2-20 µg/mL, raising concerns about potential off-target effects of high plasminogen

concentrations for future inhibitor studies (Lazarowitz, Goldberg and Choppin, 1973; Goto and Kawaoka, 1998; Goto *et al.*, 2001; LeBouder *et al.*, 2010).

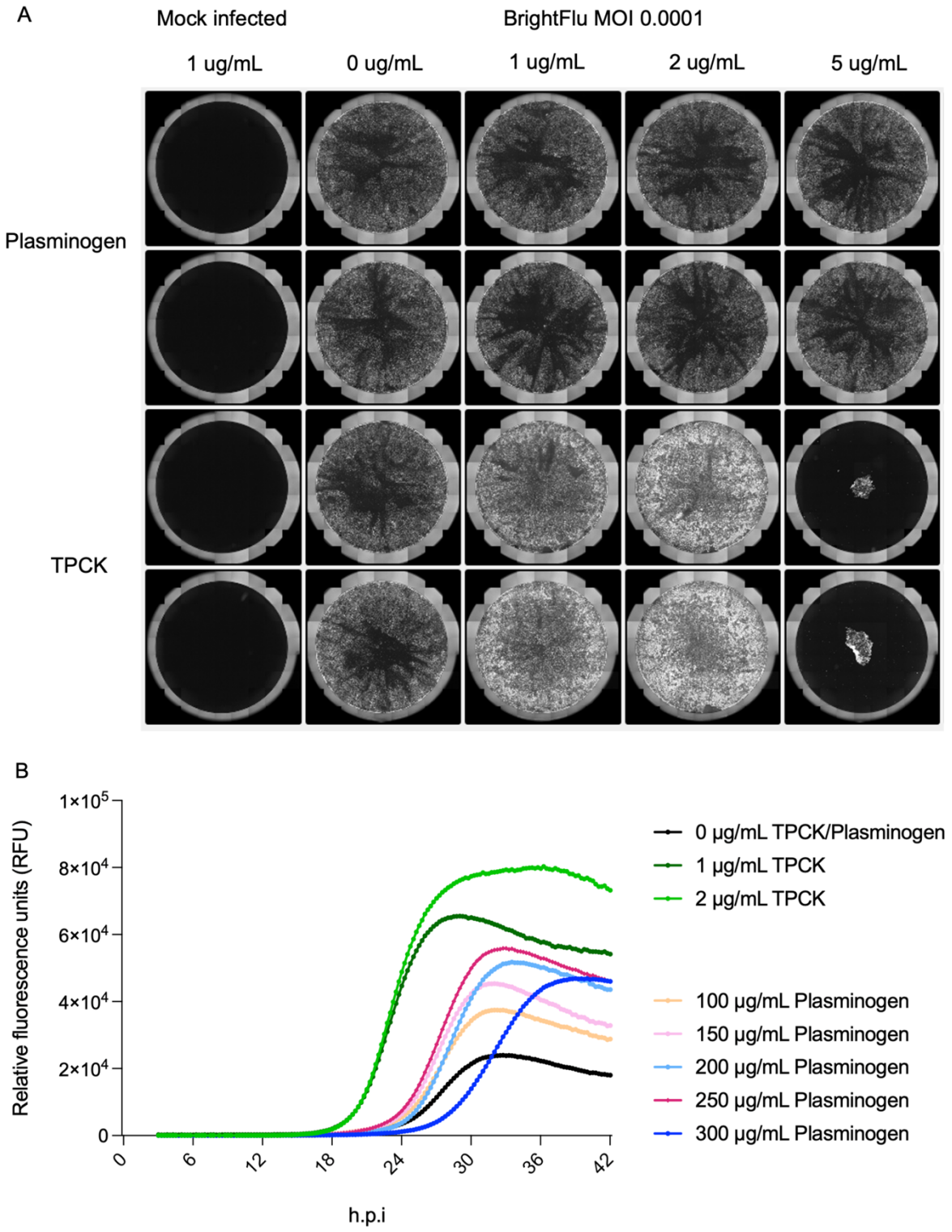

Figure 5.8: Plasminogen supports BrightFlu replication in MDCK cells. *MDCK cells were infected with BrightFlu (MOI 0.0001) and overlayed plasminogen, TPCK trypsin, or no protease. A - widefield images of BrightFlu infected MDCK cells with 0-5 µg/mL of plasminogen or TPCK. B - real-time assay monitoring virus replication kinetics in the presence of TPCK (0-2 µg/mL) or plasminogen (0-300 µg/mL). Green relative fluorescent units (RFU) were recorded every 15 minutes from 0 to 36 hours post-infection (h.p.i.), with mock infection values subtracted.*

5.2.6. Generation of a trypsin-independent chimeric influenza virus

Given that the addition of exogenous proteases was a requirement for BrightFlu replication, an alternative strategy using WSN was pursued. Unlike BrightFlu, a fluorescently tagged WSN virus was not available for experimentation, necessitating its generation. To generate a fluorescently tagged IAV that could replicate independently of trypsin, a reverse genetics system was employed to create a chimeric virus that incorporates the PR8 ZsGreen-tagged NS1 segment from BrightFlu, into WSN or MaCal/09 as a negative control (Lazarowitz, Goldberg and Choppin, 1973; Klenk *et al.*, 1975). HEK 293T cells were cotransfected with 250 ng of eight plasmids, generating four virus constructs: MaCal/09, BrightFlu-MaCal/09, WSN, BrightFlu-WSN (Table 5.1). Supernatants were harvested and MDCK cells were infected with both the BrightFlu-MaCal/09 and BrightFlu-WSN supernatants, then cultured with or without TPCK trypsin. Representative widefield images were captured at P0 in HEK 293T cells, and P1 in MDCK cells in at 488 nm to visualise cells transfected with the virus expressing a fluorescent NS1 segment.

Table 5.1: Chimeric viruses generated by reverse genetics.

Virus	**MaCal/09 plasmids**	**WSN plasmids**	**BrightFlu plasmids**	**Trypsin dependency**
MaCal/09	PB2, PB1, PA, HA, NP, NA, M, NS1			Trypsin-dependent
BrightFlu-MaCal/09	PB2, PB1, PA, HA, NP, NA, M		NS1	Trypsin-dependent
WSN		PB2, PB1, PA, HA, NP, NA, M, NS1		Trypsin-independent
BrightFlu-WSN		PB2, PB1, PA, HA, NP, NA, M	NS1	Trypsin-independent

Fluorescently tagged viruses were generated by combining seven plasmids from either WSN or MaCal/09, along with the PR8 NS1 plasmid from BrightFlu. Control viruses were generated using only WSN or MaCal/09 plasmids, without BrightFlu NS1 plasmid.

As expected, no green fluorescence was observed in the MaCal/09 control virus, regardless of the presence of TPCK at P0 in 293T cells (Figure 5.9A and B). The production of a reassorted BrightFlu-MaCal/09 virus was successful, as green fluorescence was observed in both TPCK conditions at P0 (Figure 5.9C and D). BrightFlu-MaCal/09 virus from both P0 stocks demonstrated replication in MDCK cells, only in the presence of TPCK at 24 h.p.i. (Figure 5.9E, F, G, and H). Notably, the fluorescence intensity from P0 stocks grown without TPCK were lower than that of those grown with TPCK. These results confirm the successful production of a recombinant virus expressing PR8 ZsGreen-NS1 in the background of MaCal/09, and that TPCK trypsin is required for its replication.

P0 in 293T cells

A MaCal/09 (+ TPCK)

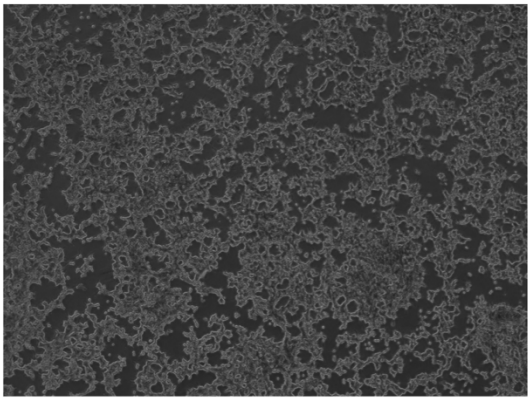

B MaCal/09 (- TPCK)

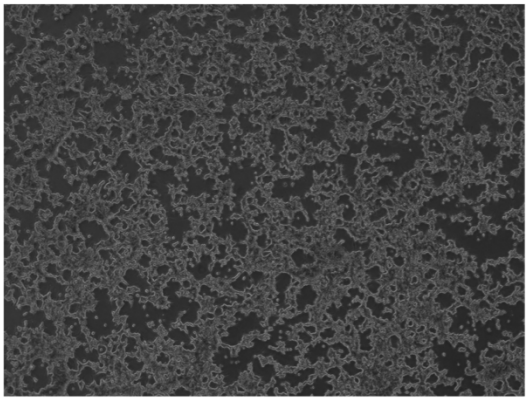

C BrightFlu-MaCal/09 (+ TPCK)

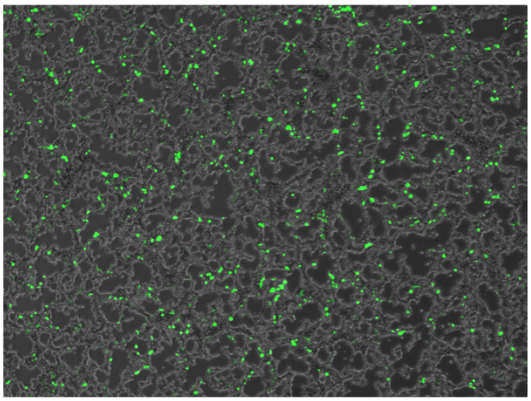

D BrightFlu-MaCal/09 (- TPCK)

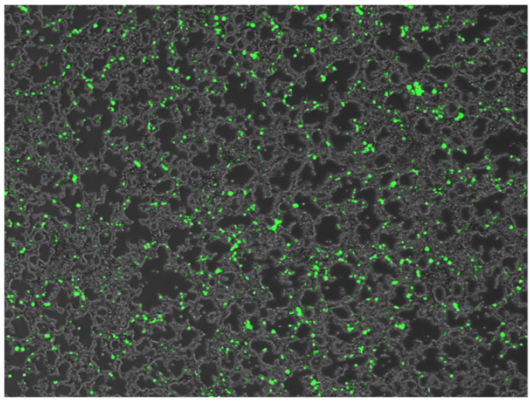

P1 in MDCK cells

E BrightFlu-MaCal/09 (+/+ TPCK)

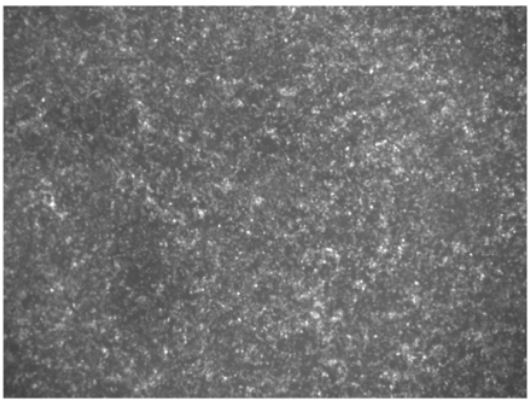

F BrightFlu-MaCal/09 (+/-TPCK)

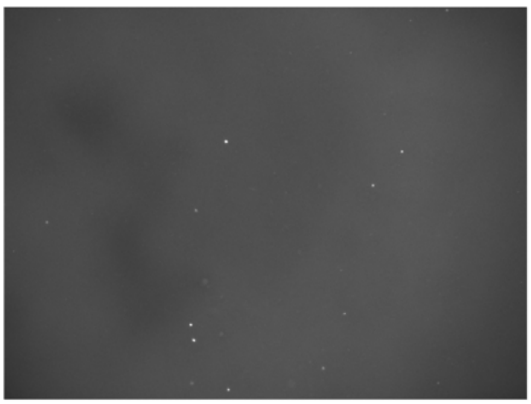

G BrightFlu-MaCal/09 (-/+ TPCK)

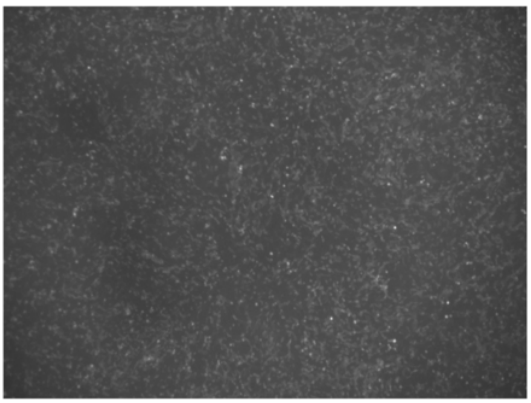

H BrightFlu-MaCal/09 (-/- TPCK)

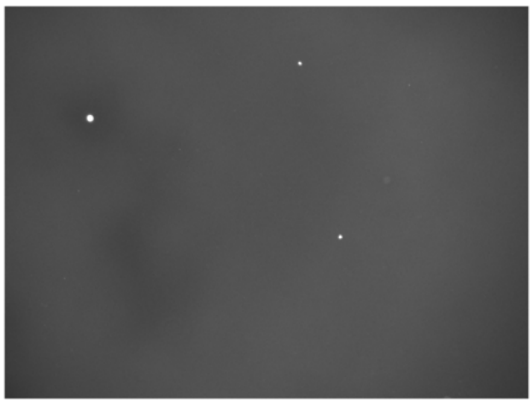

Figure 5.9: Reverse genetics of the BrightFlu-MaCal/09 chimeric virus. *A – D show P0 transfections in 293T cells, with green fluorescence and phase contrast images merged. A and B – MaCal/09 with (+) and without (-) TPCK. C and D – BrightFlu-MaCal/09 with (+) and without (-) TPCK. E – H show only green fluorescence from P1 stocks in MDCK cells at 24 h.p.i. E and F – BrightFlu-MaCal/09 from P0 stocks grown with TPCK, now grown in MDCK cells overlayed with (+/+) and without TPCK (+/-). G and H – BrightFlu-MaCal/09 from P0 stocks grown without TPCK, now grown in MDCK cells overlayed with (-/+) and without TPCK (-/-).*

As expected, no green fluorescence was observed in the WSN control virus, regardless of the presence of TPCK at P0 in 293T cells (Figure 5.10A and B). The production of a reassorted BrightFlu-WSN virus was successful, as green fluorescence was observed in both TPCK conditions, albeit with reduced fluorescence in the absence of TPCK (Figure 5.10C and D). BrightFlu-WSN virus from both P0 stocks failed to replicate in MDCK cells at 24 h.p.i., regardless of TPCK conditions (Figure 5.10E, F, G, and H). These findings indicate that while the production of a recombinant virus expressing PR8 ZsGreen-NS1 in the background of WSN was successful, it was unable to replicate in MDCK cells.

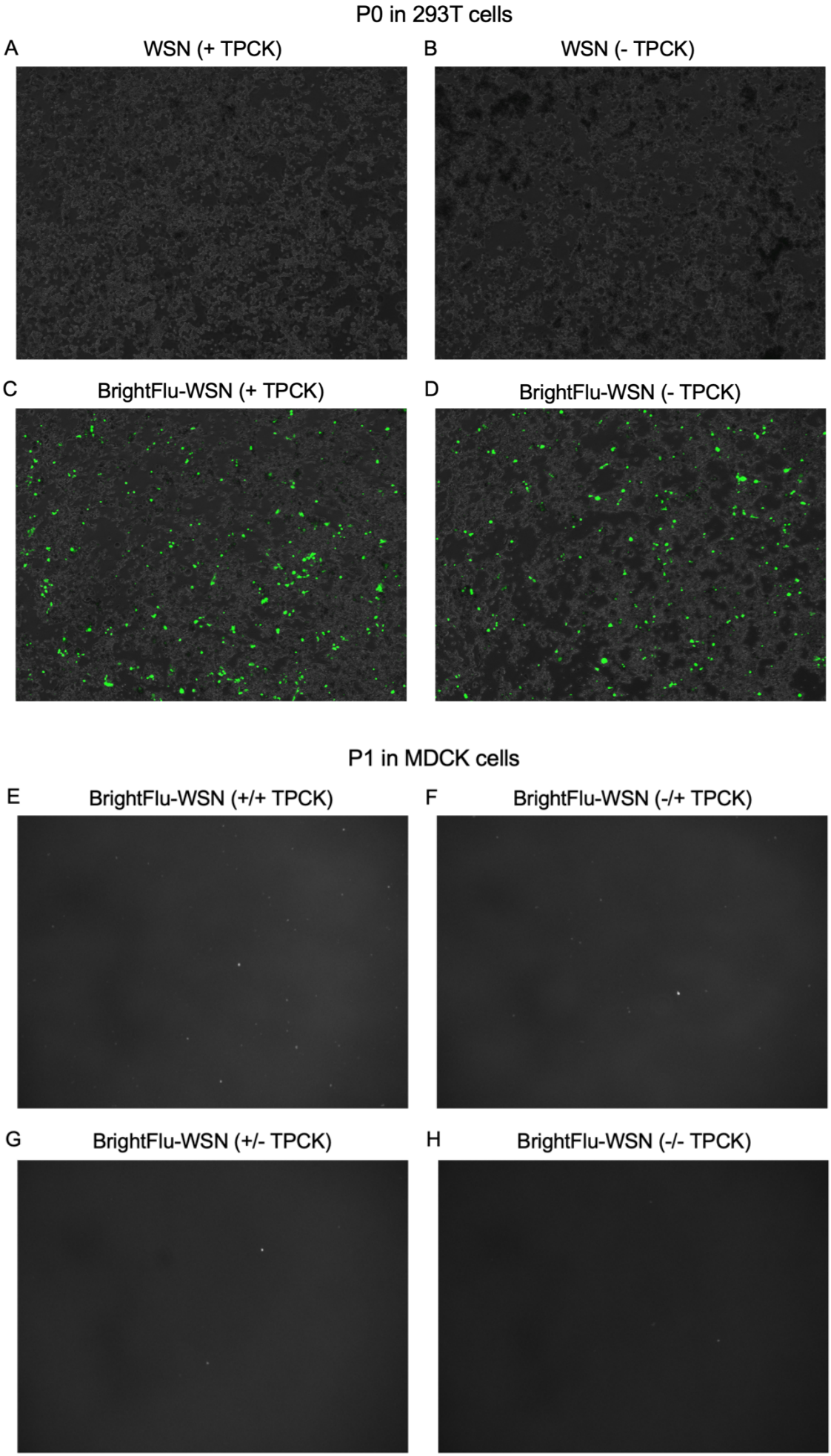
P0 in 293T cells
A
WSN (+ TPCK)
B
WSN (- TPCK)
C
BrightFlu-WSN (+ TPCK)
D
BrightFlu-WSN (- TPCK)
P1 in MDCK cells
E
BrightFlu-WSN (+/+ TPCK)
F
BrightFlu-WSN (-/+ TPCK)
G
BrightFlu-WSN (+/- TPCK)
H
BrightFlu-WSN (-/- TPCK)

Figure 5.10: Reverse genetics of the BrightFlu-WSN chimeric virus. *A – D show P0 transfections in 293T cells, with green fluorescence and phase contrast images merged. A and B – WSN with (+) and without (-) TPCK. C and D – BrightFlu-WSN with (+) and without (-) TPCK. E – H show only green fluorescence from P1 stocks in MDCK cells at 24 h.p.i. E and F – BrightFlu-WSN from P0 stocks grown with TPCK, now grown in MDCK cells overlayed with (+/+) and without TPCK (+/-). G and H – BrightFlu-WSN from P0 stocks grown without TPCK, now grown in MDCK cells overlayed with (-/+) and without TPCK (-/-).*

5.2.7. WSN replication can be measured in multiple cell types

Due to the limitations of using BrightFlu for real-time inhibitor screening across different cell types and the failure to generate a chimeric BrightFlu-WSN virus to support multicycle replication independently of trypsin, an endpoint assay was optimised using WSN. To determine if WSN was capable of multicycle replication in a range of cell types without TPCK trypsin, MDCK, HBEC3-KT, and HAEC-b cells (from a 56 year old Hispanic female) were seeded and mock treated or infected with WSN at a range of MOIs. After 24 hours, cells were fixed, stained for IAV NP, and images were captured using the Celigo Imaging Cytometer at 488nm. In MDCK cells, WSN replication was saturated at higher MOIs (1 to 0.001), decreasing in replication at 0.0001, and minimal comet formation at 0.00001 (Figure 5.11A). The MOI of 0.0001 was within the linear assay range to detect changes in virus replication. In HBEC3-KT and HAEC-b cells, WSN replication was saturated at higher MOIs (1 to 0.1), decreasing at 0.01, and minimal comet formation at 0.001 (Figure 5.11B and C). The MOI of 0.01 was within the linear range to detect changes in virus replication. These results demonstrate that MDCK cells show enhanced permissivity to WSN infection relative to bronchial epithelial cells, consistent with previous observations (Charman *et al.*, 2021). Therefore, a higher MOI of 0.0001 was selected for subsequent studies in MDCK cells, and a lower MOI of 0.01 for HBEC3-KT and HAEC-b cells. As demonstrated by the endpoint assays in Chapter 4, the number of infected cells can be quantified to measure WSN replication (numbers in each well in Figure 5.11). These data show that WSN was capable of multicycle replication in multiple cell types without TPCK trypsin, highlighting its use in inhibitor studies across a range of cell types, including primary cells and laboratory-adapted cell lines.

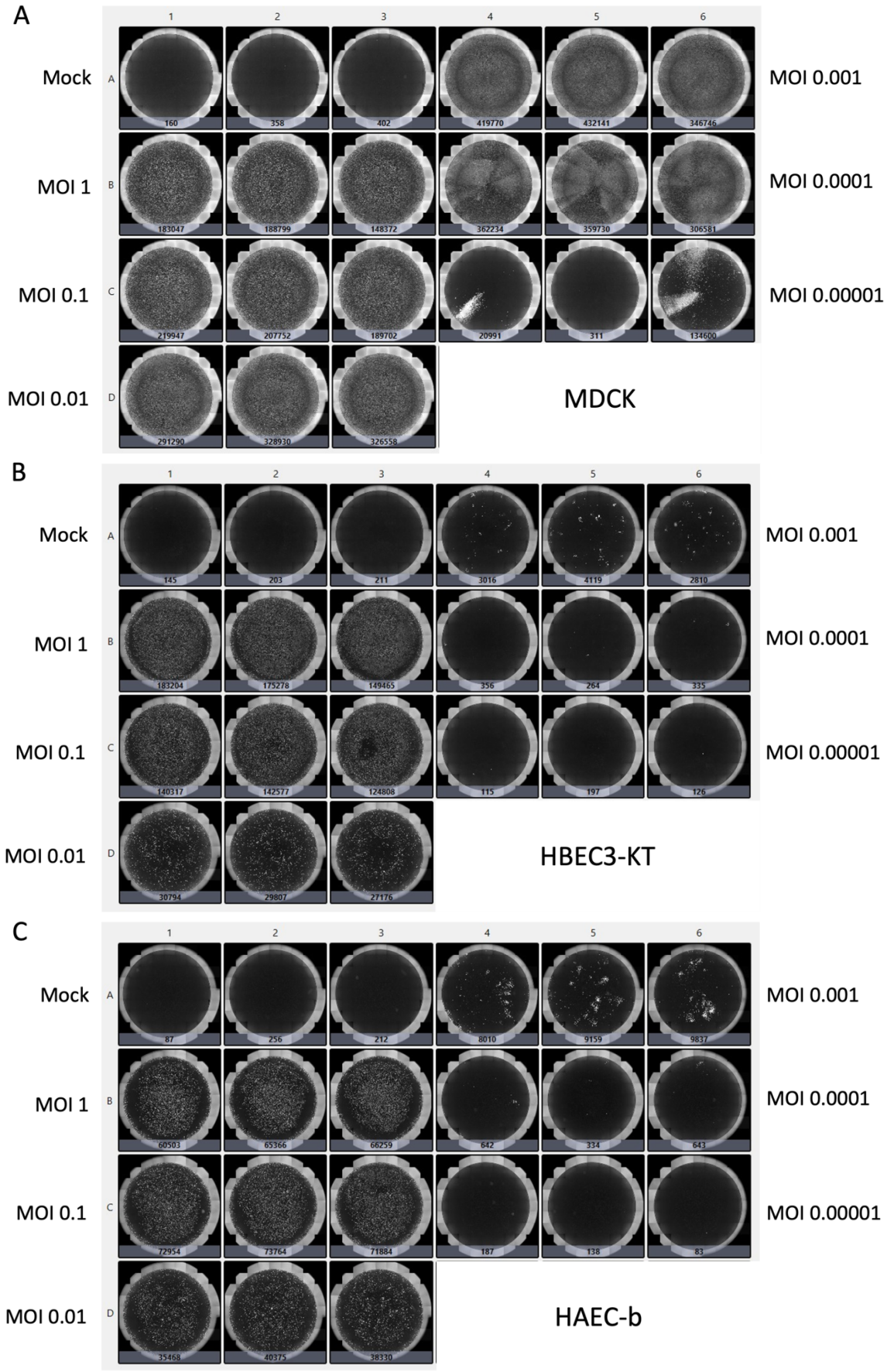

Figure 5.11: WSN replication in multiple cell types. *MDCK, HBEC3-KT, and HAEC-b cells were infected with WSN at a range of MOIs (1-0.00001). Cells were fixed at 24 hours h.p.i., stained for IAV NP, and images were captured. A - MDCK cells, B - HBEC3-KT, and C - HAEC-b from female, 56, Hispanic donor at p3.*

5.3. Discussion

The data presented in this chapter highlight the challenges of using BrightFlu for real-time inhibitor screening. The BrightFlu virus required TPCK trypsin for multicycle replication and could not be grown in more primary like cells without inducing cell detachment. Attempts to replace TPCK with alternative protease, such as TrypLE, resulted in similar detachment issues. Moreover, the addition of ALI culture secretions to the culture medium did not support BrightFlu replication. Notably, mucus within airway secretions has also been shown to be inhibitory to IAV infection *in vitro* and *in vivo*, resulting in a decreased viral titre (McAuley *et al.*, 2017). IAVs bind to highly sialylated mucins secreted in the mucus layer in a dose-dependent manner, resulting in the protection of cells to infection (Cohen *et al.*, 2013). Despite the presence of proteases capable of cleaving IAV HA in mucus, the overall inhibitory effect of ALI culture secretions on IAV infection necessitates isolating these proteases before use.

Efforts to generate a trypsin-independent virus by serially passaging BrightFlu without TPCK were unsuccessful, as the virus displayed significantly reduced replication compared to those passaged in the presence of TPCK. This contrasts with previous reports showing serially passaging PR8 through MDCK cells in the absence of TPCK produces a virus capable of replicating independently of trypsin – comparable to the levels demonstrated in the presence of TPCK (Rott *et al.*, 1984). This adapted virus was reported to contain cleaved HA, with HA1 and HA2 subunits present after infection in MDCK cells. One mutation was consistent between variants adapted to MDCK cells: a histidine to arginine substitution at the 17th position of HA1. This mutation resulted in an increase in the pH of membrane fusion, an essential step of viral entry, and has been predicted to disrupt polar contacts between HA1 and HA2 (Daniels *et al.*, 1985). Serially passaging BrightFlu without TPCK trypsin resulted in a virus with suboptimal replication relative to that of virus passaged in the presence of TPCK. It should be noted that virus generated in the absence of TPCK showed some infectivity. These findings suggest there is a small quantity of infectious virus in these samples, though, far too inefficient for use in real-time assays.

Interestingly, high concentrations of plasminogen partially supported the replication of BrightFlu but delayed the onset of replication. The use of plasminogen would therefore increase the time taken for real-time assays and raised concern about the potential off target effects of plasminogen on cells (LeBouder *et al.*, 2008). This protease contributes to WSNs ability to replicate in cells without TPCK (Lazarowitz, Goldberg and Choppin, 1973). This highlighted the potential of using WSN as an alternative to BrightFlu; however, the fluorescently tagged WSN chimeric virus failed to replicate in MDCK cells. Previous studies show the successful production of PR8 and WSN chimeric viruses (Zamarin, Ortigoza and Palese, 2006; van Wielink *et al.*, 2012; Yamada *et al.*, 2014; Chen *et al.*, 2019). However, a chimeric virus containing seven segments of PR8 and one of WSN (PB1) resulted in lower viral titres in comparison to wild-type virus, which could be alleviated with compensatory mutations (Chen *et al.*, 2019). This highlights the difficulties in creating chimeric viruses and future work should explore compensatory mutations to allow for efficient virus replication. Alternative strategies could employ intercalating viral genome dyes, such as Syto 82 and biotin labelling of the RNA and viral envelope, which have proved effective in live cell imaging of IAV replication (Liu *et al.*, 2012). However, the feasibility of these methods for the extended time period required for real-time assays have yet to be established.

The real-time assay's dependence on TPCK trypsin limits its application to less biologically relevant cell lines, such as MDCK or A549, that are resistant to TPCK cell-monolayer disassociation. Despite our efforts, we could not circumvent this issue and found it of higher priority to screen antivirals in more biologically relevant cell types, thus TPCK-independent viruses must be used for IAV multicycle replication assays in primary cell cultures. WSN was chosen for subsequent infection assays as it demonstrated successful multicycle infection in MDCK, HBEC3-KT, and HAEC-b cells without TPCK. Since a fluorescently tagged WSN virus could not be generated, an endpoint assay was chosen for inhibitor screening in alternative cell types going forward.

Together, these findings led to the establishment of two assays for subsequent inhibitor screening:

1) real-time assay using BrightFlu in MDCK cells
2) endpoint assay using WSN in MDCK, HBEC3-KT, and HAEC-b cells

These assays provide complementary platforms for antiviral screening, allowing for virus replication kinetics to be continuously monitored in the presence of inhibitors in MDCK cells alone, and to extend these findings to more relevant cell types, thus providing a broader biological context for inhibitor studies.

6. Screening epigenetic inhibitors to assess their potential as influenza virus antivirals

6.1. Introduction

Drug repurposing has emerged as a prominent strategy in drug discovery, involving the redevelopment of existing compounds for new therapeutic purposes beyond their original indications. This approach accelerates the approval process for new therapeutic applications by leveraging pre-existing safety testing (Strittmatter, 2014). Approximately one third of recently approved drugs originated from repurposed compounds (Talevi and Bellera, 2020). The urgency for rapid therapeutic deployment, highlighted during the SARS-CoV-2 pandemic, underscored the value of repurposing drugs already tested in humans (Pandey *et al.*, 2020). This strategy is particularly relevant for IAV antiviral research, where the emergence of drug-resistant strains and the persistent threat of pandemic outbreaks necessitate the development of effective inhibitors. Numerous repurposed drugs, including antiparasitics (hydroxychloroquine, chloroquine, nitazoxanide), antibiotics (azithromycin, neomycin), and calcium channel blockers (Verapamil, chlorpromazine), have demonstrated antiviral activity against IAV (Nugent and Shanley, 1984; Ooi *et al.*, 2006; Haffizulla *et al.*, 2014; Rossignol, 2014; Du *et al.*, 2020; Mao *et al.*, 2024). This chapter explores the potential of repurposing drugs as IAV inhibitors.

Host-directed antivirals have gained traction in recent years, particularly because they are less likely to produce drug resistant mutants compared to direct-acting antivirals (N. Kumar *et al.*, 2020). One approach involves modulating epigenetic modifications in both viral and host genomes to influence the outcome of viral replication. Gene expression is subjected to multiple levels of control at both DNA and RNA levels. At the DNA level, external chromatin modifications, such as DNA methylation and histone modifications, can regulate gene expression without altering the DNA sequence, making them reversible targets for altering the relative levels of host gene expression (Kanwal and Gupta, 2012). DNA methylation involves the addition of methyl groups to DNA promoters to prevent transcription. This process is catalysed by DNA methyltransferases (DNMT), such as DNMT1, DNMT3a, and DNMT3b. Histone post-

translational modifications involve acetyl or methyl groups binding to histone tails which can condense/decondense histones, thereby influencing the accessibility of DNA for transcription. While host cells can combat virus infections through epigenetic modifications, viruses can also manipulate host cell epigenetics to evade immune responses.

IAV heavily relies on host cellular machinery for its lifecycle, yet the epigenetic modifications induced by IAV within host cells remain poorly understood (Hu, Zhang and Liu, 2020). Following IAV entry, host PAMPs recognise IAV and induce IFN production. IFNs bind to their respective receptors to activate the JAK-STAT pathway, leading to the expression of ISGs and proinflammatory cytokines (Majoros *et al.*, 2017; Ezeonwumelu, Garcia-Vidal and Ballana, 2021). The IAV NS1 protein has been shown to bind DNMT3B, dissociating it from JAK-STAT signalling gene promoters, resulting in the overexpression of transcriptional suppressors of the JAK-STAT pathway to enhance viral replication (Liu *et al.*, 2019). Additionally, IAV has been reported to decrease H3K79 methylation, which suppresses the antiviral response (Marcos-Villar *et al.*, 2018). These studies suggest that IAV manipulates host cell epigenetics to reduce IFN production and enhance viral replication. Correspondingly, drugs that inhibit the natural suppression of these immunoregulatory pathways would be expected to confer antiviral protection to cells.

Another relevant epigenetic modification is N6-methyladenosine (m^6A), an abundant epigenetic transcriptional modification in mammalian cells. Methyltransfersase complexes bind to consensus sequence motifs in the mRNA to install m^6A modifications, while demethylases remove them. Recent studies have implicated m^6A modifications in regulating IAV gene expression and replication, as well as other RNA viruses, including coronaviruses, human immunodeficiency virus (HIV), and flaviviruses (Courtney *et al.*, 2017; Imam, Kim and Siddiqui, 2020; Liu *et al.*, 2021). Kumar *et al.*, (2022) showed that SARS-CoV-2 RNA undergoes m^6A modifications within host cells, and that treatment with DZNep (inhibitor of S-adenosylmethionine-dependent methyltransferase) reduced the levels of methylated RNA within cells. This inhibition subsequently reduced RNA synthesis and translation of SARS-CoV-2 proteins without leading to the

emergence of DZNep resistant mutants. These findings raised the question of whether similar epigenetic inhibitors could impact IAV replication.

Despite their potential, epigenetic inhibitors remain underexplored as IAV inhibitors. Inhibitors such as C646, a histone acetyltransferase inhibitor, have demonstrated reduced IAV titres and impacted multiple steps of the virus lifecycle (Zhao *et al.*, 2016). Other repurposed cancer drugs, Dasatinib and quercetin, have shown limited success against IAV (Torrance *et al.*, 2023). These compounds may alter epigenetic modifications to influence viral and host gene expression. This chapter focusses on screening various epigenetic inhibitors to assess their potential as IAV antivirals. A literature review of epigenetic modifications impacting the immune response was conducted, and inhibitors were chosen for their known effects on host cell immune responses to infection, particularly those regulating IFN pathways and ISG expression (Bray *et al.*, 2002; Wienerroither *et al.*, 2014; Xu *et al.*, 2018; Jiang Wang *et al.*, 2020). With the exception of favipiravir, oseltamivir, and ruxolitinib, all compounds are repurposed cancer drugs (Table 6.1).

The aim of this chapter is to utilise the real-time assay to monitor BrightFlu replication kinetics in MDCK cells in the presence of various epigenetic inhibitors, and to employ the endpoint assay to assess their inhibitory effects on WSN replication in biologically relevant cell types.

Table 6.1: List of inhibitors used in this chapter

Name	Target	Ref.
CM272	G9a (H3K9 lysine methyltransferase) and DNMT1, DNMT3a, DNMT3b.	(San José-Enériz *et al.*, 2017)
CM579	G9a (H3K9 lysine methyltransferase) and DNMT1, DNMT3a, DNMT3b.	(San José-Enériz *et al.*, 2017)
SYC-522	Dot1L histone methyltransferase (which catalyses H3K79 methylation)	(Marcos-Villar *et al.*, 2018)
DZNep	S-adenosylhomocysteine hydrolase and EZH2 (which catalyses H3K79 methylation)	(Tan *et al.*, 2007; Kumar *et al.*, 2022)
El1	EZH2 (which catalyses H3K79 methylation)	(Qi *et al.*, 2012)
Tazemetostat (EPZ)	Dot1L and EZH2 (which catalyses H3K79 methylation)	(Knutson *et al.*, 2014)
Favipiravir	RNA-dependent RNA polymerase	(Furuta *et al.*, 2013)
JIB-04	Jumonji histone demethylase and serine hydroxymethyltransferase enzyme	(Wang *et al.*, 2013; Xu *et al.*, 2018; Son *et al.*, 2022)
JQ1	BET bromodomain proteins, particularly BRD4 (which catalyses H3K122 acetylation)	(Filippakopoulos *et al.*, 2010)
Nanaomycin A (OM173- αA)	DNMT3B	(Kuck *et al.*, 2010)
Oseltamivir	IAV neuraminidase	(Moscona, 2005)
Ruxolitinib	JAK1 and JAK2 protein kinases	(Yu *et al.*, 2024)

6.2. Results

6.2.1. Optimising treatment conditions for epigenetic inhibitor screening

Unlike direct-acting antivirals such as favipiravir, epigenetic inhibitors that modulate host cell chromatin may necessitate pre-treatment of cells prior to viral infection. Previous studies have demonstrated that IFN-β can inhibit IAV replication when administered as a pre-treatment (Phipps-Yonas *et al.*, 2008; Ilyushina and Donnelly, 2014). To optimise treatment conditions for epigenetic inhibitor screening, HBEC3-KT cells were treated with DZNep and IFN-β either before infection, after infection, or both before and after infection. Cells were pre-treated with increasing concentrations of inhibitors for 24 hours prior to WSN infection (MOI of 0.01). Inhibitors were reintroduced to the overlay medium and incubated for a further 24 hours. Cells were then fixed at 24 h.p.i., and images were captured at 488 nm using the Celigo Imaging Cytometer. The number of infected cells were quantified, and fold changes were calculated relative to untreated cells.

DZNep exhibited a dose-dependent inhibition of WSN replication from 10 μM onwards (Figure 6.1A). The most pronounced reduction in viral replication occurred when cells were treated both before and after infection, compared to either pre- or post-treatment alone. Similarly, IFN-β demonstrated a dose-dependent decrease in WSN replication from 10 μM onwards, but only under pre-treatment or combined pre- and post-treatment conditions (Figure 6.1B). Post-treatment alone did not result in significant inhibition, suggesting that the antiviral activity of IFN-β is mediated by host cell responses rather than direct viral inhibition. This finding is consistent with previous studies that have shown a 24-hour pretreatment with IFN-β to be the most effective in reducing IAV replication (Phipps-Yonas *et al.*, 2008). To maintain consistency across experimental conditions, all inhibitors were applied both before and after virus infection for initial screening assays.

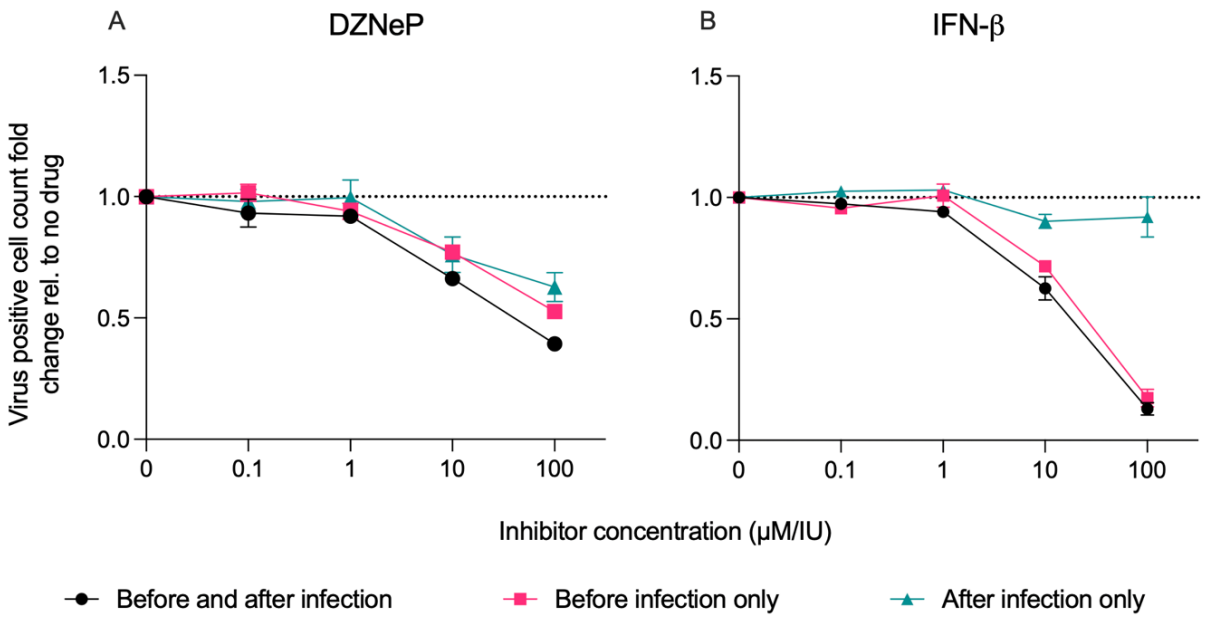

Figure 6.1: Effects of DZNep and IFN-β on WSN replication under pre- and post-infection treatment conditions. *HBEC3-KT cells were infected with WSN (MOI 0.01). Cells were treated with either DZNep (A) or IFN-β (B) under three different treatment conditions: 24 hours prior to infection (pre-treated), immediately after infection for 24 hours (post-treated), or both before and after infection (pre-and post-treated). Cells were fixed at 24 hours post infection, images were captured, and the number of virus positive cells were counted. Fold change was calculated relative to the untreated control. N = 2 technical replicates, error bars = mean ± 1 SD. Black - drug treatment before and after infection, pink - before infection only, green - after infection only.*

To determine the optimal timepoint for evaluating the effects of inhibitors on viral replication, two post-infection timepoints were assessed. HBEC3-KT cells were pre-treated with increasing concentrations of inhibitors for 24 hours, then mock-treated or infected with WSN at an MOI of 0.01. Inhibitors were reintroduced to the overlay, and cells were incubated for either 24 or 48 hours. Cells were fixed, permeabilised, stained for IAV NP and DAPI, and images were captured at 405 and 488 nm using the Celigo Imaging Cytometer. The total cell count and the number of virus infected cells were quantified, and fold changes relative to untreated cells were calculated. Both DZNep and IFN-β treatments resulted in comparable cell counts at 24 and 48 h.p.i., with more pronounced inhibition of viral replication observed at 48 hours (Figure 6.2A and B). However, at 48 h.p.i., IFN-β treatment exhibited increased variability between replicates and lacked a clear dose-dependent inhibitory effect. Prolonged exposure to the inhibitors may negatively impact cell viability, as previously noted in Chapter 4. Therefore, a 24 h.p.i. timepoint was selected for subsequent experiments to balance viral inhibition with cell health.

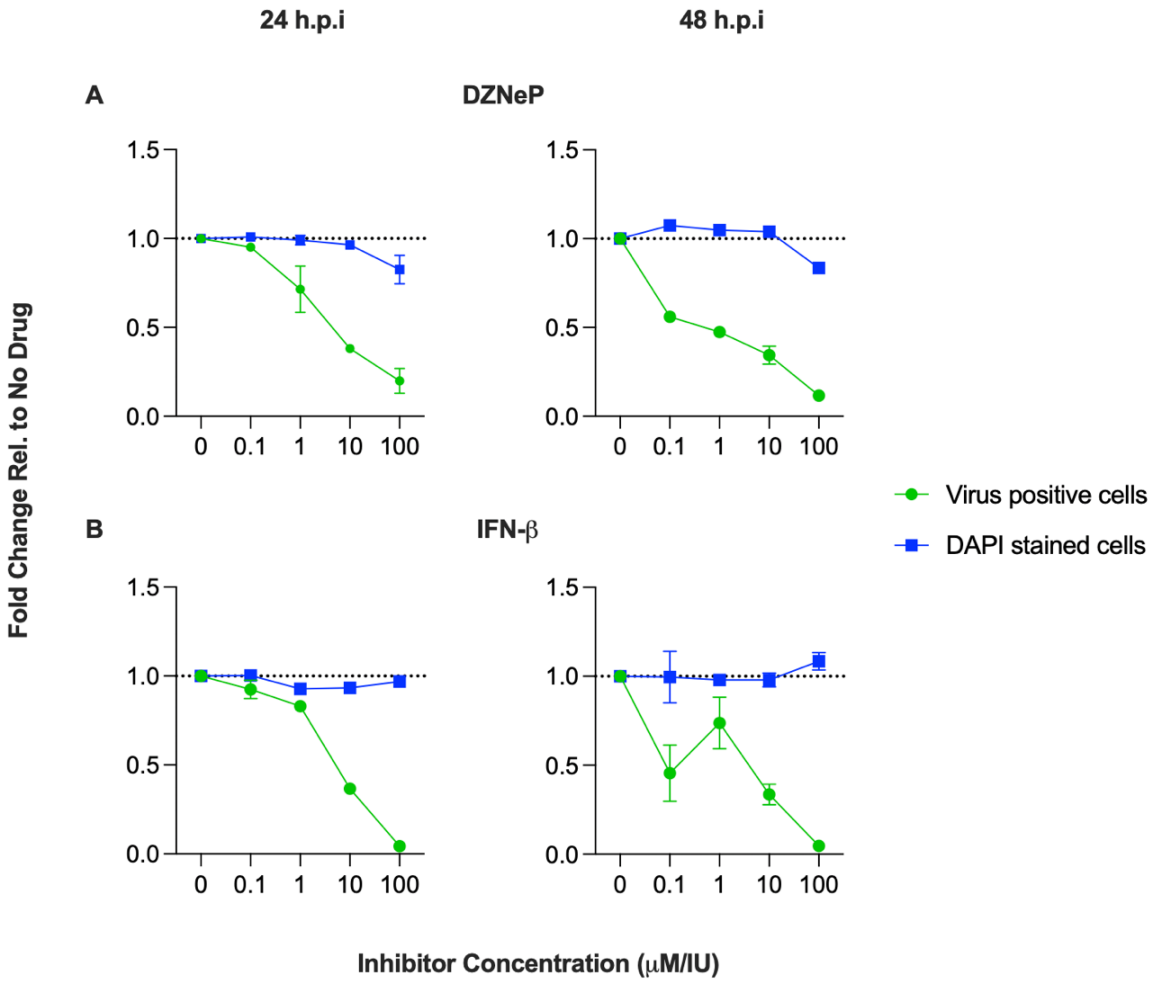

Figure 6.2: Impact of DZNep and IFN-β on WSN replication at 24 and 48 h.p.i. *HBEC3-KT cells were pre-treated with DZNep and IFN-β for 24 hours, infected with WSN, and post-treated for either 24 or 48 hours. Cells were fixed, permeabilised, stained for IAV NP and DAPI. Images were captured at 405 and 488 nm, and total cell counts and number of virus infected cells were quantified. Fold changes were calculated relative to no drug treatment. Left - 24 h.p.i., right - 48 h.p.i. Green - virus positive cells, blue - total cells. N = 2 technical replicates per timepoint. Error bars = mean ± 1 SD.*

6.2.2. Monitoring influenza virus replication kinetics in the presence of epigenetic inhibitors

MDCK cells were selected for initial screening experiments due to their established use in both real-time and endpoint assays (Chapter 4). A small panel of drugs were first evaluated to assess their impact on MDCK viability. The cells were overlayed with a range of drug concentrations (0-100 µM) and incubated for 48 hours. The drug panel included: SYC-522, DZNep, favipiravir, IFN-β, JIB-04, JQ1, OM173- αA, and oseltamivir. Controls included: DMSO as a drug carrier control, puromycin as a death control, and untreated cells as a baseline control. Following the incubation period, MTS reagent was added for 1 hour, and absorbance at 490 nm was measured using a plate reader. Absorbance fold changes were calculated relative to the untreated control.

Figure 6.3A illustrates a dose-dependent reduction in absorption with favipiravir, OM173- αA, SYC-522, DZNep, oseltamivir, and DMSO treatments. JIB-04 caused a rapid decline in absorbance from 1 µM to 100 µM, nearly approaching levels observed with the puromycin control, indicative of significant toxicity. JQ1 initially increased absorbance up to 10 µM, followed by a sharp decline at 100 µM, comparable to the absorbance value of puromycin. IFN-β exhibited minimal reduction in absorbance, even at 100 IU/mL, possibly attributed to its resuspension in cell culture medium rather than DMSO. The average absorbance value for DMSO was 0.67 at 100 µM and 0.88 at 10 µM, suggesting that DMSO reduces MDCK cell metabolism by 33% at 100 µM and 22% at 10 µM. These findings indicate that a concentration of 100 µM DMSO impairs MDCK cell metabolism, establishing 10 µM as the maximum concentration for inhibitor use in MDCK cells. Additionally, DZNep, JIB-04, and JQ1 were found to reduce MDCK cell metabolism more significantly than DMSO alone at 10 µM.

It is important to note that MTS assays may yield misleading results when chemotherapeutic inhibitors that affect the cell cycle are applied (Chan *et al.*, 2013; Wood, Tellier and Murphy, 2018). Some epigenetic inhibitors in this study, particularly DNMT inhibitors, have the potential to induce cell cycle arrest and alter cellular metabolism (Gravina *et al.*, 2010; De Beck *et al.*, 2022). Therefore, MTS assay results should be corroborated with cell counts. MDCK cells

were treated with inhibitors for 48 hours, followed by fixation and DAPI staining. Images were captured at 405 nm using the Celigo Imaging Cytometer, and the number of DAPI stained nuclei were counted. Fold changes were calculated relative to the untreated control. Figure 6.3B reveals that JIB-04 caused a sharp decrease in cell counts from 1 µM to 100 µM, approaching levels observed in the puromycin control. JQ1 displayed a similar trend, though with a less pronounced reduction in cell count. OM173- αA had minimal impact on cell count until reaching 100 µM, where a steep decline to puromycin levels were observed. SYC-522 reduced cell counts at 10 µM but exhibited a slight increase at 100 µM. Favipiravir, DZNep, oseltamivir, IFN-β, and DMSO either slightly increased or maintained cell counts comparable to the untreated control. JIB-04, OM173- αA, JQ1, and SYC-522 induced greater MDCK cell detachment than DMSO alone at 10 and 100 µM. Taken together, these findings suggest that JIB should be used at a maximum concentration of 0.1 µM, while JQ1, OM173- αA, DZNep, and SYC-522 should be limited to 10 µM. Given that 100 µM DMSO significantly reduces MDCK cell metabolism after 48 hours of treatment, all other inhibitors should also be restricted to 10 µM for real-time experiments requiring extended incubation periods.

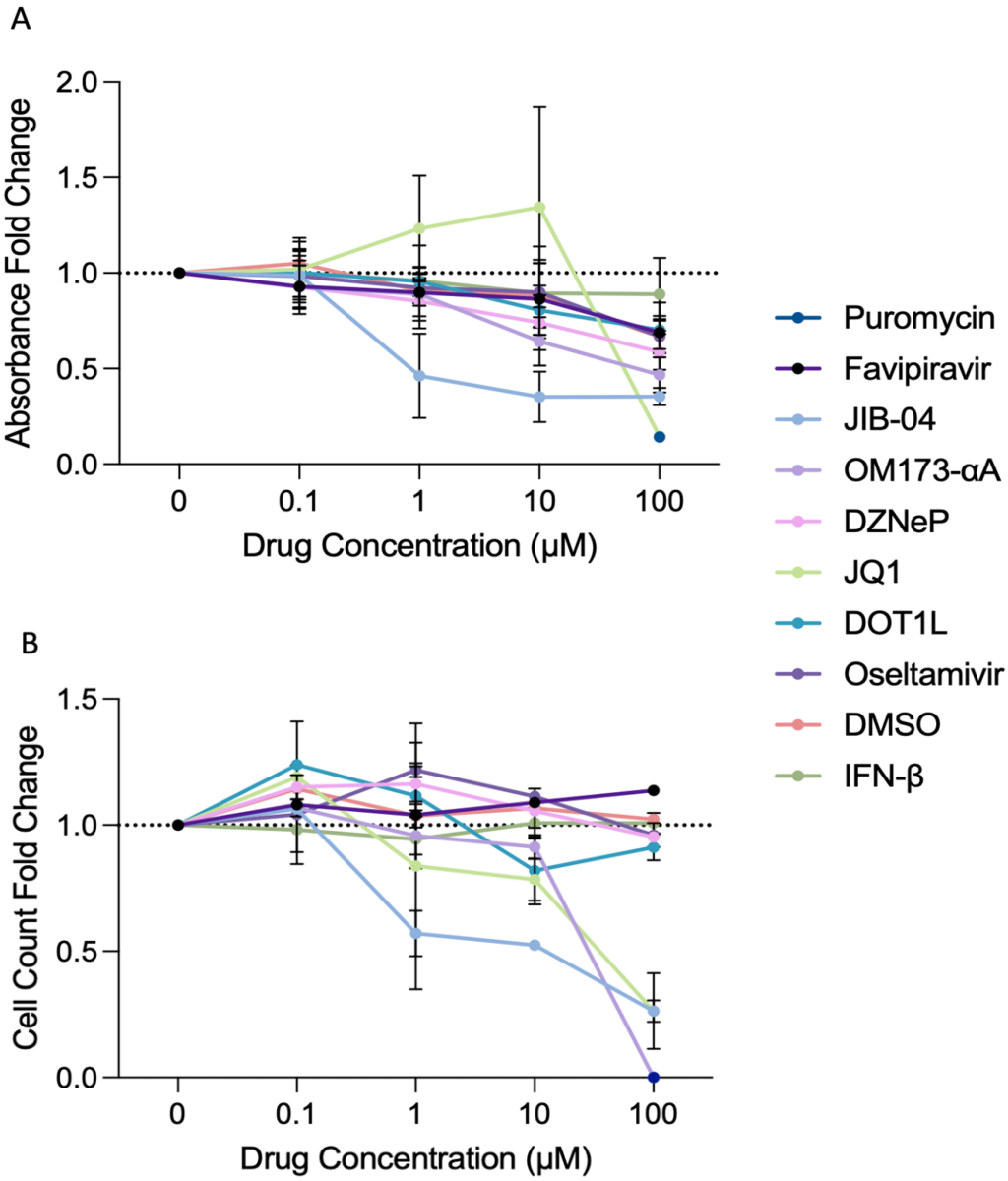

Figure 6.3: Impact of inhibitors on MDCK cell health. *A - absorbance fold change relative to untreated cells. MTS assay absorbance readings taken at 490 nm after 48 hours of drug treatment. B - cell count fold change relative to untreated cells. DAPI stained cell count after 48 hours of drug treatment. Dark blue - puromycin death control; Dark purple - favipiravir; Light blue - JIB-04; Light purple - OM173- αA; Pink - DZNep; Light green - JQ1; Medium blue - SYC-522; Medium purple - oseltamivir; Peach - DMSO; Dark Green - IFN-β. N = 3 biological replicates. Error bars = mean ± 1 SD.*

The panel of drugs were evaluated for their potential as IAV inhibitors using the real-time assay. MDCK cells were pre-treated with eight inhibitors at concentrations ranging from 0-100 μM. Inhibitors included: SYC-522, DZNep, favipiravir, IFN-β, JIB-04, JQ1, OM173-αA, oseltamivir, and DMSO as a drug carrier control. Following pre-treatment, cells were mock treated or infected with BrightFlu at an MOI of 0.001 for 1 hour. Post-infection, inhibitors were reintroduced into the overlay medium, with a control receiving no drug treatment. The cell culture plate was then incubated in a plate reader to measure green RFU expressed over 36 hours.

SYC-522 demonstrated a reduction in BrightFlu replication only at 0.1 μM (Figure 6.4A). DZNep did not exhibit the same strong dose-dependent inhibition observed in HBEC3-KT cells, but did demonstrate a progressive delay in BrightFlu replication with increasing concentrations (Figure 6.4B). Favipiravir displayed a dose-dependent inhibition of BrightFlu, consistent with the findings reported in Chapter 4 (Figure 6.4C). Surprisingly, IFN-β poorly inhibited BrightFlu replication in MDCK cells, contrary to the dose-dependent inhibition displayed in HBEC3-KT cells (Figure 6.4D). JIB-04 inhibited BrightFlu replication from 1 μM onwards; however, MTS assays and cell counts indicated a 50% reduction in cell metabolism and viability at these concentrations (Figure 6.4E). JQ1 reduced BrightFlu replication by 50% at 1 and 10 μM and completely inhibited replication at 100 μM, though 100 μM proved toxic to the cells (Figure 6.4F). OM173-αA inhibited replication by approximately one-third at 10 μM and delayed the onset of BrightFlu replication (Figure 6.4G). Oseltamivir showed dose-dependent inhibition of BrightFlu replication, similar to the effects of favipiravir (Figure 6.4H). The DMSO control resulted in a reduction in BrightFlu replication by approximately a third at 100 μM (Figure 6.4I). Overall, DZNep, favipiravir, JQ1, OM173-αA, and oseltamivir demonstrated promising inhibitory effects on BrightFlu replication using the real-time assay.

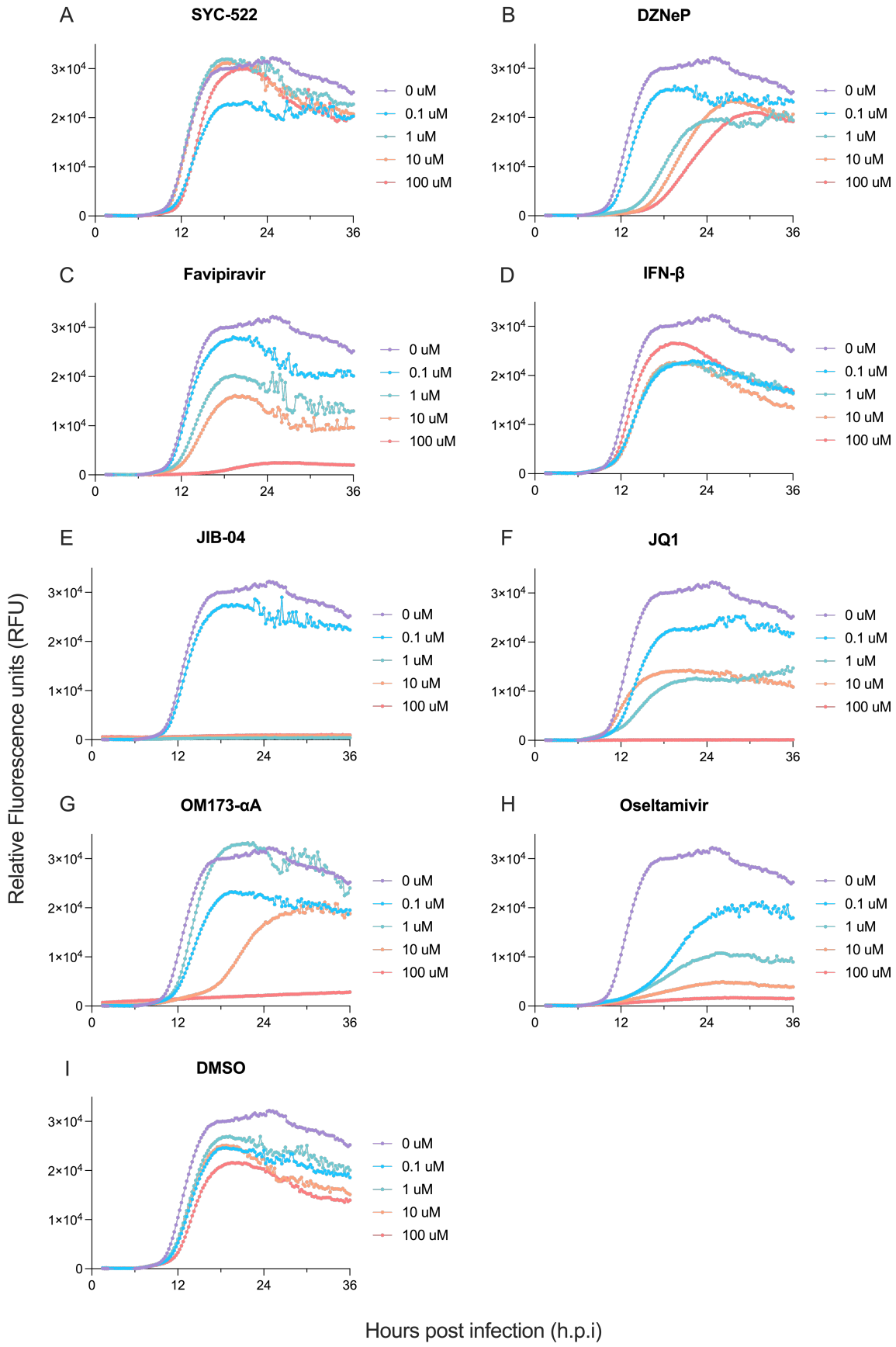

Figure 6.4: BrightFlu replication kinetic curves in the presence of epigenetic inhibitors. *MDCK cells were pre-treated with inhibitors for 24 hours, infected with BrightFlu (MOI 0.001), and post-treated with inhibitors. Green relative fluorescent units (RFU) were recorded every 15 minutes from 0 to 36 hours post-infection (h.p.i.),*

with values from mock infected cells subtracted. A – SYC-522, B – DZNep, C – favipiravir, D – IFN-β, E – JIB-04, F – JQ1, G – OM173-aA, H – oseltamivir, I – DMSO control. Purple – 0 μM, blue – 0.1 μM, green – 1 μM, orange – 10 μM, pink – 100 μM.

6.2.3. Effects of epigenetic inhibitors on influenza virus replication across multiple cell types

A larger panel of drugs were assessed for their inhibitory effects on WSN replication in multiple cell types using the end-point assay. Initially, the study focussed on the control inhibitors: favipiravir, oseltamivir, IFN-β, ruxolitinib, and DMSO as a drug carrier control. Favipiravir and oseltamivir are licenced IAV antivirals (Shiraki and Daikoku, 2020; Centers for Disease Control and Prevention, 2023). Previous experiments have established that favipiravir and IFN-β inhibit IAV replication in MDCK and HBEC3-KT cells, respectively. Ruxolitinib inhibits JAK1/2, thereby suppressing the IFN-induced antiviral response and increasing IAV replication (Randall and Goodbourn, 2008; Stewart, Randall and Adamson, 2014). The inhibitors were tested in MDCK, HBEC3-KT, and HAEC-b (56 year old Hispanic female donor) cells. These cells were pre-treated with inhibitors for 24 hours, then infected with WSN at an MOI of 0.0001 for MDCK cells and 0.01 for HBEC3-KT and HAEC-b cells. Inhibitors were reintroduced into the overlay medium, with control wells containing untreated cells or DMSO-treated cells. After 24 hours of incubation, cells were fixed, permeabilised, and stained for IAV NP and DAPI. Images were captured using the Celigo Imaging Cytometer at 405 and 488 nm. The total cell counts and number of WSN infected cells were quantified, and fold changes were calculated relative to untreated cells.

HAEC-b cells exhibited significant sensitivity to DMSO, with a 50% reduction in both total cell counts and virus infected cells at 100 µM, and approximately a one-third reduction at 10 µM (Figure 6.5A). In MDCK cells, the number of virus infected cells increased at 1 µM and remained stable at higher concentrations, although total cell counts decreased by 10% at 10 µM and 100 µM. In HBEC3-KT cells, the number of virus infected cells decreased by 10% at 1 µM and 10 µM and remained stable at 100 µM, while total cell counts dropped by 10% at 10 µM and 20% at 100 µM. Consequently, thresholds for inhibitor efficacy using the end-point assay are:

- a maximum of 10 µM for HAEC-b cells, where over 33% inhibition is required
- a maximum of 100 µM for MDCK and HBEC3-KT cells, where over 10% inhibition is required

Figure 6.5B demonstrates a dose-response relationship between increasing favipiravir concentrations and decreasing numbers of infected cells in MDCK and HAEC-b cells, but not in HBEC3-KT cells. Figure 6.5C shows a dose-response relationship between increasing oseltamivir concentrations and decreasing numbers of infected cells in all cell types. Figure 6.5D demonstrates a dose-response relationship between increasing IFN-β concentrations and decreasing numbers of infected cells in HBEC3-KT and HAEC-b cells, but not in MDCK cells. Ruxolitinib produced varied effects: it increased virus replication in HAEC-b cells (as expected) but did not show the same effect in MDCK or HBEC3-KT cells (Figure 6.5E). Among the control inhibitors tested, only oseltamivir demonstrated consistent dose-dependent inhibition of WSN replication across all cell types at 24 h.p.i.

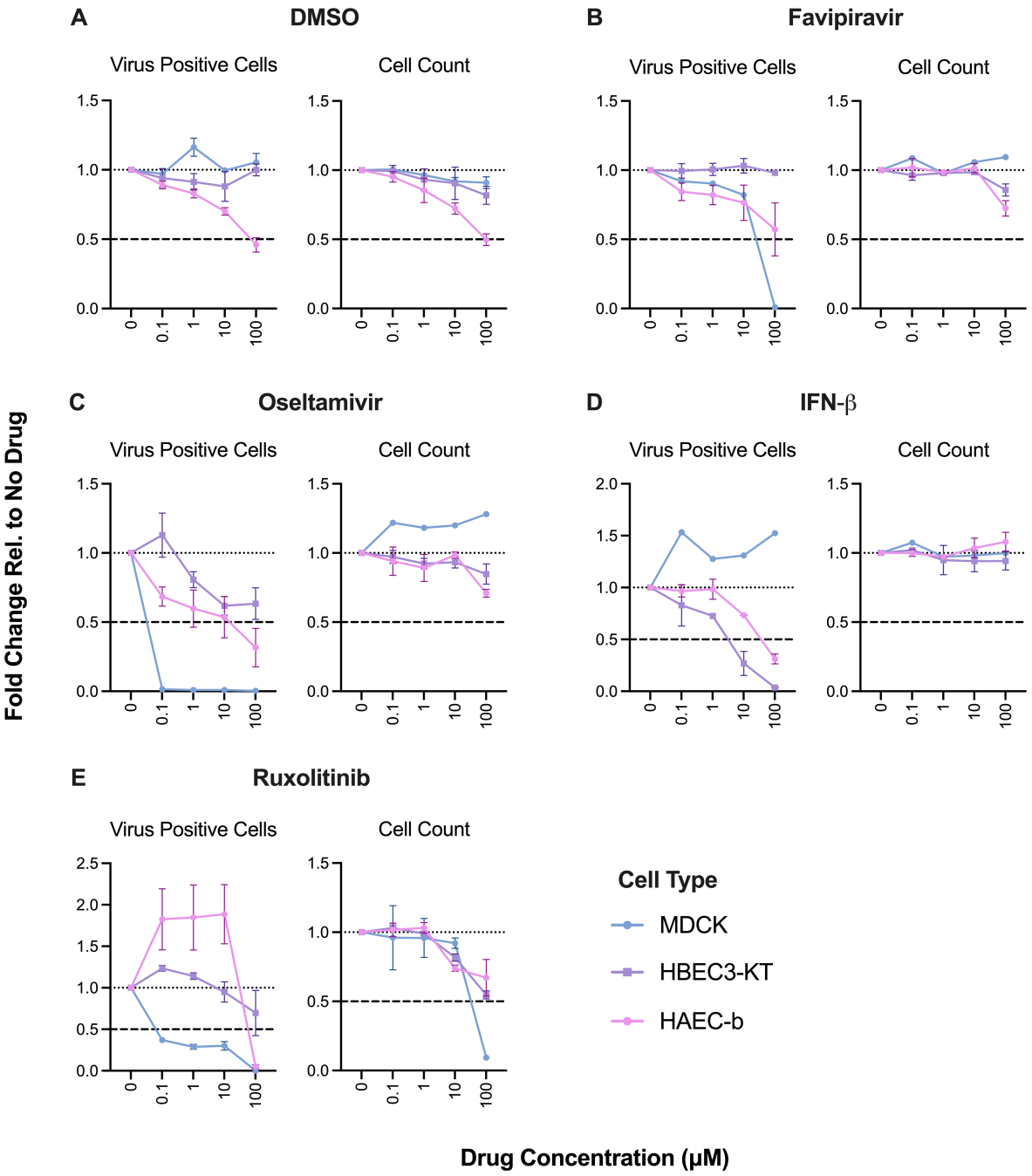

Figure 6.5: Impact of control inhibitors on WSN replication and cell count across various cell types. *MDCK, HBEC3-KT, and HAEC-b cells were pre-treated with inhibitors for 24 hours, infected with WSN, and post-treated for 24 hours. Cells were fixed, permeabilised, and stained for IAV NP and DAPI. Images were captured at 405 and 488 nm using the Celigo Imaging Cytometer. The total cell counts and number of virus-positive cells were quantified, and fold changes were calculated relative to untreated cells. Left - virus positive cell count, right - total cell count. Blue - MDCK cells, purple - HBEC3-KT cells, pink - HAEC-b cells. N = 2 biological replicates. Error bars = mean ± 1 SD.*

The inhibitory effects of epigenetic inhibitors on WSN replication were evaluated across multiple cell types using the endpoint assay. The now expanded panel of inhibitors included: CM272, CM579, SYC-522, DZNep, El1, EPZ, JIB-04, JQ1, OM173-αA. The experimental procedures and analyses were consistent with those described previously. Results were as follows:

- CM272 in HAEC-b cells achieved a 50% reduction in virus replication at 0.1 μM, 20% inhibition at 1 μM, and complete inhibition at 10 μM (Figure 6.6A). In HBEC3-KT cells, CM272 resulted in a 70% reduction in virus replication at both 0.1 and 1 μM, with complete inhibition by 10 μM, but 10 μM also caused 50% reduction in cell counts. In MDCK cells, virus replication was reduced by 50% at 1 μM, with cell detachment occurring at 10 μM.
- CM579 in HAEC-b cells showed complete inhibition of virus replication at 10 μM and 100 μM (Figure 6.6B). At 10 μM cell counts increased, whereas at 100 μM, they dropped by 30%. This effect was observed in MDCK and HBEC3-KT cells, though less pronounced, as the decrease in virus replication correlated with reduced cell numbers.
- SYC-522 in HAEC-b cells demonstrated a 60% inhibition of virus replication at 10 μM without affecting cell count (Figure 6.6C). This effect was not observed in other cells.
- DZNep exhibited dose-dependent inhibition of virus replication in MDCK cells but showed no inhibition in other cell types (Figure 6.6D).
- El1 and EPZ both inhibited virus replication from 0.1 μM onwards in MDCK cells (Figure 6.6E and F). This effect was not observed in other cells.
- JIB-04, JQ1, and OM173-αA produced spurious results across cell types and caused significant reductions in cell counts (Figure 6.6G-I).

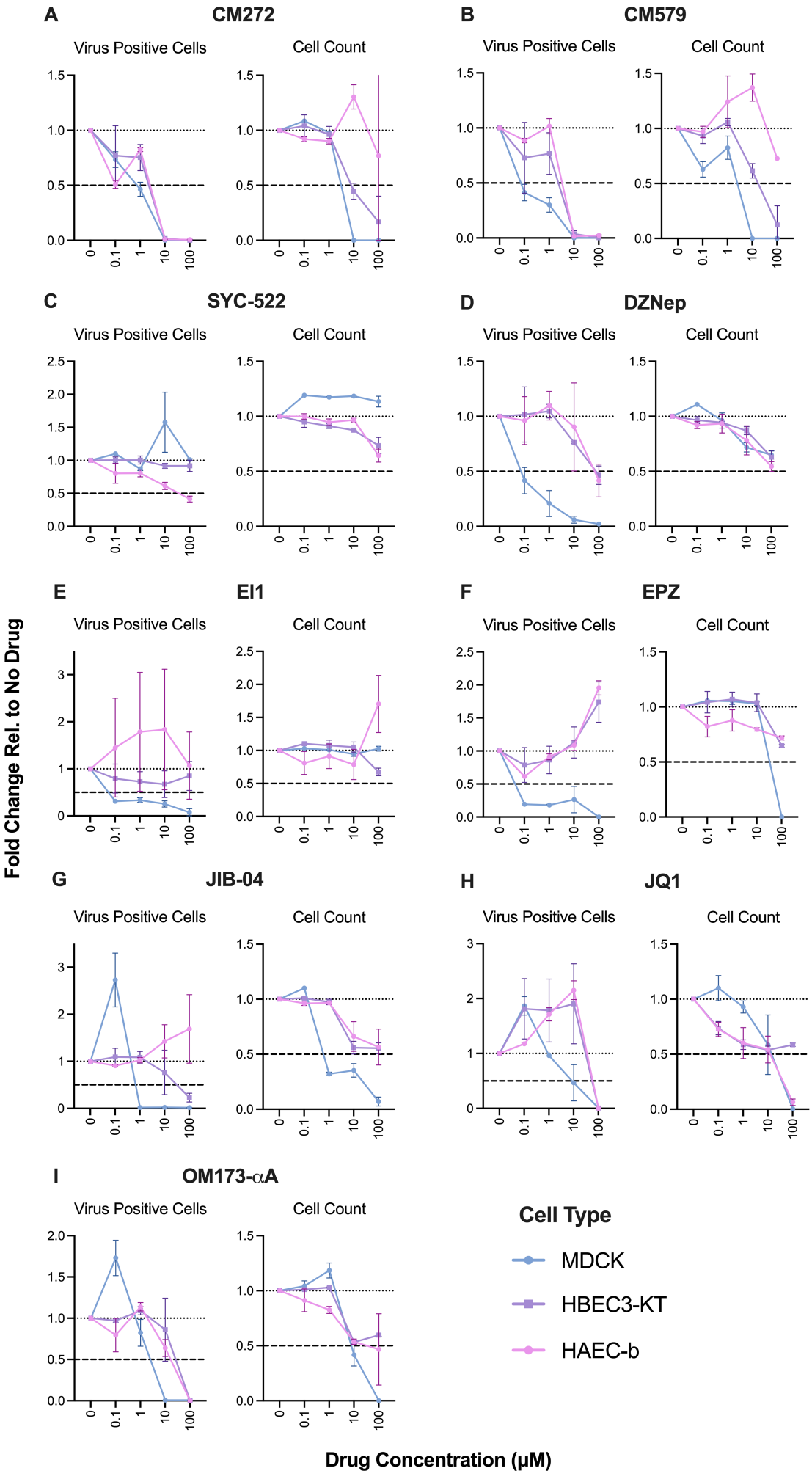
A
CM272
B
CM579
C
SYC-522
D
DZNep
E
EI1
F
EPZ
G
JIB-04
H
JQ1
I
OM173-αA
Virus Positive Cells
Cell Count
Fold Change Rel. to No Drug
Drug Concentration (μM)
Cell Type
MDCK
HBEC3-KT
HAEC-b

Figure 6.6: Impact of epigenetic inhibitors on WSN replication and cell count across various cell types. *MDCK, HBEC3-KT, and HAEC-b cells were pre-treated with inhibitors for 24 hours, infected with WSN, and post-treated for 24 hours. Cells were fixed, permeabilised, and stained for IAV NP and DAPI. Images were captured at 405 and 488 nm using the Celigo Imaging Cytometer. The total cell counts and number of virus-positive cells were quantified, and fold changes were calculated relative to untreated cells. Left – virus-positive cell count, right – total cell count. Blue – MDCK cells, purple – HBEC3-KT cells, pink – HAEC-b cells. N = 2 biological replicates. Error bars = mean ± 1 SD.*

Inhibitor screening results are summarised in Table 6.2. Inhibitors were considered successful if they met the following criteria:

1) demonstrated over 33% inhibition of WSN replication in HAEC-b cells by 10 μM and over 10% inhibition in MDCK and HBEC3-KT cells by 100 μM.
2) maintained cell counts higher than DMSO controls at the concentration where inhibition is displayed.
3) exhibited a trend of dose-dependent inhibition (Emilien, van Meurs and Maloteaux, 2000).

The successful inhibitors, highlighted in green, included: CM272, CM579, and oseltamivir in all three cell types, IFN-β in HBEC3-KT and HAEC-b cells, SYC-522 in HAEC-b cells, DZNep, El1, EPZ, favipiravir, and ruxolitinib in MDCK cells. To note: since donor variation was observed in IAV infected ALI cultures treated with favipiravir (Chapter 4), inhibitor efficacy was evaluated in HAEC-b cells from two different donors using the endpoint assay. However, due to time constraints, only one biological replicate was carried out and data are provided in the appendix.

Table 6.2: Summary of inhibitor efficacy across different cell types using the endpoint assay.

Drug	MDCK	HBEC3-KT	HAEC-b
CM272			
CM579			
SYC-522			
DZNep			
El1			
EPZ			
Favipiravir			
IFN-β			
JIB-04			
JQ1			
OM173-αA			
Oseltamivir			
Ruxolitinib			

Efficacy of all inhibitors tested in endpoint assay experiments, excluding the DMSO control, in MDCK, HBEC3-KT, and HAEC-b cells. Green – successful inhibitors meeting the criteria for effective inhibition of WSN replication while maintaining cell viability. Red – unsuccessful inhibitors either failing to inhibit virus replication or causing significant reductions in cell counts.

Drugs showing successful inhibition of IAV were investigated in combination with IFN-β treatment to determine if there were enhanced inhibitory effects using combined drug treatments. IFN-β was chosen to combine with successful inhibitors as it effectively reduced viral replication in HAEC-b cells and has an important role in the cellular antiviral immune response against IAV (Koerner *et al.*, 2007). HAEC-b (56 year old Hispanic female donor) cells were pre-treated with inhibitors and 10 IU of IFN-β for 24 hours, then infected with WSN at an MOI of 0.01. Post-infection, inhibitors and 10 IU of IFN-β were reintroduced into the overlay medium, with untreated cells and DMSO as controls. After 24 hours of incubation, cells were fixed, permeabilised, and stained for IAV NP and DAPI. Images were captured using the Celigo Imaging Cytometer at 488 nm. The number of WSN infected cells were quantified, and fold changes were calculated relative to untreated cells. The data were combined with HAEC-b cell inhibitor data from Figure 6.5 and 6.6.

CM272, CM579, and SYC-522 combined with IFN-β showed no further inhibition of IAV (Figure 6.7A, B and C). Interestingly, despite previous findings showing favipiravir lacked antiviral activity in HAEC-b cells, when combined with IFN-β treatment it demonstrated inhibition of IAV from 0.1 μM onwards – surpassing the efficacy of both inhibitors when treated independently (Figure 6.7D). Similarly, oseltamivir combined with IFN-β treatment demonstrated increased inhibition from 1 μM onwards in a dose-dependent manner (Figure 6.7E). These findings highlight the potential of combined inhibitor treatments to enhance their antiviral potential. Future work should investigate different combinations of host-directed and direct-acting antivirals to explore synergistic antiviral effects.

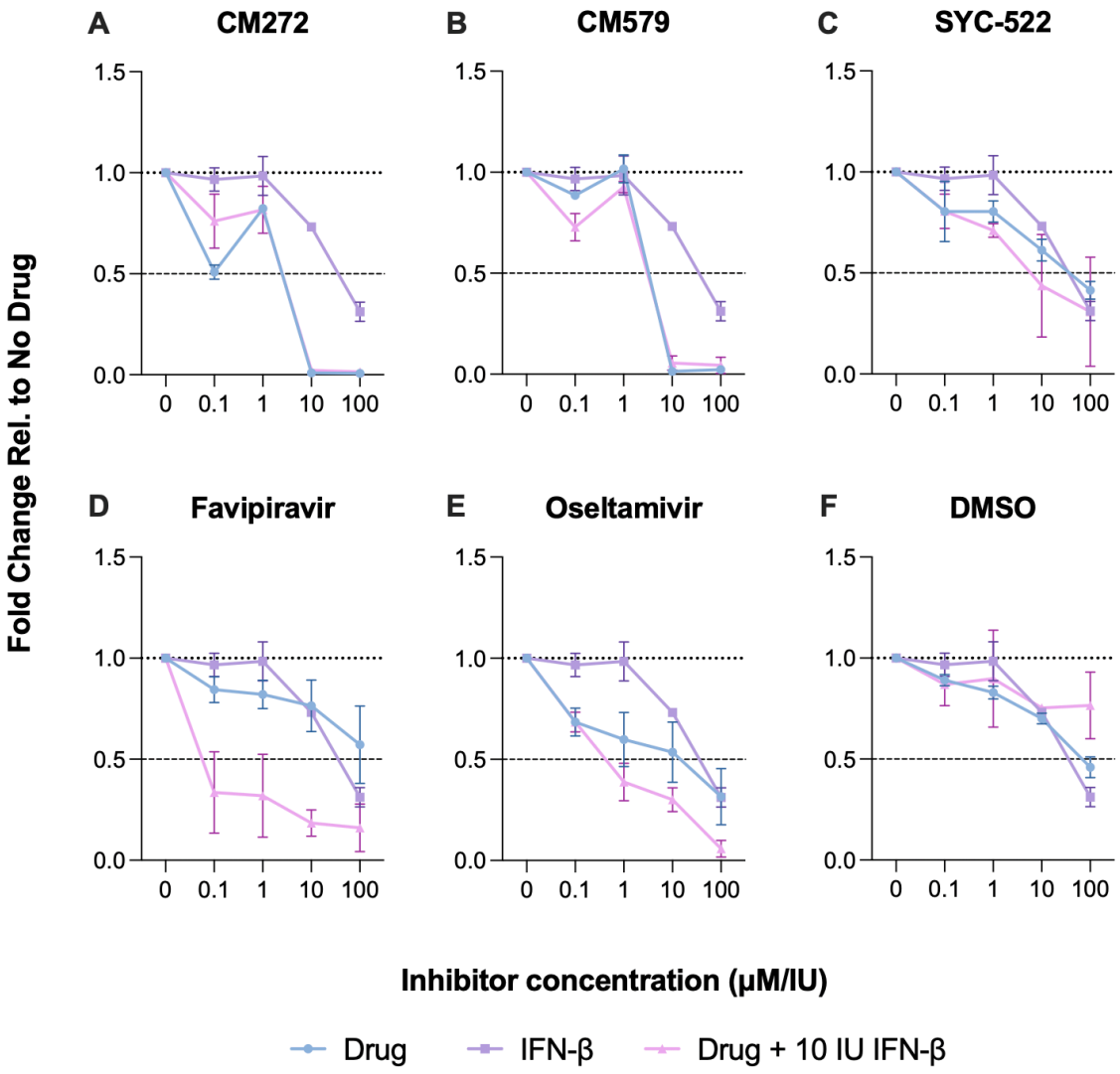

Figure 6.7: Impact of epigenetic inhibitors in combination with IFN-β treatment on WSN replication in HAEC-b cells. *HAEC-b cells were pre-treated with inhibitors and 10 IU of IFN-β for 24 hours, infected with WSN, and post-treated for 24 hours. Cells were fixed, permeabilised, and stained for IAV NP. Images were captured at 488 nm using the Celigo Imaging Cytometer. The number of virus-positive cells were quantified, and fold changes were calculated relative to untreated cells. Blue - drug only, purple - IFN-β only, pink - drug with 10 IU IFN-β. N = 2 biological replicates. Error bars = mean ± 1 SD.*

6.3. Discussion

The analysis of viral replication kinetics revealed that several inhibitors, including DZNep, favipiravir, JQ1, OM173- αA, and oseltamivir inhibited IAV replication in MDCK cells. Notably, DZNep, OM173- αA, and oseltamivir delayed the onset of viral replication in a dose-dependent manner. Although real-time monitoring of virus kinetics provided valuable insights into these inhibitors' effects, it became evident that screening these inhibitors in more biologically relevant cell types was crucial. When the inhibitors were tested across multiple cell types (MDCK, HBEC3-KT, and HAEC-b cells), there was significant variability in efficacy. For example, oseltamivir consistently demonstrated dose-dependent inhibition across all three cell types. However, favipiravir, despite also being a licenced antiviral for influenza infections, only reduced virus replication in MDCK cells and showed no inhibition in HBEC3-KT or HAEC-b cells. This finding was unexpected and underscores the importance of evaluating antiviral efficacy in multiple cell types.

Among the compounds tested, CM272 and CM597 stood out for their ability to reduce WSN replication across all cell types at 10 μM while maintaining cell viability. Their inhibitory effects on IAV have not been previously reported. CM272 is known to induce HIV RNA expression in latently infected cells (Y. Tang *et al.*, 2023). San José-Enériz *et al.* (2017) found CM272 inhibits cell proliferation and promotes apoptosis in xenogeneic models of cancers such as acute myeloid leukaemia. Interestingly, the type I IFN pathway was induced by CM272 treatment through the inhibition of G9a and DNMT activity. CM272 treatment increased the expression of ISGs (IFI44L, EPSTI1, OASL, IFI6, USP18, and ABTB2), which was attributed to decreased levels of H3K9me2 in their promoters. OASL and IFI6 activate RIG-I antiviral signalling and are upregulated in IAV infected primary bronchial epithelial cells and A549 cells, respectively (Zhu *et al.*, 2014; Villamayor *et al.*, 2023). IFI44L and USP18 are upregulated in IAV infected primary bronchial epithelial cells and increase viral replication through binding to cellular FK506-Binding Protein 5 and activation of the cGAS-STING pathway, respectively (DeDiego, Martinez-Sobrido and Topham, 2019; Zhou *et al.*, 2021; L. Tang *et al.*, 2023). EPSTI1 and ABTB2 are upregulated in patient serum samples and A549 cells infected with IAV, respectively (Josset *et*

al., 2010; Zhai *et al.*, 2015). Segovia *et al.* (2019) confirm CM272's ability to upregulate these ISGs in bladder cancer cells, reporting an additional upregulated ISG, IRF7, which amplifies IFN production and is upregulated in IAV infected primary bronchial epithelial cells and A549 cells (Ilyushina, Dickensheets and Donnelly, 2019; Wu *et al.*, 2020). Overall, the ISGs upregulated by CM272 play a role in the antiviral response to IAV infection, with both antiviral and proviral effects. Future work should involve directly measuring ISG expression by immunoblot, qPCR, and transcriptomic analyses to study the ability of CM272 and CM597 to activate ISGs and their role in the antiviral immune response to IAV infection (Charman *et al.*, 2021). Unfortunately, RNA extraction for transcriptome analysis was unsuccessful (data not shown), and the potential of CM272 and CM597 as IAV inhibitors should be further investigated.

DZNep, El1, and EPZ (all inhibitors of H3K79 methylation) demonstrated inhibition of IAV replication in MDCK cells. However, these findings contrast with previous studies where EPZ increased IAV replication in A549 cells by suppressing the expression of ISG56, Mx1, and NF-κB nuclear translocation (Marcos-Villar *et al.*, 2018). On the other hand, DZNep has been shown to decrease RNA synthesis and translation of SARS-CoV-2 proteins by reducing RNA methylation in Vero and BHK-21 cells (Kumar *et al.*, 2022). DZNep demonstrated successful inhibition in immortalised canine kidney (MDCK), African green monkey kidney (Vero), and golden hamster fibroblast (BHK-21) cells, but not in primary human bronchial cells. This highlights the variability of epigenetic inhibitor effects depending on the species and cell type used, especially between immortalised and primary cells. Interestingly, both EPZ and SYC-522 inhibit Dot1L and subsequent H3K79 methylation, yet only SYC-522 demonstrated inhibition in HAEC-b cells. Taken together, these findings underscore the need to screen potential antivirals in more biologically relevant primary cells.

Ruxolitinib decreased IAV replication in MDCK cells but increased replication in HAEC-b cells, until reaching complete inhibition at 100 μM. Previous literature demonstrates that ruxolitinib inhibits IAV replication in A549, HEK293T, NL20, and HEK293 at 100, 100, 50 and 30 μM respectively (Watanabe *et al.*, 2014; Jiongjiong Wang *et al.*, 2020; Zhang *et al.*, 2024). Contrary to this, Stewart, Randall and Adamson (2014) found ruxolitinib to have no impact on IAV

replication in MDCK cells, although they observed increased replication with an NS1 deletion mutant with ruxolitinib treatment. Notably, IFN-β inhibited IAV replication in primary cells but increased replication in MDCK cells. IFN-β binds to IFNAR which is associated with JAK tyrosine kinases. Binding results in the activation of kinases which phosphorylate STAT1/2 to associate to IRF-9 (Stark *et al.*, 1998). This complex (ISGF3) binds to DNA sequences to upregulate IFN production (García-Sastre, 2002). Non-IFN-responsive MDCK cells grow higher titres than IFN-responsive MDCK cells, indicating the MDCK cells used in this study do not respond to IFN-β treatment (Pérez-Cidoncha *et al.*, 2014). The findings from Capellini et al. (2020) indicate that MDCK cells undergo significant changes in gene expression upon extended passaging. At passage 40 TLR2, 7, 9, and 10, and IL2, 5, 12, 18 gene expression were upregulated and IL-6, NF-kB, TLR3 and 5 were downregulated. Such changes could potentially affect the cells responsiveness to IFN-β and other antiviral inhibitors. Interestingly, favipiravir and oseltamivir showed greater inhibition of IAV when combined with IFN-β treatment - a finding which could not be observed in MDCK cells due to IFN-β treatment increasing IAV replication in this cell line. The observed discrepancies emphasise the necessity of validating findings in primary cells when investigating drugs altering host cell immune responses.

Although prolonged inhibitor treatment can impact cell viability, pre-treating cells for longer than 24 hours may increase efficacy of inhibitors. DNMT inhibitors are presumed to be slow acting, as passive demethylation requires multiple cell cycles (Facciotto *et al.*, 2019). Alternatively, post-infection only inhibitor treatment may identify antivirals directly modifying viral genome, as demonstrated by DZNep's action on SARS-CoV-2 (Kumar *et al.*, 2022). These inhibitors were selected for their known effects on host cell immune responses to infection; however, in recent years more efficient virtual screening approaches have been employed to identify novel inhibitors of avian IAV NA proteins (Cheng *et al.*, 2008; An *et al.*, 2009). Virtual screening utilises a machine-learning approach to structure-based drug discovery, enabling the rapid screening of thousands of compounds and narrowing down potential inhibitors before *in vitro* testing - significantly accelerating the identification of novel antiviral compounds (Lionta *et al.*, 2014).

In summary, this chapter demonstrates that while several epigenetic drugs can inhibit IAV replication, their efficacy is highly dependent on the cell type used. The variability observed across different cell types underscores the importance of selecting appropriate cell models and conducting screenings in multiple cell types to comprehensively assess the potential of antiviral compounds. Among the inhibitors tested, two repurposed anticancer drugs, CM272 and CM579, demonstrated inhibition of IAV replication across multiple cell types, including primary cells. These compounds warrant further investigation, particularly in physiologically relevant models such as 3D ALI cultures, to provide deeper insights into their potential as antiviral inhibitors.

7. Discussion

7.1. Importance of cell type in antiviral inhibitor screening in vitro

Cell types are often selected for *in vitro* antiviral inhibitor screening based off of their permissivity to infection (Dittmar *et al.*, 2021). Immortalised cancer-derived cell lines, such as MDCK, A549, and Calu-3, are frequently used in IAV drug studies (Böttcher-Friebertshäuser *et al.*, 2011; Watanabe *et al.*, 2014, 2017; Courtin *et al.*, 2017; Haasbach *et al.*, 2017). However, these cell lines often exhibit dysregulated antiviral response pathways, leading to enhanced permissivity to infection, even in the presence of known antiviral inhibitors (Stojdl *et al.*, 2000). While these cells are pertinent for virus propagation and infection assays, the biological relevance of using such immortalised or genetically modified cell lines for drug screening is often overlooked (Powell and Waters, 2017; Chua *et al.*, 2019; Ilyushina, Dickensheets and Donnelly, 2019). For example, MDCK cells demonstrate significantly highly permissivity to IAV infection relative to bronchial epithelial cells (Figure 5.11). This mirrors the findings of Charman *et al.* (2021), who demonstrate the increased constitutive expression of immune system genes in bronchial epithelial cells increased restriction of IAV replication in comparison to immortalised cell lines. In particular, the constitutive expression of intrinsic immune factor, TRIM22, was downregulated in laboratory adapted cell lines, resulting in higher permissivity to IAV infection. Their findings demonstrate the more primary-like cells are, the more restrictive they are to IAV infection. Thus, the choice of cell type, particularly considering intrinsic immune factors, should be taken into consideration for IAV infection assays, as different cell types can influence the outcome of infection and efficacy of inhibitors. For example, chapter 6 investigates antiviral efficacy across immortalised canine kidney cells (MDCK), immortalised bronchial epithelial cells (HBEC3-KT), and primary bronchial epithelial cells (HAEC-b). Among the eight successful inhibitors identified in MDCK cells, only three were effective in HBEC3-KT and HAEC-b cells (Table 6.2). This underscores the variability in drug efficacy between cell types, as previously demonstrated by Dittmar *et al.* (2021) when screening direct-acting

and host-directed antivirals using three alternate immortalised cell lines permissive to SARS-CoV-2 infection. The authors demonstrated inhibitory concentrations of antivirals to vary substantially between IFN-deficient human hepatocyte cells (Huh7.5), IFN-deficient African green monkey kidney epithelial cells (Vero), and IFN-producing human bronchial epithelial cells (Calu-3). Interestingly, Dittmar *et al.* (2021) states:

> *"direct-acting antivirals are likely to be active against the virus in multiple cell types… in addition, host-directed antivirals that target key steps in the viral life cycle and are highly conserved and broadly expressed are also likely to emerge across cell types".*

While this proved true for the direct-acting antiviral remdesivir, its efficacy varied between all three cell lines by over 200-fold, and host-directed antivirals failed to show inhibition in all cell lines. The efficacy of host-directed antiviral hydroxychloroquine differed 10-fold between Huh7.5 and Vero cells and showed no inhibition in Calu-3 cells. Additionally, most antivirals demonstrating inhibition in Huh7.5 cells, including histone methyltransferase G9a inhibitors (host-directed antivirals), showed no inhibition in Vero and Calu-3 cells. This illustrates that while antivirals may be active in multiple permissive cell lines, there is significant variability in their efficacy, and their inhibitory effects may be cell type specific. These findings are consistent with the results obtained for both direct-acting and host-directed antivirals presented in this study (Chapter 6).

Favipiravir, a broad-spectrum direct-acting antiviral targeting viral RdRp, only reduced IAV replication in MDCK cells and showed no inhibition in HBEC3-KT or HAEC-b cells (Figure 6.5B). While oseltamivir, a direct-acting antiviral targeting IAV NA, showed dose-dependent inhibition of IAV in all cell types, it achieved only 50% inhibition before showing toxicity in bronchial cells (Figure 6.5C). Zarkoob *et al.* (2022) reported a similar trend in 3D ALI models, showing oseltamivir to only demonstrate a 50% inhibition in IAV replication at 10 μM. Both are licenced antivirals for the treatment of influenza infection. Among the six host-directed inhibitors showing IAV inhibition in MDCK cells, only two compounds, CM272 and CM579, showed inhibition in HBEC3-KT and HAEC-b cells

(Table 6.2). These findings are consistent with those reported by Fang *et al.* (2012), who demonstrated cell type to be important in epigenetic regulation of ISGs expression that influenced their permissivity to viral infection. H3K9me2 was shown to prevent the acetylation of IFN and ISG promoters, downregulating their expression. H3K9me2-mediated IFN and ISG suppression was higher in mouse embryonic fibroblasts compared to splenic dendritic cells, resulting in fibroblasts being more susceptible to viral infection. Inhibition of H3K9me2 by CM272 treatment upregulated IFN and ISG gene expression in fibroblasts, protecting them from infection. Thus, species, tissue, and cell type are particularly important in epigenetic antiviral drug discovery as the epigenetic landscape may significantly vary between cells that directly influences the outcome of this type of small molecule inhibitors and their corresponding impact on the outcome on viral infection.

7.2. Repurposing epigenetic inhibitors as antivirals

The emergence of drug-resistant IAV variants necessitates the development of effective antivirals beyond the direct-acting inhibitors currently available (Watanabe *et al.*, 2014). Epigenetic inhibitors are most well-known for their epigenetic modulation of cancer cells, but their ability to induce ISG expression makes them particularly interesting as candidates for antiviral therapy (Patnaik, Madu and Lu, 2023). Research on repurposing these inhibitors as host-directed antivirals has primarily focussed on DNA viruses, which are heavily subject to epigenetic regulation within host cells, contributing to the establishment of latent infections and subsequent reactivation (Lieberman, 2016; Nehme, Pasquereau and Herbein, 2019). Inhibitors targeting DNMT, HDAC, histone methyltransferase, and histone acetyltransferase have demonstrated both proviral and antiviral regulation of herpes simplex virus 1, adenovirus, human cytomegalovirus, Epstein-Barr virus, Kaposi's sarcoma-associated herpesvirus, HIV, and hepatitis B virus (Nehme, Pasquereau and Herbein, 2019). Notably, inhibitors of histone H3K27 methyltransferase, EZH2 and EZH1, showing inhibition of DNA viruses (herpes simplex virus, cytomegalovirus, and adenovirus) have also been reported to inhibit RNA viruses such as Zika virus (Arbuckle *et al.*, 2017). HDAC inhibitors, SAHA and tubastatin A, have also been shown to

inhibit hepatitis C virus (Sato *et al.*, 2013; Kozlov *et al.*, 2014). Moreover, a recent preprint by Muneer *et al.* (2024) demonstrates the inhibition of G9a histone methyltransferase by compound UNC064 reduced SARS-CoV-2 replication. While the antiviral potential of epigenetic inhibitors for treatment of RNA virus infections has been less well studied relative to DNA viruses, it constitutes a promising area of research currently under investigation.

Among the epigenetic inhibitors tested, CM272 and CM597 stood out for their ability to inhibit IAV replication across all cell types (Figure 6.6A and B). These inhibitors are known for their anti-tumour effects in multiple cancer models (San José-Enériz *et al.*, 2017; Segovia *et al.*, 2019; De Beck *et al.*, 2022; Moreira-Silva *et al.*, 2022). To date, only Tang *et al.* (2023) have explored CM272's antiviral effects, showing that it induced HIV RNA expression, reactivating HIV latency in brain microglia cells isolated from persons with HIV. The antiviral effects of these compounds on IAV replication have not been previously reported. CM272 and CM579 were first synthesised by San José-Enériz *et al.* (2017), where they explored the potential of inhibitors targeting G9a (histone methyltransferase) and DNMT in the treatment of blood cancers. The lead compound, CM272, upregulated ISG expression in a dose-dependent manner by reducing H3K9me2 levels at ISG promoter regions, which inhibited blood cancer cell proliferation and promoted apoptosis *in vitro* and *in vivo*. Transcriptomic analyses by Segovia *et al.* (2019) and De Beck *et al.* (2022) confirmed CM272's ability to upregulate ISGs in bladder and skin cancer cells, showing upregulation in genes of the IFN-α, IFN-γ, and TNF-α signalling pathways, leukocyte and T-cell cytotoxicity, and ubiquitin-dependent protein catabolic processes. Interestingly, seven of the ISGs (IFI44L, EPSTI1, OASL, IFI6, USP18, ABTB2, and IRF7) upregulated by CM272 treatment have previously demonstrated both antiviral and proviral effects on IAV replication, as described in the discussion of Chapter 6. CM272 and CM597 treatment showed dose-dependent inhibition of IAV replication in all cell types, with complete inhibition observed at 10 μM in HBEC3-KT and HAEC-b cells (Figure 6.6A and B). Interestingly, while these inhibitors upregulate IFN pathways, antiviral activity was not further enhanced when combined with IFN-β in HAEC-b cells (Figure 6.7A and B). Previous studies have shown that CM272 retains its inhibitory properties in 3D spheroid models and mice models of multiple cancers,

suggesting that its antiviral effects should be further investigated in 3D ALI cultures (San José-Enériz *et al.*, 2017; Moreira-Silva *et al.*, 2022). If IAV inhibition is confirmed, transcriptomic analysis could reveal gene expression changes in both uninfected and IAV infected cultures treated with the compounds.

While CM272 and CM272 exhibited greater toxicity in HBEC3-KT and MDCK cells relative to HAEC-b cells, this may be attributed to their pro-apoptotic effects in cancer-derived cell lines (Figure 6.6A and B). Despite these concerns, *in vitro* studies by San José-Enériz *et al.* (2017) report low toxicity profiles for CM272 and CM579, with maximum tolerated doses of 2.5 mg/kg^{-1} and 1 mg/kg^{-1}, respectively. *In vivo*, CM272 demonstrated minimal toxicity in mice, with no observable weight loss, indicators of sickness, or alterations of blood/liver components, rendering the compound safe to use in mice. However, its safety profile in humans remains untested and would require thorough evaluation in clinical trials. The ability of CM272 and CM597 to upregulate ISGs and inhibit IAV across multiple cell types, including primary bronchial epithelial cells, combined with low toxicity profiles, suggests these inhibitors hold potential for antiviral therapy. Further studies should focus on screening of larger libraries of G9a histone methyltransferase inhibitors for efficacy against IAV and other RNA viruses, with particular emphasis on validating their effects in more physiologically relevant models.

7.3. Development of novel in vitro 3D cell culture models

As demonstrated throughout this thesis, 2D cell cultures are valuable for initial antiviral inhibitor screening assays *in vitro*. However, their heightened permissivity to infection, dysregulated immune responses, and lack of spatial architecture limits their physiological relevance in modelling the human lung. As a result, many antivirals identified in 2D immortalised cell lines fail to show efficacy in animal models or human clinical trials (Zarkoob *et al.*, 2022). Thus, there is a pressing need to develop *in vitro* models that are predictive of drug efficacy prior to *in vivo* testing. 3D cell cultures, such as ALI, organoid, and lung-on-a-chip systems, have emerged to bridge the gap between 2D cell cultures and

animal models. In particular, primary airway epithelial cells differentiated on ALI cultures show transcriptomic profiles closely resembling that of *in vivo* tissues (Dvorak *et al.*, 2011; Pezzulo *et al.*, 2011). Importantly, 3D cultures demonstrate similar IAV replication kinetics to that of *ex vivo* tissues, and their innate immune responses to IAV infection, cellular polarisation, distribution of SA receptors, and protease secretions closely resemble that of human airway tissue compared to 2D monocultures (M. C. W. Chan *et al.*, 2010; Hui *et al.*, 2018; Zarkoob *et al.*, 2022). Collectively, these findings indicate 3D cell culture models provide a better approximation of IAV infection outcomes in humans compared to 2D cell cultures. Moreover, 3D models have demonstrated great utility in identifying viral receptors, tropism, pathologies, vaccine efficacy, and immune responses to infection previously undetectable in 2D models (Rijsbergen *et al.*, 2021). For instance, 3D ALI cultures were used to investigate the efficacy of LAIV during the 2013-2014 and 2015-2016 seasons, attributing its reduced fitness to restricted multicycle infection in MDCK cells (Hawksworth *et al.*, 2020). Thus, establishing 3D models amenable to drug discovery represents a high priority area of research.

Bioprinting is a rapidly developing tissue engineering approach to automate and customise the fabrication of 3D models (Zhang *et al.*, 2019). The layer-by-layer printing technology enables the precise placement of cells within bioink scaffolds, creating highly reproducible constructs that can model tissue specific architecture (Berg *et al.*, 2018). Bioprinting has been applied to create models for lung, heart, liver, muscle, brain, skin, bone tissues (Ryu *et al.*, 2015; Gao and Cui, 2016; Gu *et al.*, 2016; Daly *et al.*, 2018; H. Lee *et al.*, 2020; Kim *et al.*, 2021). In particular, lung organoids and lung-on-a-chip models have been generated using 3D bioprinting systems with human pluripotent stem cells and primary human tracheal epithelial cells (Huh *et al.*, 2010; Wilkinson *et al.*, 2017; Park *et al.*, 2018). However, despite their potential, 3D bioprinted lung models remain underexplored in IAV research. Berg *et al.* (2018) visualised IAV replication in bioprinted A549 cells stacked in a 3D arrangement within Matrigel scaffolds. Interestingly, they observed that increased Matrigel concentrations impacted the spatial distribution of IAV, permissivity to IAV infection, and immune responses to infection, potentially due to the limited absorption of trypsin required for viral replication. Additionally, the model was viable for only

seven days, a problem often observed when encapsulating cells within hydrogel-based scaffolds (Zhang *et al.*, 2019).

In our collaboration with Cellbricks, we validated a novel bioprinted scaffold for 3D ALI cultures using primary bronchial epithelial cells. We identified a biomaterial that supported the differentiation of HAEC-b cells to comparable levels of that observed in Transwells, and the tissue displayed ciliated, goblet, and basal cells (Figure 3.4, 3.5, and 3.12). Due to the optical transparency of the biomaterial, Membricks demonstrated similar imaging properties to Transwells in 2D and 3D cultures (Figure 3.13 and 3.14). The enhanced imaging properties of Membricks allowed for high resolution imaging of IAV infection in 3D, without embedding and sectioning procedures (Figure 3.16). Together, these findings underscore the potential of bioprinted scaffolds as alternative 3D cell culture models for IAV infection studies and drug discovery.

Although the bioprinted ALI model is a significant step forward, it represents only a small part of the lung in isolation. The absence of immune cells, vascularisation, and other cell types surrounding the epithelial layer limits its biological significance. However, bioprinting technology allows for greater complexity by incorporating these elements into the model. Park *et al.* (2018) developed a more complex bioprinted lung-on-a-chip model by differentiating primary human tracheal epithelial cells under ALI conditions on a biomaterial, surrounded by a functional flowing blood vessel network. Similar approaches could be applied to the Membrick, particularly as the bioink material (GelMA) is amenable to the fabrication of vascular network models (Zhu *et al.*, 2017). Additionally, bioinks can be modified to enhance compatibility with different cell types, opening up the possibility of developing co-culture models. Sellgren *et al.* (2014) developed a non-bioprinted lung-on-a-chip model which supported the differentiation of primary human tracheal epithelial cells under ALI conditions, co-cultured with stacked layers of endothelial cells and fibroblasts. These co-culture approaches should be applied to Membrick ALI cultures, combined with lung-on-a-chip technology, to better recapitulate the complex and dynamic microenvironment of the human lung.

Ideally, the Membrick model would have been utilised for further IAV studies and developed further to increase its complexity; however, supply chain issues led to the use of alternative bioink materials that proved incompatible with ALI conditions (Figure 3.17 and 3.19). This underscores the need to identify and optimise bioinks suitable for 3D cell cultures. Additionally, current bioprinting technologies lack the resolution to accurately print more intricate details of lung structures. I*n vitro* lung modelling still faces significant challenges in recreating the structural, mechanical, and dynamic properties of the human lung, and 3D bioprinting remains in the early stages of exploration (Francis *et al.*, 2022). Despite these challenges, we successfully validated a 3D bioprinted lung model demonstrating similar imaging properties over conventional ALI cultures, which enabled high-resolution imaging of IAV infection within tissues. These advances highlight the potential of bioprinting to enhance currently available tissue culture models for more biologically relevant *in vitro* studies of IAV infection.

7.4. The utility of imaging 3D cell culture models for antiviral drug discovery

Traditional fluorescence imaging of ALI cultures is limited by the reconstruction of individual tissue sections into a larger 3D tissue assembly, leading to a loss of spatial information. Imaging intact 3D tissues offers valuable insights into the spatial dynamics of virus replication within the native tissue architecture, crucial for understanding virus entry, cell tropism, viral clearance, and associated pathologies (Ushakov and Finke, 2023). Imaging techniques were developed to visualise IAV replication throughout the full depth of the tissue without requiring sectioning (Figure 3.16). This allowed for the observation of clusters of IAV replication at different spatial locations within the tissue. Viral replication was observed in the apical layer at 24 hours and in the basal layer at 48 hours (Figure 3.16). Notably, the clustering and predominantly vertical plane spread of IAV in these cultures reflect IAV spread *in vivo* and cannot be observed in 2D cell monolayers restricted to horizontal spread (Yang *et al.*, 2017; Ma *et al.*, 2019; Möckel *et al.*, 2022). The spatial structuring of IAV populations raises questions about how the virus selects which cells to infect. Host cell immune

responses, and the availability of proviral host factors, SA receptors and host proteases, have been implicated in the spatial structuring of IAV populations and host susceptibility to infection (Gallagher *et al.*, 2018). Using 3D ALI cultures, Matrosovich *et al.* (2004) demonstrate human IAV preferentially infects non-ciliated cells deeper in the epithelium, which predominantly express α-2,6-linked SA receptors. By contrast, ciliated cells, expressed mainly α-2,3-linked SA receptors and were more susceptible to avian IAV. Despite this preference, ciliated cells were still infected with human IAV due to high concentrations of virus released from neighbouring cells, and Thompson *et al.* (2006) also confirmed the presence of α-2,6-linked SA receptors on ciliated cells. Additionally, host proteases supporting the multicycle replication of IAV, such as HAT and TMPRSS2, are most highly expressed by ciliated cells (Takahashi *et al.*, 2001; O'Sullivan *et al.*, 2021). This means IAV can replicate in ciliated cells and travel down to its preferred cell type, non-ciliated cells. Future work should involve staining SA receptors and host proteases to determine if the spatial distribution of IAV replication travels in accordance with the distribution of these proviral host factors.

These imaging techniques were also used to evaluate the efficacy of favipiravir in 3D ALI cultures derived from two different donors. While favipiravir treatment successfully inhibited IAV replication in both donors, its efficacy was greater in donor 1 derived tissues, reducing virus replication by two thirds compared to one third in donor 2 tissues (Figure 4.12A and C). Interestingly, donor 2 derived tissues were less permissive to infection, showing a six-fold reduction in total virus volume compared to donor 1 tissues (Figure 4.13). These findings highlight donor variation – a well-documented phenomenon (Rijsbergen *et al.*, 2021). Differential gene expression of IFNs (IFN-α, IFN-ß, IFN-λ), and ISGs (IFIT1, IFIT3, IRF7, MX1, and OAS1), has been documented in ALI cultures from different donors infected with IAV (Mindaye *et al.*, 2017; Ilyushina, Dickensheets and Donnelly, 2019). ALI cultures also demonstrate donor variation in mucus production, which is upregulated in response to IAV infection (Pezzulo *et al.*, 2011; Barbier *et al.*, 2012; Bovard *et al.*, 2020; Bukowy-Bieryłło *et al.*, 2022). These factors can influence IAV replication and antiviral efficacy between donors. A key observation was the altered spatial distribution of IAV replication following favipiravir treatment. In donor 2 derived tissues, two distinct viral

populations emerged at different tissue depths, suggesting favipiravir may alter the spatial distribution of viral replication in a donor-dependent manner (Figure 4.12B and C). Similar findings have been observed with oseltamivir, which restricted IAV replication to localised areas *in vivo* (Manicassamy *et al.*, 2010). These results emphasise the importance of 3D imaging to assess not only overall antiviral efficacy but also how treatment affects viral spread and distribution within tissues.

Despite the success of these imaging techniques, limitations remain. The imaging workflow, based on the expression of a ZsGreen-tagged NS1 protein, assumed correlation with viral replication. BrightFlu fluorescent units demonstrated a correlation to infectious virus titres in MDCK cells, but this was not confirmed in HAEC-b cells (Figure 4.1). However, Mindaye *et al.* (2017) demonstrate IAV infected ALI cultures from three donors produced significantly different expression of viral proteins, NS1, M1, and NP, despite the similar viral titre between donors. Though real-time IAV imaging studies utilise NS1 tags to monitor virus replication, plaque assays should be carried out to quantify infectious virus released from infected tissues (Manicassamy *et al.*, 2010; Möckel *et al.*, 2022). Additionally, the time required to capture high-resolution images and manually process them restricted the number of biological repeats, resulting in an insufficient sample size to draw firm conclusions. Unfortunately, automated imaging methods were unsuccessful due to the presence of mucus on the tissues, impairing optical transparency for continuous real-time measurements (Figure 4.9). Two-photon fluorescence microscopy has been used for automated live cell imaging of IAV infections *in vivo*, and offers less photobleaching and deeper tissue penetration than confocal microscopy (Centonze and White, 1998; Palomino-Segura *et al.*, 2018; Ueki *et al.*, 2020; MacLean *et al.*, 2022). Due to the heterogeneity of IAV populations, capturing whole tissues using lightsheet microscopy would be advantageous. To rapidly acquire images of entire 3D tissues it compromises in resolution subpar to that of confocal imaging, but has shown success in live cell imaging of IAV infections *in vivo* (Bhagwat *et al.*, 2020; Joseph *et al.*, 2022). Additionally, batch-processing of 3D images using automated software like MATLAB or Fiji plugins (e.g. GIANI) could be used to accelerate image analysis, bypassing the need for manual processing and analysis (Barry *et al.*, 2022). By implementing these automated

techniques, the throughput of 3D antiviral screening could be significantly increased. Scaling up the ALI model from 24-well to 96-well formats would allow for larger sample sizes and more robust analysis of antiviral efficacy across multiple donors. Overall, the development of 3D imaging methods allowed for the visualisation of viral spatial dynamics within native tissue architecture and could be applied to assess the impact of antivirals on viral spread and distribution in airway models that utilise cells from multiple donors to explore the impact of sex, age, and ethnicity on the outcome of inhibitors identified to restrict IAV replication.

7.5. Conclusions and Future Work

The rapid development and deployment of effective therapeutics against IAV are crucial for pandemic preparedness. Conventional *in vitro* antiviral screening assays predominantly rely on 2D immortalised cell lines, though they poorly reflect the microenvironment of the human lung and often demonstrate drug efficacy that does not translate well to complex animal models or clinical trials. Here, HAEC-b cells were used in both 2D and 3D culture systems to assess the efficacy of inhibitors against IAV using advanced imaging platforms. 2D antiviral screening assays revealed significant variability in inhibitor efficacy between MDCK, HBEC3-KT, and HAEC-b cells. Established IAV antivirals, favipiravir and oseltamivir, exhibited reduced efficacy in HBEC3-KT and HAEC-b cells relative to MDCK cells. Two repurposed cancer drugs, CM272 and CM579, demonstrated inhibition of IAV replication across all cell types, achieving complete viral inhibition in HAEC-b cells at a concentration of 10 μM, whilst maintaining cell viability. Additionally, two 3D air-liquid interface (ALI) models were established by differentiating HAEC-b cells on novel bioprinted scaffolds and Transwell inserts. These models, combined with advanced imaging techniques, enabled us to visualise the spatial localisation of IAV replication within the native tissue architecture. Favipiravir was shown to inhibit IAV replication and alter the spatial distribution of viral populations, potentially in a donor-dependent manner. Collectively, these findings underscore the importance of screening antiviral inhibitors in biologically relevant *in vitro*

models and highlight the potential of repurposed epigenetic inhibitors as host-directed therapies against IAV.

Future work should further explore the antiviral potential of epigenetic inhibitors, such as CM272 and CM579. Their mechanism of action should be investigated, initially through measuring ISG expression upon inhibitor treatment. These inhibitors demonstrated antiviral efficacy within a small-scale screening; however, increasing the throughput of inhibitor screening experiments would allow for increased numbers of novel inhibitors to be tested, and to explore different combination therapies. Additionally, increasing the pool of donors will allow for the impact of donor variability on the efficacy of antivirals to be studied, and to extend this to the 3D cell culture models established to validate these findings.

Appendices

Appendix A: Effects of epigenetic inhibitors on influenza virus replication across different donors

Since donor variation was observed in 3D ALI cultures (Chapter 4), the inhibitory effects of inhibitors on WSN replication were evaluated between the same two donors using the endpoint assay. HAEC-b cells derived from a 56 year old Hispanic female donor and a 71 year old Caucasian male donor were pre-treated with inhibitors. The experimental procedures and analyses were consistent with those described previously. It should be highlighted that due to time constraints, only one biological replicate was carried out for the male donor. The data from donor 1 cells were combined with donor 2 cell inhibitor data from Figure 6.5 and 6.6 to compare inhibitor efficacy between donors.

Similar inhibitory effects were observed between donors for control inhibitors: favipiravir, oseltamivir, and ruxolitinib (Appendix figure 1B, C, E). Though, favipiravir and oseltamivir decreased cell counts in male donor cells relative to female. IFN-ß showed higher efficacy in donor 1 cells whist maintaining cell counts (Appendix figure 6.8D). Epigenetic inhibitors: CM579, SYC-522, DZNep, JIB-04, JQ1, and OM173-αA showed similar inhibition of IAV between donors (Appendix figure 6.9B, C, D, G, H, I). While CM272 showed dose-dependent inhibition of IAV in both donors, its effects were less pronounced in donor 1 cells (Appendix figure 2A). Interestingly, CM272 decreased cell counts in donor 1 cells, contrasting with donor 2 cells. El1 and EPZ decreased cell counts more in donor 1 cells than donor 2, leading to a decrease in virus positive cells (Appendix figure 2E and F). Together, these findings suggest the efficacy of antiviral inhibitors may be donor-dependent, and more biological repeats should be carried out to confirm these observations.

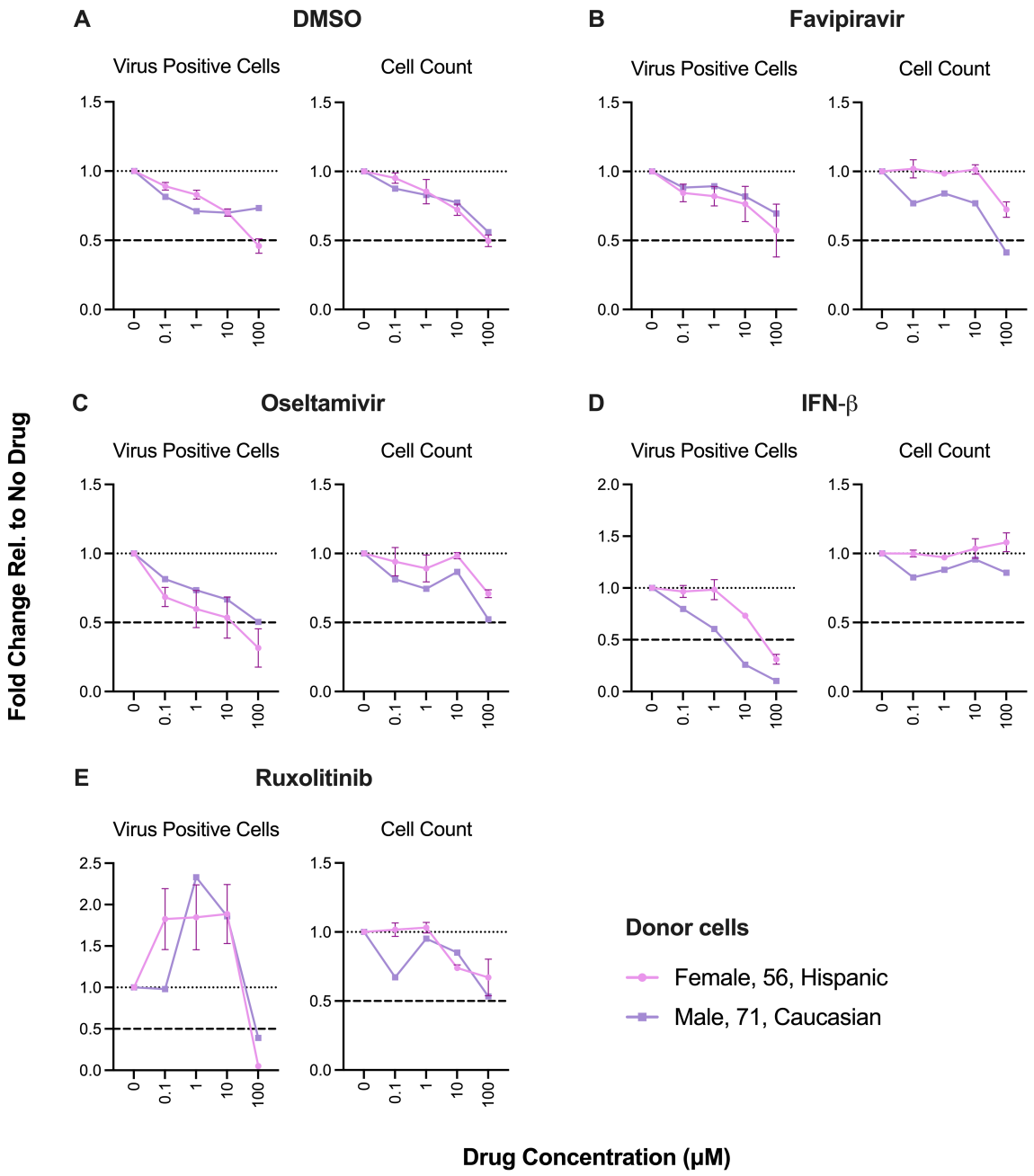

Appendix figure 1: Impact of control inhibitors on WSN replication and cell count across different donors. *HAEC-b cells from donor 1 and 2 were pre-treated with inhibitors for 24 hours, infected with WSN, and post-treated for 24 hours. Cells were fixed, permeabilised, and stained for IAV NP and DAPI. Images were captured at 405 and 488 nm using the Celigo Imaging Cytometer. The total cell counts and number of virus-positive cells were quantified, and fold changes were calculated relative to untreated cells. Left - virus positive cell count, right - total cell count. Pink - Female, 56, Hispanic donor cells purple - male, 71, Caucasian. N = 2 biological replicates for donor 2. Error bars = mean ± 1 SD. N = 1 biological replicate for donor 1.*

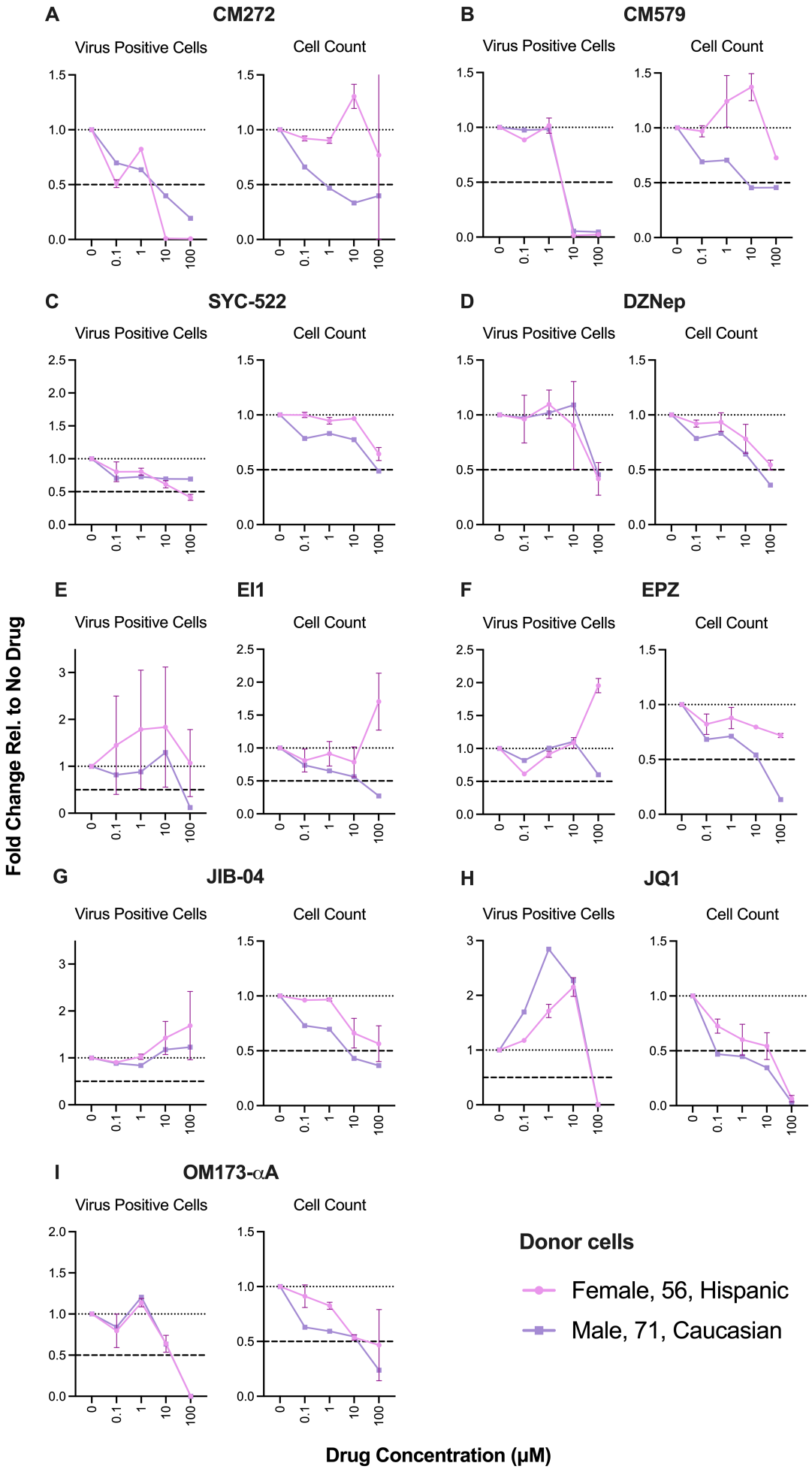
A
CM272
B
CM579
C
SYC-522
D
DZNep
E
EI1
F
EPZ
G
JIB-04
H
JQ1
I
OM173-αA
Virus Positive Cells
Cell Count
Fold Change Rel. to No Drug
Drug Concentration (μM)
Donor cells
Female, 56, Hispanic
Male, 71, Caucasian

Appendix figure 2: Impact of epigenetic inhibitors on WSN replication and cell count across different donors. *HAEC-b cells from donor 1 and 2 were pre-treated with inhibitors for 24 hours, infected with WSN, and post-treated for 24 hours. Cells were fixed, permeabilised, and stained for IAV NP and DAPI. Images were captured at 405 and 488 nm using the Celigo Imaging Cytometer. The total cell counts and number of virus-positive cells were quantified, and fold changes were calculated relative to untreated cells. Left – virus-positive cell count, right – total cell count. Pink – Female, 56, Hispanic donor cells purple – male, 71, Caucasian. N = 2 biological replicates for donor 2. Error bars = mean ± 1 SD. N = 1 biological replicate for donor 1.*

References

Aghayan, H.-R., Goodarzi, P. and Arjmand, B. (2015) 'GMP-Compliant Human Adipose Tissue-Derived Mesenchymal Stem Cells for Cellular Therapy', in K. Turksen (ed.) *Stem Cells and Good Manufacturing Practices: Methods, Protocols, and Regulations*. New York, NY: Springer, pp. 93–107. Available at: https://doi.org/10.1007/7651_2014_112.

Alam, S.T. *et al.* (2021) 'Challenges to COVID-19 vaccine supply chain: Implications for sustainable development goals', *International Journal of Production Economics*, 239, p. 108193. Available at: https://doi.org/10.1016/j.ijpe.2021.108193.

Alexopoulou, L. *et al.* (2001) 'Recognition of double-stranded RNA and activation of NF-kappaB by Toll-like receptor 3', *Nature*, 413(6857), pp. 732–738. Available at: https://doi.org/10.1038/35099560.

Ali, S.T. *et al.* (2022) 'Prediction of upcoming global infection burden of influenza seasons after relaxation of public health and social measures during the COVID-19 pandemic: a modelling study', *The Lancet Global Health*, 10(11), pp. e1612–e1622. Available at: https://doi.org/10.1016/S2214-109X(22)00358-8.

Amler, A.-K. *et al.* (2021) '3D bioprinting of tissue-specific osteoblasts and endothelial cells to model the human jawbone', *Scientific Reports*, 11(1), p. 4876. Available at: https://doi.org/10.1038/s41598-021-84483-4.

Amorim, M.J. *et al.* (2011) 'A Rab11- and Microtubule-Dependent Mechanism for Cytoplasmic Transport of Influenza A Virus Viral RNA', *Journal of Virology*, 85(9), pp. 4143–4156. Available at: https://doi.org/10.1128/jvi.02606-10.

An, J. *et al.* (2009) 'A novel small-molecule inhibitor of the avian influenza H5N1 virus determined through computational screening against the neuraminidase', *Journal of Medicinal Chemistry*, 52(9), pp. 2667–2672. Available at: https://doi.org/10.1021/jm800455g.

Aoki, F.Y. *et al.* (2003) 'Early administration of oral oseltamivir increases the benefits of influenza treatment', *The Journal of Antimicrobial Chemotherapy*, 51(1), pp. 123–129. Available at: https://doi.org/10.1093/jac/dkg007.

Arbuckle, J.H. *et al.* (2017) 'Inhibitors of the Histone Methyltransferases EZH2/1 Induce a Potent Antiviral State and Suppress Infection by Diverse Viral Pathogens', *mBio*, 8(4), pp. e01141-17. Available at: https://doi.org/10.1128/mBio.01141-17.

Assou, S. *et al.* (2023) 'The Transcriptome Landscape of the In Vitro Human Airway Epithelium Response to SARS-CoV-2', *International Journal of Molecular Sciences*, 24(15), p. 12017. Available at: https://doi.org/10.3390/ijms241512017.

Awatade, N.T. *et al.* (2023) 'Comparison of commercially available differentiation media on cell morphology, function, and anti-viral responses in conditionally reprogrammed human bronchial epithelial cells', *Scientific*

Reports, 13(1), p. 11200. Available at: https://doi.org/10.1038/s41598-023-37828-0.

Bai, H. *et al.* (2022) 'Mechanical control of innate immune responses against viral infection revealed in a human lung alveolus chip', *Nature Communications*, 13(1), p. 1928. Available at: https://doi.org/10.1038/s41467-022-29562-4.

Baker, R.E. *et al.* (2020) 'The impact of COVID-19 nonpharmaceutical interventions on the future dynamics of endemic infections', *Proceedings of the National Academy of Sciences of the United States of America*, 117(48), pp. 30547–30553. Available at: https://doi.org/10.1073/pnas.2013182117.

Balharry, D., Sexton, K. and BéruBé, K.A. (2008) 'An in vitro approach to assess the toxicity of inhaled tobacco smoke components: Nicotine, cadmium, formaldehyde and urethane', *Toxicology*, 244(1), pp. 66–76. Available at: https://doi.org/10.1016/j.tox.2007.11.001.

Banerjee, I. *et al.* (2014) 'Influenza A virus uses the aggresome processing machinery for host cell entry', *Science*, 346(6208), pp. 473–477. Available at: https://doi.org/10.1126/science.1257037.

Baranovich, T. *et al.* (2010) 'Emergence of H274Y oseltamivir-resistant A(H1N1) influenza viruses in Japan during the 2008-2009 season', *Journal of Clinical Virology: The Official Publication of the Pan American Society for Clinical Virology*, 47(1), pp. 23–28. Available at: https://doi.org/10.1016/j.jcv.2009.11.003.

Baranovich, T. *et al.* (2013) 'T-705 (Favipiravir) Induces Lethal Mutagenesis in Influenza A H1N1 Viruses In Vitro', *Journal of Virology*, 87(7), pp. 3741–3751. Available at: https://doi.org/10.1128/jvi.02346-12.

Barbier, D. *et al.* (2012) 'Influenza A Induces the Major Secreted Airway Mucin MUC5AC in a Protease–EGFR–Extracellular Regulated Kinase–Sp1–Dependent Pathway', *American Journal of Respiratory Cell and Molecular Biology*, 47(2), pp. 149–157. Available at: https://doi.org/10.1165/rcmb.2011-0405OC.

Barr, I.G. and Subbarao, K. (2024) 'Implications of the apparent extinction of B/Yamagata-lineage human influenza viruses', *npj Vaccines*, 9(1), pp. 1–3. Available at: https://doi.org/10.1038/s41541-024-01010-y.

Barry, D.J. *et al.* (2022) 'GIANI – open-source software for automated analysis of 3D microscopy images', *Journal of Cell Science*, 135(10), p. jcs259511. Available at: https://doi.org/10.1242/jcs.259511.

Bashtrykov, P. *et al.* (2014) 'The UHRF1 Protein Stimulates the Activity and Specificity of the Maintenance DNA Methyltransferase DNMT1 by an Allosteric Mechanism', *The Journal of Biological Chemistry*, 289(7), pp. 4106–4115. Available at: https://doi.org/10.1074/jbc.M113.528893.

Baxter, R. *et al.* (2011) 'Evaluation of the safety, reactogenicity and immunogenicity of FluBlok® trivalent recombinant baculovirus-expressed hemagglutinin influenza vaccine administered intramuscularly to healthy adults 50-64 years of age', *Vaccine*, 29(12), pp. 2272–2278. Available at: https://doi.org/10.1016/j.vaccine.2011.01.039.

Beghein, E. and Gettemans, J. (2017) 'Nanobody Technology: A Versatile Toolkit for Microscopic Imaging, Protein–Protein Interaction Analysis, and Protein Function Exploration', *Frontiers in Immunology*, 8, p. 771. Available at: https://doi.org/10.3389/fimmu.2017.00771.

Bekkat-Berkani, R. *et al.* (2016) 'Evidence update: GlaxoSmithKline's inactivated quadrivalent influenza vaccines', *Expert Review of Vaccines*, 15(2), pp. 201–214. Available at: https://doi.org/10.1586/14760584.2016.1113878.

Belser, J.A. *et al.* (2007) 'DAS181, a novel sialidase fusion protein, protects mice from lethal avian influenza H5N1 virus infection', *The Journal of Infectious Diseases*, 196(10), pp. 1493–1499. Available at: https://doi.org/10.1086/522609.

Belser, J.A. *et al.* (2016) 'Complexities in Ferret Influenza Virus Pathogenesis and Transmission Models', *Microbiology and Molecular Biology Reviews*, 80(3), pp. 733–744. Available at: https://doi.org/10.1128/mmbr.00022-16.

Benam, K.H., Novak, R., *et al.* (2016) 'Matched-Comparative Modeling of Normal and Diseased Human Airway Responses Using a Microengineered Breathing Lung Chip', *Cell Systems*, 3(5), pp. 456-466.e4. Available at: https://doi.org/10.1016/j.cels.2016.10.003.

Benam, K.H., Villenave, R., *et al.* (2016) 'Small airway-on-a-chip enables analysis of human lung inflammation and drug responses in vitro', *Nature Methods*, 13(2), pp. 151–157. Available at: https://doi.org/10.1038/nmeth.3697.

Bennet, T.J. *et al.* (2021) 'Airway-On-A-Chip: Designs and Applications for Lung Repair and Disease', *Cells*, 10(7), p. 1602. Available at: https://doi.org/10.3390/cells10071602.

Berg, J. *et al.* (2018) 'Optimization of cell-laden bioinks for 3D bioprinting and efficient infection with influenza A virus', *Scientific Reports*, 8, p. 13877. Available at: https://doi.org/10.1038/s41598-018-31880-x.

Bertram, S. *et al.* (2010) 'Novel insights into proteolytic cleavage of influenza virus hemagglutinin', *Reviews in Medical Virology*, 20(5), pp. 298–310. Available at: https://doi.org/10.1002/rmv.657.

Bertrams, W. *et al.* (2022) 'Transcriptomic comparison of primary human lung cells with lung tissue samples and the human A549 lung cell line highlights cell type specific responses during infections with influenza A virus', *Scientific Reports*, 12(1), p. 20608. Available at: https://doi.org/10.1038/s41598-022-24792-4.

BéruBé, K. *et al.* (2010) 'Human primary bronchial lung cell constructs: The new respiratory models', *Toxicology*, 278(3), pp. 311–318. Available at: https://doi.org/10.1016/j.tox.2010.04.004.

Bhagwat, A.R. *et al.* (2020) 'Quantitative live cell imaging reveals influenza virus manipulation of Rab11A transport through reduced dynein association', *Nature Communications*, 11(1), p. 23. Available at: https://doi.org/10.1038/s41467-019-13838-3.

Bhatia, S.N. and Ingber, D.E. (2014) ‘Microfluidic organs-on-chips’, *Nature Biotechnology*, 32(8), pp. 760–772. Available at: https://doi.org/10.1038/nbt.2989.

Bhowmick, R. *et al.* (2018) ‘A Three-Dimensional Human Tissue-Engineered Lung Model to Study Influenza A Infection’, *Tissue Engineering. Part A*, 24(19–20), pp. 1468–1480. Available at: https://doi.org/10.1089/ten.tea.2017.0449.

Bieniasz, P.D. (2004) ‘Intrinsic immunity: a front-line defense against viral attack’, *Nature Immunology*, 5(11), pp. 1109–1115. Available at: https://doi.org/10.1038/ni1125.

Blaising, J., Polyak, S.J. and Pécheur, E.-I. (2014) ‘Arbidol as a broad-spectrum antiviral: An update’, *Antiviral Research*, 107, pp. 84–94. Available at: https://doi.org/10.1016/j.antiviral.2014.04.006.

Bloom, J.D., Gong, L.I. and Baltimore, D. (2010) ‘Permissive Secondary Mutations Enable the Evolution of Influenza Oseltamivir Resistance’, *Science*, 328(5983), pp. 1272–1275. Available at: https://doi.org/10.1126/science.1187816.

Both, G.W. *et al.* (1983) ‘Antigenic drift in influenza virus H3 hemagglutinin from 1968 to 1980: multiple evolutionary pathways and sequential amino acid changes at key antigenic sites.’, *Journal of Virology*, 48(1), pp. 52–60.

Böttcher, C. *et al.* (1999) ‘Structure of influenza haemagglutinin at neutral and at fusogenic pH by electron cryo-microscopy’, *FEBS Letters*, 463(3), pp. 255–259. Available at: https://doi.org/10.1016/S0014-5793(99)01475-1.

Böttcher, E. *et al.* (2006) ‘Proteolytic Activation of Influenza Viruses by Serine Proteases TMPRSS2 and HAT from Human Airway Epithelium’, *Journal of Virology*, 80(19), pp. 9896–9898. Available at: https://doi.org/10.1128/JVI.01118-06.

Böttcher-Friebertshäuser, E. *et al.* (2010) ‘Cleavage of Influenza Virus Hemagglutinin by Airway Proteases TMPRSS2 and HAT Differs in Subcellular Localization and Susceptibility to Protease Inhibitors’, *Journal of Virology*, 84(11), pp. 5605–5614. Available at: https://doi.org/10.1128/JVI.00140-10.

Böttcher-Friebertshäuser, E. *et al.* (2011) ‘Inhibition of Influenza Virus Infection in Human Airway Cell Cultures by an Antisense Peptide-Conjugated Morpholino Oligomer Targeting the Hemagglutinin-Activating Protease TMPRSS2’, *Journal of Virology*, 85(4), pp. 1554–1562. Available at: https://doi.org/10.1128/JVI.01294-10.

Bouvier, N.M. and Palese, P. (2008) ‘THE BIOLOGY OF INFLUENZA VIRUSES’, *Vaccine*, 26(Suppl 4), pp. D49–D53.

Bovard, D. *et al.* (2020) ‘Comparison of the basic morphology and function of 3D lung epithelial cultures derived from several donors’, *Current Research in Toxicology*, 1, pp. 56–69. Available at: https://doi.org/10.1016/j.crtox.2020.08.002.

Bowman, G.D. and Poirier, M.G. (2015) 'Post-Translational Modifications of Histones That Influence Nucleosome Dynamics', *Chemical Reviews*, 115(6), pp. 2274–2295. Available at: https://doi.org/10.1021/cr500350x.

Boyoglu-Barnum, S. *et al.* (2021) 'Quadrivalent influenza nanoparticle vaccines induce broad protection', *Nature*, 592(7855), pp. 623–628. Available at: https://doi.org/10.1038/s41586-021-03365-x.

Brass, A.L. *et al.* (2009) 'IFITM Proteins Mediate the Innate Immune Response to Influenza A H1N1 Virus, West Nile Virus and Dengue Virus', *Cell*, 139(7), pp. 1243–1254. Available at: https://doi.org/10.1016/j.cell.2009.12.017.

Bray, M. *et al.* (2002) '3-Deazaneplanocin A induces massively increased interferon-α production in Ebola virus-infected mice', *Antiviral Research*, 55(1), pp. 151–159. Available at: https://doi.org/10.1016/S0166-3542(02)00018-9.

Breslin, S. and O'Driscoll, L. (2016) 'The relevance of using 3D cell cultures, in addition to 2D monolayer cultures, when evaluating breast cancer drug sensitivity and resistance', *Oncotarget*, 7(29), pp. 45745–45756. Available at: https://doi.org/10.18632/oncotarget.9935.

Bright, R.A. *et al.* (2006) 'Adamantane resistance among influenza A viruses isolated early during the 2005-2006 influenza season in the United States', *JAMA*, 295(8), pp. 891–894. Available at: https://doi.org/10.1001/jama.295.8.joc60020.

Brown, E.G. (2000) 'Influenza virus genetics', *Biomedicine & Pharmacotherapy*, 54(4), pp. 196–209. Available at: https://doi.org/10.1016/S0753-3322(00)89026-5.

Brown, L. *et al.* (2023) 'Cost of illness of the vaccine-preventable diseases influenza, herpes zoster and pneumococcal disease in France', *The European Journal of Public Health*, 34(1), pp. 170–175. Available at: https://doi.org/10.1093/eurpub/ckad212.

Bui, M., Whittaker, G. and Helenius, A. (1996) 'Effect of M1 protein and low pH on nuclear transport of influenza virus ribonucleoproteins', *Journal of Virology*, 70(12), pp. 8391–8401. Available at: https://doi.org/10.1128/JVI.70.12.8391-8401.1996.

Bukowy-Bieryłło, Z. *et al.* (2022) '*In vitro* differentiation of ciliated cells in ALI-cultured human airway epithelium – The framework for functional studies on airway differentiation in ciliopathies', *European Journal of Cell Biology*, 101(1), p. 151189. Available at: https://doi.org/10.1016/j.ejcb.2021.151189.

Bullough, P.A. *et al.* (1994) 'Structure of influenza haemagglutinin at the pH of membrane fusion', *Nature*, 371(6492), pp. 37–43. Available at: https://doi.org/10.1038/371037a0.

Button, B. *et al.* (2012) 'A periciliary brush promotes the lung health by separating the mucus layer from airway epithelia', *Science (New York, N.Y.)*, 337(6097), pp. 937–941. Available at: https://doi.org/10.1126/science.1223012.

Byrn, R.A. *et al.* (2015) 'Preclinical activity of VX-787, a first-in-class, orally bioavailable inhibitor of the influenza virus polymerase PB2 subunit', *Antimicrobial Agents and Chemotherapy*, 59(3), pp. 1569–1582. Available at: https://doi.org/10.1128/AAC.04623-14.

Cacciamali, A., Villa, R. and Dotti, S. (2022) '3D Cell Cultures: Evolution of an Ancient Tool for New Applications', *Frontiers in Physiology*, 13, p. 836480. Available at: https://doi.org/10.3389/fphys.2022.836480.

Cai, C. *et al.* (2022) 'The RING finger protein family in health and disease', *Signal Transduction and Targeted Therapy*, 7(1), pp. 1–23. Available at: https://doi.org/10.1038/s41392-022-01152-2.

Capellini, F.M. *et al.* (2020) 'Characterization of MDCK cells and evaluation of their ability to respond to infectious and non-infectious stressors', *Cytotechnology*, 72(1), pp. 97–109. Available at: https://doi.org/10.1007/s10616-019-00360-z.

Carrat, F. and Flahault, A. (2007) 'Influenza vaccine: The challenge of antigenic drift', *Vaccine*, 25(39), pp. 6852–6862. Available at: https://doi.org/10.1016/j.vaccine.2007.07.027.

Carter, N.J. and Curran, M.P. (2011) 'Live attenuated influenza vaccine (FluMist®; Fluenz™): a review of its use in the prevention of seasonal influenza in children and adults', *Drugs*, 71(12), pp. 1591–1622. Available at: https://doi.org/10.2165/11206860-000000000-00000.

Caserta, L.C. *et al.* (2024) 'Spillover of highly pathogenic avian influenza H5N1 virus to dairy cattle', *Nature*, pp. 1–8. Available at: https://doi.org/10.1038/s41586-024-07849-4.

Caspard, H. *et al.* (2017) 'Live-Attenuated Influenza Vaccine Effectiveness in Children From 2009 to 2015–2016: A Systematic Review and Meta-Analysis', *Open Forum Infectious Diseases*, 4(3), p. ofx111. Available at: https://doi.org/10.1093/ofid/ofx111.

de Castro Martin, I.F. *et al.* (2017) 'Influenza virus genome reaches the plasma membrane via a modified endoplasmic reticulum and Rab11-dependent vesicles', *Nature Communications*, 8(1), p. 1396. Available at: https://doi.org/10.1038/s41467-017-01557-6.

Centers for Disease Control and Prevention (2023) *Influenza Antiviral Medications: Clinician Summary*, *Centers for Disease Control and Prevention*. Available at: https://www.cdc.gov/flu/professionals/antivirals/summary-clinicians.htm (Accessed: 14 August 2024).

Centers for Disease Control and Prevention (2024) *Technical Report: June 2024 Highly Pathogenic Avian Influenza A(H5N1) Viruses*, *Avian Influenza (Bird Flu)*. Available at: https://www.cdc.gov/bird-flu/php/technical-report/h5n1-06052024.html (Accessed: 4 September 2024).

Centonze, V.E. and White, J.G. (1998) 'Multiphoton excitation provides optical sections from deeper within scattering specimens than confocal imaging',

Biophysical Journal, 75(4), pp. 2015–2024. Available at: https://doi.org/10.1016/S0006-3495(98)77643-X.

Chai, N. *et al.* (2016) 'Two Escape Mechanisms of Influenza A Virus to a Broadly Neutralizing Stalk-Binding Antibody', *PLoS pathogens*, 12(6), p. e1005702. Available at: https://doi.org/10.1371/journal.ppat.1005702.

Chan, G.K.Y. *et al.* (2013) 'A simple high-content cell cycle assay reveals frequent discrepancies between cell number and ATP and MTS proliferation assays', *PloS One*, 8(5), p. e63583. Available at: https://doi.org/10.1371/journal.pone.0063583.

Chan, M.C.W. *et al.* (2010) 'Tropism and Innate Host Responses of the 2009 Pandemic H1N1 Influenza Virus in ex Vivo and in Vitro Cultures of Human Conjunctiva and Respiratory Tract', *The American Journal of Pathology*, 176(4), pp. 1828–1840. Available at: https://doi.org/10.2353/ajpath.2010.091087.

Chan, R.W.Y. *et al.* (2009) 'DAS181 Inhibits H5N1 Influenza Virus Infection of Human Lung Tissues', *Antimicrobial Agents and Chemotherapy*, 53(9), pp. 3935–3941. Available at: https://doi.org/10.1128/AAC.00389-09.

Chan, R.W.Y. *et al.* (2010) 'Influenza H5N1 and H1N1 Virus Replication and Innate Immune Responses in Bronchial Epithelial Cells Are Influenced by the State of Differentiation', *PLOS ONE*, 5(1), p. e8713. Available at: https://doi.org/10.1371/journal.pone.0008713.

Chan, W. *et al.* (2008) 'The cold adapted and temperature sensitive influenza A/Ann Arbor/6/60 virus, the master donor virus for live attenuated influenza vaccines, has multiple defects in replication at the restrictive temperature', *Virology*, 380(2), pp. 304–311. Available at: https://doi.org/10.1016/j.virol.2008.07.027.

Charman, M. *et al.* (2021) 'Constitutive TRIM22 Expression in the Respiratory Tract Confers a Pre-Existing Defence Against Influenza A Virus Infection', *Frontiers in Cellular and Infection Microbiology*, 11, p. 689707. Available at: https://doi.org/10.3389/fcimb.2021.689707.

Chen, J. *et al.* (1998) 'Structure of the Hemagglutinin Precursor Cleavage Site, a Determinant of Influenza Pathogenicity and the Origin of the Labile Conformation', *Cell*, 95(3), pp. 409–417. Available at: https://doi.org/10.1016/S0092-8674(00)81771-7.

Chen, J. *et al.* (2022) 'TBK1-METTL3 axis facilitates antiviral immunity', *Cell Reports*, 38(7). Available at: https://doi.org/10.1016/j.celrep.2022.110373.

Chen, K.-Y. *et al.* (2019) 'Influenza virus polymerase subunits co-evolve to ensure proper levels of dimerization of the heterotrimer', *PLOS Pathogens*, 15(10), p. e1008034. Available at: https://doi.org/10.1371/journal.ppat.1008034.

Chen, L. *et al.* (2017) 'Histone Deacetylase 1 Plays an Acetylation-Independent Role in Influenza A Virus Replication', *Frontiers in Immunology*, 8. Available at: https://doi.org/10.3389/fimmu.2017.01757.

Chen, R. and Holmes, E.C. (2008) ‘The evolutionary dynamics of human influenza B virus’, *Journal of Molecular Evolution*, 66(6), pp. 655–663. Available at: https://doi.org/10.1007/s00239-008-9119-z.

Chen, X. *et al.* (2018) ‘Host Immune Response to Influenza A Virus Infection’, *Frontiers in Immunology*, 9, p. 320. Available at: https://doi.org/10.3389/fimmu.2018.00320.

Cheng, L.S. *et al.* (2008) ‘Ensemble-Based Virtual Screening Reveals Potential Novel Antiviral Compounds for Avian Influenza Neuraminidase’, *Journal of Medicinal Chemistry*, 51(13), pp. 3878–3894. Available at: https://doi.org/10.1021/jm8001197.

Cheng, Y. *et al.* (2019) ‘Targeting epigenetic regulators for cancer therapy: mechanisms and advances in clinical trials’, *Signal Transduction and Targeted Therapy*, 4(1), pp. 1–39. Available at: https://doi.org/10.1038/s41392-019-0095-0.

Chokki, M. *et al.* (2004) ‘Human Airway Trypsin-Like Protease Increases Mucin Gene Expression in Airway Epithelial Cells’, *American Journal of Respiratory Cell and Molecular Biology*, 30(4), pp. 470–478. Available at: https://doi.org/10.1165/rcmb.2003-0199OC.

Chua, S.C.J.H. *et al.* (2019) ‘Alternative Experimental Models for Studying Influenza Proteins, Host–Virus Interactions and Anti-Influenza Drugs’, *Pharmaceuticals*, 12(4), p. 147. Available at: https://doi.org/10.3390/ph12040147.

Claas, E.C. *et al.* (1998) ‘Human influenza A H5N1 virus related to a highly pathogenic avian influenza virus’, *Lancet (London, England)*, 351(9101), pp. 472–477. Available at: https://doi.org/10.1016/S0140-6736(97)11212-0.

Clark, M.P. *et al.* (2014) ‘Discovery of a novel, first-in-class, orally bioavailable azaindole inhibitor (VX-787) of influenza PB2’, *Journal of Medicinal Chemistry*, 57(15), pp. 6668–6678. Available at: https://doi.org/10.1021/jm5007275.

Cohen, M. *et al.* (2013) ‘Influenza A penetrates host mucus by cleaving sialic acids with neuraminidase’, *Virology Journal*, 10, p. 321. Available at: https://doi.org/10.1186/1743-422X-10-321.

Collins, P.J. *et al.* (2009) ‘Structural basis for oseltamivir resistance of influenza viruses’, *Vaccine*, 27(45), pp. 6317–6323. Available at: https://doi.org/10.1016/j.vaccine.2009.07.017.

Commission on a Global Health Risk Framework for the Future and National Academy of Medicine, Secretariat (2016) *The Neglected Dimension of Global Security: A Framework to Counter Infectious Disease Crises*. Washington (DC): National Academies Press (US). Available at: http://www.ncbi.nlm.nih.gov/books/NBK368394/ (Accessed: 4 September 2024).

Copeland, C.S. *et al.* (1986) ‘Assembly of influenza hemagglutinin trimers and its role in intracellular transport.’, *Journal of Cell Biology*, 103(4), pp. 1179–1191. Available at: https://doi.org/10.1083/jcb.103.4.1179.

Couceiro, J.N., Paulson, J.C. and Baum, L.G. (1993) 'Influenza virus strains selectively recognize sialyloligosaccharides on human respiratory epithelium; the role of the host cell in selection of hemagglutinin receptor specificity', *Virus Research*, 29(2), pp. 155–165. Available at: https://doi.org/10.1016/0168-1702(93)90056-s.

Courtin, N. *et al.* (2017) 'Antiviral activity of formyl peptide receptor 2 antagonists against influenza viruses', *Antiviral Research*, 143, pp. 252–261. Available at: https://doi.org/10.1016/j.antiviral.2017.05.001.

Courtney, D.G. *et al.* (2017) 'Epitranscriptomic enhancement of influenza A virus gene expression and replication', *Cell host & microbe*, 22(3), pp. 377–386.e5. Available at: https://doi.org/10.1016/j.chom.2017.08.004.

Cox, M.M.J., Patriarca, P.A. and Treanor, J. (2008) 'FluBlok, a recombinant hemagglutinin influenza vaccine', *Influenza and Other Respiratory Viruses*, 2(6), pp. 211–219. Available at: https://doi.org/10.1111/j.1750-2659.2008.00053.x.

Cox, N.J. and Fukuda, K. (1998) 'Influenza', *Infectious Disease Clinics of North America*, 12(1), pp. 27–38. Available at: https://doi.org/10.1016/s0891-5520(05)70406-2.

Cox, N.J. and Subbarao, K. (2000) 'Global epidemiology of influenza: past and present', *Annual Review of Medicine*, 51, pp. 407–421. Available at: https://doi.org/10.1146/annurev.med.51.1.407.

Cros, J.F. and Palese, P. (2003) 'Trafficking of viral genomic RNA into and out of the nucleus: influenza, Thogoto and Borna disease viruses', *Virus Research*, 95(1), pp. 3–12. Available at: https://doi.org/10.1016/S0168-1702(03)00159-X.

Cusack, M. *et al.* (2020) 'Distinct contributions of DNA methylation and histone acetylation to the genomic occupancy of transcription factors', *Genome Research*, 30(10), pp. 1393–1406. Available at: https://doi.org/10.1101/gr.257576.119.

Dahmani, I., Ludwig, K. and Chiantia, S. (2019) 'Influenza A matrix protein M1 induces lipid membrane deformation via protein multimerization', *Bioscience Reports*, 39(8), p. BSR20191024. Available at: https://doi.org/10.1042/BSR20191024.

Daly, A.C. *et al.* (2018) '3D printed microchannel networks to direct vascularisation during endochondral bone repair', *Biomaterials*, 162, pp. 34–46. Available at: https://doi.org/10.1016/j.biomaterials.2018.01.057.

Daniels, R.S. *et al.* (1985) 'Fusion mutants of the influenza virus hemagglutinin glycoprotein', *Cell*, 40(2), pp. 431–439. Available at: https://doi.org/10.1016/0092-8674(85)90157-6.

Davis, A.S. *et al.* (2015) 'Validation of Normal Human Bronchial Epithelial Cells as a Model for Influenza A Infections in Human Distal Trachea', *Journal of Histochemistry & Cytochemistry*, 63(5), pp. 312–328. Available at: https://doi.org/10.1369/0022155415570968.

De Beck, L. *et al.* (2022) 'Inhibiting Histone and DNA Methylation Improves Cancer Vaccination in an Experimental Model of Melanoma', *Frontiers in Immunology*, 13. Available at: https://doi.org/10.3389/fimmu.2022.799636.

DeDiego, M.L., Martinez-Sobrido, L. and Topham, D.J. (2019) 'Novel Functions of IFI44L as a Feedback Regulator of Host Antiviral Responses', *Journal of Virology*, 93(21), pp. e01159-19. Available at: https://doi.org/10.1128/JVI.01159-19.

Desai, T.M. *et al.* (2014) 'IFITM3 Restricts Influenza A Virus Entry by Blocking the Formation of Fusion Pores following Virus-Endosome Hemifusion', *PLOS Pathogens*, 10(4), p. e1004048. Available at: https://doi.org/10.1371/journal.ppat.1004048.

Di Pietro, A. *et al.* (2013) 'TRIM22 Inhibits Influenza A Virus Infection by Targeting the Viral Nucleoprotein for Degradation', *Journal of Virology*, 87(8), pp. 4523–4533. Available at: https://doi.org/10.1128/JVI.02548-12.

Dias, A. *et al.* (2009) 'The cap-snatching endonuclease of influenza virus polymerase resides in the PA subunit', *Nature*, 458(7240), pp. 914–918. Available at: https://doi.org/10.1038/nature07745.

Diebold, S.S. *et al.* (2004) 'Innate Antiviral Responses by Means of TLR7-Mediated Recognition of Single-Stranded RNA', *Science*, 303(5663), pp. 1529–1531. Available at: https://doi.org/10.1126/science.1093616.

Digard, P. *et al.* (1999) 'Modulation of Nuclear Localization of the Influenza Virus Nucleoprotein through Interaction with Actin Filaments', *Journal of Virology*, 73(3), pp. 2222–2231. Available at: https://doi.org/10.1128/jvi.73.3.2222-2231.1999.

DiLillo, D.J. *et al.* (2014) 'Broadly neutralizing hemagglutinin stalk-specific antibodies require FcγR interactions for protection against influenza virus in vivo', *Nature Medicine*, 20(2), pp. 143–151. Available at: https://doi.org/10.1038/nm.3443.

Dittmar, M. *et al.* (2021) 'Drug repurposing screens reveal cell-type-specific entry pathways and FDA-approved drugs active against SARS-Cov-2', *Cell Reports*, 35(1), p. 108959. Available at: https://doi.org/10.1016/j.celrep.2021.108959.

Dobson, J. *et al.* (2015) 'Oseltamivir treatment for influenza in adults: a meta-analysis of randomised controlled trials', *The Lancet*, 385(9979), pp. 1729–1737. Available at: https://doi.org/10.1016/S0140-6736(14)62449-1.

Domingo, E. (1997) 'Rapid evolution of viral RNA genomes', *The Journal of Nutrition*, 127(5 Suppl), pp. 958S-961S. Available at: https://doi.org/10.1093/jn/127.5.958S.

van Doorn, E. *et al.* (2017) 'Evaluating the immunogenicity and safety of a BiondVax-developed universal influenza vaccine (Multimeric-001) either as a standalone vaccine or as a primer to H5N1 influenza vaccine: Phase IIb study protocol', *Medicine*, 96(11), p. e6339. Available at: https://doi.org/10.1097/MD.0000000000006339.

Dou, D. *et al.* (2018) 'Influenza A Virus Cell Entry, Replication, Virion Assembly and Movement', *Frontiers in Immunology*, 9. Available at: https://doi.org/10.3389/fimmu.2018.01581.

Drake, J.W. (1993) 'Rates of spontaneous mutation among RNA viruses', *Proceedings of the National Academy of Sciences of the United States of America*, 90(9), pp. 4171–4175. Available at: https://doi.org/10.1073/pnas.90.9.4171.

Drake, J.W. and Holland, J.J. (1999) 'Mutation rates among RNA viruses', *Proceedings of the National Academy of Sciences of the United States of America*, 96(24), pp. 13910–13913.

Du, X. *et al.* (2020) 'Direct inhibitory effect on viral entry of influenza A and SARS-CoV-2 viruses by azithromycin', *Cell Proliferation*, 54(1), p. e12953. Available at: https://doi.org/10.1111/cpr.12953.

DuBois, R.M. *et al.* (2011) 'Acid Stability of the Hemagglutinin Protein Regulates H5N1 Influenza Virus Pathogenicity', *PLOS Pathogens*, 7(12), p. e1002398. Available at: https://doi.org/10.1371/journal.ppat.1002398.

Dugger, S.A., Platt, A. and Goldstein, D.B. (2018) 'Drug development in the era of precision medicine', *Nature Reviews Drug Discovery*, 17(3), pp. 183–196. Available at: https://doi.org/10.1038/nrd.2017.226.

Dvorak, A. *et al.* (2011) 'Do Airway Epithelium Air–Liquid Cultures Represent the In Vivo Airway Epithelium Transcriptome?', *American Journal of Respiratory Cell and Molecular Biology*, 44(4), pp. 465–473. Available at: https://doi.org/10.1165/rcmb.2009-0453OC.

Dye, B.R. *et al.* (2016) 'A bioengineered niche promotes in vivo engraftment and maturation of pluripotent stem cell derived human lung organoids', *eLife*. Edited by J. Rossant, 5, p. e19732. Available at: https://doi.org/10.7554/eLife.19732.

Ehre, C. *et al.* (2012) 'Overexpressing mouse model demonstrates the protective role of Muc5ac in the lungs', *Proceedings of the National Academy of Sciences of the United States of America*, 109(41), pp. 16528–16533. Available at: https://doi.org/10.1073/pnas.1206552109.

Ekiert, D.C. *et al.* (2009) 'Antibody recognition of a highly conserved influenza virus epitope', *Science (New York, N.Y.)*, 324(5924), pp. 246–251. Available at: https://doi.org/10.1126/science.1171491.

Elliott, A.D. (2020) 'Confocal Microscopy: Principles and Modern Practices', *Current protocols in cytometry*, 92(1), p. e68. Available at: https://doi.org/10.1002/cpcy.68.

Emilien, G., van Meurs, W. and Maloteaux, J.-M. (2000) 'The dose-response relationship in Phase I clinical trials and beyond: use, meaning, and assessment', *Pharmacology & Therapeutics*, 88(1), pp. 33–58. Available at: https://doi.org/10.1016/S0163-7258(00)00077-2.

Everitt, A.R. *et al.* (2012) 'IFITM3 restricts the morbidity and mortality associated with influenza', *Nature*, 484(7395), pp. 519–523. Available at: https://doi.org/10.1038/nature10921.

Ezeonwumelu, I.J., Garcia-Vidal, E. and Ballana, E. (2021) 'JAK-STAT Pathway: A Novel Target to Tackle Viral Infections', *Viruses*, 13(12), p. 2379. Available at: https://doi.org/10.3390/v13122379.

Facciotto, C. *et al.* (2019) 'Drug screening approach combines epigenetic sensitization with immunochemotherapy in cancer', *Clinical Epigenetics*, 11(1), p. 192. Available at: https://doi.org/10.1186/s13148-019-0781-3.

Fang, J. *et al.* (2012) 'Epigenetic Changes Mediated by MicroRNA miR29 Activate Cyclooxygenase 2 and Lambda-1 Interferon Production during Viral Infection', *Journal of Virology*, 86(2), pp. 1010–1020. Available at: https://doi.org/10.1128/JVI.06169-11.

Fang, T.C. *et al.* (2012) 'Histone H3 lysine 9 di-methylation as an epigenetic signature of the interferon response', *Journal of Experimental Medicine*, 209(4), pp. 661–669. Available at: https://doi.org/10.1084/jem.20112343.

Fang, Y. and Eglen, R.M. (2017) 'Three-Dimensional Cell Cultures in Drug Discovery and Development', *Slas Discovery*, 22(5), pp. 456–472. Available at: https://doi.org/10.1177/1087057117696795.

Feeley, E.M. *et al.* (2011) 'IFITM3 Inhibits Influenza A Virus Infection by Preventing Cytosolic Entry', *PLoS Pathogens*, 7(10), p. e1002337. Available at: https://doi.org/10.1371/journal.ppat.1002337.

Felipe Fumero, E. *et al.* (2024) 'Epigenetic control over the cell-intrinsic immune response antagonizes self-renewal in acute myeloid leukemia', *Blood*, 143(22), pp. 2284–2299. Available at: https://doi.org/10.1182/blood.2023021640.

Feng, L. *et al.* (2021) 'Impact of COVID-19 outbreaks and interventions on influenza in China and the United States', *Nature Communications*, 12(1), p. 3249. Available at: https://doi.org/10.1038/s41467-021-23440-1.

Filippakopoulos, P. *et al.* (2010) 'Selective inhibition of BET bromodomains', *Nature*, 468(7327), pp. 1067–1073. Available at: https://doi.org/10.1038/nature09504.

Finberg, R.W. *et al.* (2019) 'Phase 2b Study of Pimodivir (JNJ-63623872) as Monotherapy or in Combination With Oseltamivir for Treatment of Acute Uncomplicated Seasonal Influenza A: TOPAZ Trial', *The Journal of Infectious Diseases*, 219(7), pp. 1026–1034. Available at: https://doi.org/10.1093/infdis/jiy547.

Fischer, W.A. *et al.* (2015) 'Restricted Replication of the Live Attenuated Influenza A Virus Vaccine during Infection of Primary Differentiated Human Nasal Epithelial Cells', *Vaccine*, 33(36), pp. 4495–4504. Available at: https://doi.org/10.1016/j.vaccine.2015.07.023.

Flamand, M.N., Tegowski, M. and Meyer, K.D. (2023) 'The Proteins of mRNA Modification: Writers, Readers, and Erasers', *Annual Review of Biochemistry*, 92(Volume 92, 2023), pp. 145–173. Available at: https://doi.org/10.1146/annurev-biochem-052521-035330.

Florentino, R.M. *et al.* (2022) 'Biofabrication of synthetic human liver tissue with advanced programmable functions', *iScience*, 25(12), p. 105503. Available at: https://doi.org/10.1016/j.isci.2022.105503.

Francis, I. *et al.* (2022) 'Recent advances in lung-on-a-chip models', *Drug Discovery Today*, 27(9), pp. 2593–2602. Available at: https://doi.org/10.1016/j.drudis.2022.06.004.

Francis, J.N. *et al.* (2015) 'A novel peptide-based pan-influenza A vaccine: A double blind, randomised clinical trial of immunogenicity and safety', *Vaccine*, 33(2), pp. 396–402. Available at: https://doi.org/10.1016/j.vaccine.2014.06.006.

Francis, T. and Moore, A.E. (1940) 'A STUDY OF THE NEUROTROPIC TENDENCY IN STRAINS OF THE VIRUS OF EPIDEMIC INFLUENZA', *The Journal of Experimental Medicine*, 72(6), pp. 717–728.

Fu, B. *et al.* (2015) 'TRIM32 Senses and Restricts Influenza A Virus by Ubiquitination of PB1 Polymerase', *PLoS Pathogens*, 11(6), p. e1004960. Available at: https://doi.org/10.1371/journal.ppat.1004960.

Fu, B. *et al.* (2017) 'ZMPSTE24 defends against influenza and other pathogenic viruses', *The Journal of Experimental Medicine*, 214(4), pp. 919–929. Available at: https://doi.org/10.1084/jem.20161270.

Fu, Y. *et al.* (2018) 'Ciliostasis of airway epithelial cells facilitates influenza A virus infection', *Veterinary Research*, 49(1), p. 65. Available at: https://doi.org/10.1186/s13567-018-0568-0.

Fulcher, M.L. and Randell, S.H. (2013) 'Human Nasal and Tracheo-Bronchial Respiratory Epithelial Cell Culture', in S.H. Randell and M.L. Fulcher (eds) *Epithelial Cell Culture Protocols: Second Edition*. Totowa, NJ: Humana Press, pp. 109–121. Available at: https://doi.org/10.1007/978-1-62703-125-7_8.

Funnell, S.G.P. *et al.* (2020) 'Emerging preclinical evidence does not support broad use of hydroxychloroquine in COVID-19 patients', *Nature Communications*, 11(1), p. 4253. Available at: https://doi.org/10.1038/s41467-020-17907-w.

Furuta, Y. *et al.* (2002a) 'In Vitro and In Vivo Activities of Anti-Influenza Virus Compound T-705', *Antimicrobial Agents and Chemotherapy*, 46(4), pp. 977–981. Available at: https://doi.org/10.1128/AAC.46.4.977-981.2002.

Furuta, Y. *et al.* (2002b) 'In Vitro and In Vivo Activities of Anti-Influenza Virus Compound T-705', *Antimicrobial Agents and Chemotherapy*, 46(4), p. 977. Available at: https://doi.org/10.1128/AAC.46.4.977-981.2002.

Furuta, Y. *et al.* (2005) 'Mechanism of Action of T-705 against Influenza Virus', *Antimicrobial Agents and Chemotherapy*, 49(3), pp. 981–986. Available at: https://doi.org/10.1128/AAC.49.3.981-986.2005.

Furuta, Y. *et al.* (2013) 'Favipiravir (T-705), a novel viral RNA polymerase inhibitor', *Antiviral research*, 100(2), p. 10.1016/j.antiviral.2013.09.015. Available at: https://doi.org/10.1016/j.antiviral.2013.09.015.

Gack, M.U. *et al.* (2007) 'TRIM25 RING-finger E3 ubiquitin ligase is essential for RIG-I-mediated antiviral activity', *Nature*, 446(7138), pp. 916–920. Available at: https://doi.org/10.1038/nature05732.

Gack, M.U. *et al.* (2009) 'Influenza A virus NS1 targets the ubiquitin ligase TRIM25 to evade recognition by the host viral RNA sensor RIG-I', *Cell Host & Microbe*, 5(5), pp. 439–449. Available at: https://doi.org/10.1016/j.chom.2009.04.006.

Gadagkar, S.R. and Call, G.B. (2015) 'Computational tools for fitting the Hill equation to dose–response curves', *Journal of Pharmacological and Toxicological Methods*, 71, pp. 68–76. Available at: https://doi.org/10.1016/j.vascn.2014.08.006.

Gallagher, M.E. *et al.* (2018) 'Causes and Consequences of Spatial Within-Host Viral Spread', *Viruses*, 10(11), p. 627. Available at: https://doi.org/10.3390/v10110627.

Ganesan, S., Comstock, A.T. and Sajjan, U.S. (2013) 'Barrier function of airway tract epithelium', *Tissue Barriers*, 1(4), p. e24997. Available at: https://doi.org/10.4161/tisb.24997.

Gao, G. and Cui, X. (2016) 'Three-dimensional bioprinting in tissue engineering and regenerative medicine', *Biotechnology Letters*, 38(2), pp. 203–211. Available at: https://doi.org/10.1007/s10529-015-1975-1.

Gao, Y. *et al.* (2009) 'Identification of Amino Acids in HA and PB2 Critical for the Transmission of H5N1 Avian Influenza Viruses in a Mammalian Host', *PLOS Pathogens*, 5(12), p. e1000709. Available at: https://doi.org/10.1371/journal.ppat.1000709.

Gao, Z. *et al.* (2021) 'Single-nucleotide methylation specifically represses type I interferon in antiviral innate immunity', *The Journal of Experimental Medicine*, 218(3), p. e20201798. Available at: https://doi.org/10.1084/jem.20201798.

García-Sastre, A. *et al.* (1998) 'Influenza A virus lacking the NS1 gene replicates in interferon-deficient systems', *Virology*, 252(2), pp. 324–330. Available at: https://doi.org/10.1006/viro.1998.9508.

García-Sastre, A. (2002) 'Mechanisms of inhibition of the host interferon α/ß-mediated antiviral responses by viruses', *Microbes and Infection*, 4(6), pp. 647–655. Available at: https://doi.org/10.1016/S1286-4579(02)01583-6.

Gauvin, R. *et al.* (2012) 'Microfabrication of complex porous tissue engineering scaffolds using 3D projection stereolithography', *Biomaterials*, 33(15), pp. 3824–3834. Available at: https://doi.org/10.1016/j.biomaterials.2012.01.048.

GBD 2017 Influenza Collaborators (2019) 'Mortality, morbidity, and hospitalisations due to influenza lower respiratory tract infections, 2017: an analysis for the Global Burden of Disease Study 2017', *The Lancet. Respiratory*

Medicine, 7(1), pp. 69–89. Available at: https://doi.org/10.1016/S2213-2600(18)30496-X.

Geiss, G.K. *et al.* (2002) 'Cellular transcriptional profiling in influenza A virus-infected lung epithelial cells: The role of the nonstructural NS1 protein in the evasion of the host innate defense and its potential contribution to pandemic influenza', *Proceedings of the National Academy of Sciences of the United States of America*, 99(16), pp. 10736–10741. Available at: https://doi.org/10.1073/pnas.112338099.

Gerovac, B.J. *et al.* (2014) 'Submersion and hypoxia inhibit ciliated cell differentiation in a notch-dependent manner', *American Journal of Respiratory Cell and Molecular Biology*, 51(4), pp. 516–525. Available at: https://doi.org/10.1165/rcmb.2013-0237OC.

Ghebrehewet, S., MacPherson, P. and Ho, A. (2016) 'Influenza', *The BMJ*, 355, p. i6258. Available at: https://doi.org/10.1136/bmj.i6258.

Gillespie, J.L. *et al.* (2016) 'A Versatile Method for Immunofluorescent Staining of Cells Cultured on Permeable Membrane Inserts', *Medical Science Monitor Basic Research*, 22, pp. 91–94. Available at: https://doi.org/10.12659/MSMBR.900656.

Goetz, L.H. and Schork, N.J. (2018) 'Personalized Medicine: Motivation, Challenges and Progress', *Fertility and sterility*, 109(6), pp. 952–963. Available at: https://doi.org/10.1016/j.fertnstert.2018.05.006.

Goldhill, D.H. *et al.* (2018) 'The mechanism of resistance to favipiravir in influenza', *Proceedings of the National Academy of Sciences of the United States of America*, 115(45), pp. 11613–11618. Available at: https://doi.org/10.1073/pnas.1811345115.

Goldhill, D.H. *et al.* (2021) 'Favipiravir-resistant influenza A virus shows potential for transmission', *PLoS Pathogens*, 17(6), p. e1008937. Available at: https://doi.org/10.1371/journal.ppat.1008937.

Golebiewski, L. *et al.* (2011) 'The Avian Influenza Virus NS1 ESEV PDZ Binding Motif Associates with Dlg1 and Scribble To Disrupt Cellular Tight Junctions ▿', *Journal of Virology*, 85(20), pp. 10639–10648. Available at: https://doi.org/10.1128/JVI.05070-11.

Gopinathan, J. and Noh, I. (2018) 'Recent trends in bioinks for 3D printing', *Biomaterials Research*, 22(1), p. 11. Available at: https://doi.org/10.1186/s40824-018-0122-1.

Goto, H. *et al.* (2001) 'Plasminogen-Binding Activity of Neuraminidase Determines the Pathogenicity of Influenza A Virus', *Journal of Virology*, 75(19), pp. 9297–9301. Available at: https://doi.org/10.1128/JVI.75.19.9297-9301.2001.

Goto, H. and Kawaoka, Y. (1998) 'A novel mechanism for the acquisition of virulence by a human influenza A virus', *Proceedings of the National Academy of Sciences of the United States of America*, 95(17), pp. 10224–10228.

Gottlieb, T.A. *et al.* (1993) 'Actin microfilaments play a critical role in endocytosis at the apical but not the basolateral surface of polarized epithelial cells', *The Journal of Cell Biology*, 120(3), pp. 695–710. Available at: https://doi.org/10.1083/jcb.120.3.695.

Götz, V. *et al.* (2016) 'Influenza A viruses escape from MxA restriction at the expense of efficient nuclear vRNP import', *Scientific Reports*, 6(1), p. 23138. Available at: https://doi.org/10.1038/srep23138.

Gould, P.S., Easton, A.J. and Dimmock, N.J. (2017) 'Live Attenuated Influenza Vaccine contains Substantial and Unexpected Amounts of Defective Viral Genomic RNA', *Viruses*, 9(10), p. 269. Available at: https://doi.org/10.3390/v9100269.

de Graaf, M. and Fouchier, R.A.M. (2014) 'Role of receptor binding specificity in influenza A virus transmission and pathogenesis', *The EMBO Journal*, 33(8), pp. 823–841. Available at: https://doi.org/10.1002/embj.201387442.

Gravina, G.L. *et al.* (2010) 'Biological rationale for the use of DNA methyltransferase inhibitors as new strategy for modulation of tumor response to chemotherapy and radiation', *Molecular Cancer*, 9, p. 305. Available at: https://doi.org/10.1186/1476-4598-9-305.

Grewal, S.I.S. and Jia, S. (2007) 'Heterochromatin revisited', *Nature Reviews Genetics*, 8(1), pp. 35–46. Available at: https://doi.org/10.1038/nrg2008.

Grigoryev, S.A. (2012) 'Nucleosome spacing and chromatin higher-order folding', *Nucleus*, 3(6), pp. 493–499. Available at: https://doi.org/10.4161/nucl.22168.

Grix, T. *et al.* (2018) 'Bioprinting Perfusion-Enabled Liver Equivalents for Advanced Organ-on-a-Chip Applications', *Genes*, 9(4), p. 176. Available at: https://doi.org/10.3390/genes9040176.

Groves, H.E. *et al.* (2021) 'The impact of the COVID-19 pandemic on influenza, respiratory syncytial virus, and other seasonal respiratory virus circulation in Canada: A population-based study', *Lancet Regional Health. Americas*, 1, p. 100015. Available at: https://doi.org/10.1016/j.lana.2021.100015.

Gu, Q. *et al.* (2016) 'Functional 3D Neural Mini-Tissues from Printed Gel-Based Bioink and Human Neural Stem Cells', *Advanced Healthcare Materials*, 5(12), pp. 1429–1438. Available at: https://doi.org/10.1002/adhm.201600095.

Gubareva, L.V. *et al.* (2019) 'Assessing baloxavir susceptibility of influenza viruses circulating in the United States during the 2016/17 and 2017/18 seasons', *Eurosurveillance*, 24(3), p. 1800666. Available at: https://doi.org/10.2807/1560-7917.ES.2019.24.3.1800666.

Gubareva, L.V., Kaiser, L. and Hayden, F.G. (2000) 'Influenza virus neuraminidase inhibitors', *The Lancet*, 355(9206), pp. 827–835. Available at: https://doi.org/10.1016/S0140-6736(99)11433-8.

Guillot, L. *et al.* (2005) 'Involvement of Toll-like Receptor 3 in the Immune Response of Lung Epithelial Cells to Double-stranded RNA and Influenza A Virus

*', *Journal of Biological Chemistry*, 280(7), pp. 5571–5580. Available at: https://doi.org/10.1074/jbc.M410592200.

Haasbach, E. *et al.* (2017) 'The MEK-inhibitor CI-1040 displays a broad anti-influenza virus activity *in vitro* and provides a prolonged treatment window compared to standard of care *in vivo*', *Antiviral Research*, 142, pp. 178–184. Available at: https://doi.org/10.1016/j.antiviral.2017.03.024.

Haffizulla, J. *et al.* (2014) 'Effect of nitazoxanide in adults and adolescents with acute uncomplicated influenza: a double-blind, randomised, placebo-controlled, phase 2b/3 trial', *The Lancet Infectious Diseases*, 14(7), pp. 609–618. Available at: https://doi.org/10.1016/S1473-3099(14)70717-0.

Han, L. *et al.* (2019) 'Structural Insights for Anti-Influenza Vaccine Design', *Computational and Structural Biotechnology Journal*, 17, pp. 475–483. Available at: https://doi.org/10.1016/j.csbj.2019.03.009.

Harrington, W.N., Kackos, C.M. and Webby, R.J. (2021) 'The evolution and future of influenza pandemic preparedness', *Experimental & Molecular Medicine*, 53(5), pp. 737–749. Available at: https://doi.org/10.1038/s12276-021-00603-0.

Hause, B.M. *et al.* (2014) 'Characterization of a Novel Influenza Virus in Cattle and Swine: Proposal for a New Genus in the Orthomyxoviridae Family', *mBio*, 5(2), pp. e00031-14. Available at: https://doi.org/10.1128/mBio.00031-14.

Hawksworth, A. *et al.* (2020) 'Replication of live attenuated influenza vaccine viruses in human nasal epithelial cells is associated with H1N1 vaccine effectiveness', *Vaccine*, 38(26), pp. 4209–4218. Available at: https://doi.org/10.1016/j.vaccine.2020.04.004.

He, Y.-F. *et al.* (2011) 'Tet-mediated formation of 5-carboxylcytosine and its excision by TDG in mammalian DNA', *Science (New York, N.Y.)*, 333(6047), pp. 1303–1307. Available at: https://doi.org/10.1126/science.1210944.

Heintzmann, R. and Sheppard, C.J.R. (2007) 'The sampling limit in fluorescence microscopy', *Micron*, 38(2), pp. 145–149. Available at: https://doi.org/10.1016/j.micron.2006.07.017.

Hiscott, J. *et al.* (2006) 'MasterCARD: a priceless link to innate immunity', *Trends in Molecular Medicine*, 12(2), pp. 53–56. Available at: https://doi.org/10.1016/j.molmed.2005.12.003.

Houser, K. and Subbarao, K. (2015) 'Influenza Vaccines: Challenges and Solutions', *Cell host & microbe*, 17(3), pp. 295–300. Available at: https://doi.org/10.1016/j.chom.2015.02.012.

Hsiao, A. *et al.* (2023) 'Recombinant or Standard-Dose Influenza Vaccine in Adults under 65 Years of Age', *New England Journal of Medicine*, 389(24), pp. 2245–2255. Available at: https://doi.org/10.1056/NEJMoa2302099.

Hsu, A.C.-Y. *et al.* (2012) 'Critical Role of Constitutive Type I Interferon Response in Bronchial Epithelial Cell to Influenza Infection', *PLoS ONE*, 7(3), p. e32947. Available at: https://doi.org/10.1371/journal.pone.0032947.

Hsu, D. *et al.* (2024) 'Safety and immunogenicity of mRNA-based seasonal influenza vaccines formulated to include multiple A/H3N2 strains with or without the B/Yamagata strain in US adults aged 50–75 years: a phase 1/2, open-label, randomised trial', *The Lancet Infectious Diseases*, 0(0). Available at: https://doi.org/10.1016/S1473-3099(24)00493-6.

Hu, J., Zhang, L. and Liu, X. (2020) 'Role of Post-translational Modifications in Influenza A Virus Life Cycle and Host Innate Immune Response', *Frontiers in Microbiology*, 11, p. 517461. Available at: https://doi.org/10.3389/fmicb.2020.517461.

Huang, Y. *et al.* (2021) 'Research Progress, Challenges, and Breakthroughs of Organoids as Disease Models', *Frontiers in Cell and Developmental Biology*, 9, p. 740574. Available at: https://doi.org/10.3389/fcell.2021.740574.

Huchting, J. *et al.* (2018) 'Prodrugs of the Phosphoribosylated Forms of Hydroxypyrazinecarboxamide Pseudobase T-705 and Its De-Fluoro Analogue T-1105 as Potent Influenza Virus Inhibitors', *Journal of Medicinal Chemistry*, 61(14), pp. 6193–6210. Available at: https://doi.org/10.1021/acs.jmedchem.8b00617.

Huchting, J. *et al.* (2019) 'Cell line-dependent activation and antiviral activity of T-1105, the non-fluorinated analogue of T-705 (favipiravir)', *Antiviral Research*, 167, pp. 1–5. Available at: https://doi.org/10.1016/j.antiviral.2019.04.002.

Huh, D. *et al.* (2010) 'Reconstituting Organ-Level Lung Functions on a Chip', *Science (New York, N.Y.)*, 328(5986), pp. 1662–1668. Available at: https://doi.org/10.1126/science.1188302.

Hui, K.P.Y. *et al.* (2018) 'Tropism, replication competence, and innate immune responses of influenza virus: an analysis of human airway organoids and ex-vivo bronchus cultures', *The Lancet Respiratory Medicine*, 6(11), pp. 846–854. Available at: https://doi.org/10.1016/S2213-2600(18)30236-4.

Husain, M. (2024) 'Influenza A Virus and Acetylation: The Picture Is Becoming Clearer', *Viruses*, 16(1), p. 131. Available at: https://doi.org/10.3390/v16010131.

Husain, M. and Cheung, C.-Y. (2014) 'Histone Deacetylase 6 Inhibits Influenza A Virus Release by Downregulating the Trafficking of Viral Components to the Plasma Membrane via Its Substrate, Acetylated Microtubules', *Journal of Virology*, 88(19), pp. 11229–11239. Available at: https://doi.org/10.1128/jvi.00727-14.

Hutchinson, E.C. *et al.* (2010) 'Genome packaging in influenza A virus', *Journal of General Virology*, 91(2), pp. 313–328. Available at: https://doi.org/10.1099/vir.0.017608-0.

Hutchinson, E.C. *et al.* (2014) 'Conserved and host-specific features of influenza virion architecture', *Nature communications*, 5, p. 4816. Available at: https://doi.org/10.1038/ncomms5816.

Hutchinson, E.C. and Fodor, E. (2012) 'Nuclear import of the influenza A virus transcriptional machinery', *Vaccine*, 30(51), pp. 7353–7358. Available at: https://doi.org/10.1016/j.vaccine.2012.04.085.

Ibricevic, A. *et al.* (2006) 'Influenza Virus Receptor Specificity and Cell Tropism in Mouse and Human Airway Epithelial Cells', *Journal of Virology*, 80(15), pp. 7469–7480. Available at: https://doi.org/10.1128/jvi.02677-05.

Ilyushina, N.A., Dickensheets, H. and Donnelly, R.P. (2019) 'A comparison of interferon gene expression induced by influenza A virus infection of human airway epithelial cells from two different donors', *Virus Research*, 264, pp. 1–7. Available at: https://doi.org/10.1016/j.virusres.2019.02.002.

Ilyushina, N.A. and Donnelly, R.P. (2014) '*In vitro* anti-influenza A activity of interferon (IFN)-λ1 combined with IFN-β or oseltamivir carboxylate', *Antiviral Research*, 111, pp. 112–120. Available at: https://doi.org/10.1016/j.antiviral.2014.09.008.

Imai, M. *et al.* (2012) 'Experimental adaptation of an influenza H5 HA confers respiratory droplet transmission to a reassortant H5 HA/H1N1 virus in ferrets', *Nature*, 486(7403), pp. 420–428. Available at: https://doi.org/10.1038/nature10831.

Imam, H., Kim, G.-W. and Siddiqui, A. (2020) 'Epitranscriptomic(N6-methyladenosine) Modification of Viral RNA and Virus-Host Interactions', *Frontiers in Cellular and Infection Microbiology*, 10, p. 584283. Available at: https://doi.org/10.3389/fcimb.2020.584283.

Ioannidis, I. *et al.* (2013) 'Toll-Like Receptor Expression and Induction of Type I and Type III Interferons in Primary Airway Epithelial Cells', *Journal of Virology*, 87(6), pp. 3261–3270. Available at: https://doi.org/10.1128/jvi.01956-12.

Isakova-Sivak, I. and Rudenko, L. (2024) 'Next-generation influenza vaccines based on mRNA technology', *The Lancet Infectious Diseases* [Preprint]. Available at: https://doi.org/10.1016/S1473-3099(24)00562-0.

Iuliano, A.D. *et al.* (2018) 'Estimates of global seasonal influenza-associated respiratory mortality: a modelling study', *The Lancet*, 391(10127), pp. 1285–1300. Available at: https://doi.org/10.1016/S0140-6736(17)33293-2.

Jagger, B.W. *et al.* (2012) 'An Overlapping Protein-Coding Region In Influenza A Virus Segment 3 Modulates the Host Response', *Science (New York, N.Y.)*, 337(6091), pp. 199–204. Available at: https://doi.org/10.1126/science.1222213.

Jaroch, K., Jaroch, A. and Bojko, B. (2018) 'Cell cultures in drug discovery and development: The need of reliable *in vitro-in vivo* extrapolation for pharmacodynamics and pharmacokinetics assessment', *Journal of Pharmaceutical and Biomedical Analysis*, 147, pp. 297–312. Available at: https://doi.org/10.1016/j.jpba.2017.07.023.

Javaherian, S., Paz, A.C. and McGuigan, A.P. (2014) 'Chapter 12 - Micropatterning Cells on Permeable Membrane Filters', in M. Piel and M. Théry (eds) *Methods in Cell Biology*. Academic Press (Micropatterning in Cell Biology

Part C), pp. 171–189. Available at: https://doi.org/10.1016/B978-0-12-800281-0.00012-9.

Jefferson, T. *et al.* (2014) 'Neuraminidase inhibitors for preventing and treating influenza in adults and children', *The Cochrane Database of Systematic Reviews*, 2014(4), p. CD008965. Available at: https://doi.org/10.1002/14651858.CD008965.pub4.

Jia, N. *et al.* (2014) 'Glycomic Characterization of Respiratory Tract Tissues of Ferrets: Implications for its Use in Influenza Virus Infection Studies *', *Journal of Biological Chemistry*, 289(41), pp. 28489–28504. Available at: https://doi.org/10.1074/jbc.M114.588541.

Johnson, N.P.A.S. and Mueller, J. (2002) 'Updating the accounts: global mortality of the 1918-1920 "Spanish" influenza pandemic', *Bulletin of the History of Medicine*, 76(1), pp. 105–115. Available at: https://doi.org/10.1353/bhm.2002.0022.

Joseph, J.G. *et al.* (2022) 'Biomechanical Role of Epsin in Influenza A Virus Entry', *Membranes*, 12(9), p. 859. Available at: https://doi.org/10.3390/membranes12090859.

Josset, L. *et al.* (2010) 'Gene Expression Signature-Based Screening Identifies New Broadly Effective Influenza A Antivirals', *PLoS ONE*, 5(10), p. e13169. Available at: https://doi.org/10.1371/journal.pone.0013169.

Kackos, C.M. *et al.* (2023) 'Seasonal quadrivalent mRNA vaccine prevents and mitigates influenza infection', *npj Vaccines*, 8(1), pp. 1–11. Available at: https://doi.org/10.1038/s41541-023-00752-5.

Kadam, R.U. and Wilson, I.A. (2017) 'Structural basis of influenza virus fusion inhibition by the antiviral drug Arbidol', *Proceedings of the National Academy of Sciences of the United States of America*, 114(2), pp. 206–214. Available at: https://doi.org/10.1073/pnas.1617020114.

Kalashnikova, A.A., Rogge, R.A. and Hansen, J.C. (2016) 'Linker histone H1 and protein-protein interactions', *Biochimica et biophysica acta*, 1859(3), pp. 455–461. Available at: https://doi.org/10.1016/j.bbagrm.2015.10.004.

Kanwal, R. and Gupta, S. (2012) 'Epigenetic modifications in cancer', *Clinical genetics*, 81(4), pp. 303–311. Available at: https://doi.org/10.1111/j.1399-0004.2011.01809.x.

Kapałczyńska, M. *et al.* (2018) '2D and 3D cell cultures – a comparison of different types of cancer cell cultures', *Archives of Medical Science : AMS*, 14(4), pp. 910–919. Available at: https://doi.org/10.5114/aoms.2016.63743.

Kaur, G. and Dufour, J.M. (2012) 'Cell lines: Valuable tools or useless artifacts', *Spermatogenesis*, 2(1), pp. 1–5. Available at: https://doi.org/10.4161/spmg.19885.

Kawaoka, Y., Krauss, S. and Webster, R.G. (1989) 'Avian-to-human transmission of the PB1 gene of influenza A viruses in the 1957 and 1968 pandemics', *Journal*

of Virology, 63(11), pp. 4603–4608. Available at: https://doi.org/10.1128/JVI.63.11.4603-4608.1989.

Keitel, W.A. *et al.* (1994) 'High doses of purified influenza A virus hemagglutinin significantly augment serum and nasal secretion antibody responses in healthy young adults', *Journal of Clinical Microbiology*, 32(10), pp. 2468–2473. Available at: https://doi.org/10.1128/jcm.32.10.2468-2473.1994.

Keitel, W.A. *et al.* (1996) 'Increasing doses of purified influenza virus hemagglutinin and subvirion vaccines enhance antibody responses in the elderly', *Clinical and Diagnostic Laboratory Immunology*, 3(5), pp. 507–510. Available at: https://doi.org/10.1128/cdli.3.5.507-510.1996.

Keshavarz, M. *et al.* (2021) 'Epigenetic reprogramming mechanisms of immunity during influenza A virus infection', *Microbes and Infection*, 23(8), p. 104831. Available at: https://doi.org/10.1016/j.micinf.2021.104831.

Khademhosseini, A. *et al.* (2006) 'Microscale technologies for tissue engineering and biology', *Proceedings of the National Academy of Sciences of the United States of America*, 103(8), p. 2480. Available at: https://doi.org/10.1073/pnas.0507681102.

Kieninger, D. *et al.* (2013) 'Immunogenicity, reactogenicity and safety of an inactivated quadrivalent influenza vaccine candidate versus inactivated trivalent influenza vaccine: a phase III, randomized trial in adults aged ≥18 years', *BMC infectious diseases*, 13, p. 343. Available at: https://doi.org/10.1186/1471-2334-13-343.

Kim, B.S. *et al.* (2021) 'Engineering of diseased human skin equivalent using 3D cell printing for representing pathophysiological hallmarks of type 2 diabetes in vitro', *Biomaterials*, 272, p. 120776. Available at: https://doi.org/10.1016/j.biomaterials.2021.120776.

Kirkpatrick, E. *et al.* (2018) 'The influenza virus hemagglutinin head evolves faster than the stalk domain', *Scientific Reports*, 8(1), p. 10432. Available at: https://doi.org/10.1038/s41598-018-28706-1.

Klein, S. *et al.* (2023) 'IFITM3 blocks influenza virus entry by sorting lipids and stabilizing hemifusion', *Cell Host & Microbe*, 31(4), pp. 616-633.e20. Available at: https://doi.org/10.1016/j.chom.2023.03.005.

Klenk, H.-D. *et al.* (1975) 'Activation of influenza A viruses by trypsin treatment', *Virology*, 68(2), pp. 426–439. Available at: https://doi.org/10.1016/0042-6822(75)90284-6.

Klenk, H.D. and Garten, W. (1994) 'Host cell proteases controlling virus pathogenicity', *Trends in Microbiology*, 2(2), pp. 39–43. Available at: https://doi.org/10.1016/0966-842x(94)90123-6.

Knowles, M.R. and Boucher, R.C. (2002) 'Mucus clearance as a primary innate defense mechanism for mammalian airways', *The Journal of Clinical Investigation*, 109(5), pp. 571–577. Available at: https://doi.org/10.1172/JCI15217.

Knutson, S.K. *et al.* (2014) 'Selective inhibition of EZH2 by EPZ-6438 leads to potent antitumor activity in EZH2-mutant non-Hodgkin lymphoma', *Molecular Cancer Therapeutics*, 13(4), pp. 842–854. Available at: https://doi.org/10.1158/1535-7163.MCT-13-0773.

Koerner, I. *et al.* (2007) 'Protective Role of Beta Interferon in Host Defense against Influenza A Virus', *Journal of Virology*, 81(4), pp. 2025–2030. Available at: https://doi.org/10.1128/jvi.01718-06.

Kolakofsky, D., Kowalinski, E. and Cusack, S. (2012) 'A structure-based model of RIG-I activation', *RNA*, 18(12), pp. 2118–2127. Available at: https://doi.org/10.1261/rna.035949.112.

Kolobukhina, L.V. *et al.* (2008) '[Evaluation of the efficacy of wiferon and arbidol in adult influenza]', *Voprosy Virusologii*, 53(1), pp. 31–33.

Komeno, T. *et al.* (2022) 'Analysis of the responsible site for favipiravir resistance in RNA-dependent RNA polymerase of influenza virus A/PR/8/34 (H1N1) using site-directed mutagenesis', *Antiviral Research*, 205, p. 105387. Available at: https://doi.org/10.1016/j.antiviral.2022.105387.

Kozlov, M.V. *et al.* (2014) 'Selective inhibitor of histone deacetylase 6 (tubastatin A) suppresses proliferation of hepatitis C virus replicon in culture of human hepatocytes', *Biochemistry (Moscow)*, 79(7), pp. 637–642. Available at: https://doi.org/10.1134/S0006297914070050.

Krammer, F. *et al.* (2018) 'Influenza', *Nature Reviews. Disease Primers*, 4(1), p. 3. Available at: https://doi.org/10.1038/s41572-018-0002-y.

Krammer, F. and Palese, P. (2015) 'Advances in the development of influenza virus vaccines', *Nature Reviews Drug Discovery*, 14(3), pp. 167–182. Available at: https://doi.org/10.1038/nrd4529.

Kreuder, A.-E. *et al.* (2020) 'Inspired by the human placenta: a novel 3D bioprinted membrane system to create barrier models', *Scientific Reports*, 10, p. 15606. Available at: https://doi.org/10.1038/s41598-020-72559-6.

Kroeker, A.L. *et al.* (2012) 'Response of Primary Human Airway Epithelial Cells to Influenza Infection: A Quantitative Proteomic Study', *Journal of Proteome Research*, 11(8), pp. 4132–4146. Available at: https://doi.org/10.1021/pr300239r.

Kuck, D. *et al.* (2010) 'Nanaomycin A selectively inhibits DNMT3B and reactivates silenced tumor suppressor genes in human cancer cells', *Molecular Cancer Therapeutics*, 9(11), pp. 3015–3023. Available at: https://doi.org/10.1158/1535-7163.MCT-10-0609.

Kühl, L. *et al.* (2023) 'Human Lung Organoids—A Novel Experimental and Precision Medicine Approach', *Cells*, 12(16), p. 2067. Available at: https://doi.org/10.3390/cells12162067.

Kumar, H., Kawai, T. and Akira, S. (2011) 'Pathogen recognition by the innate immune system', *International Reviews of Immunology*, 30(1), pp. 16–34. Available at: https://doi.org/10.3109/08830185.2010.529976.

Kumar, N. *et al.* (2020) 'Host-Directed Antiviral Therapy', *Clinical Microbiology Reviews*, 33(3), pp. e00168-19. Available at: https://doi.org/10.1128/CMR.00168-19.

Kumar, R. *et al.* (2022) 'S-adenosylmethionine-dependent methyltransferase inhibitor DZNep blocks transcription and translation of SARS-CoV-2 genome with a low tendency to select for drug-resistant viral variants', *Antiviral Research*, 197, p. 105232. Available at: https://doi.org/10.1016/j.antiviral.2021.105232.

Kumar, S. *et al.* (2020) 'Oseltamivir analogs with potent anti-influenza virus activity', *Drug Discovery Today*, 25(8), pp. 1389–1402. Available at: https://doi.org/10.1016/j.drudis.2020.06.004.

Lacroix, G. *et al.* (2018) 'Air–Liquid Interface In Vitro Models for Respiratory Toxicology Research: Consensus Workshop and Recommendations', *Applied in Vitro Toxicology*, 4(2), pp. 91–106. Available at: https://doi.org/10.1089/aivt.2017.0034.

Lai, J.C.C. *et al.* (2010) 'Formation of virus-like particles from human cell lines exclusively expressing influenza neuraminidase', *The Journal of General Virology*, 91(Pt 9), pp. 2322–2330. Available at: https://doi.org/10.1099/vir.0.019935-0.

Lam, T. *et al.* (2019) 'Photopolymerizable gelatin and hyaluronic acid for stereolithographic 3D bioprinting of tissue-engineered cartilage', *Journal of Biomedical Materials Research Part B: Applied Biomaterials*, 107(8), pp. 2649–2657. Available at: https://doi.org/10.1002/jbm.b.34354.

Lattanzi, W. *et al.* (2021) 'Basic and Preclinical Research for Personalized Medicine', *Journal of Personalized Medicine*, 11(5), p. 354. Available at: https://doi.org/10.3390/jpm11050354.

Laver, W.G. (1971) 'Separation of two polypeptide chains from the hemagglutinin subunit of influenza virus', *Virology*, 45(1), pp. 275–288. Available at: https://doi.org/10.1016/0042-6822(71)90134-6.

Lazarowitz, S.G. and Choppin, P.W. (1975) 'Enhancement of the infectivity of influenza A and B viruses by proteolytic cleavage of the hemagglutinin polypeptide', *Virology*, 68(2), pp. 440–454. Available at: https://doi.org/10.1016/0042-6822(75)90285-8.

Lazarowitz, S.G., Compans, R.W. and Choppin, P.W. (1973) 'Proteolytic cleavage of the hemagglutinin polypeptide of influenza virus. Function of the uncleaved polypeptide HA', *Virology*, 52(1), pp. 199–212. Available at: https://doi.org/10.1016/0042-6822(73)90409-1.

Lazarowitz, S.G., Goldberg, A.R. and Choppin, P.W. (1973) 'Proteolytic cleavage by plasmin of the HA polypeptide of influenza virus: Host cell activation of serum plasminogen', *Virology*, 56(1), pp. 172–180. Available at: https://doi.org/10.1016/0042-6822(73)90296-1.

Le Goffic, R. *et al.* (2007) 'Cutting Edge: Influenza A Virus Activates TLR3-Dependent Inflammatory and RIG-I-Dependent Antiviral Responses in Human

Lung Epithelial Cells1', *The Journal of Immunology*, 178(6), pp. 3368–3372. Available at: https://doi.org/10.4049/jimmunol.178.6.3368.

LeBouder, F. *et al.* (2008) 'Annexin II Incorporated into Influenza Virus Particles Supports Virus Replication by Converting Plasminogen into Plasmin', *Journal of Virology*, 82(14), pp. 6820–6828. Available at: https://doi.org/10.1128/jvi.00246-08.

LeBouder, F. *et al.* (2010) 'Plasminogen promotes influenza A virus replication through an annexin 2-dependent pathway in the absence of neuraminidase', *Journal of General Virology*, 91(11), pp. 2753–2761. Available at: https://doi.org/10.1099/vir.0.023804-0.

Lee, H. *et al.* (2020) 'Application of Gelatin Bioinks and Cell-Printing Technology to Enhance Cell Delivery Capability for 3D Liver Fibrosis-on-a-Chip Development', *ACS biomaterials science & engineering*, 6(4), pp. 2469–2477. Available at: https://doi.org/10.1021/acsbiomaterials.9b01735.

Lee, I.T. *et al.* (2023) 'Safety and immunogenicity of a phase 1/2 randomized clinical trial of a quadrivalent, mRNA-based seasonal influenza vaccine (mRNA-1010) in healthy adults: interim analysis', *Nature Communications*, 14(1), p. 3631. Available at: https://doi.org/10.1038/s41467-023-39376-7.

Lee, J. *et al.* (2019) 'Comparison of Pathogenicity and Transmissibility of Influenza B and D Viruses in Pigs', *Viruses*, 11(10), p. 905. Available at: https://doi.org/10.3390/v11100905.

Lee, L.Y.Y. *et al.* (2020) 'Baloxavir treatment of ferrets infected with influenza A(H1N1)pdm09 virus reduces onward transmission', *PLoS Pathogens*, 16(4), p. e1008395. Available at: https://doi.org/10.1371/journal.ppat.1008395.

Lee, S.S., Viboud, C. and Petersen, E. (2022) 'Understanding the rebound of influenza in the post COVID-19 pandemic period holds important clues for epidemiology and control', *International Journal of Infectious Diseases*, 122, pp. 1002–1004. Available at: https://doi.org/10.1016/j.ijid.2022.08.002.

Lee, W. *et al.* (2023) 'A single-cell atlas of in vitro multiculture systems uncovers the in vivo lineage trajectory and cell state in the human lung', *Experimental & Molecular Medicine*, 55(8), pp. 1831–1842. Available at: https://doi.org/10.1038/s12276-023-01076-z.

Lefkowitz, R.B. *et al.* (2024) 'Epigenetic Control of Innate Immunity: Consequences of Acute Respiratory Virus Infection', *Viruses*, 16(2), p. 197. Available at: https://doi.org/10.3390/v16020197.

Leneva, I.A. *et al.* (2005) '[Sensitivity of various influenza virus strains to arbidol. Influence of arbidol combination with different antiviral drugs on reproduction of influenza virus A]', *Terapevticheskii Arkhiv*, 77(8), pp. 84–88.

Leneva, I.A. *et al.* (2016) 'Virus susceptibility and clinical effectiveness of anti-influenza drugs during the 2010-2011 influenza season in Russia', *International journal of infectious diseases: IJID: official publication of the International Society for Infectious Diseases*, 43, pp. 77–84. Available at: https://doi.org/10.1016/j.ijid.2016.01.001.

Lessler, J. *et al.* (2009) 'Incubation periods of acute respiratory viral infections: a systematic review', *The Lancet. Infectious Diseases*, 9(5), pp. 291–300. Available at: https://doi.org/10.1016/S1473-3099(09)70069-6.

Levene, R.E., Shrestha, S.D. and Gaglia, M.M. (2021) 'The Influenza A Virus Host Shutoff Factor PA-X Is Rapidly Turned Over in a Strain-Specific Manner', *Journal of Virology*, 95(8), pp. e02312-20. Available at: https://doi.org/10.1128/JVI.02312-20.

Li, M., Rao, P. and Krug, R.M. (2001) 'The active sites of the influenza cap-dependent endonuclease are on different polymerase subunits', *The EMBO Journal*, 20(8), pp. 2078–2086. Available at: https://doi.org/10.1093/emboj/20.8.2078.

Li, W. *et al.* (2008) 'Activation of Interleukin-32 Pro-Inflammatory Pathway in Response to Influenza A Virus Infection', *PLOS ONE*, 3(4), p. e1985. Available at: https://doi.org/10.1371/journal.pone.0001985.

Li, W. *et al.* (2010) 'IL-32: A Host Proinflammatory Factor against Influenza Viral Replication Is Upregulated by Aberrant Epigenetic Modifications during Influenza A Virus Infection', *The Journal of Immunology*, 185(9), pp. 5056–5065. Available at: https://doi.org/10.4049/jimmunol.0902667.

Li, Y. *et al.* (2016) 'Activation of RNase L is dependent on OAS3 expression during infection with diverse human viruses', *Proceedings of the National Academy of Sciences*, 113(8), pp. 2241–2246. Available at: https://doi.org/10.1073/pnas.1519657113.

Li, Y. and Tang, X.X. (2021) 'Abnormal Airway Mucus Secretion Induced by Virus Infection', *Frontiers in Immunology*, 12, p. 701443. Available at: https://doi.org/10.3389/fimmu.2021.701443.

Lieberman, P.M. (2016) 'Epigenetics and Genetics of Viral Latency', *Cell host & microbe*, 19(5), pp. 619–628. Available at: https://doi.org/10.1016/j.chom.2016.04.008.

Lionta, E. *et al.* (2014) 'Structure-Based Virtual Screening for Drug Discovery: Principles, Applications and Recent Advances', *Current Topics in Medicinal Chemistry*, 14(16), pp. 1923–1938. Available at: https://doi.org/10.2174/1568026614666140929124445.

Liu, J. *et al.* (2021) 'The m6A methylome of SARS-CoV-2 in host cells', *Cell Research*, 31(4), pp. 404–414. Available at: https://doi.org/10.1038/s41422-020-00465-7.

Liu, S. *et al.* (2019) 'Epigenetic Modification Is Regulated by the Interaction of Influenza A Virus Nonstructural Protein 1 with the De Novo DNA Methyltransferase DNMT3B and Subsequent Transport to the Cytoplasm for K48-Linked Polyubiquitination', *Journal of Virology*, 93(7), pp. e01587-18. Available at: https://doi.org/10.1128/JVI.01587-18.

Liu, S.-L. *et al.* (2012) 'High-efficiency dual labeling of influenza virus for single-virus imaging', *Biomaterials*, 33(31), pp. 7828–7833. Available at: https://doi.org/10.1016/j.biomaterials.2012.07.026.

Liu, X. *et al.* (2024) 'RNA N6-methyladenosine methylation in influenza A virus infection', *Frontiers in Microbiology*, 15. Available at: https://doi.org/10.3389/fmicb.2024.1401997.

Liu, Z. *et al.* (2024) 'Modified human skin cell isolation protocol and its influence on keratinocyte and melanocyte culture', *Regenerative Therapy*, 26, pp. 203–212. Available at: https://doi.org/10.1016/j.reth.2024.05.014.

Locatelli, M. and Faure-Dupuy, S. (2023) 'Virus hijacking of host epigenetic machinery to impair immune response', *Journal of Virology*, 97(9), pp. e00658-23. Available at: https://doi.org/10.1128/jvi.00658-23.

Loewa, A., Feng, J.J. and Hedtrich, S. (2023) 'Human disease models in drug development', *Nature Reviews Bioengineering*, 1(8), pp. 545–559. Available at: https://doi.org/10.1038/s44222-023-00063-3.

Long, J.S. *et al.* (2019) 'Host and viral determinants of influenza A virus species specificity', *Nature Reviews Microbiology*, 17(2), pp. 67–81. Available at: https://doi.org/10.1038/s41579-018-0115-z.

Lu, Y. *et al.* (1995) 'Binding of the influenza virus NS1 protein to double-stranded RNA inhibits the activation of the protein kinase that phosphorylates the elF-2 translation initiation factor', *Virology*, 214(1), pp. 222–228. Available at: https://doi.org/10.1006/viro.1995.9937.

Ludwig, S. *et al.* (1995) 'European swine virus as a possible source for the next influenza pandemic?', *Virology*, 212(2), pp. 555–561. Available at: https://doi.org/10.1006/viro.1995.1513.

Luger, K., Dechassa, M.L. and Tremethick, D.J. (2012) 'New insights into nucleosome and chromatin structure: an ordered state or a disordered affair?', *Nature reviews. Molecular cell biology*, 13(7), pp. 436–447. Available at: https://doi.org/10.1038/nrm3382.

Lund, J.M. *et al.* (2004) 'Recognition of single-stranded RNA viruses by Toll-like receptor 7', *Proceedings of the National Academy of Sciences of the United States of America*, 101(15), pp. 5598–5603. Available at: https://doi.org/10.1073/pnas.0400937101.

Ma, J. *et al.* (2019) 'Effects of the PA-X and PB1-F2 Proteins on the Virulence of the 2009 Pandemic H1N1 Influenza A Virus in Mice', *Frontiers in Cellular and Infection Microbiology*, 9. Available at: https://doi.org/10.3389/fcimb.2019.00315.

MacIntyre, C.R. *et al.* (2018) 'The role of pneumonia and secondary bacterial infection in fatal and serious outcomes of pandemic influenza a(H1N1)pdm09', *BMC Infectious Diseases*, 18(1), p. 637. Available at: https://doi.org/10.1186/s12879-018-3548-0.

MacLean, A.J. *et al.* (2022) 'Secondary influenza challenge triggers resident memory B cell migration and rapid relocation to boost antibody secretion at infected sites', *Immunity*, 55(4), pp. 718-733.e8. Available at: https://doi.org/10.1016/j.immuni.2022.03.003.

Majdoul, S. and Compton, A.A. (2022) ‘Lessons in self-defence: inhibition of virus entry by intrinsic immunity’, *Nature Reviews Immunology*, 22(6), pp. 339–352. Available at: https://doi.org/10.1038/s41577-021-00626-8.

Majoros, A. *et al.* (2017) ‘Canonical and Non-Canonical Aspects of JAK-STAT Signaling: Lessons from Interferons for Cytokine Responses’, *Frontiers in Immunology*, 8, p. 29. Available at: https://doi.org/10.3389/fimmu.2017.00029.

Malakhov, M.P. *et al.* (2006) ‘Sialidase Fusion Protein as a Novel Broad-Spectrum Inhibitor of Influenza Virus Infection’, *Antimicrobial Agents and Chemotherapy*, 50(4), pp. 1470–1479. Available at: https://doi.org/10.1128/AAC.50.4.1470-1479.2006.

Manicassamy, B. *et al.* (2010) ‘Analysis of in vivo dynamics of influenza virus infection in mice using a GFP reporter virus’, *Proceedings of the National Academy of Sciences*, 107(25), pp. 11531–11536. Available at: https://doi.org/10.1073/pnas.0914994107.

Mänz, B. *et al.* (2013) ‘Pandemic Influenza A Viruses Escape from Restriction by Human MxA through Adaptive Mutations in the Nucleoprotein’, *PLOS Pathogens*, 9(3), p. e1003279. Available at: https://doi.org/10.1371/journal.ppat.1003279.

Mao, T. *et al.* (2024) ‘Intranasal neomycin evokes broad-spectrum antiviral immunity in the upper respiratory tract’, *Proceedings of the National Academy of Sciences*, 121(18), p. e2319566121. Available at: https://doi.org/10.1073/pnas.2319566121.

Marazzi, I. *et al.* (2012) ‘Suppression of the antiviral response by an influenza histone mimic’, *Nature*, 483(7390), pp. 428–433. Available at: https://doi.org/10.1038/nature10892.

Marcos-Villar, L. *et al.* (2018) ‘Epigenetic control of influenza virus: role of H3K79 methylation in interferon-induced antiviral response’, *Scientific Reports*, 8(1), p. 1230. Available at: https://doi.org/10.1038/s41598-018-19370-6.

Martin, K. and Helenius, A. (1991) ‘Transport of incoming influenza virus nucleocapsids into the nucleus.’, *Journal of Virology*, 65(1), pp. 232–244.

Matrosovich, M. *et al.* (2000) ‘Early alterations of the receptor-binding properties of H1, H2, and H3 avian influenza virus hemagglutinins after their introduction into mammals’, *Journal of Virology*, 74(18), pp. 8502–8512. Available at: https://doi.org/10.1128/jvi.74.18.8502-8512.2000.

Matrosovich, M.N. *et al.* (2004a) ‘Human and avian influenza viruses target different cell types in cultures of human airway epithelium’, *Proceedings of the National Academy of Sciences*, 101(13), pp. 4620–4624. Available at: https://doi.org/10.1073/pnas.0308001101.

Matrosovich, M.N. *et al.* (2004b) ‘Neuraminidase is important for the initiation of influenza virus infection in human airway epithelium’, *Journal of Virology*, 78(22), pp. 12665–12667. Available at: https://doi.org/10.1128/JVI.78.22.12665-12667.2004.

Mazel-Sanchez, B. *et al.* (2023) 'Influenza A virus exploits transferrin receptor recycling to enter host cells', *Proceedings of the National Academy of Sciences of the United States of America*, 120(21), p. e2214936120. Available at: https://doi.org/10.1073/pnas.2214936120.

McAuley, J.L. *et al.* (2017) 'The cell surface mucin MUC1 limits the severity of influenza A virus infection', *Mucosal Immunology*, 10(6), pp. 1581–1593. Available at: https://doi.org/10.1038/mi.2017.16.

McBride, J.M. *et al.* (2017) 'Phase 2 Randomized Trial of the Safety and Efficacy of MHAA4549A, a Broadly Neutralizing Monoclonal Antibody, in a Human Influenza A Virus Challenge Model', *Antimicrobial Agents and Chemotherapy*, 61(11), pp. e01154-17. Available at: https://doi.org/10.1128/AAC.01154-17.

McSharry, J.J. *et al.* (2004) 'Phenotypic Drug Susceptibility Assay for Influenza Virus Neuraminidase Inhibitors', *Clinical and Diagnostic Laboratory Immunology*, 11(1), pp. 21–28. Available at: https://doi.org/10.1128/CDLI.11.1.21-28.2004.

Medaglia, C. *et al.* (2022) 'An anti-influenza combined therapy assessed by single cell RNA-sequencing', *Communications Biology*, 5(1), pp. 1–14. Available at: https://doi.org/10.1038/s42003-022-04013-4.

Meischel, T. *et al.* (2021) 'IFITM Proteins That Restrict the Early Stages of Respiratory Virus Infection Do Not Influence Late-Stage Replication', *Journal of Virology*, 95(20), pp. e00837-21. Available at: https://doi.org/10.1128/JVI.00837-21.

Meroni, G. and Diez-Roux, G. (2005) 'TRIM/RBCC, a novel class of "single protein RING finger" E3 ubiquitin ligases', *BioEssays*, 27(11), pp. 1147–1157. Available at: https://doi.org/10.1002/bies.20304.

Mezhenskaya, D. *et al.* (2021) 'Universal Live-Attenuated Influenza Vaccine Candidates Expressing Multiple M2e Epitopes Protect Ferrets against a High-Dose Heterologous Virus Challenge', *Viruses*, 13(7), p. 1280. Available at: https://doi.org/10.3390/v13071280.

Miki, M. *et al.* (2003) 'Effect of human airway trypsin-like protease on intracellular free Ca2+ concentration in human bronchial epithelial cells', *The journal of medical investigation: JMI*, 50(1–2), pp. 95–107.

Miller, A.J. *et al.* (2019) 'Generation of lung organoids from human pluripotent stem cells in vitro', *Nature Protocols*, 14(2), pp. 518–540. Available at: https://doi.org/10.1038/s41596-018-0104-8.

Miller, J.L. and Grant, P.A. (2013) 'The Role of DNA Methylation and Histone Modifications in Transcriptional Regulation in Humans', *Sub-cellular biochemistry*, 61, pp. 289–317. Available at: https://doi.org/10.1007/978-94-007-4525-4_13.

Min, J.-Y. *et al.* (2007) 'A site on the influenza A virus NS1 protein mediates both inhibition of PKR activation and temporal regulation of viral RNA synthesis', *Virology*, 363(1), pp. 236–243. Available at: https://doi.org/10.1016/j.virol.2007.01.038.

Min, J.-Y. and Krug, R.M. (2006) 'The primary function of RNA binding by the influenza A virus NS1 protein in infected cells: Inhibiting the 2′-5′ oligo (A) synthetase/RNase L pathway', *Proceedings of the National Academy of Sciences*, 103(18), pp. 7100–7105. Available at: https://doi.org/10.1073/pnas.0602184103.

Mindaye, S.T. *et al.* (2017) 'Impact of Influenza A Virus Infection on the Proteomes of Human Bronchoepithelial Cells from Different Donors', *Journal of Proteome Research*, 16(9), pp. 3287–3297. Available at: https://doi.org/10.1021/acs.jproteome.7b00286.

Mishin, V.P. *et al.* (2019) 'Susceptibility of Influenza A, B, C, and D Viruses to Baloxavir1', *Emerging Infectious Diseases*, 25(10), pp. 1969–1972. Available at: https://doi.org/10.3201/eid2510.190607.

Möckel, M. *et al.* (2022) 'Human 3D Airway Tissue Models for Real-Time Microscopy: Visualizing Respiratory Virus Spreading', *Cells*, 11(22), p. 3634. Available at: https://doi.org/10.3390/cells11223634.

Mohn, K.G.-I. *et al.* (2015) 'Longevity of B-Cell and T-Cell Responses After Live Attenuated Influenza Vaccination in Children', *The Journal of Infectious Diseases*, 211(10), pp. 1541–1549. Available at: https://doi.org/10.1093/infdis/jiu654.

Moore, L.D., Le, T. and Fan, G. (2013) 'DNA Methylation and Its Basic Function', *Neuropsychopharmacology*, 38(1), pp. 23–38. Available at: https://doi.org/10.1038/npp.2012.112.

Moreira-Silva, F. *et al.* (2022) 'G9a inhibition by CM-272: Developing a novel anti-tumoral strategy for castration-resistant prostate cancer using 2D and 3D *in vitro* models', *Biomedicine & Pharmacotherapy*, 150, p. 113031. Available at: https://doi.org/10.1016/j.biopha.2022.113031.

Mori, S. *et al.* (2022) 'Donor-to-donor variability of a human three-dimensional bronchial epithelial model: A case study of cigarette smoke exposure', *Toxicology in Vitro*, 82, p. 105391. Available at: https://doi.org/10.1016/j.tiv.2022.105391.

Morrison, O. and Thakur, J. (2021) 'Molecular Complexes at Euchromatin, Heterochromatin and Centromeric Chromatin', *International Journal of Molecular Sciences*, 22(13). Available at: https://doi.org/10.3390/ijms22136922.

Moscona, A. (2005) 'Neuraminidase Inhibitors for Influenza', *New England Journal of Medicine*, 353(13), pp. 1363–1373. Available at: https://doi.org/10.1056/NEJMra050740.

Moss, R.B. *et al.* (2012) 'A phase II study of DAS181, a novel host directed antiviral for the treatment of influenza infection', *The Journal of Infectious Diseases*, 206(12), pp. 1844–1851. Available at: https://doi.org/10.1093/infdis/jis622.

Mu, S. *et al.* (2023) 'The combined effect of oseltamivir and favipiravir on influenza A virus evolution in patients hospitalized with severe influenza', *Antiviral Research*, 216, p. 105657. Available at: https://doi.org/10.1016/j.antiviral.2023.105657.

Mukherjee, S., Vipat, V.C. and Chakrabarti, A.K. (2013) 'Infection with influenza A viruses causes changes in promoter DNA methylation of inflammatory genes', *Influenza and Other Respiratory Viruses*, 7(6), pp. 979–986. Available at: https://doi.org/10.1111/irv.12127.

Mullard, A. (2018) 'FDA approves first new flu drug in 20 years', *Nature Reviews Drug Discovery*, 17(12), pp. 853–853. Available at: https://doi.org/10.1038/nrd.2018.219.

Muneer, A. *et al.* (2024) 'Targeting G9a translational mechanism of SARS-CoV-2 pathogenesis for multifaceted therapeutics of COVID-19 and its sequalae'. bioRxiv, p. 2024.03.04.583415. Available at: https://doi.org/10.1101/2024.03.04.583415.

Nachbagauer, R. *et al.* (2021) 'A chimeric hemagglutinin-based universal influenza virus vaccine approach induces broad and long-lasting immunity in a randomized, placebo-controlled phase I trial', *Nature Medicine*, 27(1), pp. 106–114. Available at: https://doi.org/10.1038/s41591-020-1118-7.

Nagesh, P.T. and Husain, M. (2016) 'Influenza A Virus Dysregulates Host Histone Deacetylase 1 That Inhibits Viral Infection in Lung Epithelial Cells', *Journal of Virology*, 90(9), pp. 4614–4625. Available at: https://doi.org/10.1128/JVI.00126-16.

Nehme, Z., Pasquereau, S. and Herbein, G. (2019) 'Control of viral infections by epigenetic-targeted therapy', *Clinical Epigenetics*, 11(1), p. 55. Available at: https://doi.org/10.1186/s13148-019-0654-9.

Nelson, M.I. and Worobey, M. (2018) 'Origins of the 1918 Pandemic: Revisiting the Swine "Mixing Vessel" Hypothesis', *American Journal of Epidemiology*, 187(12), pp. 2498–2502. Available at: https://doi.org/10.1093/aje/kwy150.

Neumann, G., Hughes, M.T. and Kawaoka, Y. (2000) 'Influenza A virus NS2 protein mediates vRNP nuclear export through NES-independent interaction with hCRM1', *The EMBO Journal*, 19(24), pp. 6751–6758. Available at: https://doi.org/10.1093/emboj/19.24.6751.

Nguyen, T.-Q., Rollon, R. and Choi, Y.-K. (2021) 'Animal Models for Influenza Research: Strengths and Weaknesses', *Viruses*, 13(6), p. 1011. Available at: https://doi.org/10.3390/v13061011.

Nichol, J.W. *et al.* (2010) 'Cell-laden microengineered gelatin methacrylate hydrogels', *Biomaterials*, 31(21), pp. 5536–5544. Available at: https://doi.org/10.1016/j.biomaterials.2010.03.064.

Nogales, A. *et al.* (2018) 'Modulation of Innate Immune Responses by the Influenza A NS1 and PA-X Proteins', *Viruses*, 10(12), p. 708. Available at: https://doi.org/10.3390/v10120708.

Noshi, T. *et al.* (2018) 'In vitro characterization of baloxavir acid, a first-in-class cap-dependent endonuclease inhibitor of the influenza virus polymerase PA subunit', *Antiviral Research*, 160, pp. 109–117. Available at: https://doi.org/10.1016/j.antiviral.2018.10.008.

Nugent, K.M. and Shanley, J.D. (1984) 'Verapamil inhibits influenza A virus replication', *Archives of Virology*, 81(1), pp. 163–170. Available at: https://doi.org/10.1007/BF01309305.

Oh, D.Y. and Hurt, A.C. (2016) 'Using the Ferret as an Animal Model for Investigating Influenza Antiviral Effectiveness', *Frontiers in Microbiology*, 7. Available at: https://doi.org/10.3389/fmicb.2016.00080.

Omoto, S. *et al.* (2018) 'Characterization of influenza virus variants induced by treatment with the endonuclease inhibitor baloxavir marboxil', *Scientific Reports*, 8(1), p. 9633. Available at: https://doi.org/10.1038/s41598-018-27890-4.

O'Neill, R.E. *et al.* (1995) 'Nuclear Import of Influenza Virus RNA Can Be Mediated by Viral Nucleoprotein and Transport Factors Required for Protein Import (*)', *Journal of Biological Chemistry*, 270(39), pp. 22701–22704. Available at: https://doi.org/10.1074/jbc.270.39.22701.

O'Neill, R.E., Talon, J. and Palese, P. (1998) 'The influenza virus NEP (NS2 protein) mediates the nuclear export of viral ribonucleoproteins.', *The EMBO Journal*, 17(1), pp. 288–296. Available at: https://doi.org/10.1093/emboj/17.1.288.

Ooi, E.E. *et al.* (2006) 'In vitro inhibition of human influenza A virus replication by chloroquine', *Virology Journal*, 3, p. 39. Available at: https://doi.org/10.1186/1743-422X-3-39.

Orr, J.C. and Hynds, R.E. (2021) 'Stem Cell–derived Respiratory Epithelial Cell Cultures as Human Disease Models', *American Journal of Respiratory Cell and Molecular Biology*, 64(6), pp. 657–668. Available at: https://doi.org/10.1165/rcmb.2020-0440TR.

Osterwald, S. *et al.* (2012) 'A three-dimensional colocalization RNA interference screening platform to elucidate the alternative lengthening of telomeres pathway', *Biotechnology Journal*, 7(1), pp. 103–116. Available at: https://doi.org/10.1002/biot.201000474.

O'Sullivan, M.J. *et al.* (2021) 'In well-differentiated primary human bronchial epithelial cells, TGF-β1 and TGF-β2 induce expression of furin', *American Journal of Physiology-Lung Cellular and Molecular Physiology*, 320(2), pp. L246–L253. Available at: https://doi.org/10.1152/ajplung.00423.2020.

Otani, T. and Furuse, M. (2020) 'Tight Junction Structure and Function Revisited', *Trends in Cell Biology*, 30(10), pp. 805–817. Available at: https://doi.org/10.1016/j.tcb.2020.08.004.

Palomino-Segura, M. *et al.* (2018) 'Imaging Cell Interaction in Tracheal Mucosa During Influenza Virus Infection Using Two-photon Intravital Microscopy', *Journal of Visualized Experiments : JoVE*, (138), p. 58355. Available at: https://doi.org/10.3791/58355.

Pampaloni, F., Reynaud, E.G. and Stelzer, E.H.K. (2007) 'The third dimension bridges the gap between cell culture and live tissue', *Nature Reviews Molecular*

Cell Biology, 8(10), pp. 839–845. Available at: https://doi.org/10.1038/nrm2236.

Pan, C. and Fan, Y. (2016) 'Role of H1 Linker Histones in Mammalian Development and Stem Cell Differentiation', *Biochimica et biophysica acta*, 1859(3), pp. 496–509. Available at: https://doi.org/10.1016/j.bbagrm.2015.12.002.

Pandey, A. *et al.* (2020) 'Potential therapeutic targets for combating SARS-CoV-2: Drug repurposing, clinical trials and recent advancements', *Life Sciences*, 256, p. 117883. Available at: https://doi.org/10.1016/j.lfs.2020.117883.

Pang, I.K. and Iwasaki, A. (2011) 'Inflammasomes as mediators of immunity against influenza virus', *Trends in immunology*, 32(1), pp. 34–41. Available at: https://doi.org/10.1016/j.it.2010.11.004.

Park, A. and Iwasaki, A. (2020) 'Type I and Type III Interferons – Induction, Signaling, Evasion, and Application to Combat COVID-19', *Cell Host & Microbe*, 27(6), pp. 870–878. Available at: https://doi.org/10.1016/j.chom.2020.05.008.

Park, J.Y. *et al.* (2018) 'Development of a functional airway-on-a-chip by 3D cell printing', *Biofabrication*, 11(1), p. 015002. Available at: https://doi.org/10.1088/1758-5090/aae545.

Park, S.E., Georgescu, A. and Huh, D. (2019) 'Organoids-on-a-chip', *Science*, 364(6444), pp. 960–965. Available at: https://doi.org/10.1126/science.aaw7894.

Parvin, J.D. *et al.* (1986) 'Measurement of the mutation rates of animal viruses: influenza A virus and poliovirus type 1', *Journal of Virology*, 59(2), pp. 377–383. Available at: https://doi.org/10.1128/JVI.59.2.377-383.1986.

Patil, G. *et al.* (2018) 'TRIM41-Mediated Ubiquitination of Nucleoprotein Limits Influenza A Virus Infection', *Journal of Virology*, 92(16), pp. e00905-18. Available at: https://doi.org/10.1128/JVI.00905-18.

Patnaik, E., Madu, C. and Lu, Y. (2023) 'Epigenetic Modulators as Therapeutic Agents in Cancer', *International Journal of Molecular Sciences*, 24(19), p. 14964. Available at: https://doi.org/10.3390/ijms241914964.

Paules, C. and Subbarao, K. (2017) 'Influenza', *The Lancet*, 390(10095), pp. 697–708. Available at: https://doi.org/10.1016/S0140-6736(17)30129-0.

Payne, A.M. (1953) 'The influenza programme of WHO', *Bulletin of the World Health Organization*, 8(5–6), pp. 755–774.

Pendás, A.M. *et al.* (2002) 'Defective prelamin A processing and muscular and adipocyte alterations in Zmpste24 metalloproteinase–deficient mice', *Nature Genetics*, 31(1), pp. 94–99. Available at: https://doi.org/10.1038/ng871.

Pepelanova, I. *et al.* (2018) 'Gelatin-Methacryloyl (GelMA) Hydrogels with Defined Degree of Functionalization as a Versatile Toolkit for 3D Cell Culture and Extrusion Bioprinting', *Bioengineering*, 5(3), p. 55. Available at: https://doi.org/10.3390/bioengineering5030055.

Pérez-Cidoncha, M. *et al.* (2014) 'An Unbiased Genetic Screen Reveals the Polygenic Nature of the Influenza Virus Anti-Interferon Response', *Journal of Virology*, 88(9), pp. 4632–4646. Available at: https://doi.org/10.1128/JVI.00014-14.

Petpiroon, N. *et al.* (2023) 'Development of lung tissue models and their applications', *Life Sciences*, 334, p. 122208. Available at: https://doi.org/10.1016/j.lfs.2023.122208.

Petrich, A. *et al.* (2021) 'Influenza A M2 recruits M1 to the plasma membrane: A fluorescence fluctuation microscopy study', *Biophysical Journal*, 120(24), pp. 5478–5490. Available at: https://doi.org/10.1016/j.bpj.2021.11.023.

Pezzulo, A.A. *et al.* (2011) 'The air-liquid interface and use of primary cell cultures are important to recapitulate the transcriptional profile of in vivo airway epithelia', *American Journal of Physiology - Lung Cellular and Molecular Physiology*, 300(1), pp. L25–L31. Available at: https://doi.org/10.1152/ajplung.00256.2010.

Pflug, A. *et al.* (2017) 'Structural insights into RNA synthesis by the influenza virus transcription-replication machine', *Virus Research*, 234, pp. 103–117. Available at: https://doi.org/10.1016/j.virusres.2017.01.013.

Pharo, E.A. *et al.* (2020) 'Host–Pathogen Responses to Pandemic Influenza H1N1pdm09 in a Human Respiratory Airway Model', *Viruses*, 12(6), p. 679. Available at: https://doi.org/10.3390/v12060679.

Phipps-Yonas, H. *et al.* (2008) 'Interferon-ß Pretreatment of Conventional and Plasmacytoid Human Dendritic Cells Enhances Their Activation by Influenza Virus', *PLOS Pathogens*, 4(10), p. e1000193. Available at: https://doi.org/10.1371/journal.ppat.1000193.

Pichlmair, A. *et al.* (2006) 'RIG-I-Mediated Antiviral Responses to Single-Stranded RNA Bearing 5'-Phosphates', *Science*, 314(5801), pp. 997–1001. Available at: https://doi.org/10.1126/science.1132998.

Ping, X.-L. *et al.* (2014) 'Mammalian WTAP is a regulatory subunit of the RNA N6-methyladenosine methyltransferase', *Cell Research*, 24(2), pp. 177–189. Available at: https://doi.org/10.1038/cr.2014.3.

Pinto, L.H. and Lamb, R.A. (2006) 'The M2 Proton Channels of Influenza A and B Viruses *', *Journal of Biological Chemistry*, 281(14), pp. 8997–9000. Available at: https://doi.org/10.1074/jbc.R500020200.

Pinto, R.M. *et al.* (2021) 'Accessory Gene Products of Influenza A Virus', *Cold Spring Harbor Perspectives in Medicine*, 11(12), p. a038380. Available at: https://doi.org/10.1101/cshperspect.a038380.

Plotch, S.J. *et al.* (1981) 'A unique cap(m7GpppXm)-dependent influenza virion endonuclease cleaves capped RNAs to generate the primers that initiate viral RNA transcription', *Cell*, 23(3), pp. 847–858. Available at: https://doi.org/10.1016/0092-8674(81)90449-9.

Ponce de León, V. and Barrera-Rodríguez, R. (2005) 'Changes in P-glycoprotein activity are mediated by the growth of a tumour cell line as multicellular spheroids', *Cancer Cell International*, 5(1), p. 20. Available at: https://doi.org/10.1186/1475-2867-5-20.

Powell, J.D. and Waters, K.M. (2017) 'Influenza-Omics and the Host Response: Recent Advances and Future Prospects', *Pathogens*, 6(2), p. 25. Available at: https://doi.org/10.3390/pathogens6020025.

Probst, C., Schneider, S. and Loskill, P. (2018) 'High-throughput organ-on-a-chip systems: Current status and remaining challenges', *Current Opinion in Biomedical Engineering*, 6, pp. 33–41. Available at: https://doi.org/10.1016/j.cobme.2018.02.004.

Pshenichnaya, N.Y. *et al.* (2019) 'Clinical efficacy of umifenovir in influenza and ARVI (study ARBITR)', *Terapevticheskii Arkhiv*, 91(3), pp. 56–63. Available at: https://doi.org/10.26442/00403660.2019.03.000127.

de la Puente, P. *et al.* (2015) '3D tissue-engineered bone marrow as a novel model to study pathophysiology and drug resistance in multiple myeloma', *Biomaterials*, 73, pp. 70–84. Available at: https://doi.org/10.1016/j.biomaterials.2015.09.017.

Qi, W. *et al.* (2012) 'Selective inhibition of Ezh2 by a small molecule inhibitor blocks tumor cells proliferation', *Proceedings of the National Academy of Sciences of the United States of America*, 109(52), pp. 21360–21365. Available at: https://doi.org/10.1073/pnas.1210371110.

Qin, S. *et al.* (2014) 'Structural basis for histone mimicry and hijacking of host proteins by influenza virus protein NS1', *Nature Communications*, 5(1), p. 3952. Available at: https://doi.org/10.1038/ncomms4952.

Rajsbaum, R. *et al.* (2012) 'Species-specific inhibition of RIG-I ubiquitination and IFN induction by the influenza A virus NS1 protein', *PLoS pathogens*, 8(11), p. e1003059. Available at: https://doi.org/10.1371/journal.ppat.1003059.

Ramaiahgari, S.C. *et al.* (2019) 'The Power of Resolution: Contextualized Understanding of Biological Responses to Liver Injury Chemicals Using High-throughput Transcriptomics and Benchmark Concentration Modeling', *Toxicological Sciences: An Official Journal of the Society of Toxicology*, 169(2), pp. 553–566. Available at: https://doi.org/10.1093/toxsci/kfz065.

Ramirez, R.D. *et al.* (2004) 'Immortalization of human bronchial epithelial cells in the absence of viral oncoproteins', *Cancer Research*, 64(24), pp. 9027–9034. Available at: https://doi.org/10.1158/0008-5472.CAN-04-3703.

Randall, R.E. and Goodbourn, S. (2008) 'Interferons and viruses: an interplay between induction, signalling, antiviral responses and virus countermeasures', *Journal of General Virology*, 89(1), pp. 1–47. Available at: https://doi.org/10.1099/vir.0.83391-0.

Rayner, R.E. *et al.* (2019) 'Optimization of Normal Human Bronchial Epithelial (NHBE) Cell 3D Cultures for in vitro Lung Model Studies', *Scientific Reports*, 9(1), p. 500. Available at: https://doi.org/10.1038/s41598-018-36735-z.

Rehwinkel, J. *et al.* (2010) 'RIG-I detects viral genomic RNA during negative-strand RNA virus infection', *Cell*, 140(3), pp. 397–408. Available at: https://doi.org/10.1016/j.cell.2010.01.020.

Reich, S. *et al.* (2014) 'Structural insight into cap-snatching and RNA synthesis by influenza polymerase', *Nature*, 516(7531), pp. 361–366. Available at: https://doi.org/10.1038/nature14009.

Richter, M. *et al.* (2021) 'From Donor to the Lab: A Fascinating Journey of Primary Cell Lines', *Frontiers in Cell and Developmental Biology*, 9, p. 711381. Available at: https://doi.org/10.3389/fcell.2021.711381.

Rigby, R.E. *et al.* (2019) 'PA-X antagonises MAVS-dependent accumulation of early type I interferon messenger RNAs during influenza A virus infection', *Scientific Reports*, 9, p. 7216. Available at: https://doi.org/10.1038/s41598-019-43632-6.

Rijsbergen, L.C. *et al.* (2021) 'In Vitro Modelling of Respiratory Virus Infections in Human Airway Epithelial Cells – A Systematic Review', *Frontiers in Immunology*, 12. Available at: https://www.frontiersin.org/journals/immunology/articles/10.3389/fimmu.2021.683002 (Accessed: 22 February 2024).

Riss, T.L. *et al.* (2004) 'Cell Viability Assays', in S. Markossian et al. (eds) *Assay Guidance Manual*. Bethesda (MD): Eli Lilly & Company and the National Center for Advancing Translational Sciences. Available at: http://www.ncbi.nlm.nih.gov/books/NBK144065/ (Accessed: 26 June 2024).

Robertson, J.S., Schubert, M. and Lazzarini, R.A. (1981) 'Polyadenylation sites for influenza virus mRNA', *Journal of Virology*, 38(1), pp. 157–163. Available at: https://doi.org/10.1128/JVI.38.1.157-163.1981.

Rock, J.R. *et al.* (2009) 'Basal cells as stem cells of the mouse trachea and human airway epithelium', *Proceedings of the National Academy of Sciences of the United States of America*, 106(31), pp. 12771–12775. Available at: https://doi.org/10.1073/pnas.0906850106.

Roman, V. *et al.* (2023) 'Cell Culture Model Evolution and Its Impact on Improving Therapy Efficiency in Lung Cancer', *Cancers*, 15(20), p. 4996. Available at: https://doi.org/10.3390/cancers15204996.

Romanelli, R.J. *et al.* (2023) 'The Societal and Indirect Economic Burden of Seasonal Influenza in the United Kingdom', *Rand Health Quarterly*, 10(4). Available at: https://www.ncbi.nlm.nih.gov/pmc/articles/PMC10501821/ (Accessed: 3 September 2024).

Rose, M.C. and Voynow, J.A. (2006) 'Respiratory Tract Mucin Genes and Mucin Glycoproteins in Health and Disease', *Physiological Reviews*, 86(1), pp. 245–278. Available at: https://doi.org/10.1152/physrev.00010.2005.

Ross, A.J. *et al.* (2007) 'Transcriptional Profiling of Mucociliary Differentiation in Human Airway Epithelial Cells', *American Journal of Respiratory Cell and Molecular Biology*, 37(2), pp. 169–185. Available at: https://doi.org/10.1165/rcmb.2006-0466OC.

Rossignol, J.-F. (2014) ‘Nitazoxanide: a first-in-class broad-spectrum antiviral agent’, *Antiviral Research*, 110, pp. 94–103. Available at: https://doi.org/10.1016/j.antiviral.2014.07.014.

Rossman, J.S. and Lamb, R.A. (2011) ‘Influenza Virus Assembly and Budding’, *Virology*, 411(2), pp. 229–236. Available at: https://doi.org/10.1016/j.virol.2010.12.003.

Rota, P.A. *et al.* (1990) ‘Cocirculation of two distinct evolutionary lineages of influenza type B virus since 1983’, *Virology*, 175(1), pp. 59–68. Available at: https://doi.org/10.1016/0042-6822(90)90186-u.

Rott, R. *et al.* (1984) ‘Studies on the adaptation of influenza viruses to MDCK cells.’, *The EMBO Journal*, 3(13), pp. 3329–3332.

Rott, R. *et al.* (1995) ‘Influenza viruses, cell enzymes, and pathogenicity’, *American Journal of Respiratory and Critical Care Medicine*, 152(4 Pt 2), pp. S16-19. Available at: https://doi.org/10.1164/ajrccm/152.4_Pt_2.S16.

Rubin, B.K. (2002) ‘Physiology of airway mucus clearance’, *Respiratory Care*, 47(7), pp. 761–768.

Rust, M.J. *et al.* (2004) ‘Assembly of endocytic machinery around individual influenza viruses during viral entry’, *Nature Structural & Molecular Biology*, 11(6), pp. 567–573. Available at: https://doi.org/10.1038/nsmb769.

Ryu, S. *et al.* (2015) ‘Nanothin Coculture Membranes with Tunable Pore Architecture and Thermoresponsive Functionality for Transfer-Printable Stem Cell-Derived Cardiac Sheets’, *ACS nano*, 9(10), pp. 10186–10202. Available at: https://doi.org/10.1021/acsnano.5b03823.

Salgueiro, L. *et al.* (2022) ‘Generation of Human Lung Organoid Cultures from Healthy and Tumor Tissue to Study Infectious Diseases’, *Journal of Virology*, 96(7), pp. e00098-22. Available at: https://doi.org/10.1128/jvi.00098-22.

Salk, J.E. and Suriano, P.C. (1949) ‘Importance of antigenic composition of influenza virus vaccine in protecting against the natural disease; observations during the winter of 1947-1948’, *American Journal of Public Health and the Nation’s Health*, 39(3), pp. 345–355. Available at: https://doi.org/10.2105/ajph.39.3.345.

San José-Enériz, E. *et al.* (2017) ‘Discovery of first-in-class reversible dual small molecule inhibitors against G9a and DNMTs in hematological malignancies’, *Nature Communications*, 8, p. 15424. Available at: https://doi.org/10.1038/ncomms15424.

Sands, P., Mundaca-Shah, C. and Dzau, V.J. (2016) ‘The Neglected Dimension of Global Security — A Framework for Countering Infectious-Disease Crises’, *New England Journal of Medicine*, 374(13), pp. 1281–1287. Available at: https://doi.org/10.1056/NEJMsr1600236.

Sangawa, H. *et al.* (2013) ‘Mechanism of Action of T-705 Ribosyl Triphosphate against Influenza Virus RNA Polymerase’, *Antimicrobial Agents and*

Chemotherapy, 57(11), pp. 5202–5208. Available at: https://doi.org/10.1128/AAC.00649-13.

Sato, A. *et al.* (2013) 'Suppressive effect of the histone deacetylase inhibitor suberoylanilide hydroxamic acid (SAHA) on hepatitis C virus replication', *Journal of Cellular Biochemistry*, 114(9), pp. 1987–1996. Available at: https://doi.org/10.1002/jcb.24541.

Schindelin, J. *et al.* (2012) 'Fiji: an open-source platform for biological-image analysis', *Nature Methods*, 9(7), pp. 676–682. Available at: https://doi.org/10.1038/nmeth.2019.

Schreiber, A. *et al.* (2020) 'Dissecting the mechanism of signaling-triggered nuclear export of newly synthesized influenza virus ribonucleoprotein complexes', *Proceedings of the National Academy of Sciences of the United States of America*, 117(28), pp. 16557–16566. Available at: https://doi.org/10.1073/pnas.2002828117.

Schulz, O. *et al.* (2005) 'Toll-like receptor 3 promotes cross-priming to virus-infected cells', *Nature*, 433(7028), pp. 887–892. Available at: https://doi.org/10.1038/nature03326.

Schuurmans, Carl.C.L. *et al.* (2021) 'Hyaluronic acid and chondroitin sulfate (meth)acrylate-based hydrogels for tissue engineering: Synthesis, characteristics and pre-clinical evaluation', *Biomaterials*, 268, p. 120602. Available at: https://doi.org/10.1016/j.biomaterials.2020.120602.

Sederdahl, B.K. and Williams, J.V. (2020) 'Epidemiology and Clinical Characteristics of Influenza C Virus', *Viruses*, 12(1). Available at: https://doi.org/10.3390/v12010089.

Segovia, C. *et al.* (2019) 'Inhibition of a G9a/DNMT network triggers immune-mediated bladder cancer regression', *Nature Medicine*, 25(7), pp. 1073–1081. Available at: https://doi.org/10.1038/s41591-019-0499-y.

Sellgren, K.L. *et al.* (2014) 'A biomimetic multicellular model of the airways using primary human cells', *Lab on a Chip*, 14(17), pp. 3349–3358. Available at: https://doi.org/10.1039/c4lc00552j.

Semba, J.A., Mieloch, A.A. and Rybka, J.D. (2020) 'Introduction to the state-of-the-art 3D bioprinting methods, design, and applications in orthopedics', *Bioprinting*, 18, p. e00070. Available at: https://doi.org/10.1016/j.bprint.2019.e00070.

Seth, R.B. *et al.* (2005) 'Identification and Characterization of MAVS, a Mitochondrial Antiviral Signaling Protein that Activates NF-κB and IRF3', *Cell*, 122(5), pp. 669–682. Available at: https://doi.org/10.1016/j.cell.2005.08.012.

Shao, W. *et al.* (2017) 'Evolution of Influenza A Virus by Mutation and Re-Assortment', *International Journal of Molecular Sciences*, 18(8), p. 1650. Available at: https://doi.org/10.3390/ijms18081650.

Shaw, M.L. *et al.* (2008) 'Cellular Proteins in Influenza Virus Particles', *PLoS Pathogens*, 4(6). Available at: https://doi.org/10.1371/journal.ppat.1000085.

Shet, A. *et al.* (2021) 'Impact of the SARS-CoV-2 pandemic on routine immunisation services: evidence of disruption and recovery from 170 countries and territories', *The Lancet. Global Health*, 10(2), pp. e186–e194. Available at: https://doi.org/10.1016/S2214-109X(21)00512-X.

Shi, L. *et al.* (2007) 'Antiviral activity of arbidol against influenza A virus, respiratory syncytial virus, rhinovirus, coxsackie virus and adenovirus in vitro and in vivo', *Archives of Virology*, 152(8), pp. 1447–1455. Available at: https://doi.org/10.1007/s00705-007-0974-5.

Shinya, K. *et al.* (2006) 'Avian flu: influenza virus receptors in the human airway', *Nature*, 440(7083), pp. 435–436. Available at: https://doi.org/10.1038/440435a.

Shiraki, K. and Daikoku, T. (2020) 'Favipiravir, an anti-influenza drug against life-threatening RNA virus infections', *Pharmacology & Therapeutics*, 209, p. 107512. Available at: https://doi.org/10.1016/j.pharmthera.2020.107512.

Short, K.R. *et al.* (2014) 'Pathogenesis of influenza-induced acute respiratory distress syndrome', *The Lancet. Infectious Diseases*, 14(1), pp. 57–69. Available at: https://doi.org/10.1016/S1473-3099(13)70286-X.

Short, K.R. *et al.* (2016) 'Influenza virus damages the alveolar barrier by disrupting epithelial cell tight junctions', *The European Respiratory Journal*, 47(3), pp. 954–966. Available at: https://doi.org/10.1183/13993003.01282-2015.

Si, L. *et al.* (2021) 'A human-airway-on-a-chip for the rapid identification of candidate antiviral therapeutics and prophylactics', *Nature Biomedical Engineering*, 5(8), pp. 815–829. Available at: https://doi.org/10.1038/s41551-021-00718-9.

Silva, S. *et al.* (2023) 'Air-liquid interface (ALI) impact on different respiratory cell cultures', *European Journal of Pharmaceutics and Biopharmaceutics*, 184, pp. 62–82. Available at: https://doi.org/10.1016/j.ejpb.2023.01.013.

Skehel, J.J. *et al.* (1982) 'Changes in the conformation of influenza virus hemagglutinin at the pH optimum of virus-mediated membrane fusion', *Proceedings of the National Academy of Sciences of the United States of America*, 79(4), pp. 968–972. Available at: https://doi.org/10.1073/pnas.79.4.968.

Skehel, J.J. and Wiley, D.C. (2000) 'Receptor binding and membrane fusion in virus entry: the influenza hemagglutinin', *Annual Review of Biochemistry*, 69, pp. 531–569. Available at: https://doi.org/10.1146/annurev.biochem.69.1.531.

Sleeman, K. *et al.* (2010) 'In Vitro Antiviral Activity of Favipiravir (T-705) against Drug-Resistant Influenza and 2009 A(H1N1) Viruses', *Antimicrobial Agents and Chemotherapy*, 54(6), pp. 2517–2524. Available at: https://doi.org/10.1128/aac.01739-09.

Smyrek, I. and Stelzer, E.H.K. (2017) 'Quantitative three-dimensional evaluation of immunofluorescence staining for large whole mount spheroids with light sheet microscopy', *Biomedical Optics Express*, 8(2), pp. 484–499. Available at: https://doi.org/10.1364/BOE.8.000484.

Son, J. *et al.* (2022) 'JIB-04 Has Broad-Spectrum Antiviral Activity and Inhibits SARS-CoV-2 Replication and Coronavirus Pathogenesis', *mBio*, 13(1), pp. e03377-21. Available at: https://doi.org/10.1128/mbio.03377-21.

Sonntag, F. *et al.* (2010) 'Design and prototyping of a chip-based multi-micro-organoid culture system for substance testing, predictive to human (substance) exposure', *Journal of Biotechnology*, 148(1), pp. 70–75. Available at: https://doi.org/10.1016/j.jbiotec.2010.02.001.

Spiess, A.-N. and Neumeyer, N. (2010) 'An evaluation of R2 as an inadequate measure for nonlinear models in pharmacological and biochemical research: a Monte Carlo approach', *BMC Pharmacology*, 10, p. 6. Available at: https://doi.org/10.1186/1471-2210-10-6.

Stachulski, A.V. *et al.* (2021) 'Therapeutic Potential of Nitazoxanide: An Appropriate Choice for Repurposing versus SARS-CoV-2?', *ACS infectious diseases*, 7(6), pp. 1317–1331. Available at: https://doi.org/10.1021/acsinfecdis.0c00478.

Stark, G.R. *et al.* (1998) 'HOW CELLS RESPOND TO INTERFERONS', *Annual Review of Biochemistry*, 67(Volume 67, 1998), pp. 227–264. Available at: https://doi.org/10.1146/annurev.biochem.67.1.227.

Stewart, C.E., Randall, R.E. and Adamson, C.S. (2014) 'Inhibitors of the Interferon Response Enhance Virus Replication In Vitro', *PLoS ONE*, 9(11), p. e112014. Available at: https://doi.org/10.1371/journal.pone.0112014.

Stojdl, D.F. *et al.* (2000) 'Exploiting tumor-specific defects in the interferon pathway with a previously unknown oncolytic virus', *Nature Medicine*, 6(7), pp. 821–825. Available at: https://doi.org/10.1038/77558.

Strittmatter, S.M. (2014) 'Overcoming Drug Development Bottlenecks With Repurposing: Old drugs learn new tricks', *Nature Medicine*, 20(6), pp. 590–591. Available at: https://doi.org/10.1038/nm.3595.

Sugawara, K. *et al.* (1991) 'Antigenic Characterization of the Nucleoprotein and Matrix Protein of Influenza C Virus with Monoclonal Antibodies', *Journal of General Virology*, 72(1), pp. 103–109. Available at: https://doi.org/10.1099/0022-1317-72-1-103.

Sun, D. *et al.* (2022) 'Why 90% of clinical drug development fails and how to improve it?', *Acta Pharmaceutica Sinica B*, 12(7), pp. 3049–3062. Available at: https://doi.org/10.1016/j.apsb.2022.02.002.

Sun, S. and Barreiro, L.B. (2020) 'The epigenetically-encoded memory of the innate immune system', *Current Opinion in Immunology*, 65, pp. 7–13. Available at: https://doi.org/10.1016/j.coi.2020.02.002.

Tai, C.Y. *et al.* (1998) 'Characterization of human influenza virus variants selected in vitro in the presence of the neuraminidase inhibitor GS 4071', *Antimicrobial Agents and Chemotherapy*, 42(12), pp. 3234–3241. Available at: https://doi.org/10.1128/AAC.42.12.3234.

Takahashi, K. *et al.* (2003) 'In Vitro and in Vivo Activities of T-705 and Oseltamivir against Influenza Virus', *Antiviral Chemistry and Chemotherapy*, 14(5), pp. 235–241. Available at: https://doi.org/10.1177/095632020301400502.

Takahashi, M. *et al.* (2001) 'Localization of human airway trypsin-like protease in the airway: an immunohistochemical study', *Histochemistry and Cell Biology*, 115(3), pp. 181–187. Available at: https://doi.org/10.1007/s004180000243.

Takashita, E. *et al.* (2016) 'Antiviral susceptibility of influenza viruses isolated from patients pre- and post-administration of favipiravir', *Antiviral Research*, 132, pp. 170–177. Available at: https://doi.org/10.1016/j.antiviral.2016.06.007.

Takashita, E. *et al.* (2019) 'Human-to-Human Transmission of Influenza A(H3N2) Virus with Reduced Susceptibility to Baloxavir, Japan, February 2019', *Emerging Infectious Diseases*, 25(11), pp. 2108–2111. Available at: https://doi.org/10.3201/eid2511.190757.

Talevi, A. and Bellera, C.L. (2020) 'Challenges and opportunities with drug repurposing: finding strategies to find alternative uses of therapeutics', *Expert Opinion on Drug Discovery*, 15(4), pp. 397–401. Available at: https://doi.org/10.1080/17460441.2020.1704729.

Talon, J. *et al.* (2000) 'Activation of Interferon Regulatory Factor 3 Is Inhibited by the Influenza A Virus NS1 Protein', *Journal of Virology*, 74(17), pp. 7989–7996.

Tan, G.S. *et al.* (2014) 'Characterization of a broadly neutralizing monoclonal antibody that targets the fusion domain of group 2 influenza A virus hemagglutinin', *Journal of Virology*, 88(23), pp. 13580–13592. Available at: https://doi.org/10.1128/JVI.02289-14.

Tan, J. *et al.* (2007) 'Pharmacologic disruption of Polycomb-repressive complex 2-mediated gene repression selectively induces apoptosis in cancer cells', *Genes & Development*, 21(9), pp. 1050–1063. Available at: https://doi.org/10.1101/gad.1524107.

Tang, C.Y. *et al.* (2021) 'Cell-Adapted Mutations and Antigenic Diversity of Influenza B Viruses in Missouri, 2019–2020 Season', *Viruses*, 13(10), p. 1896. Available at: https://doi.org/10.3390/v13101896.

Tang, L. *et al.* (2023) 'USP18 promotes innate immune responses and apoptosis in influenza A virus-infected A549 cells via cGAS-STING pathway', *Virology*, 585, pp. 240–247. Available at: https://doi.org/10.1016/j.virol.2023.06.012.

Tang, Y. *et al.* (2023) 'Brain microglia serve as a persistent HIV reservoir despite durable antiretroviral therapy', *The Journal of Clinical Investigation*, 133(12), p. e167417. Available at: https://doi.org/10.1172/JCI167417.

Taubenberger, J.K. (1998) 'Influenza virus hemagglutinin cleavage into HA1, HA2: No laughing matter', *Proceedings of the National Academy of Sciences of the United States of America*, 95(17), p. 9713. Available at: https://doi.org/10.1073/pnas.95.17.9713.

Taubenberger, J.K. and Morens, D.M. (2010) 'Influenza: The Once and Future Pandemic', *Public Health Reports*, 125(Suppl 3), pp. 16–26.

Thompson, C.I. *et al.* (2006) 'Infection of human airway epithelium by human and avian strains of influenza a virus', *Journal of Virology*, 80(16), pp. 8060–8068. Available at: https://doi.org/10.1128/JVI.00384-06.

Throsby, M. *et al.* (2008) 'Heterosubtypic neutralizing monoclonal antibodies cross-protective against H5N1 and H1N1 recovered from human IgM+ memory B cells', *PloS One*, 3(12), p. e3942. Available at: https://doi.org/10.1371/journal.pone.0003942.

Tilmanis, D. *et al.* (2017) 'The susceptibility of circulating human influenza viruses to tizoxanide, the active metabolite of nitazoxanide', *Antiviral Research*, 147, pp. 142–148. Available at: https://doi.org/10.1016/j.antiviral.2017.10.002.

Tinoco, J.C. *et al.* (2014) 'Immunogenicity, reactogenicity, and safety of inactivated quadrivalent influenza vaccine candidate versus inactivated trivalent influenza vaccine in healthy adults aged ≥18 years: A phase III, randomized trial', *Vaccine*, 32(13), pp. 1480–1487. Available at: https://doi.org/10.1016/j.vaccine.2014.01.022.

Torrance, B.L. *et al.* (2023) 'Senolytic treatment with dasatinib and quercetin does not improve overall influenza responses in aged mice', *Frontiers in Aging*, 4, p. 1212750. Available at: https://doi.org/10.3389/fragi.2023.1212750.

Treanor, J. (2020) 'History of Live, Attenuated Influenza Vaccine', *Journal of the Pediatric Infectious Diseases Society*, 9(Supplement_1), pp. S3–S9. Available at: https://doi.org/10.1093/jpids/piz086.

Triana-Baltzer, G.B. *et al.* (2009) 'Inhibition of Neuraminidase Inhibitor-Resistant Influenza Virus by DAS181, a Novel Sialidase Fusion Protein', *PLoS ONE*, 4(11), p. e7838. Available at: https://doi.org/10.1371/journal.pone.0007838.

Trifonov, V., Khiabanian, H. and Rabadan, R. (2009) 'Geographic Dependence, Surveillance, and Origins of the 2009 Influenza A (H1N1) Virus', *New England Journal of Medicine*, 361(2), pp. 115–119. Available at: https://doi.org/10.1056/NEJMp0904572.

Ueki, H. *et al.* (2020) 'Multicolor two-photon imaging of in vivo cellular pathophysiology upon influenza virus infection using the two-photon IMPRESS', *Nature Protocols*, 15(3), pp. 1041–1065. Available at: https://doi.org/10.1038/s41596-019-0275-y.

UK Health Security Agency (2024) *Flu vaccines for the 2024 to 2025 season*, *GOV.UK*. Available at: https://www.gov.uk/government/publications/flu-vaccines-for-the-current-season/flu-vaccines-for-the-2023-to-2024-season (Accessed: 2 September 2024).

Ushakov, D.S. and Finke, S. (2023) 'Chapter Three - Tissue optical clearing and 3D imaging of virus infections', in S. Finke and D. Ushakov (eds) *Advances in Virus Research*. Academic Press (Imaging in Virus Research), pp. 89–121. Available at: https://doi.org/10.1016/bs.aivir.2023.06.003.

Uyeki, T.M. *et al.* (2022) 'Influenza', *Lancet (London, England)*, 400(10353), p. 693. Available at: https://doi.org/10.1016/S0140-6736(22)00982-5.

Van Norman, G.A. (2019) 'Limitations of Animal Studies for Predicting Toxicity in Clinical Trials', *JACC: Basic to Translational Science*, 4(7), pp. 845–854. Available at: https://doi.org/10.1016/j.jacbts.2019.10.008.

Vanderlinden, E. *et al.* (2016) 'Distinct Effects of T-705 (Favipiravir) and Ribavirin on Influenza Virus Replication and Viral RNA Synthesis', *Antimicrobial Agents and Chemotherapy*, 60(11), pp. 6679–6691. Available at: https://doi.org/10.1128/aac.01156-16.

Varga, Z.T. and Palese, P. (2011) 'The influenza A virus protein PB1-F2', *Virulence*, 2(6), pp. 542–546. Available at: https://doi.org/10.4161/viru.2.6.17812.

Vaughan, M.B. *et al.* (2006) 'A three-dimensional model of differentiation of immortalized human bronchial epithelial cells', *Differentiation; Research in Biological Diversity*, 74(4), pp. 141–148. Available at: https://doi.org/10.1111/j.1432-0436.2006.00069.x.

Villamayor, L. *et al.* (2023) 'Interferon alpha inducible protein 6 is a negative regulator of innate immune responses by modulating RIG-I activation', *Frontiers in Immunology*, 14, p. 1105309. Available at: https://doi.org/10.3389/fimmu.2023.1105309.

Wagner, I. *et al.* (2013) 'A dynamic multi-organ-chip for long-term cultivation and substance testing proven by 3D human liver and skin tissue co-culture', *Lab on a Chip*, 13(18), pp. 3538–3547. Available at: https://doi.org/10.1039/c3lc50234a.

van de Wakker, S.I., Fischer, M.J.E. and Oosting, R.S. (2017) 'New drug-strategies to tackle viral-host interactions for the treatment of influenza virus infections', *European Journal of Pharmacology*, 809, pp. 178–190. Available at: https://doi.org/10.1016/j.ejphar.2017.05.038.

Wang, Jiang *et al.* (2020) 'BRD4 inhibition exerts anti-viral activity through DNA damage-dependent innate immune responses', *PLoS Pathogens*, 16(3), p. e1008429. Available at: https://doi.org/10.1371/journal.ppat.1008429.

Wang, Jiongjiong *et al.* (2020) 'In Vitro and In Vivo Antiviral Activity of Gingerenone A on Influenza A Virus Is Mediated by Targeting Janus Kinase 2', *Viruses*, 12(10), p. 1141. Available at: https://doi.org/10.3390/v12101141.

Wang, L. *et al.* (2013) 'A small molecule modulates Jumonji histone demethylase activity and selectively inhibits cancer growth', *Nature communications*, 4, p. 2035. Available at: https://doi.org/10.1038/ncomms3035.

Wang, L. *et al.* (2017) 'Comparative influenza protein interactomes identify the role of plakophilin 2 in virus restriction', *Nature Communications*, 8, p. 13876. Available at: https://doi.org/10.1038/ncomms13876.

Wang, M. *et al.* (2004) '[Efficacy and safety of arbidol in treatment of naturally acquired influenza]', *Zhongguo Yi Xue Ke Xue Yuan Xue Bao. Acta Academiae Medicinae Sinicae*, 26(3), pp. 289–293.

Wang, M. *et al.* (2022) 'Molecularly cleavable bioinks facilitate high-performance digital light processing-based bioprinting of functional volumetric soft tissues', *Nature Communications*, 13(1), p. 3317. Available at: https://doi.org/10.1038/s41467-022-31002-2.

Wang, X. *et al.* (2000) 'Influenza A virus NS1 protein prevents activation of NF-kappaB and induction of alpha/beta interferon', *Journal of Virology*, 74(24), pp. 11566–11573. Available at: https://doi.org/10.1128/jvi.74.24.11566-11573.2000.

Wang, Y. and Jeon, H. (2022) '3D cell cultures toward quantitative high-throughput drug screening', *Trends in Pharmacological Sciences*, 43(7), pp. 569–581. Available at: https://doi.org/10.1016/j.tips.2022.03.014.

Wanner, A., Salathé, M. and O'Riordan, T.G. (1996) 'Mucociliary clearance in the airways', *American Journal of Respiratory and Critical Care Medicine*, 154(6 Pt 1), pp. 1868–1902. Available at: https://doi.org/10.1164/ajrccm.154.6.8970383.

Watanabe, K. *et al.* (2017) 'Structure-based drug discovery for combating influenza virus by targeting the PA–PB1 interaction', *Scientific Reports*, 7(1), p. 9500. Available at: https://doi.org/10.1038/s41598-017-10021-w.

Watanabe, T. *et al.* (2014) 'Influenza Virus-Host Interactome Screen as a Platform for Antiviral Drug Development', *Cell Host & Microbe*, 16(6), pp. 795–805. Available at: https://doi.org/10.1016/j.chom.2014.11.002.

Webster, R.G. *et al.* (1982) 'Molecular mechanisms of variation in influenza viruses', *Nature*, 296(5853), pp. 115–121. Available at: https://doi.org/10.1038/296115a0.

Webster, R.G. *et al.* (1992) 'Evolution and ecology of influenza A viruses.', *Microbiological Reviews*, 56(1), pp. 152–179.

Wei, Y. *et al.* (2024) 'Exploring TRIM proteins' role in antiviral defense against influenza A virus and respiratory coronaviruses', *Frontiers in Cellular and Infection Microbiology*, 14. Available at: https://doi.org/10.3389/fcimb.2024.1420854.

Weis, W. *et al.* (1988) 'Structure of the influenza virus haemagglutinin complexed with its receptor, sialic acid', *Nature*, 333(6172), pp. 426–431. Available at: https://doi.org/10.1038/333426a0.

Wen, Z. *et al.* (2013) 'A spheroid-based 3-D culture model for pancreatic cancer drug testing, using the acid phosphatase assay', *Brazilian Journal of Medical and Biological Research = Revista Brasileira De Pesquisas Medicas E Biologicas*, 46(7), pp. 634–642. Available at: https://doi.org/10.1590/1414-431X20132647.

Whitcutt, M.J., Adler, K.B. and Wu, R. (1988) 'A biphasic chamber system for maintaining polarity of differentiation of cultured respiratory tract epithelial cells', *In Vitro Cellular & Developmental Biology: Journal of the Tissue Culture*

Association, 24(5), pp. 420–428. Available at: https://doi.org/10.1007/BF02628493.

White, S.K. *et al.* (2016) 'Serologic evidence of exposure to influenza D virus among persons with occupational contact with cattle', *Journal of Clinical Virology: The Official Publication of the Pan American Society for Clinical Virology*, 81, pp. 31–33. Available at: https://doi.org/10.1016/j.jcv.2016.05.017.

van Wielink, R. *et al.* (2012) 'Effect of natural and chimeric haemagglutinin genes on influenza A virus replication in baby hamster kidney cells', *Journal of Biotechnology*, 162(2–3), pp. 197–201. Available at: https://doi.org/10.1016/j.jbiotec.2012.10.005.

Wienerroither, S. *et al.* (2014) 'Regulation of NO Synthesis, Local Inflammation, and Innate Immunity to Pathogens by BET Family Proteins', *Molecular and Cellular Biology*, 34(3), pp. 415–427. Available at: https://doi.org/10.1128/MCB.01353-13.

Wiley, D.C. and Skehel, J.J. (1987) 'The structure and function of the hemagglutinin membrane glycoprotein of influenza virus', *Annual Review of Biochemistry*, 56, pp. 365–394. Available at: https://doi.org/10.1146/annurev.bi.56.070187.002053.

Wilke, C.O. *et al.* (2001) 'Evolution of digital organisms at high mutation rates leads to survival of the flattest', *Nature*, 412(6844), pp. 331–333. Available at: https://doi.org/10.1038/35085569.

Wilkinson, D.C. *et al.* (2017) 'Development of a Three-Dimensional Bioengineering Technology to Generate Lung Tissue for Personalized Disease Modeling', *Stem Cells Translational Medicine*, 6(2), pp. 622–633. Available at: https://doi.org/10.5966/sctm.2016-0192.

Wille, M. and Barr, I.G. (2022) 'Resurgence of avian influenza virus', *Science*, 376(6592), pp. 459–460. Available at: https://doi.org/10.1126/science.abo1232.

Wise, H.M. *et al.* (2012) 'Identification of a Novel Splice Variant Form of the Influenza A Virus M2 Ion Channel with an Antigenically Distinct Ectodomain', *PLOS Pathogens*, 8(11), p. e1002998. Available at: https://doi.org/10.1371/journal.ppat.1002998.

Wong, C.Y.J., Ong, H.X. and Traini, D. (2022) 'The application of in vitro cellular assays for analysis of electronic cigarettes impact on the airway', *Life Sciences*, 298, p. 120487. Available at: https://doi.org/10.1016/j.lfs.2022.120487.

Wood, K., Tellier, M. and Murphy, S. (2018) 'DOT1L and H3K79 Methylation in Transcription and Genomic Stability', *Biomolecules*, 8(1), p. 11. Available at: https://doi.org/10.3390/biom8010011.

World Health Organization (2011) *Pandemic preparedness*. Available at: https://www.who.int/europe/news-room/fact-sheets/item/pandemic-preparedness (Accessed: 4 September 2024).

World Health Organization (2023) *Influenza (Seasonal)*. Available at: https://www.who.int/news-room/fact-sheets/detail/influenza-(seasonal) (Accessed: 5 September 2024).

World Health Organization (2024) *Recommendations announced for influenza vaccine composition for the 2024-2025 northern hemisphere influenza season*. Available at: https://www.who.int/news/item/23-02-2024-recommendations-announced-for-influenza-vaccine-composition-for-the-2024-2025-northern-hemisphere-influenza-season (Accessed: 11 March 2025).

Wu, W. *et al*. (2020) 'IRF7 Is Required for the Second Phase Interferon Induction during Influenza Virus Infection in Human Lung Epithelia', *Viruses*, 12(4), p. 377. Available at: https://doi.org/10.3390/v12040377.

Wu, X. and Zhang, Y. (2017) 'TET-mediated active DNA demethylation: mechanism, function and beyond', *Nature Reviews. Genetics*, 18(9), pp. 517–534. Available at: https://doi.org/10.1038/nrg.2017.33.

Xia, S. *et al*. (2020) 'Coupled CRC 2D and ALI 3D Cultures Express Receptors of Emerging Viruses and Are More Suitable for the Study of Viral Infections Compared to Conventional Cell Lines', *Stem Cells International*, 2020, p. 2421689. Available at: https://doi.org/10.1155/2020/2421689.

Xiong, X. *et al*. (2013) 'Receptor binding by an H7N9 influenza virus from humans', *Nature*, 499(7459), pp. 496–499. Available at: https://doi.org/10.1038/nature12372.

Xu, M. *et al*. (2018) 'SHMT2 and the BRCC36/BRISC deubiquitinase regulate HIV-1 Tat K63-ubiquitylation and destruction by autophagy', *PLoS Pathogens*, 14(5), p. e1007071. Available at: https://doi.org/10.1371/journal.ppat.1007071.

Yamada, H. *et al*. (2014) 'Dextran sulfate-resistant A/Puerto Rico/8/34 influenza virus is associated with the emergence of specific mutations in the neuraminidase glycoprotein', *Antiviral Research*, 111, pp. 69–77. Available at: https://doi.org/10.1016/j.antiviral.2014.09.002.

Yamauchi, Y. *et al*. (2011) 'Histone Deacetylase 8 Is Required for Centrosome Cohesion and Influenza A Virus Entry', *PLOS Pathogens*, 7(10), p. e1002316. Available at: https://doi.org/10.1371/journal.ppat.1002316.

Yamaya, M. *et al*. (1992) 'Differentiated structure and function of cultures from human tracheal epithelium', *The American Journal of Physiology*, 262(6 Pt 1), pp. L713-724. Available at: https://doi.org/10.1152/ajplung.1992.262.6.L713.

Yan, N. and Chen, Z.J. (2012) 'Intrinsic antiviral immunity', *Nature Immunology*, 13(3), pp. 214–222. Available at: https://doi.org/10.1038/ni.2229.

Yang, H. *et al*. (2012) 'Structure and Receptor Complexes of the Hemagglutinin from a Highly Pathogenic H7N7 Influenza Virus', *Journal of Virology*, 86(16), pp. 8645–8652. Available at: https://doi.org/10.1128/jvi.00281-12.

Yang, J. *et al*. (2017) 'Pathogenicity of modified bat influenza virus with different M genes and its reassortment potential with swine influenza A virus',

Journal of General Virology, 98(4), pp. 577–584. Available at: https://doi.org/10.1099/jgv.0.000715.

Yasuhara, A. *et al.* (2022) 'A broadly protective human monoclonal antibody targeting the sialidase activity of influenza A and B virus neuraminidases', *Nature Communications*, 13(1), p. 6602. Available at: https://doi.org/10.1038/s41467-022-34521-0.

Yasuoka, S. *et al.* (1997) 'Purification, characterization, and localization of a novel trypsin-like protease found in the human airway', *American Journal of Respiratory Cell and Molecular Biology*, 16(3), pp. 300–308. Available at: https://doi.org/10.1165/ajrcmb.16.3.9070615.

Yoneyama, M. and Fujita, T. (2007) 'RIG-I family RNA helicases: cytoplasmic sensor for antiviral innate immunity', *Cytokine & Growth Factor Reviews*, 18(5–6), pp. 545–551. Available at: https://doi.org/10.1016/j.cytogfr.2007.06.023.

You, S. *et al.* (2023) 'High cell density and high-resolution 3D bioprinting for fabricating vascularized tissues', *Science Advances*, 9(8), p. eade7923. Available at: https://doi.org/10.1126/sciadv.ade7923.

Yu, Y. *et al.* (2024) 'A panel of janus kinase inhibitors identified with anti-inflammatory effects protect mice from lethal influenza virus infection', *Antimicrobial Agents and Chemotherapy*, 68(4), p. e0135023. Available at: https://doi.org/10.1128/aac.01350-23.

Yuan, Z. *et al.* (2022) 'Hydroxychloroquine blocks SARS-CoV-2 entry into the endocytic pathway in mammalian cell culture', *Communications Biology*, 5(1), pp. 1–12. Available at: https://doi.org/10.1038/s42003-022-03841-8.

Zaderer, V. *et al.* (2019) 'Turning the World Upside-Down in Cellulose for Improved Culturing and Imaging of Respiratory Challenges within a Human 3D Model', *Cells*, 8(10), p. 1292. Available at: https://doi.org/10.3390/cells8101292.

Zamarin, D., Ortigoza, M.B. and Palese, P. (2006) 'Influenza A Virus PB1-F2 Protein Contributes to Viral Pathogenesis in Mice', *Journal of Virology*, 80(16), pp. 7976–7983. Available at: https://doi.org/10.1128/jvi.00415-06.

Zanin, M. *et al.* (2016) 'The interaction between respiratory pathogens and mucus', *Cell host & microbe*, 19(2), pp. 159–168. Available at: https://doi.org/10.1016/j.chom.2016.01.001.

Zaraket, H., Bridges, O.A. and Russell, C.J. (2013) 'The pH of Activation of the Hemagglutinin Protein Regulates H5N1 Influenza Virus Replication and Pathogenesis in Mice', *Journal of Virology*, 87(9), pp. 4826–4834. Available at: https://doi.org/10.1128/jvi.03110-12.

Zarkoob, H. *et al.* (2022) 'Modeling SARS-CoV-2 and influenza infections and antiviral treatments in human lung epithelial tissue equivalents', *Communications Biology*, 5, p. 810. Available at: https://doi.org/10.1038/s42003-022-03753-7.

Zeng, H. *et al.* (2011) 'The 2009 Pandemic H1N1 and Triple-Reassortant Swine H1N1 Influenza Viruses Replicate Efficiently but Elicit an Attenuated Inflammatory Response in Polarized Human Bronchial Epithelial Cells', *Journal of Virology*, 85(2), pp. 686–696. Available at: https://doi.org/10.1128/jvi.01568-10.

Zenilman, J.M. *et al.* (2015) 'Phase 1 clinical trials of DAS181, an inhaled sialidase, in healthy adults', *Antiviral Research*, 123, pp. 114–119. Available at: https://doi.org/10.1016/j.antiviral.2015.09.008.

Zhai, Y. *et al.* (2015) 'Host Transcriptional Response to Influenza and Other Acute Respiratory Viral Infections – A Prospective Cohort Study', *PLoS Pathogens*, 11(6), p. e1004869. Available at: https://doi.org/10.1371/journal.ppat.1004869.

Zhang, B. *et al.* (2019) '3D Bioprinting: A Novel Avenue for Manufacturing Tissues and Organs', *Engineering*, 5(4), pp. 777–794. Available at: https://doi.org/10.1016/j.eng.2019.03.009.

Zhang, J. *et al.* (2024) 'Influenza A virus infection activates STAT3 to enhance SREBP2 expression, cholesterol biosynthesis, and virus replication', *iScience*, 27(8). Available at: https://doi.org/10.1016/j.isci.2024.110424.

Zhao, D. *et al.* (2016) 'C646, a Novel p300/CREB-Binding Protein-Specific Inhibitor of Histone Acetyltransferase, Attenuates Influenza A Virus Infection', *Antimicrobial Agents and Chemotherapy*, 60(3), pp. 1902–1906. Available at: https://doi.org/10.1128/AAC.02055-15.

Zhao, Z. *et al.* (2023) 'Host DNA Demethylation Induced by DNMT1 Inhibition Up-Regulates Antiviral OASL Protein during Influenza a Virus Infection', *Viruses*, 15(8), p. 1646. Available at: https://doi.org/10.3390/v15081646.

Zhong, S., Salomoni, P. and Pandolfi, P.P. (2000) 'The transcriptional role of PML and the nuclear body', *Nature Cell Biology*, 2(5), pp. E85–E90. Available at: https://doi.org/10.1038/35010583.

Zhou, A. *et al.* (2021) 'Comprehensive Transcriptomic Analysis Identifies Novel Antiviral Factors Against Influenza A Virus Infection', *Frontiers in Immunology*, 12. Available at: https://doi.org/10.3389/fimmu.2021.632798.

Zhou, J. *et al.* (2018) 'Differentiated human airway organoids to assess infectivity of emerging influenza virus', *Proceedings of the National Academy of Sciences*, 115(26), pp. 6822–6827. Available at: https://doi.org/10.1073/pnas.1806308115.

Zhu, J. *et al.* (2014) 'Antiviral Activity of Human OASL Protein Is Mediated by Enhancing Signaling of the RIG-I RNA Sensor', *Immunity*, 40(6), pp. 936–948. Available at: https://doi.org/10.1016/j.immuni.2014.05.007.

Zhu, W. *et al.* (2017) 'Direct 3D bioprinting of prevascularized tissue constructs with complex microarchitecture', *Biomaterials*, 124, pp. 106–115. Available at: https://doi.org/10.1016/j.biomaterials.2017.01.042.

Zhu, Y. *et al*. (2020) ‘Human TRA2A determines influenza A virus host adaptation by regulating viral mRNA splicing’, *Science Advances*, 6(25), p. eaaz5764. Available at: https://doi.org/10.1126/sciadv.aaz5764.

Zhu, Y. *et al*. (2023) ‘N6-methyladenosine reader protein YTHDC1 regulates influenza A virus NS segment splicing and replication’, *PLOS Pathogens*, 19(4), p. e1011305. Available at: https://doi.org/10.1371/journal.ppat.1011305.

Ziegler, T. *et al*. (2022) ‘Global Influenza Surveillance and Response System: 70 years of responding to the expected and preparing for the unexpected’, *The Lancet*, 400(10357), pp. 981–982. Available at: https://doi.org/10.1016/S0140-6736(22)01741-X.